



Real-space correlations in dissipative quantum systems





Real-space correlations in dissipative quantum systems

Inaugural-Dissertation

zur

Erlangung des Doktorgrades

der Mathematisch-Naturwissenschaftlichen Fakultät

der Universität zu Köln

vorgelegt von

Etienne Gärtner

aus Leverkusen





Bibliografische Information der Deutschen Nationalbibliothek

Die Deutsche Nationalbibliothek verzeichnet diese Publikation in der Deutschen Nationalbibliografie; detaillierte bibliografische Daten sind im Internet über <http://dnb.d-nb.de> abrufbar.

1. Aufl. - Göttingen: Cuvillier, 2014
Zugl.: Köln, Univ., Diss., 2014

© CUVILLIER VERLAG, Göttingen 2014
Nonnenstieg 8, 37075 Göttingen
Telefon: 0551-54724-0
Telefax: 0551-54724-21
www.cuvillier.de

Alle Rechte vorbehalten. Ohne ausdrückliche Genehmigung des Verlages ist es nicht gestattet, das Buch oder Teile daraus auf fotomechanischem Weg (Fotokopie, Mikrokopie) zu vervielfältigen.

1. Auflage, 2014

Gedruckt auf umweltfreundlichem, säurefreiem Papier aus nachhaltiger Forstwirtschaft

ISBN 978-3-95404-850-2
eISBN 978-3-7369-4850-1



Die vorliegende Dissertation wurde angenommen durch die
Mathematisch-Naturwissenschaftliche Fakultät der Universität zu Köln.

Berichterstatter: Priv. Doz. Dr. Ralf Bulla
(Gutachter)

Prof. Dr. Simon Trebst

Tag der mündlichen Prüfung: 27.06.2014





Contents

Abstract	1
Kurzzusammenfassung	3
1. Introduction	5
2. Introduction of the models	9
2.1. Dissipative oscillator model	9
2.2. Two-spin-boson model	14
3. Correlation functions	19
3.1. Resolvent and equations of motion	19
3.2. Lehmann-representation and spectral functions	22
3.3. Average site occupation and displacement amplitude	23
3.4. Bath single particle propagator	26
3.4.1. Dissipative oscillator model	26
3.4.2. Two-spin-boson model	28
3.5. Bath displacement-displacement correlator	30
3.5.1. Dissipative oscillator model	30
3.5.2. Two-spin-boson model	31
4. Bath spectral functions	33
4.1. Dissipative oscillator model	33
4.2. Two-spin-boson model	36
4.3. Free bath propagator in position space	37
4.4. Impurity scattering matrix	42
5. Numerical Renormalization Group	45
5.1. Logarithmic discretisation	49
5.2. Mapping onto a chain-Hamiltonian	56
5.3. Diagonalisation and truncation	60
5.4. Obtaining spectral functions from NRG data	67
5.5. Numerical implementation	71
5.5.1. Storage of the Hamiltonian	71
5.5.2. Exact Diagonalisation	75
5.5.3. Lanczos Algorithm	76
5.5.4. Operator transformation	78



6. Results	81
6.1. Dissipative oscillator model	81
6.1.1. Analytic results for $U = 0$	81
6.1.2. Identification of fixed points	90
6.1.3. Determination of the phase diagram	100
6.1.4. Impurity scattering matrix and local averages	103
6.1.5. Conclusion	112
6.2. Two-spin-boson model	113
6.2.1. Identification of fixed points	113
6.2.2. Zero inter-impurity distance	114
6.2.3. Finite inter-impurity distances	117
6.2.4. Impurity scattering matrix and local averages	122
6.2.5. Conclusion	127
Summary	129
Outlook	130
A. Impurity displacement-displacement correlation function	131
B. Calculation of the ξ_n	133
References	135
Danksagungen	141
Erklärung	145
Lebenslauf	147



Abstract

In this thesis two different dissipative quantum impurity systems are studied. The dissipative environment in both models is described by a one-dimensional chain of bosons with an ohmic spectral density. By coupling to the impurities, the translational invariance in the environment is broken. It is investigated to what extent impurities of different nature can be traced in the environment by means of static thermal averages as a function of distance to the impurities.

In the first model, an oscillator is used as the impurity in the system. The impurity oscillator can act on itself via density-density interactions. For zero self-interaction, the system is studied analytically via equations of motion, as all relevant propagators can be expressed in terms of the bare ones. In the limit of infinite self-interaction, the system then transforms into the renowned spin-boson model [27, 51]. Here, the system shows a Kosterlitz-Thouless quantum phase transition as a function of the coupling strength between impurity and an ohmic environment. This transition can be observed between a delocalised phase where the reduced two-level impurity system performs oscillations between the two states and a localised phase where the impurity is frozen in either of those two remaining states. In the range from zero to infinite self-interaction the system is elusive to a purely analytic treatment. To investigate the model in that regime, the Numerical Renormalization Group method (NRG) is employed. Based on the NRG results, a renormalization-group flow of the system-parameters is suggested, incorporating a whole line of quantum-phase-transitions as a function of coupling strength between impurity and environment.

As a second model two identical spin-1/2 impurities are coupled at a variable distance to the environment. The model has been studied before in case of zero inter-impurity distance [41, 24], where the chosen interaction of the spins via their z -component to the bath induces a ferromagnetic interaction between the spins. In the two-dimensional subspace of parallel aligned spins there is again a quantum phase transition of the Kosterlitz-Thouless nature as a function of the coupling strength between impurities and environment. For infinite distance, each spin is independently treatable and the system can be described by two uncoupled spin-boson models. A wide range of impurity distances is studied within this thesis in order to trace the quantum phase transition between zero and infinite inter-impurity distance. To this end, a two-channel NRG for Bosonic models is developed that is capable of dealing with both limits. Details on the algorithm and its implementation are presented in this work.

In the delocalised phases of the models, the average site occupation in the environment is changed due to the presence of the impurities. This change is found to drop in a power-law manner with growing distance to the impurities, where different phases show different power-law exponents. In addition, the change in the average displacement of the environmental bosons due to the coupling to the impurities is calculated. While this change is highly sensitive to numerical noise in intermediate parameter



regimes, power-laws can be extrapolated as well for a large range of parameters. Between the two spin-1/2 impurities of the second model the changes in the thermal averages remain comparably large, indicating an effective coupling of the impurities which is mediated by the common environment. In conclusion, no intrinsic length scale is found in the environment in either of the models. The implemented bosonic two-channel NRG proved successful in describing the physics of the two-spin-boson model in its delocalised phase.



Kurzzusammenfassung

In der vorliegenden Arbeit werden dissipative Quantenstörstellen-Systeme betrachtet, in denen verschieden geartete Störstellen an eine gemeinsame dissipative Umgebung koppeln. Die dissipative Umgebung wird hierbei in beiden Fällen durch eine eindimensionale Kette von Bosonen mit ohmscher Spektraldichte beschrieben. Da durch die Kopplung von Störstellen an die Umgebung deren Translationsinvarianz gebrochen wird, ergibt sich die Frage, inwiefern verschiedenartige Störstellen innerhalb der eindimensionalen Kette nachweisbar sind. Hierzu werden statische thermische Erwartungswerte innerhalb der Kette als Funktion des Abstandes zu den Störstellen in beiden Modellen betrachtet.

In dem zuerst betrachteten Modell fungiert ein Oszillator als Störstelle, der mit sich selbst durch Dichte-Dichte-Wechselwirkungen interagieren kann. Bei Abwesenheit dieser Selbstwechselwirkung können die Bewegungsgleichungen des betrachteten, rein bosonischen Modells, vollständig analytisch gelöst werden. Im Grenzfall unendlich starker Selbstwechselwirkung geht das Modell in das bekannte Spin-Boson Modell über [27, 51]. Dieses zeigt einen Kosterlitz-Thouless Quantenphasenübergang in Abhängigkeit der Kopplungsstärke zwischen Störstellenoszillator und Umgebung. Hierbei findet der Übergang zwischen einer delokalisierten Phase und einer lokalisierten Phase auf der Störstelle statt. Während in der delokalisierten Phase eine endliche Tunnelwahrscheinlichkeit zwischen den beiden möglichen Zuständen der Störstelle besteht, wird die Störstelle in der lokalisierten Phase durch die starke Kopplung an ihre Umgebung in einem der beiden Zustände eingefroren und ein Tunneln ist nicht mehr möglich. Da das System für endliche Selbstwechselwirkungsstärken nicht analytisch lösbar ist, verwenden wir in diesem Parameterregime die Numerische Renormierungsgruppenmethode (NRG), um Resultate zu erhalten. Basierend auf den Ergebnissen der NRG-Berechnungen wird ein Phasendiagramm entwickelt, welches eine Linie von Quantenphasenübergängen als Funktion der Kopplungsstärke zwischen Störstellenoszillator und Umgebung für alle Werte der Selbstwechselwirkung der Störstelle aufweist.

Für das zweite betrachtete Modell werden zwei magnetische Spin-1/2 Momente als Störstellen gewählt, die in einem endlichen Abstand voneinander an die gemeinsame Umgebung koppeln. Dieses Modell wurde bereits ausgiebig für den Fall untersucht, dass beide Störstellen lokal an die gleiche Stelle der Umgebung koppeln [41, 24]. In dem Fall induziert die Kopplung beider Störstellen-Spins über deren z -Komponente an die gemeinsame Umgebung effektiv eine ferromagnetische Wechselwirkung. Innerhalb des zweidimensionalen Unterraums parallel ausgerichteter Spins findet dann wieder ein Kosterlitz-Thouless Quantenphasenübergang als Funktion der Kopplungsstärke zwischen Störstellen und Umgebung statt. Im Fall unendlich weit separierter Spins werden diese unabhängig voneinander und die korrekte Beschreibung des Modells ist die zweier unabhängiger Spin-Boson Modelle. Das Modell wird für verschiedene Abstände mehrerer Größenordnungen zwischen den beiden Störstellen untersucht, um die Grenzfälle



keines und unendlich großen Abstandes miteinander in Verbindung zu bringen. Zu diesem Zweck wird eine Zwei-Kanal-NRG für bosonische Modelle entwickelt, mit deren Hilfe beide Grenzfälle untersucht werden können. Details zur Zwei-Kanal-NRG und ihrer Implementierung werden in der Arbeit vorgestellt.

In allen Phasen der betrachteten Modelle wird die lokale Besetzung der einzelnen Umgebungsoszillatoren durch die Anwesenheit der Störstellen erhöht. Hierbei fällt die zusätzliche Besetzung als Funktion des Abstandes zu den Störstellen nach einem Potenzgesetz ab. Des Weiteren wird die Änderung der mittleren Auslenkung der Umgebungsoszillatoren durch die Anwesenheit der Störstellen untersucht. Es zeigt sich, dass diese Berechnungen für große Abstände numerisch ungenau werden, da dort starke Oszillationen der freien Propagatoren vorliegen. Dennoch zeigen sich für eine Vielzahl von Parametern und kleine bis mittlere Abstände zu den Störstellen ebenfalls Potenzgesetze für die Änderung der mittleren Oszillatorauslenkung in der Umgebung. Zwischen den beiden Störstellen des zweiten Modells ergeben sich vergleichsweise starke Änderungen in den Erwartungswerten der Umgebung, die auf eine indirekte Wechselwirkung der Spins miteinander durch die gemeinsame Umgebung hindeutet. Aus den untersuchten Modellen lassen sich für die verschiedenen Störstellen keine typischen Längenskalen ableiten.



1. Introduction

Ever since Richard P. Feynman's keynote speech at the first conference on physics and computation at the MIT in 1981, where he presented his idea of a quantum computer as a simulator of quantum mechanical systems [16], computer scientists and physicists alike expended huge efforts to actually realise such a device. The simulation of quantum mechanical systems by means of other, controllable quantum systems has shown first promising results in recent years as the field of quantum optics has grown to a point where one-, two-, and three-dimensional optical lattices can be constructed by interference of laser light. In these optical lattices, ultracold atomic gases could then be efficiently controlled to simulate solid states of matter. There, e. g. the paramount model of solid state theoretical physics, the Hubbard model, has been shown to be realizable in case of bosonic particles [21].

While the prospect of a quantum simulator is fascinating and desirable to actually probe the models that physicists claim to describe nature, a second branch has emerged that is interested in quantum systems to perform calculations which are not possible on a classical computer.

As the algorithms needed for such a quantum computer are entirely different from classical computer algorithms, only a handful have been devised so far which are known to outperform any classical algorithm. The most prominent ones are those of quantum Fourier transform and its application to the factorisation of large integer numbers and the quantum search, or Grover's algorithm, useful e. g. in the solution of the travelling salesman problem [36].

However, it is not only algorithms that need to be invented in the field of quantum computation but also means to build quantum mechanical systems and control them with high accuracy. Like the NAND logic gate is the universal gate of classical computer, making it possible to build any other logic gate from a number of NAND gates, "any multiple qubit logic gate may be composed from CNOT and single qubit gates" [36], making those the universal building blocks of a quantum computer.

Since at first no physicist had the knowledge of how to build single quantum bits and perform controlled operations on them, a wide field of possible systems have been proposed and built, culminating only recently in the 2012 Physics Nobel prize for Serge Haroche and David J. Wineland "for ground-breaking experimental methods that enable measuring and manipulation of individual quantum systems" [38].

To the author the most promising candidates for scalable arrays of quantum bits, out of which quantum registers may be composed, are quantum dots already realised in GaAs semiconductor devices [43] and recently also in silicon-based semiconductors [17], circuit-quantum electro dynamics (QED) [49, 15] and the aforementioned optical lattice systems with ultra cold atomic gases [29]. Besides these, there is the rather new class of topological insulators where stable topological excitations (particles) may e. g. arise in between the surfaces of topological insulator/superconductor heterostructures [34]. Those topological excitations may then be stable against decoherence, like the

two Majorana-Fermions at the ends of a superconducting nano-wire that have been proposed and arguably been measured [35].

While multiple qubits in a quantum register should behave independently, their connection to the same environment may spoil that independence, as they start to influence each other via the environment. In this work two qubits, modelled by magnetic spin-1/2 impurities, are investigated that are coupled at a finite distance to the same dissipative environment. From the spin-boson model it is known that there exists a phase for weak coupling where the spin is not localised in either of its states $|\uparrow\rangle$ or $|\downarrow\rangle$ and may thus explore the whole $SU(2)$ Bloch sphere, while for strong coupling it is localised in one of those configurations, completely destroying its quantum mechanical nature [27]. As a second spin is coupled in direct vicinity of the first, the environment mediates an effective ferromagnetic interaction between the spins, rendering them no longer independent [41].

Within the Numerical Renormalization Group (NRG) it is investigated at which point the two spins can be treated independently as the distance between them is increased. To this end a two-channel bosonic NRG is developed that can deal with the model and its limit of two independent spin-boson models. The two-channel NRG is first tested on a model incorporating a single oscillator as an impurity. While the latter model only involves a single channel, a self-interaction of the impurity oscillator provides accessible limits, where the numerical implementation of the two-channel NRG can be tested. Furthermore signals of the different impurities are traced in the environment by means of thermal averages and their changes due to the presence of the impurities.

Outline

The thesis presented here is structured as follows. The two dissipative quantum impurity models under discussion, named the dissipative oscillator model (do) and the two-spin-boson model (2sbm) are introduced in detail in section 2. For the environment, a one-dimensional chain of bosons in real space is chosen to which the different impurities are then connected. While the one-dimensional character of the environment allows for a convenient calculation of distance-dependent averages, it is not the generic kind of system to show an ohmic spectrum of excitations, as studied here. The latter is only achieved in this thesis by tuning the particle dispersion and thus in real space the hopping amplitudes of excitations between the different sites in the chain. For the chosen dispersion, however, long range hopping amplitudes that drop in a power-law manner emerge in real-space. To which extent such a dispersion can be achieved in, e. g. optical lattice experiments with very shallow potentials, remains elusive at this point in time. In higher dimensional systems an ohmic spectrum is more likely to appear without the need of such long-range hopping. There the calculation of the distance-dependent averages—of interest in this thesis—turns out to be more complicated to obtain numerically.

Section 3 introduces the concept of correlation functions and illustrates how they may be obtained from a set of equations of motion. Afterwards, the representation of correlation functions in terms of Lehmann-sums and their connection to spectral functions via their imaginary part are stated. The connection between thermal expectation values for the site occupation as well as the average displacement of the environmental oscillators to corresponding correlation functions is drawn in sections 3.4 and 3.5 respectively. The processes that need to be averaged involve both free propagation between different sites and scattering at either one of the impurities.

The scattering processes are encoded in so-called scattering matrices which are purely described in terms of impurity correlation functions. In case of the dissipative oscillator model the scattering matrix is a complex function whereas for the two-spin-boson model it obtains a more complex, 2×2 matrix structure of complex functions. Both the free bath correlators for different distances and the scattering matrices entering the thermal average processes are derived in section 4. Here, it is also shown how the bath spectral functions which enter the different models are connected to the dispersion relation of the bosonic particles in the chain and how the long-range, real-space hopping amplitudes emerge.

Section 5 focuses on the discussion of the Numerical Renormalization Group (NRG) and its application to both models. After its introduction a discussion of how spectral functions can be obtained from the numerical data provided by the NRG follows. Section 5.5 examines the actual implementation of the NRG employing sparse matrix storage formats and Lanczos diagonalisation routines for the appearing Hamiltonians. The computational demands of the current NRG implementation are compared to an implementation which uses dense matrix representations and exact diagonalisation routines as is typical for a single channel NRG.

The results obtained for the two models under discussion are presented in section 6. In both models the renormalization group flow and the fixed point structure of the Hamiltonians that are set up within the NRG are discussed.

Section 6.1 presents the results that have been derived for the dissipative oscillator model. For every value of the self-interaction of the impurity oscillator, the NRG data suggest a quantum phase transition in the dissipative oscillator model as a function of the coupling strength between impurity and environment. In the scattering matrix the pole at the bare oscillator frequency is found to be shifted to lower frequencies as the coupling strength to the environment increases. At the same time, the peak is broadened and its height increased until it finally vanishes beyond the quantum critical point. With the results for the scattering matrix, finally the thermal averages in the environment are calculated as a function of distance to the impurity oscillator. Both the average site occupation and the average displacement of the oscillators are found to change strongest right at the impurity. Going away from the impurity those changes then drop in a power-law manner for a large range of parameters.

For the two-spin-boson model the results are collected in section 6.2. There the fixed point spectra for finite inter-impurity distance are compared to those for zero



distance between the impurities. A localised and a delocalised phase are found to exist for every distance investigated in this work. In the spectrum of the scattering matrix a low energy peak appears that can be assigned to a renormalized tunnelling rate on the impurities. This peak is suppressed as the localised phase is entered and the impurities are each locked in a single configuration. The distance dependent averages that are calculated in the environment show clear peaks right at the position of the two impurities. In between the impurities, it is possible to see their influence on each other by a comparably large finite effect on the environmental oscillators. Far away from the two impurities, the changes they cause in the environment drop in a power-law manner.

As the different techniques used in this thesis are close to identical for the two models under discussion their application to both models is presented consecutively. This is to emphasise similarities and differences between the two models. In each section, the method at hand is first applied to the dissipative oscillator model, followed by an application of the technique to the two-spin-boson model.



2. Introduction of the models

It is the purpose of this work to study the extent to which different quantum impurity systems, coupled to a common dissipative environment, may influence each other via that environment. Both the low-energy physics of the impurities and different thermal averages in the environment will be determined. Thereby it can be estimated to what extent the impurities effectively influence the environment and thus may also influence each other.

For the quantum impurity systems an oscillator of bosonic nature and two spin-1/2 particles that are coupled at a finite distance R to a common environment are chosen. The dissipative environment itself is modelled in real-space by a one-dimensional chain of bosonic orbitals. The signals that are investigated in the environment are the change of the average site occupation $\Delta\langle\hat{n}_x\rangle$ and the change of the average of the squared displacement $\Delta\langle(a_x + a_x^\dagger)^2\rangle$ of the oscillators at position x in the chain due to the coupling of the impurities to the chain. In the following the two different models under investigation in this work are introduced, which are both connected to the renowned spin-boson model, already investigated by Leggett et al. in 1987 [27]. In that case, a two-state system is coupled to a dissipative environment and the setup is such that the bare two-state system may tunnel between its two states with a rate Δ . As the coupling to the environment is increased the tunnelling rate is suppressed until it eventually becomes zero, freezing the spin in either of its two possible configurations and thereby destroying its quantum mechanical nature.

The otherwise harmonic oscillator in the dissipative oscillator model discussed here features a self-interaction which, as it is increased, projects out higher lying states of the impurity until only two states are left that can be identified with a spin-1/2 system. In case of the two spins of the second model they become independent in the limit of infinite distance R between them and thus each behave as the single spin-1/2 in the spin-boson model.

2.1. Dissipative oscillator model

The first model under investigation features an oscillator with frequency Δ that is subject to dissipation introduced by an environment. The single oscillator here and in the following is termed the impurity as it has in general a different character from the oscillators of the environment. Its Hamiltonian is given by

$$H_{\text{imp}} = \Delta\left(\hat{n}_b + \frac{1}{2}\right) + \epsilon\left(\frac{b + b^\dagger}{2}\right) + \frac{U}{2}\hat{n}_b(\hat{n}_b - 1) \quad (2.1)$$

where b^\dagger creates an excitation of the oscillator that features, apart The underlying potential in real-space is still quadratic, rendering the oscillator harmonic. However, the self-interaction via its density makes coherent states of the harmonic oscillator, which are the next best thing to a classical particle moving in a square potential well,

decohere in time as the eigenenergies of the different states $|n\rangle$ are no longer multiples of the bare oscillator frequency Δ . The environment of the impurity is modelled by an infinite chain of bosons. In real space the bosonic operator $a_{x_i}^\dagger$ creates a particle at position $x_i = ia$ in the chain. Here a is the lattice spacing and $i \in \mathbb{Z}$. The particle can hop with an amplitude $t_{x_i, x_j} = t_{|x_i - x_j|}$ between any two sites x_i and x_j . Typically hopping amplitudes fall off with growing distance $|x_{ij}| = |x_i - x_j|$. In this model the hopping amplitudes are considered to be real and the lattice spacing a to unity are set in the following. Thus the Hamiltonian describing the translational invariant environment can be written as

$$H_{\text{bath}} = \sum_{i,j \in \mathbb{Z}} t_{|x_i - x_j|} a_{x_i}^\dagger a_{x_j} = \sum_{x,y \in \mathbb{Z}} t_{|x|} a_y^\dagger a_{y-x}. \quad (2.2)$$

Dissipation is introduced into the model by coupling the displacement of the impurity to the displacement of the bosonic degree of freedom at the origin of the bath. The interaction part of the model is then given by

$$H_{\text{int}} = \frac{\sqrt{\alpha}}{2} (b + b^\dagger) (a_0 + a_0^\dagger). \quad (2.3)$$

Here α parametrises the coupling strength between the impurity and the bath. Thus the total Hamiltonian of the dissipative oscillator model is given by

$$H_{\text{do}} = H_{\text{imp}} + H_{\text{bath}} + H_{\text{int}},$$

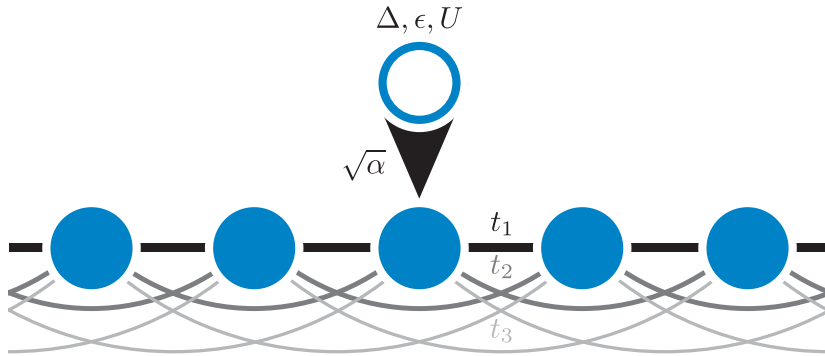
where H_{imp} describes the oscillator of interest (the impurity), H_{bath} describes the free environment and H_{int} comprises the interaction between the oscillator and the bath as mentioned above.

In figure 1, a sketch of the system around the origin is shown which comprises all relevant energy-scales. In order to diagonalise the bath part of the Hamiltonian a Fourier-transformation of the lattice is performed via

$$a_k = \frac{1}{\sqrt{2\pi}} \sum_{x \in \mathbb{Z}} a_x e^{ikx}, \quad a_x = \frac{1}{\sqrt{2\pi}} \int_{-\pi}^{\pi} a_k e^{-ikx} dk. \quad (2.4)$$

Here the integral in k -space is over the first Brillouin-zone. Applying the Fourier-transformation to the bath part of the Hamiltonian leads to

$$\begin{aligned} H_{\text{bath}} &= \frac{1}{2\pi} \sum_{x,y} t_{|x|} \int_{-\pi}^{\pi} \int_{-\pi}^{\pi} a_k^\dagger a_{k'} e^{i(k-k')y} e^{ik'x} dk dk' \\ &= \sum_x t_{|x|} \int_{-\pi}^{\pi} \int_{-\pi}^{\pi} a_k^\dagger a_{k'} \delta(k - k') e^{ik'x} dk dk' \\ &= \int_{-\pi}^{\pi} a_k^\dagger a_k \sum_x t_{|x|} e^{ikx} dk \\ &= \int_{-\pi}^{\pi} \omega(k) a_k^\dagger a_k dk \end{aligned}$$


Figure 1:

The impurity (circle) with energy-scales Δ, ϵ, U couples with a strength $\sqrt{\alpha}$ to the origin of a linear chain of bosons (disks). The bosons in the chain can hop between any two sites where the hopping amplitudes t_x decrease with the distance x between the sites in a power-law manner. Here, only the first three hopping amplitudes t_1, t_2 and t_3 are depicted for clarity.

where $\omega(k) = \sum_x t_{|x|} e^{ikx}$ is the dispersion of the bath-modes. The interaction part of the model is likewise transformed to

$$H_{\text{int}} = \frac{1}{2} \sqrt{\frac{\alpha}{2\pi}} (b + b^\dagger) \int_{-\pi}^{\pi} (a_k + a_k^\dagger) dk.$$

The total Hamiltonian describing the oscillator with bare frequency Δ which can be damped by the coupling to a one dimensional chain of bosons thus reads

$$H_{\text{do}} = H_{\text{imp}} + \int_{-\pi}^{\pi} \omega(k) a_k^\dagger a_k dk + \frac{1}{2} \sqrt{\frac{\alpha}{2\pi}} (b + b^\dagger) \int_{-\pi}^{\pi} (a_k + a_k^\dagger) dk \quad (2.5)$$

in momentum space.

Until now there were not any specific hopping parameters $t_{|x|}$ chosen, they were merely considered to be real and expected to drop with growing distance. The $t_{|x|}$ are connected to the spectral function of the bath via the dispersion relation $\omega(k)$. In this work, models which show a power-law behaviour in the spectral function of the chain are investigated. The spectral function here is parametrised as

$$J(\omega) = \begin{cases} \alpha\pi(s+1)\omega^s\omega_c^{1-s} & , \text{ for } 0 \leq \omega \leq \omega_c \\ 0 & , \text{ else.} \end{cases} \quad (2.6)$$

Here $s > -1$ is the power-law exponent, α parametrises the coupling strength between bath and impurity and ω_c is a high-frequency cutoff. Throughout this thesis only models that show an ohmic spectral density where $s = 1$ are investigated. In section

4.1 it will be discussed that the spectral function $J(\omega)$ is connected to the imaginary part of the local retarded Green's function $\langle\langle a_0, a_0^\dagger \rangle\rangle_{\omega+i\epsilon}$ at the origin of the bath in real space as

$$\begin{aligned} J(\omega) &= -\alpha \lim_{\epsilon \rightarrow 0} \text{Im}[\langle\langle a_0, a_0^\dagger \rangle\rangle_{\omega+i\epsilon}] \\ &= \frac{\alpha}{2} \int_{-\pi}^{\pi} \delta(\omega - \omega(k)) dk. \end{aligned} \quad (2.7)$$

In the spectral function $J(\omega)$ all information on the single-particle-excitations of the non-interacting bath, which couples to the impurity, is comprised. Besides it will be shown in section 4.1 how one has to adjust the dispersion $\omega(k)$ in order to arrive at the desired behaviour (2.6) of the spectral function. Furthermore it will be validated that the corresponding hopping amplitudes $t_{|x|}$ do drop in a power-law manner in real space as $t_{|x|} \sim |x|^{-(s+2)/(s+1)}$. For the later treatment of the model by means of the Numerical Renormalization Group (NRG) the Hamiltonian is presented here directly in frequency space, which is the usual representation to start with in the NRG-community. Expressing the bath excitations directly in terms of their corresponding frequencies ω instead of their momenta k , the Hamiltonian of the dissipative oscillator model can be rewritten as

$$H = H_{\text{imp}} + \int_0^{\omega_c} g(\omega) a_\omega^\dagger a_\omega d\omega + \frac{1}{2} (b + b^\dagger) \int_0^{\omega_c} h(\omega) (a_\omega + a_\omega^\dagger) d\omega. \quad (2.8)$$

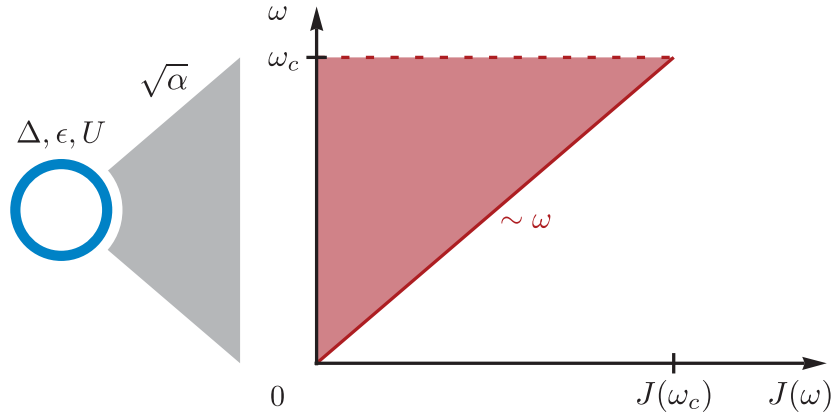
Here the function $g(\omega)$ comprises the possible excitations of the bath modes at frequency ω and the function $h(\omega)$ encodes the coupling of the impurity to those excitations. The functions $g(\omega)$ and $h(\omega)$ are connected to the spectral function $J(\omega)$ [12] by:

$$J(\omega) = \pi \left| \frac{\partial g(\omega)}{\partial \omega} \right|^{-1} h^2(\omega). \quad (2.9)$$

Figure 2 depicts the situation where the impurity couples to a continuous bath that is described by its spectral function $J(\omega)$ given by (2.6) for an ohmic environment with $s = 1$. As the high-frequency cutoff ω_c should represent the largest energy-scale in the problem, all other parameters in the model will be given in units of that cutoff. This way ω_c is factored out leaving the dimensionless Hamiltonian

$$\boxed{\frac{H_{\text{do}}}{\omega_c} = H_{\text{imp}} \left(\frac{\Delta}{\omega_c}, \frac{\epsilon}{\omega_c}, \frac{U}{\omega_c} \right) + \int_0^1 g(\omega) a_\omega^\dagger a_\omega d\omega + \frac{1}{2} (b + b^\dagger) \int_0^1 h(\omega) (a_\omega + a_\omega^\dagger) d\omega.} \quad (2.10)$$

For fixed power-law exponent s and high frequency cutoff ω_c , the model possesses four remaining parameters: the bare frequency of the impurity oscillator Δ , its displacement ϵ , its self-interaction strength U via its local density and finally the coupling strength α of the impurity to the environment. In the following all parameters $X \in \{\Delta, \epsilon, U\}$ are given in units of ω_c and the explicit notation is dropped, keeping only the bare parameter name ($X \hat{=} \frac{X}{\omega_c}$).


Figure 2:

The impurity (circle) with energy-scales Δ, ϵ, U couples with a strength $\sqrt{\alpha}$ to a continuous bath of bosons characterised by the spectral density $J(\omega)$. Here the bath features an ohmic spectral density $J(\omega) \sim \omega$ and corresponds in real-space to the linear chain as depicted in figure 1.

Large- U limit: the spin-boson model

The dissipative oscillator model transforms into the spin-boson model as the on-site interaction U is made stronger and stronger. If the impurity Hamiltonian H_{imp} is expressed in the basis of eigenstates $|n\rangle$ of the number operator $b^\dagger b$, its diagonal elements read

$$\langle n | H_{\text{imp}} | n \rangle = \Delta \left(n + \frac{1}{2} \right) + \frac{U}{2} n(n-1).$$

In the limit of $U \rightarrow \infty$ all states with $n > 1$ are separated from the low energy sector of the theory by an infinite amount of energy and therefore can be effectively projected out. Hence the impurity Hamiltonian is restricted to the two-dimensional basis $\{|0\rangle \hat{=} |\uparrow\rangle, |1\rangle \hat{=} |\downarrow\rangle\}$ where it reads

$$\lim_{U \rightarrow \infty} H_{\text{imp}} = \frac{1}{2} \begin{pmatrix} -\Delta & \epsilon \\ \epsilon & \Delta \end{pmatrix} = \frac{\epsilon}{2} \sigma_x - \frac{\Delta}{2} \sigma_z$$

after the ground-state-energy is shifted by an amount of $-\Delta$. Likewise the interaction part H_{int} is transformed to

$$H_{\text{int}} = \sqrt{\frac{\alpha}{2\pi}} \frac{\sigma_x}{2} \int_{-\pi}^{\pi} (a_k + a_k^\dagger) dk.$$

Thus the total Hamiltonian reads

$$H_{\text{sbm}} = \frac{\epsilon}{2} \sigma_x + \frac{\Delta}{2} \sigma_z + \int_{-\pi}^{\pi} \omega(k) a_k^\dagger a_k dk + \sqrt{\frac{\alpha}{2\pi}} \frac{\sigma_x}{2} \int_{-\pi}^{\pi} (a_k + a_k^\dagger) dk. \quad (2.11)$$

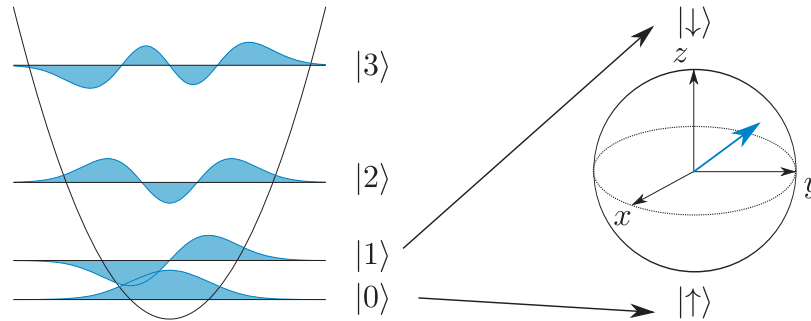


Figure 3:

As the density-density interaction U is increased, all states but the lowest two $|0\rangle$ and $|1\rangle$ of the oscillator are projected out. Those can then be mapped onto a spin-degree of freedom living on the $SU(2)$ sphere.

which is the Hamiltonian of the well studied spin-boson model [27] in momentum representation. Figure 3 depicts the situation where the higher lying oscillator states $|n\rangle$ with $n > 1$ are shifted due to the interaction U . In the end only the two lowest states remain in the theory which then can be mapped onto a spin-1/2 degree of freedom living on the $SU(2)$ sphere. It will be shown numerically in section 6.1.3 that the low energy spectrum of the spin-boson model and the displaced oscillator model agree already for values of $U \sim 10^3$.

In the simplest case of a magnetic field of strength Δ only applied in x -direction and no coupling to the environment, measuring the chance that the spin has returned to an initial state $|\sigma(0)\rangle = |\uparrow\rangle$ after time t leads to the perfect periodic result $\langle \uparrow | \sigma(t) \rangle = \cos(\Delta t/2)$. As the coupling to the environment in z -direction is switched on two things will happen. First of all the oscillations get damped as the environment leads to dissipation. Second of all the frequency Δ of the spin oscillations is decreased as the spin becomes somewhat dressed by environmental fluctuations and is no longer free. Ultimately, strong coupling of the environment to the spin will pin it in a single state for which then $\langle \uparrow | \sigma(t) \rangle = \text{const}$ follows and the quantum mechanical nature of the spin has been destroyed.

2.2. Two-spin-boson model

The second model investigated in this work is termed the two-spin-boson model. It describes two spin-1/2 particles that couple to a common dissipative environment. Here the environment is again modelled by the one-dimensional chain of bosons introduced in the dissipative oscillator model (cf. equation (2.2)). Each of the two spins now couples to a lattice site $\pm r$ with a total of $R = 2r$ environmental lattice sites in between them where $r = 0, 1/2, 1, 3/2, \dots$. Of interest in this study is the behaviour of the two spins as the distance R between them is increased. The Hamiltonian of the model has again the general form

$$H_{2\text{sbm}} = H_{\text{imp}} + H_{\text{bath}} + H_{\text{int}}.$$

Here the impurity part now describes the two spins $\mathbf{S}_i = \frac{1}{2}\boldsymbol{\sigma}_i$, ($i = 1, 2$) that feel a local magnetic field $B_{\text{loc},i} = (\Delta_i, 0, \varepsilon_i)^T$ and couple to each other directly via their z -components with an Ising coupling strength K :

$$H_{\text{imp}} = \frac{\Delta_1}{2}\sigma_{x,1} + \frac{\Delta_2}{2}\sigma_{x,2} + \frac{\varepsilon_1}{2}\sigma_{z,1} + \frac{\varepsilon_2}{2}\sigma_{z,2} + \frac{K}{4}\sigma_{z,1}\sigma_{z,2}. \quad (2.12)$$

In the environment the bosons can again hop between any two sites y and $y - x$ with an amplitude $t_{|x|}$ that only depends on the modulus of the distance x . Here the lattice spacing a has already been set to unity such that $x, y \in \mathbb{Z}$. Thus the bath part of the Hamiltonian is again given by

$$H_{\text{bath}} = \sum_{x,y \in \mathbb{Z}} t_{|x|} a_y^\dagger a_{y-x}. \quad (2.13)$$

The spins are coupled via their z -component to the displacement of the harmonic oscillators to which the individual spins couple. It is the same kind of interaction as in the standard spin-boson model. Spin 1 couples to the oscillator at site $+r$ while spin 2 couples to the oscillator that resides at site $-r$ with a respective coupling strength of $\sqrt{\alpha_{1/2}}$. This leads to an interaction part of the Hamiltonian that reads

$$H_{\text{int}} = \sqrt{\alpha_1} \frac{\sigma_{z,1}}{2} (a_r + a_r^\dagger) + \sqrt{\alpha_2} \frac{\sigma_{z,2}}{2} (a_{-r} + a_{-r}^\dagger) \quad (2.14)$$

in real space. A sketch of the system in real space is presented in figure 4.

In the limit of $r \rightarrow \infty$ the spins do not feel each other (if $K = 0$ is set, which is the only reasonable value for a direct coupling amongst the spins in this limit). In that limit the physics of two spin independent spins is recovered. Each of the spins behaves as the single spin in the spin-boson model whose behaviour depends on the local coupling strength to the bath and the spectrum of that bath.

The two-spin-boson model is studied by means of the Numerical Renormalization Group (NRG), (cf. section 5), as a purely analytical treatment does not suffice to solve the model for a large set of model parameters. In the NRG one typically maps the environment seen by the impurity onto a semi-infinite, one-dimensional chain and couples the impurity to the first site of that chain. The current model features two spins that do not couple to the original one-dimensional chain in real space at the same site. Hence, they do not see locally the same environment. The standard scheme in the mapping of that environment onto an object that is iteratively treatable (the semi-infinite chain) thus has to be altered.

In a first step, the bath is once more Fourier-transformed. There a splitting of the bath modes into symmetric and antisymmetric linear combinations of modes with opposite momentum $\pm k$ is performed. Those combinations are referred to as even

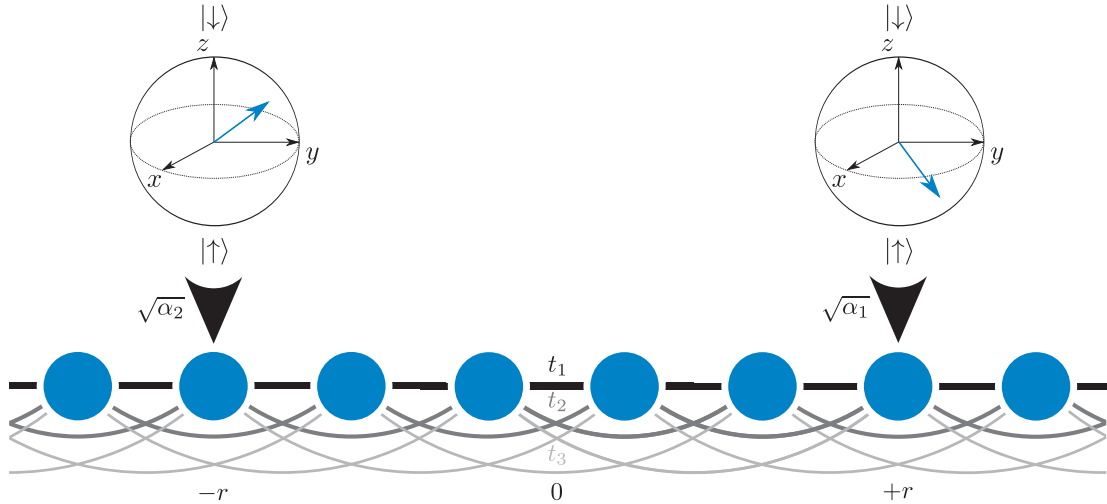


Figure 4:

Two independent spins that couple to a common linear bosonic chain at positions $\pm r$ with respective couplings $\sqrt{\alpha_{1/2}}$. To each spin a magnetic field may be applied (not shown) and the spins may interact directly via an Ising-type interaction as long as they are close to each other. Further interaction between the two spins needs then to be mediated by the common environment.

and odd throughout the remainder of the work. After the mapping it turns out that the even/odd combination of the two spins $\sigma_{e/o} = \frac{1}{2}(\sigma_1 \pm \sigma_2)$ couple to the even/odd modes of the bath only. This kind of setup can be understood as two impurity-objects that each couple to a single bath with a characteristic spectrum. The standard mapping of the bath onto the semi-infinite chain, necessary for performing the NRG, can then be applied to each of the two environments individually. The impurities still formally couple to each other via H_{imp} . However, they lose their local nature as the even/odd spin combinations $\sigma_{e/o}$ are now extensive objects with a size of R .

The Fourier-transformed bath Hamiltonian reads

$$H_{\text{bath}} = \int_{-\pi}^{\pi} \omega(k) a_k^\dagger a_k dk \quad (2.15)$$

where $\omega(k) = \sum_x t_{|x|} e^{ikx}$ is the dispersion of the bath modes. The introduction of even and odd bath mode operators as

$$a_{k,e} = \begin{cases} a_0, & k = 0 \\ \frac{a_k + a_{-k}}{\sqrt{2}}, & k > 0 \end{cases}; \quad a_{k,o} = \begin{cases} 0, & k = 0 \\ -i \frac{a_k - a_{-k}}{\sqrt{2}}, & k > 0 \end{cases}. \quad (2.16)$$

turns out useful in rewriting the interaction part of the Hamiltonian. It can be easily verified that all $a_{k,s}$, $s = e, o$ obey the standard bosonic commutation relations. The bath part can then be written as

$$H_{\text{bath}} = \omega(0)a_0^\dagger a_0 + \sum_{s=e,o} \int_{0^+}^{\pi} \omega(k) a_{k,s}^\dagger a_{k,s} dk \quad (2.17)$$

where it was used, that the dispersions $\omega(k)$ considered in this thesis (cf. section 4.1) are even functions of k . The integrals $\int_{0^+}^{\pi}$ indicate that the zero mode is not integrated over. In the following both coupling strengths $\sqrt{\alpha_i}$ are considered to be equal to $\sqrt{\alpha}$. Therefore the interaction part of the Hamiltonian reads

$$H_{\text{int}} = \sqrt{\alpha} \frac{\sigma_{z,1}}{2} (a_r + a_r^\dagger) + \sqrt{\alpha} \frac{\sigma_{z,2}}{2} (a_{-r} + a_{-r}^\dagger) \quad (2.18)$$

$$= \frac{1}{2} \sqrt{\frac{\alpha}{2\pi}} \int_{-\pi}^{\pi} \left[a_k (\sigma_{z,1} e^{-ikr} + \sigma_{z,2} e^{ikr}) + a_k^\dagger (\sigma_{z,1} e^{ikr} + \sigma_{z,2} e^{-ikr}) \right] dk \quad (2.19)$$

$$= \sqrt{\frac{\alpha}{2\pi}} \sigma_{z,e} (a_{0,e} + a_{0,e}^\dagger) + \sqrt{\frac{\alpha}{\pi}} \sigma_{z,e} \int_{0^+}^{\pi} (a_{k,e} + a_{k,e}^\dagger) \cos(kr) dk \\ + \sqrt{\frac{\alpha}{\pi}} \sigma_{z,o} \int_{0^+}^{\pi} (a_{k,o} + a_{k,o}^\dagger) \sin(kr) dk \quad (2.20)$$

The even/odd combinations $\sigma_{z,e/o} = \frac{1}{2}(\sigma_{z,1} \pm \sigma_{z,2})$ couple to the even/odd modes of the bath only. In an effective theory for the even and the odd spin combinations the spectral functions of the even and the odd bath read

$$J_e(\omega, R) = \alpha \left[\frac{1}{2} \int_{-\epsilon}^{\epsilon} \delta(\omega - \omega(0)) dk + \int_{0^+}^{\pi} \cos^2(kR/2) \delta(\omega - \omega(k)) dk \right] \quad (2.21)$$

$$J_o(\omega, R) = \alpha \int_{0^+}^{\pi} \sin^2(kR/2) \delta(\omega - \omega(k)) dk \quad (2.22)$$

in momentum space. Here, a small $\epsilon > 0$ is introduced such that the zero mode in $J_e(\omega, R)$ is integrated over in k -space. By introducing the functions

$$h_s(k, R) = \sqrt{\frac{J_s(\omega(k), R)}{\pi} \frac{\partial}{\partial k'} \omega(k')|_{k'=k}} \quad (2.23)$$

the Hamiltonian of the model can be rewritten as

$$H_{2\text{sbm}} = H_{\text{imp}} + \sum_{s=e,o} \int_0^{\pi} \omega(k) a_{k,s}^\dagger a_{k,s} dk + \sigma_{z,s} \int_0^{\pi} h_s(k, R) [a_{k,s} + a_{k,s}^\dagger] dk \quad (2.24)$$

where now strictly speaking the integral for the odd modes has again to exclude a zero mode since there is no odd zero mode. The impurity part of the Hamiltonian expressed in the even and odd spin operators reads

$$H_{\text{imp}} = \sum_{s=e,o} \sigma_{x,s} \Delta_s + \sigma_{z,s} \varepsilon_s + \frac{K}{4} (\mathbb{1}_e - \mathbb{1}_o) \quad (2.25)$$

with the definitions $\Delta_{e,o} = (\Delta_1 \pm \Delta_2)/2$ and $\varepsilon_{e,o} = (\varepsilon_1 \pm \varepsilon_2)/2$. The identity operators $\mathbb{1}_{e,o}$ in the common basis $\{|\uparrow\uparrow\rangle, |\downarrow\downarrow\rangle, |\uparrow\downarrow\rangle, |\downarrow\uparrow\rangle\}$ are then given by

$$\mathbb{1}_e = |\uparrow\uparrow\rangle\langle\uparrow\uparrow| + |\downarrow\downarrow\rangle\langle\downarrow\downarrow|, \quad (2.26)$$

$$\mathbb{1}_o = |\uparrow\downarrow\rangle\langle\uparrow\downarrow| + |\downarrow\uparrow\rangle\langle\downarrow\uparrow|. \quad (2.27)$$

The Hamiltonian in equation (2.24) can also be expressed in a frequency picture in which it will be studied by means of a two bath bosonic NRG (to be explained in more detail in section 5). Here, the high-frequency cutoff ω_c of the environment is introduced into the theory that marks the highest energies in the bath (the ones corresponding to momenta at the edges of the one-dimensional Brillouin-zone). Thereby, all other model parameters are expressed in units of that cutoff. In frequency space the Hamiltonian of the two-spin-boson model then becomes

$$H_{2\text{sbm}} = H_{\text{imp}} + \sum_{s=e,o} \int_0^1 g_s(\omega, R) a_{\omega,s}^\dagger a_{\omega,s} d\omega + \sigma_{z,s} \int_0^1 h_s(\omega, R) [a_{\omega,s} + a_{\omega,s}^\dagger] d\omega \quad (2.28)$$

where now R marks the total distance of the two spin-1/2 impurities. The functions $g_s(\omega, R)$ and $h_s(\omega, R)$ now have to combine to the even/odd spectral functions $J_{e/o}(\omega, R)$ in frequency space individually like

$$J_s(\omega, R) = \pi \left| \frac{\partial g_s(\omega, R)}{\partial \omega} \right|^{-1} h_s^2(\omega, R), \quad s = e, o. \quad (2.29)$$

In section 4.2 the even and odd spectral functions in frequency space will be derived for the case that the environment does locally show an ohmic spectral density. The Hamiltonian $H_{2\text{sbm}}$ in its frequency representation (2.28) is the starting point for the Numerical Renormalization Group mappings to be applied in sections 5.1-5.3 after the general philosophy of the NRG has been introduced.

In the next section, the concept of correlation functions is introduced. These can—at least in case of local correlators—be interpreted as probability-distributions of finding corresponding physical processes of interest in the system. The physical observables of interest in this thesis are discussed in that section as well. Afterwards the spectral functions $J(\omega)$ and $J_{e/o}(\omega, R)$ appearing in the dissipative oscillator model and the two-spin-boson model are connected to imaginary parts of corresponding bath propagators in section 4.



3. Correlation functions

One focus of this thesis is to understand how the dissipative environment to which the impurity systems are coupled is affected by the presence of those impurities. In the present work, thermal averages $\Delta\langle\dots\rangle := \langle\dots\rangle - \langle\dots\rangle_0$ between the clean system where the impurities are absent and a situation where they are coupled to the environment are investigated.

The thermal averages are calculated from spectral functions which are themselves imaginary parts of certain correlation functions. In the following the concept of correlation functions is introduced and a set of equations of motion is given from which they may be calculated. Afterwards, the representation of correlation functions in terms of Lehmann-sums and the concept of spectral functions and their connection to corresponding correlation functions are introduced in section 3.2.

The desired thermal averages, namely the average site occupation and the displacement amplitude, are introduced in section 3.3. In the sections 3.4 and 3.5, the spectral functions which are needed in the calculations of the thermal averages are derived both for the dissipative oscillator model and the two-spin-boson model. Those spectral functions contain always a free contribution from the clean system and a part that describes the interaction of the impurities with their environment. The interactions are fully encoded in impurity correlation functions which are termed scattering matrices and which are defined as well in section 3.4.

3.1. Resolvent and equations of motion

A quantum mechanical system with a Hamiltonian H can in general be subject to an external, time dependent driving force $F(t)$. In such a situation it is desirable to know how the system adapts to the external force. Answering that question is intimately linked to the concept of Green's functions, also referred to as correlation functions. In this section, the general strategy is outlined how to obtain the answer of a quantum mechanical system to an external driving force and see where exactly correlation functions enter the field.

The problem of a general force $F(t)$, to which the system has to adapt, can be reduced to that of a signal which has the form of a delta peak in time $\sim \delta(t - t')$. The problem for a general function $F(t)$ is then found by summing up the systems answers to delta peaks at different times with the corresponding amplitude $F(t')$ using the identity

$$F(t) = \int_{-\infty}^{\infty} F(t')\delta(t - t') dt'. \quad (3.1)$$

To see how the system adapts to a force which is peaked in time it is necessary to solve the inhomogeneous, time dependent Schrödinger equation where the inhomogeneity is given by that delta peak in time:

$$(i\partial_t - H)\tilde{G}^R(t - t') = \delta(t - t'). \quad (3.2)$$

Here, Planck's constant \hbar has been set to one. The solution of equation (3.2) is then named the retarded Green's function $\tilde{G}^R(t - t')$ which is finite only for times $t > t'$ and encodes the systems reaction to the signal $\delta(t - t')$. Note that up to now, no restriction has been made on the kind of Hamiltonian H or its formulation up to now. The Hamiltonian may be a linear differential operator like that of a free massive particle or an operator in second quantisation like that describing a free electron gas. Equation (3.2) can be formally solved for H with the help of the Laplace transformation [1]. Given a function $\tilde{f}(t)$ that is zero for all negative times one can define its Laplace transform $\mathcal{L}[\tilde{f}] = f(z)$ via

$$f(z) = \int_0^\infty \tilde{f}(t)e^{izt} dt, \quad (3.3)$$

where $z = \omega + i\epsilon$ is a frequency with a small, positive imaginary part ϵ which is needed for the convergence of the integral. Integrating the Schrödinger equation (3.2) that way leads to

$$\begin{aligned} 1 &= \int_{t'}^\infty \delta(t - t')e^{iz(t-t')} dt = \int_{t'}^\infty [(i\partial_t - H)\tilde{G}^R(t - t')]e^{iz(t-t')} dt \\ &= \int_{t'}^\infty [(z - H)\tilde{G}^R(t - t')]e^{iz(t-t')} dt - iG^R(0) \\ &= (z - H)G^R(z). \end{aligned} \quad (3.4)$$

Here, $G^R(z)$ is the Laplace transform of the real time retarded Green's function. In the second equation, an integration by parts has been performed, where the small imaginary part in z suppresses the contribution of $\tilde{G}^R(t)$ at infinity. For the third equation the boundary condition $\tilde{G}^R(0) = 0$ was employed, which should hold since the system cannot adapt instantaneously to the driving force $\delta(t - t')$.

Thus, after the Laplace transformation the problem is formally solved by inverting the operator $(z - H)$. The solution $G^R(z) = (z - H)^{-1}$ is often referred to as the resolvent operator of the model at hand (cf. for example [57]). In order to invert the operator $(z - H)$, a basis $\{|n\rangle\}$ and thus a representation in which to formulate the linear operator H has to be chosen. This basis allows to calculate any matrix element $\langle n|G^R(z)|m\rangle$ of the retarded Green's function in frequency space. Conveniently, the operator $G^R(z)$ is diagonalised by going to the eigenbasis $|\eta\rangle = a_\eta^\dagger|0\rangle$ of a Hamiltonian with $H|\eta\rangle = E_\eta|\eta\rangle$. Here a_η^\dagger should formally create the excited state $|\eta\rangle$ out of a well-chosen vacuum state $|0\rangle$. The choice of the eigenbasis results in matrix elements

$$\begin{aligned} G^R(\eta, \eta', \omega + i\epsilon) &= \langle \eta|G^R(\omega + i\epsilon)|\eta'\rangle = (\omega + i\epsilon - E_{\eta'})^{-1}\delta_{\eta, \eta'} \\ &\stackrel{\epsilon \rightarrow 0}{=} \delta_{\eta, \eta'} [(\omega - E_{\eta'})^{-1} - i\pi\delta(\omega - E_{\eta'})]. \end{aligned} \quad (3.5)$$

The retarded Green's function $G^R(\eta, \eta', \omega)$ thus has a simple pole on the real axis right at the eigenenergy $E_{\eta'}$ of the system. Its negative imaginary part can be interpreted as

the frequency dependent probability distribution of creating an excitation $|\eta'\rangle = a_{\eta'}^\dagger|0\rangle$ in the system. This excitation is only possible right at the energy $E_{\eta'}$. By taking the trace of the operator $G^R(z)$, the systems density of states $\rho(\omega)$ can be obtained as

$$\begin{aligned} -\lim_{\epsilon \rightarrow 0} \text{Im}[\text{Tr}(G^R(\omega + i\epsilon))] &= -\lim_{\epsilon \rightarrow 0} \text{Im} \left[\sum_n \langle n | \frac{1}{\omega + i\epsilon - E_n} | n \rangle \right] \\ &= \pi \sum_n \delta(\omega - E_n) =: \pi \rho(\omega), \end{aligned} \quad (3.6)$$

which encodes information on all possible excitations of the system. In the following the short hand notation $\langle\langle a_\eta, a_{\eta'}^\dagger \rangle\rangle_z := G^R(\eta, \eta', z)$ for the retarded Green's function is used.

Beyond excitations to eigenstates, correlation functions $\langle\langle \hat{A}, \hat{B} \rangle\rangle_z$ of two arbitrary bosonic operators \hat{A} and \hat{B} can be considered. Here the operators \hat{A} and \hat{B} may create/annihilate more complicated excitations of a system like e. g. $a_x + a_x^\dagger$ which are not necessarily eigenstates of H and might dissipate in time. The correlator $\langle\langle \hat{A}, \hat{B} \rangle\rangle_z = G^R(\hat{A}, \hat{B}, z)$ is then defined as the Laplace-transform of the retarded Green's function $G^R(\hat{A}, \hat{B}, t)$ that reads

$$G^R(\hat{A}, \hat{B}, t) = -i\Theta(t)\langle[\hat{A}(t), \hat{B}(0)]\rangle. \quad (3.7)$$

and is finite only for positive times [3]. Here, $\langle \dots \rangle = \text{Tr}[e^{-\beta(H-\mu N)} \dots] / \mathcal{Z}$ is the thermal average in a grand canonical ensemble, \mathcal{Z} is the partition function and $[\cdot, \cdot]$ is the commutator. The particle number is given by N and μ is the chemical potential of the system. In case of the bath single particle propagator $G_{x,y}(z)$ between two sites x and y in the bosonic chain its retarded Green's function in real time encapsulates information on the process of creating a particle at position y at time zero and later on being able to destroy it at position x at time t .

The time-dependence of the operator \hat{A} is introduced via the Heisenberg representation as

$$\hat{A}(t) = e^{i(H-\mu N)t} \hat{A} e^{-i(H-\mu N)t}. \quad (3.8)$$

The correlator $\langle\langle \hat{A}, \hat{B} \rangle\rangle_z$ can be obtained by performing the Laplace transformation

$$\langle\langle \hat{A}, \hat{B} \rangle\rangle_z = -i \int_0^\infty \langle[\hat{A}(t), \hat{B}(0)]\rangle e^{izt} dt. \quad (3.9)$$

There are several ways to obtain a desired correlation function $\langle\langle \hat{A}, \hat{B} \rangle\rangle_z$. One way is to express the right hand side of equation (3.9) in the eigenbasis of the operator $H - \mu N$. In the literature, the result is referred to as a Lehmann sum [3] and is presented in the next section. It requires the knowledge of the eigenbasis of the operator $H - \mu N$, which may not be accessible analytically for most systems.

Another approach is that of *equations of motion*. To this end the time derivative of $G^R(t - t')$ is Laplace-transformed to obtain

$$z\langle\langle \hat{A}, \hat{B} \rangle\rangle_z = \langle[\hat{A}, \hat{B}]\rangle + \langle\langle \hat{A}, [H - \mu N, \hat{B}] \rangle\rangle_z, \quad (3.10)$$

$$z\langle\langle \hat{A}, \hat{B} \rangle\rangle_z = \langle[\hat{A}, \hat{B}]\rangle - \langle\langle [H - \mu N, \hat{A}], \hat{B} \rangle\rangle_z. \quad (3.11)$$

That way a whole set of equations may be derived which connect different correlators of the system. In certain cases those equations may be solved analytically without the need to obtain the eigenbasis of the operator $H - \mu N$. They also allow to read off the physical processes that contribute to a correlator. In the following the technique of *equations of motions* is employed both for the dissipative oscillator model with Hamiltonian (2.5) and the two-spin-boson model with Hamiltonian (2.24) in order to derive expressions for correlation functions both in the bath and at the impurities. In these calculations a central quantity of interest is the scattering matrix or \mathcal{T} -Matrix of the impurities. This matrix contains all information on the interactions between the bath and the impurities. It is defined below in section 3.4 for both models and will be investigated closer in section 4.4.

3.2. Lehmann-representation and spectral functions

By employing the technique of *equations of motion* in order to obtain a desired correlator $\langle\langle \hat{A}, \hat{B} \rangle\rangle_z$, this correlator is connected to a set of other correlators and thermal averages. The set of equations derived for all relevant correlators will however not always reduce to analytic expressions. In such a situation, the right hand side of equation (3.9) still needs to be evaluated. Here the Lehmann representation is useful as it can be evaluated numerically as long as the eigenstates and -energies of a system are accessible by some means.

Given a complete set of eigenstates $\{|n\rangle\}$ and corresponding energies E_n of the operator $H - \mu N$, the Laplace-transformed retarded Green's function $G^R(\hat{A}, \hat{B}, z)$ can be evaluated by inserting a resolution of identity $\mathbb{1} = \sum_m |m\rangle\langle m|$ between the operators $\hat{A}(t)$ and $\hat{B}(0)$ on the right hand side of equation (3.9). Performing the integral over time results in

$$G^R(\hat{A}, \hat{B}, z) = \frac{1}{Z} \sum_{n,m} \frac{e^{-\beta E_n} - e^{-\beta E_m}}{z + E_n - E_m} \langle n | \hat{A} | m \rangle \langle m | \hat{B} | n \rangle. \quad (3.12)$$

The only frequency dependent parts are the fractions $(z + E_n - E_m)$ which may be evaluated on the real axis as in (3.5) to read

$$\lim_{\epsilon \rightarrow 0} \frac{1}{\omega + i\epsilon + E_n - E_m} = \frac{1}{\omega + E_n - E_m} - i\pi \delta(\omega + E_n - E_m). \quad (3.13)$$

The retarded Green's function thus has simple poles on the real frequency axis at frequencies $\omega_{mn} = E_m - E_n$. These frequencies correspond to transitions between two states $|n\rangle$ and $|m\rangle$ in the system which are connected by the operators \hat{A} and \hat{B} . Formally, a spectral function $A(\eta, \eta', \omega)$ is introduced as the negative imaginary part of $G^R(\eta, \eta', z)$, evaluated on the real axis and weighted by $1/\pi$:

$$A(\eta, \eta', \omega) = -\frac{1}{\pi} \lim_{\epsilon \rightarrow 0} \text{Im} [G^R(\eta, \eta', z = \omega + i\epsilon)] = \delta(\omega - E_\eta) \delta_{\eta, \eta'}. \quad (3.14)$$

The spectral function $A(\eta, \eta', \omega)$ directly encodes at which frequency the state $|\eta\rangle$ may be excited out of the vacuum. A general spectral function $A(\hat{A}, \hat{B}, \omega)$ is then defined as the negative imaginary part of the corresponding correlator, once more evaluated on the real axis and weighted by $1/\pi$:

$$A(\hat{A}, \hat{B}, \omega) = -\frac{1}{\pi} \lim_{\epsilon \rightarrow 0} \text{Im} [G^R(\hat{A}, \hat{B}, z = \omega + i\epsilon)] \quad (3.15)$$

$$= \frac{1}{\mathcal{Z}} \sum_{n,m} [e^{-\beta E_n} - e^{-\beta E_m}] \langle n | \hat{A} | m \rangle \langle m | \hat{B} | n \rangle \delta(\omega + E_n - E_m). \quad (3.16)$$

The total weight contained in a spectral function is given by

$$\int_{-\infty}^{\infty} A(\hat{A}, \hat{B}, \omega) d\omega = \frac{1}{\mathcal{Z}} \sum_{n,m} [e^{-\beta E_n} - e^{-\beta E_m}] \langle n | \hat{A} | m \rangle \langle m | \hat{B} | n \rangle \quad (3.17)$$

$$= \frac{1}{\mathcal{Z}} \sum_{n,m} e^{-\beta E_n} [\langle n | \hat{A} | m \rangle \langle m | \hat{B} | n \rangle - \langle n | \hat{B} | m \rangle \langle m | \hat{A} | n \rangle] \quad (3.18)$$

$$= \langle [\hat{A}, \hat{B}] \rangle \quad (3.19)$$

which is the thermal expectation value of the commutator between \hat{A} and \hat{B} .

3.3. Average site occupation and displacement amplitude

In a clean system where the impurities do not couple to the chain, the one-dimensional chain is translational invariant. There the average site occupation $\langle \hat{n}_x \rangle$ and the average square of the displacement amplitude $\langle (a_x + a_x^\dagger)^2 \rangle$ are constant as a function of x . As soon as the coupling between the impurities and the chain is switched on, translational invariance in the system is broken and a space dependence in those quantities can be expected. Details of this space dependence are determined by the nature of the impurities and their coupling to the bath oscillators. The local averages in the environment are linked to different correlation functions, as will be derived in the following.

To obtain the single particle propagator of the environment, the operators $\hat{A} = a_x$ and $\hat{B} = a_x^\dagger$ are chosen in equation (3.15). They correspond to an annihilation/creation of a bosonic particle at position x in the chain. From the retarded Green's function $G^R(a_x, a_x^\dagger, z = \omega + i\epsilon)$ the corresponding spectral function $A(x, \omega) := A(a_x, a_x^\dagger, \omega)$ is obtained (cf. equation (3.15)), which reads

$$\begin{aligned} A(x, \omega) &= -\frac{1}{\pi} \lim_{\epsilon \rightarrow 0} \text{Im} [G^R(a_x, a_x^\dagger, z = \omega + i\epsilon)] \\ &= \frac{1}{\mathcal{Z}} \sum_{n,m} [e^{-\beta E_n} - e^{-\beta E_m}] |\langle n | a_x | m \rangle|^2 \delta(\omega + E_n - E_m). \end{aligned} \quad (3.20)$$

At each site x the spectral function $A(x, \omega)$ is normalised as

$$\int_{-\infty}^{\infty} A(x, \omega) d\omega = \langle [a_x, a_x^\dagger] \rangle = 1. \quad (3.21)$$

Using the Bose-Einstein distribution function $n_B(\omega, \beta) = (e^{\beta\omega} - 1)^{-1}$ and the auxiliary identity

$$\int_{-\infty}^{\infty} \frac{e^{-\beta E_n} - e^{-\beta E_m}}{e^{\beta\omega} - 1} \delta(\omega + E_n - E_m) d\omega = \frac{e^{-\beta E_n} - e^{-\beta E_m}}{e^{\beta(E_m - E_n)} - 1} = e^{-\beta E_m} \quad (3.22)$$

the spectral function $A(x, \omega)$ can be connected to the average site occupation $\langle \hat{n}_x \rangle$ at position x as

$$\langle \hat{n}_x \rangle = \langle a_x^\dagger a_x \rangle = \frac{1}{\mathcal{Z}} \sum_{n,m} e^{-\beta E_m} |\langle n | a_x | m \rangle|^2 \quad (3.23)$$

$$= \frac{1}{\mathcal{Z}} \sum_{n,m} \int_{-\infty}^{\infty} \frac{e^{-\beta E_n} - e^{-\beta E_m}}{e^{\beta\omega} - 1} \delta(\omega + E_n - E_m) d\omega |\langle n | a_x | m \rangle|^2 \quad (3.24)$$

$$= \int_{-\infty}^{\infty} A(x, \omega) n_B(\omega, \beta) d\omega. \quad (3.25)$$

Thus, the average site occupation is given by the integral over the spectral function $A(x, \omega)$ over the whole frequency range, weighted by the function $n_B(\omega, \beta)$ that encapsulates the thermal population of a bosonic state at frequency ω for a given temperature $k_B T = \beta^{-1}$ (k_B being the Boltzmann-constant, T the temperature and β the dimensionless, inverse temperature).

Choosing the operators $\hat{A} = \hat{B} = a_x + a_x^\dagger$, the local displacement-displacement correlation function of the environment is defined as

$$D_x^R(z) = \langle\langle a_x + a_x^\dagger, a_x + a_x^\dagger \rangle\rangle_z \quad (3.26)$$

and its corresponding spectral function reads

$$A_{\text{dis}}(x, \omega) = -\frac{1}{\pi} \lim_{\epsilon \rightarrow 0} \text{Im} [D_x^R(z = \omega + i\epsilon)]. \quad (3.27)$$

This function is then normalised as

$$\int_{-\infty}^{\infty} A_{\text{dis}}(x, \omega) d\omega = \langle [a_x + a_x^\dagger, a_x + a_x^\dagger] \rangle = \langle 0 \rangle = 0. \quad (3.28)$$

That the integral over $A_{\text{dis}}(x, \omega)$ vanishes can be traced back to the statement that the imaginary part of $D_x^R(z)$ is antisymmetric on the real axis.

Like before, a local operator-average can be connected to the displacement spectral function $A_{\text{dis}}(x, \omega)$. The corresponding quantity is the square of the displacement amplitude $\langle (a_x + a_x^\dagger)^2 \rangle$:

$$\langle (a_x + a_x^\dagger)^2 \rangle = \frac{1}{\mathcal{Z}} \sum_{n,m} e^{-\beta E_m} |\langle n | a_x + a_x^\dagger | m \rangle|^2 \quad (3.29)$$

$$= \int_{-\infty}^{\infty} A_{\text{dis}}(x, \omega) n_B(\omega, \beta) d\omega. \quad (3.30)$$

In this work spectral functions and corresponding expectation values are always calculated in their zero temperature limit. To this end a truncated set of eigenstates and -energies of a system together with matrix-elements (like $\langle n | \hat{A} | m \rangle$) of a desired operator \hat{A} is obtained via the Numerical Renormalization Group (see section 5). The next step is to combine all those informations to a continuous spectral function for which the integrals (3.25) and (3.30) can be evaluated numerically. The details of how to obtain spectral functions from data provided by the NRG will be given in section 5.4.

In the limit of zero temperature the Bose-Einstein distribution function turns into the Heavyside stepfunction as

$$\lim_{\beta \rightarrow \infty} \frac{1}{e^{\beta\omega} - 1} = \begin{cases} -1 & , \omega \leq 0 \\ 0 & , \omega > 0 \end{cases} = -\Theta(-\omega). \quad (3.31)$$

The integrations in equation (3.25) and (3.30) therefore only need to be performed over the negative frequency domain in the limit of zero temperature. Thus the integrals that need to be evaluated for the local averages simplify to

$$\langle \hat{n}_x \rangle = - \int_{-\infty}^0 A(x, \omega) d\omega \quad (3.32)$$

$$\langle (a_x + a_x^\dagger)^2 \rangle = - \int_{-\infty}^0 A_{\text{dis}}(x, \omega) d\omega \quad (3.33)$$

where the spectral functions $A(x, \omega)$ and $A_{\text{dis}}(x, \omega)$ are meant as their zero temperature limit.

In this section the connection of the local averages for the site occupation $\langle \hat{n}_x \rangle$ and for the displacement amplitude squared $\langle (a_x + a_x^\dagger)^2 \rangle$ to corresponding propagators via their spectral functions has been established. In the following, the propagators required to evaluate the integrals (3.32) and (3.33) are investigated further. To this end the equations of motion (3.10) and (3.11) are employed for both the dissipative oscillator model and the two-spin-boson model to obtain the single particle propagators and the displacement-displacement correlators of the bath in the following. In section 4 the knowledge of those single particle propagators is being used to explain how the bath spectral functions $J(\omega)$ and $J_{e/o}(\omega)$, which entered the different models, can be understood in terms of the underlying propagators.

3.4. Bath single particle propagator

In order to calculate the spectral function $A(x, \omega)$ that enters the equation for the average site occupation $\langle \hat{n}_x \rangle$ in (3.32) the knowledge of the local single particle propagator $G_{x,x}(z)$ for an arbitrary site x in the chain is needed. As also non-local propagators $G_{x,y}(z)$ between different sites x and y in the chain will appear in the derivation of the local propagator, the more general case is considered first and only later reduced to its local version with $x = y$. First, the propagator $G_{x,y}(z)$ is Fourier-transformed to momentum space. Since the chain-Hamiltonian is diagonal in k -space, the equations of motion will obtain a less complex form making it easier to apply them. The real-space propagator $G_{x,y}(z)$ is transformed as

$$G_{x,y}(z) = \langle\langle a_x, a_y^\dagger \rangle\rangle_z = \frac{1}{2\pi} \int_{-\pi}^{\pi} \int_{-\pi}^{\pi} \langle\langle a_k, a_{k'}^\dagger \rangle\rangle_z e^{-ikx} e^{ik'y} dk dk'. \quad (3.34)$$

In the following, the appearing correlators $G_{k,k'}(z) = \langle\langle a_k, a_{k'}^\dagger \rangle\rangle_z$ are calculated separately for the two models under discussion.

3.4.1. Dissipative oscillator model

The first step is to investigate the single particle propagator $G_{k,k'}(z)$ in k -space where the Hamiltonian of the system is that of the dissipative oscillator model H_{do} . In the following, propagators with an upper index (0), like $G_{x,y}^{(0)}(z)$, are free propagators referring to $H_0 = H_{\text{imp}} + H_{\text{bath}}$ which denotes the Hamiltonian of the non-interacting theory. Applying the first equation of motion (3.10) to the free propagator $G_{k,k'}^{(0)}(z)$ results in

$$G_{k,k'}^{(0)}(z) = \frac{\delta(k - k')}{z - \omega(k')}. \quad (3.35)$$

The free propagator $G_{k,k'}^{(0)}(z)$ is diagonal in k -space and has a simple pole at the excitation energy $\omega(k)$. It will appear repeatedly in the following expressions for the full propagator $G_{k,k'}(z)$. Employing equation (3.10) to the full propagator leads to

$$\begin{aligned} z \langle\langle a_k, a_{k'}^\dagger \rangle\rangle_z &= \delta(k - k') + \omega(k') \langle\langle a_k, a_{k'}^\dagger \rangle\rangle_z + \frac{1}{2} \sqrt{\frac{\alpha}{2\pi}} \langle\langle a_k, b + b^\dagger \rangle\rangle_z \\ \Rightarrow \langle\langle a_k, a_{k'}^\dagger \rangle\rangle_z &= G_{k,k'}^{(0)}(z) + \frac{1}{2} \sqrt{\frac{\alpha}{2\pi}} \langle\langle a_k, b + b^\dagger \rangle\rangle_z G_{k',k'}^{(0)}(z). \end{aligned} \quad (3.36)$$

The full propagator is thus given by the free propagator which is diagonal in k -space, plus a propagator that connects the bath to the impurity. To progress further, equation (3.11) is applied to $\langle\langle a_k, b + b^\dagger \rangle\rangle_z$ leading to

$$\begin{aligned}
z \langle\langle a_k, b + b^\dagger \rangle\rangle_z &= \omega(k) \langle\langle a_k, b + b^\dagger \rangle\rangle_z + \frac{1}{2} \sqrt{\frac{\alpha}{2\pi}} \langle\langle b + b^\dagger, b + b^\dagger \rangle\rangle_z \\
\Rightarrow \langle\langle a_k, b + b^\dagger \rangle\rangle_z &= G_{k,k}^{(0)}(z) \frac{1}{2} \sqrt{\frac{\alpha}{2\pi}} \langle\langle b + b^\dagger, b + b^\dagger \rangle\rangle_z.
\end{aligned} \tag{3.37}$$

The full propagator reads

$$\langle\langle a_k, a_{k'}^\dagger \rangle\rangle_z = G_{k,k'}^{(0)}(z) + \frac{\alpha}{4} \frac{1}{2\pi} G_{k,k}^{(0)}(z) \langle\langle b + b^\dagger, b + b^\dagger \rangle\rangle_z G_{k',k'}^{(0)}(z)$$

which can be used in expression (3.34) to obtain

$$\begin{aligned}
&\langle\langle a_x, a_y^\dagger \rangle\rangle_z \\
&= \frac{1}{2\pi} \int_{-\pi}^{\pi} \int_{-\pi}^{\pi} e^{-ikx} e^{ik'y} \left[\frac{\delta(k - k')}{z - \omega(k')} + \frac{\alpha}{4} \frac{1}{2\pi} \frac{\langle\langle b + b^\dagger, b + b^\dagger \rangle\rangle_z}{[z - \omega(k)][z - \omega(k')]} \right] dk dk' \\
&= \frac{1}{2\pi} \int_{-\pi}^{\pi} \frac{e^{ik(y-x)}}{z - \omega(k)} dk \\
&+ \frac{\alpha}{4} \langle\langle b + b^\dagger, b + b^\dagger \rangle\rangle_z \left[\frac{1}{2\pi} \int_{-\pi}^{\pi} \frac{e^{-ikx}}{z - \omega(k)} dk \right] \left[\frac{1}{2\pi} \int_{-\pi}^{\pi} \frac{e^{ik'y}}{z - \omega(k')} dk' \right]
\end{aligned} \tag{3.38}$$

for the full real-space propagator. The real-space propagator that connects the sites x and y in the non-interacting case reads

$$G_{x,y}^{(0)}(z) = \langle\langle a_x, a_y^\dagger \rangle\rangle_z = \frac{1}{2\pi} \int_{-\pi}^{\pi} \frac{e^{ik(y-x)}}{z - \omega(k)} dk = G_{0,y-x}^{(0)}(z)$$

and is only dependent on the distance between the sites $y - x$. The full propagator can be rewritten as

$$G_{x,y}(z, T) = G_{x,y}^{(0)}(z) + G_{x,0}^{(0)}(z) \mathcal{T}_{\text{do}}(z, T) G_{0,y}^{(0)}(z) \tag{3.39}$$

where the impurity \mathcal{T} -matrix for the dissipative oscillator model is inserted. It is defined as

$$\mathcal{T}_{\text{do}}(z, T) := \frac{\alpha}{4} \langle\langle b + b^\dagger, b + b^\dagger \rangle\rangle_z(T). \tag{3.40}$$

Unlike the bare propagators $G_{x,y}^{(0)}(z)$ and $G_{k,k'}^{(0)}(z)$ which are all temperature independent (cf. equation (3.35)), the scattering matrix $\mathcal{T}_{\text{do}}(z, T)$ in general shows a temperature dependence. From equation (3.39) the physical processes contributing to the full propagator from site y to site x can be directly read off. The first term is the free propagator between the two sites describing the propagation of a bosonic particle as if no impurity were present. The second term describes the process of a particle propagating freely from site y to site 0 which is connected to the impurity. There

the particle scatters off of the impurity; this process is described by the \mathcal{T} -matrix. Afterwards the particle propagates freely onward to site x . Evaluating expression (3.39) for the same site $x = y$ leads to

$$\begin{aligned} G_x(z, T) &= G_x^{(0)}(z) + G_{x,0}^{(0)}(z)\mathcal{T}_{\text{do}}(z, T)G_{0,x}^{(0)}(z) \\ &= G_0^{(0)}(z) + G_{x,0}^{(0)}(z)\mathcal{T}_{\text{do}}(z, T)G_{0,x}^{(0)}(z), \end{aligned} \quad (3.41)$$

which is dependent on the distance x to the impurity only through the free propagators connecting the origin with the position x . Here the short hand notation $G_x(z, T) = G_{x,x}(z, T)$ for local propagators is used which depend only on one site index. In the last equation the translational invariance of the bath in the non-interacting case was used, by which $G_x^{(0)}(z) = G_0^{(0)}(z)$ holds for all sites x . The average site occupation $\langle \hat{n}_x \rangle_0$ in the non-interacting system is a constant since the system is homogeneous. As we are interested in the effects on the bath which are caused by the coupling of the impurity oscillator to the origin of the chain, we will concentrate on the change in the average site occupation. We derive $\Delta \langle \hat{n}_x \rangle := \langle \hat{n}_x \rangle - \langle \hat{n}_x \rangle_0$ to be

$$\Delta \langle \hat{n}_x \rangle \stackrel{(3.25)}{=} -\frac{1}{\pi} \int_{-\infty}^{\infty} \text{Im}[G_x(\omega, T) - G_x^{(0)}(\omega)]n_B(\omega, T) d\omega \quad (3.42)$$

$$= -\frac{1}{\pi} \int_{-\infty}^{\infty} \text{Im}[G_{x,0}^{(0)}(\omega)\mathcal{T}_{\text{do}}(\omega, T)G_{0,x}^{(0)}(\omega)]n_B(\omega, T) d\omega. \quad (3.43)$$

In the limit of zero temperature this expression simplifies to

$$\Delta \langle \hat{n}_x \rangle = \frac{1}{\pi} \int_{-\infty}^0 \text{Im} \left[G_{x,0}^{(0)}(\omega)\mathcal{T}_{\text{do}}(\omega, T=0)G_{0,x}^{(0)}(\omega) \right] d\omega. \quad (3.44)$$

Results on the change in the average site occupation in case of the dissipative oscillator model are given in section 6.1.4.

3.4.2. Two-spin-boson model

In case of the two-spin-boson model the same strategy as above is pursued in order to calculate the single particle propagator in k -space $G_{k,k'}(z)$. The free bath propagator $G_{k,k'}^{(0)}(z)$ is the same as for the dissipative oscillator model since the one-dimensional chain is the same in both models. To calculate the full propagator $G_{k,k'}(z)$, the equation of motion (3.10) is applied to the system where now the Hamiltonian is given by $H_{2\text{sbm}}$ (cf. equation (2.24)). This results in

$$\langle\langle a_k, a_{k'}^\dagger \rangle\rangle_z = G_{k,k'}^{(0)}(z) + \frac{1}{2} \sqrt{\frac{\alpha}{2\pi}} \langle\langle a_k, \sigma_{z,1} e^{-ik'r} + \sigma_{z,2} e^{ik'r} \rangle\rangle_z G_{k',k'}^{(0)}(z). \quad (3.45)$$

For the interaction part of the Hamiltonian the intermediate result from equation (2.19) is used which is still expressed in the original impurity operators. Again the full propagator of the interacting model is given by the bare one plus a correlator that encapsulates the interaction of the bosonic modes with the impurities. Next the correlator $\langle\langle a_k, \sigma_{z,1}e^{-ik'r} + \sigma_{z,2}e^{ik'r} \rangle\rangle_z$ is expressed in terms of a correlator that purely incorporates impurity degrees of freedom by applying equation (3.11) to it:

$$\langle\langle a_k, \sigma_{z,1}e^{-ik'r} + \sigma_{z,2}e^{ik'r} \rangle\rangle_z = \frac{1}{2} \sqrt{\frac{\alpha}{2\pi}} G_{k,k}^{(0)}(z) \langle\langle \sigma_{z,1}e^{ikr} + \sigma_{z,2}e^{-ikr}, \sigma_{z,1}e^{-ik'r} + \sigma_{z,2}e^{ik'r} \rangle\rangle_z. \quad (3.46)$$

Using this result in the expression for the propagator $G_{k,k'}(z)$ (3.45) it follows

$$G_{k,k'}(z) = G_{k,k'}^{(0)}(z) + \frac{\alpha}{8\pi} G_{k,k}^{(0)}(z) \langle\langle \sigma_{z,1}e^{ikr} + \sigma_{z,2}e^{-ikr}, \sigma_{z,1}e^{-ik'r} + \sigma_{z,2}e^{ik'r} \rangle\rangle_z G_{k',k'}^{(0)}(z). \quad (3.47)$$

The propagator in k -space is then used in equation (3.34) to obtain the real-space propagator

$$G_{x,y}(z, T) = G_{x,y}^{(0)}(z) + (G_{x,r}^{(0)}(z), G_{x,-r}^{(0)}(z)) \mathcal{T}_{2\text{sbm}}(z, T) (G_{r,y}^{(0)}(z), G_{-r,y}^{(0)}(z))^T. \quad (3.48)$$

Here again an impurity \mathcal{T} -matrix is defined where now $\mathcal{T}_{2\text{sbm}}(z, T)$ is a 2×2 matrix with entries

$$\mathcal{T}_{2\text{sbm}}(z, T)_{ij} = \frac{\sqrt{\alpha_i \alpha_j}}{4} \langle\langle \sigma_{z,i}, \sigma_{z,j} \rangle\rangle_z(T), \quad i, j = 1, 2 \quad (3.49)$$

that can in general show a temperature dependence. The physical processes contributing to $G_{x,y}(z, T)$ are easy to interpret. Again there is a part describing the free propagation of a particle from site y to site x as if no impurities were present. The additional processes are free propagation from site y to either of the impurities, residing at $\pm r$ in the chain. There the bosonic particle can scatter and either remain at the impurity or be propagated to the site of the other impurity. Afterwards the particle propagates freely from its current position to the final position x in the chain. With the result for the real-space propagator (3.48) at hand the change in the average site occupation $\Delta \langle \hat{n}_x \rangle$ at zero temperature is obtained to read

$$\Delta \langle \hat{n}_x \rangle = \frac{1}{\pi} \int_{-\infty}^0 \text{Im} \left[(G_{x,r}^{(0)}(\omega), G_{x,-r}^{(0)}(\omega)) \mathcal{T}_{2\text{sbm}}(\omega, T=0) (G_{r,x}^{(0)}(\omega), G_{-r,x}^{(0)}(\omega))^T \right] d\omega \quad (3.50)$$

in case of the two-spin-boson model. Results on the change in the average site occupation in case of the two-spin-boson model are given in section 6.2.4.

3.5. Bath displacement-displacement correlator

Besides the change of the average site occupation $\Delta\langle\hat{n}_x\rangle$ another focus is the change of the expectation to displace an oscillator at site x due to the presence of the impurities. To this end, the average square of the displacement amplitude $\langle(a_x + a_x^\dagger)^2\rangle$, which is connected to the imaginary part of the displacement-displacement correlation function $\langle\langle a_x + a_x^\dagger, a_x + a_x^\dagger \rangle\rangle_z$, is investigated. First the more general correlator $D_{x,y}(z) := \langle\langle a_x + a_x^\dagger, a_y + a_y^\dagger \rangle\rangle_z$ is derived for both the damped harmonic oscillator model and the two-spin-boson model. Then its local version where $x = y$ is investigated. In a first step, the correlator is again Fourier-transformed to momentum space in which the original chain-Hamiltonian of the bath is diagonal:

$$\begin{aligned} D_{x,y}(z) &= \langle\langle a_x, a_y \rangle\rangle_z + \langle\langle a_x, a_y^\dagger \rangle\rangle_z + \langle\langle a_x^\dagger, a_y \rangle\rangle_z + \langle\langle a_x^\dagger, a_y^\dagger \rangle\rangle_z \\ &= \frac{1}{2\pi} \int_{-\pi}^{\pi} \int_{-\pi}^{\pi} \left[\langle\langle a_k, a_{k'} \rangle\rangle_z e^{-i(kx+k'y)} + \langle\langle a_k, a_{k'}^\dagger \rangle\rangle_z e^{-i(kx-k'y)} \right. \\ &\quad \left. + \langle\langle a_k^\dagger, a_{k'} \rangle\rangle_z e^{i(kx-k'y)} + \langle\langle a_k^\dagger, a_{k'}^\dagger \rangle\rangle_z e^{i(kx+k'y)} \right] dk dk' \end{aligned} \quad (3.51)$$

which can be decomposed into four different correlation functions that all need to be evaluated independently. The single particle propagator $\langle\langle a_x, a_y^\dagger \rangle\rangle_z$ was already calculated in the previous section. The three other correlators will be evaluated for both models in the following in their Fourier-transformed version, i. e. $\langle\langle a_k, a_{k'} \rangle\rangle_z$, $\langle\langle a_k^\dagger, a_{k'} \rangle\rangle_z$ and $\langle\langle a_k^\dagger, a_{k'}^\dagger \rangle\rangle_z$, using the equations of motion.

3.5.1. Dissipative oscillator model

Applying the equation of motion (3.10) in case of the dissipative oscillator model (cf. equation (2.5)) to the correlator $\langle\langle a_k, a_{k'} \rangle\rangle_z$ and solving for it leads to

$$\begin{aligned} \langle\langle a_k, a_{k'} \rangle\rangle_z &= \frac{1}{2} \sqrt{\frac{\alpha}{2\pi}} \langle\langle a_k, b + b^\dagger \rangle\rangle_z G_{k',k'}^{(0)}(-z) \\ &\stackrel{(3.37)}{=} \frac{1}{2\pi} G_{k,k}^{(0)}(z) \mathcal{T}_{\text{do}}(z, T) G_{k',k'}^{(0)}(-z). \end{aligned} \quad (3.52)$$

Here, again the impurity scattering matrix $\mathcal{T}_{\text{do}}(z, T)$ of the dissipative oscillator model is used (cf. equation (3.40)). With that the corresponding real space correlator reads

$$\langle\langle a_x, a_y \rangle\rangle_z = G_{x,0}^{(0)}(z) \mathcal{T}_{\text{do}}(z, T) G_{0,y}^{(0)}(-z) \quad (3.53)$$

where

$$\langle\langle a_y, a_0^\dagger \rangle\rangle_z^{(0)} = \langle\langle a_0^\dagger, a_y \rangle\rangle_{-z}^{(0)} = \langle\langle a_0, a_y^\dagger \rangle\rangle_z^{(0)} \quad (3.54)$$

is used in order to switch the indices 0 and y in the last bare propagator. By using the identity

$$G(\hat{A}^\dagger, \hat{B}^\dagger, z) = G(\hat{A}, \hat{B}, -z) \quad (3.55)$$

which can be shown with the help of the Lehmann-representation for correlators (cf. (3.12)), also the propagator $\langle\langle a_x^\dagger, a_y^\dagger \rangle\rangle_z = \langle\langle a_x, a_y \rangle\rangle_{-z}$ is obtained. In the Lehmann-representation one can furthermore show that

$$G(\hat{A}, \hat{B}, z) = G(\hat{B}, \hat{A}, -z). \quad (3.56)$$

Thereby, $\mathcal{T}_{\text{do}}(z, T) = \mathcal{T}_{\text{do}}(-z, T)$ holds, since $\hat{A} = \hat{B} = b + b^\dagger$ for the impurity's \mathcal{T} -matrix. Thus the correlator $\langle\langle a_x^\dagger, a_y^\dagger \rangle\rangle_z$ reads

$$\langle\langle a_x^\dagger, a_y^\dagger \rangle\rangle_z = G_{x,0}^{(0)}(-z) \mathcal{T}_{\text{do}}(z, T) G_{0,y}^{(0)}(z). \quad (3.57)$$

The first identity for correlators (3.55) may also be used to obtain the last correlator $\langle\langle a_x, a_y^\dagger \rangle\rangle_z$ directly from the single particle propagator that was calculated in the previous section in its real space representation. It is given by

$$\langle\langle a_x, a_y^\dagger \rangle\rangle_z = G_{x,y}^{(0)}(-z) + \frac{1}{2\pi} G_{x,0}^{(0)}(-z) \mathcal{T}_{\text{do}}(z, T) G_{0,y}^{(0)}(-z) \quad (3.58)$$

All four correlators in (3.51) can then be combined to obtain

$$D_{x,y}(z, T) = D_{x,y}^{(0)}(z) + D_{x,0}^{(0)}(z) \mathcal{T}_{\text{do}}(z, T) D_{0,y}^{(0)}(z) \quad (3.59)$$

which has exactly the same structure as the equation for the single particle propagator $G_{x,y}(z, T)$ (cf. (3.39)). Here the free displacement-displacement correlation function in case of the non-interacting system is used that reads

$$D_{x,y}^{(0)}(z) = \langle\langle a_x, a_y^\dagger \rangle\rangle_z^{(0)} + \langle\langle a_x^\dagger, a_y \rangle\rangle_z^{(0)}. \quad (3.60)$$

With (3.59), the change in the average of the squared displacement amplitude due to the presence of the impurity in the system reads

$$\Delta \langle (a_x + a_x^\dagger)^2 \rangle = \frac{1}{\pi} \int_{-\infty}^0 \text{Im} [D_{x,0}^{(0)}(\omega) \mathcal{T}_{\text{do}}(\omega, T=0) D_{0,x}^{(0)}(\omega)] d\omega \quad (3.61)$$

in its zero temperature limit. The results on the change of the squared displacement amplitude are presented in section 6.1.4 for the dissipative oscillator model.

3.5.2. Two-spin-boson model

The correlator $\langle\langle a_k, a_{k'} \rangle\rangle_z$ is also evaluated for the two-spin-boson model (2.24) by employing the first equation of motion (3.10). It reads

$$\begin{aligned} \langle\langle a_k, a_{k'} \rangle\rangle_z &= \frac{1}{2} \sqrt{\frac{\alpha}{2\pi}} \langle\langle a_k, \sigma_{z,1} e^{ik'r} + \sigma_{z,2} e^{-ik'r} \rangle\rangle_z G_{k',k'}^{(0)}(-z) \\ &\stackrel{(3.46)}{=} \frac{1}{2\pi} G_{k,k}^{(0)}(z) (e^{ikr}, e^{-ikr}) \mathcal{T}_{2\text{sbm}}(z, T) (e^{ik'r}, e^{-ik'r})^T G_{k',k'}^{(0)}(-z). \end{aligned} \quad (3.62)$$

Here the 2×2 \mathcal{T} -matrix of the two-spin-boson model (cf. equation (3.49)) is used again. The real space correlator $\langle\langle a_x, a_y \rangle\rangle_z$ is then obtained as

$$\langle\langle a_x, a_y \rangle\rangle_z = \left(G_{x,r}^{(0)}(z), G_{x,-r}^{(0)}(z) \right) \mathcal{T}_{2\text{sbm}}(z, T) \left(G_{r,y}^{(0)}(-z), G_{-r,y}^{(0)}(-z) \right)^T \quad (3.63)$$

With the same methodology the correlator $\langle\langle a_k^\dagger, a_{k'}^\dagger \rangle\rangle_z$ is calculated that reads

$$\langle\langle a_k^\dagger, a_{k'}^\dagger \rangle\rangle_z = \frac{1}{2\pi} G_{k,k}^{(0)}(-z) (e^{-ikr}, e^{ikr}) \mathcal{T}_{2\text{sbm}}(z, T) (e^{-ik'r}, e^{ik'r})^T G_{k',k'}^{(0)}(z). \quad (3.64)$$

The corresponding correlator in real space reads

$$\langle\langle a_x^\dagger, a_y^\dagger \rangle\rangle_z = \left(G_{x,r}^{(0)}(-z), G_{x,-r}^{(0)}(-z) \right) \mathcal{T}_{2\text{sbm}}(z, T) \left(G_{r,y}^{(0)}(z), G_{-r,y}^{(0)}(z) \right)^T. \quad (3.65)$$

The final correlator $\langle\langle a_k^\dagger, a_{k'} \rangle\rangle_z$ turns out to read

$$\langle\langle a_k^\dagger, a_{k'} \rangle\rangle_z = G_{k,k'}^{(0)}(-z) + \frac{1}{2\pi} G_{k,k}^{(0)}(-z) (e^{-ikr}, e^{ikr}) \mathcal{T}_{2\text{sbm}}(z, T) (e^{ik'r}, e^{-ik'r})^T G_{k',k'}^{(0)}(z) \quad (3.66)$$

which, transformed to real space leads to the correlator

$$\langle\langle a_x^\dagger, a_y \rangle\rangle_z = G_{x,y}^{(0)}(-z) + \left(G_{x,r}^{(0)}(-z), G_{x,-r}^{(0)}(-z) \right) \mathcal{T}_{2\text{sbm}}(z, T) \left(G_{r,y}^{(0)}(z), G_{-r,y}^{(0)}(z) \right)^T. \quad (3.67)$$

Combined with the expression (3.48) for the single particle propagator $\langle\langle a_x, a_y^\dagger \rangle\rangle_z$ of the two-spin-boson model, all four correlators necessary to calculate the displacement-displacement correlator $D_{x,y}(z, T)$ are known. It reads

$$D_{x,y}(z, T) = D_{x,y}^{(0)}(z) + \left(D_{x,r}^{(0)}(z), D_{x,-r}^{(0)}(z) \right) \mathcal{T}_{2\text{sbm}}(z, T) \left(D_{r,y}^{(0)}(z), D_{-r,y}^{(0)}(z) \right)^T \quad (3.68)$$

which has again the same exact structure as equation (3.48) for the single particle propagator. The change in the average displacement amplitude squared in case of the two-spin-boson model can then be calculated at zero temperature from

$$\Delta \langle (a_x + a_x^\dagger)^2 \rangle = \frac{1}{\pi} \int_{-\infty}^0 \text{Im} \left[\left(D_{x,r}^{(0)}(\omega), D_{x,-r}^{(0)}(\omega) \right) \mathcal{T}_{2\text{sbm}}(\omega, T=0) \left(D_{r,x}^{(0)}(\omega), D_{-r,x}^{(0)}(\omega) \right)^T \right] d\omega. \quad (3.69)$$

The results for the change of the squared displacement amplitude of the bath oscillators in case of the two-spin-boson-model can be found in section 6.2.4.



4. Bath spectral functions

In the previous section the concept of propagators and their connection to spectral functions was introduced. In this section it is demonstrated how the different spectral $J(\omega)$ in the dissipative oscillator model and the two separate spectral functions $J_e(\omega, R)$ and $J_o(\omega, R)$ in the two-spin-boson model can be understood in terms of the underlying propagators. Furthermore, the up to now arbitrary dispersion $\omega(k)$ of the one-dimensional chain is fixed in order to arrive at a local soft-gap spectral density $J(\omega) \sim \omega^s$. With that dispersion $\omega(k)$ the real-space hopping amplitudes t_x of the chain are calculated. These amplitudes are derived to drop in a power-law manner with growing distance x . Afterwards, in section 4.3 the free propagators and displacement-displacement correlation functions of the bosonic chain are discussed and it is discussed how they are obtained numerically. Finally, in section 4.4 the different scattering matrices of the two models are further investigated.

4.1. Dissipative oscillator model

In the dissipative oscillator model the impurity oscillator couples only to the origin of the bath and thus only feels local excitations of its environment. The spectrum of excitations of the environment at the origin is given by the spectral function corresponding to the local Green function $G_0^{(0)}(z)$ in real space. It constitutes of all single particle excitations of the bosonic degree of freedom at the origin of the chain and is given by

$$A_0^{(0)}(\omega) = -\frac{1}{\pi} \lim_{\epsilon \rightarrow 0} \text{Im}[G_0^{(0)}(\omega + i\epsilon)] \quad (4.1)$$

$$= \frac{1}{2\pi} \int_{-\pi}^{\pi} \delta(\omega - \omega(k)) dk. \quad (4.2)$$

The impurity operator $(b + b^\dagger)/2$ is coupled to the origin of the bath with a coupling strength $\sqrt{\alpha}/\omega_c$ in units of the high-frequency cutoff. The Fourier-transformation adds another factor of $1/\sqrt{2\pi}$. Processes where the impurity interacts with the bath and the bath acts back on the impurity both come with this factor. Thus, in an effective theory for the impurity, each excitation of the bath in k -space can contribute with a strength of $\alpha/2\pi\omega_c^2$. In the definition of the spectral function $A_0^{(0)}(\omega)$ a factor of π is divided out of the imaginary part of the local propagator $G_0^{(0)}(z)$. As the whole propagator enters the theory this factor needs to be restored in the definition of the bath spectral function $J(\omega)$. Thus, the bath spectral function for the effective theory of the impurity is given by

$$J(\omega) = \alpha\pi A_0^{(0)}(\omega) = \frac{\alpha}{2\omega_c^2} \int_{-\pi}^{\pi} \delta(\omega - \omega(k)) dk. \quad (4.3)$$

In order to obtain a spectral function of a desired form in frequency space, one has to choose a dispersion $\omega(k)$ accordingly. In the following, the choice

$$\omega(k) = \left| \frac{k}{\pi} \right|^{\frac{1}{s+1}} \omega_c \quad (4.4)$$

leads to the desired spectral function (2.6)

$$J(\omega) = \alpha\pi(s+1)\omega^s\omega_c^{1-s}, \quad 0 \leq \omega \leq \omega_c.$$

Here, $s > -1$ is again the power-law exponent of the bath spectral function and the momenta k in the dispersion were rescaled such that $\omega(k) \leq \omega_c$. In order to solve the integral over k in equation (4.4), the zeros of the function $\omega - \omega(k)$ need to be known. For a fixed frequency ω these are given by

$$k_{\pm} = \pm\pi \left[\frac{\omega}{\omega_c} \right]^{s+1}. \quad (4.5)$$

There, the inverse modulus of the derivative of $\omega - \omega(k_{\pm})$ reads

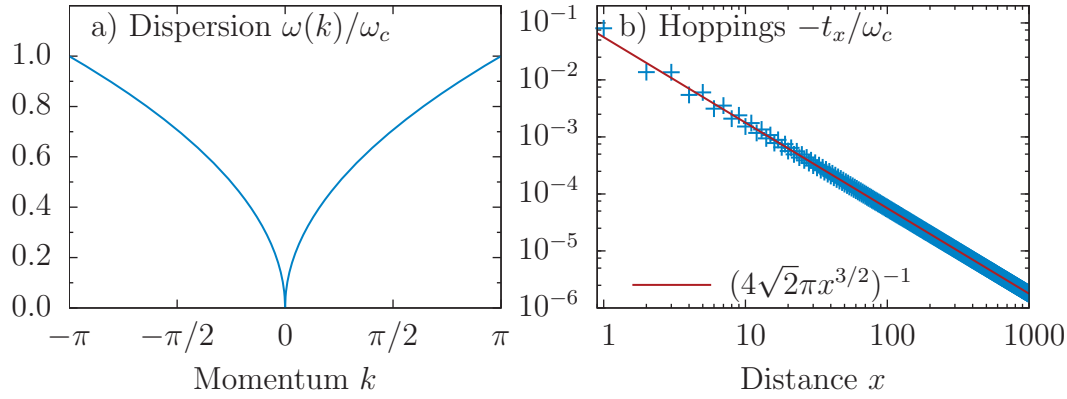
$$|\omega'(k_{\pm})|^{-1} = (s+1)\pi\omega^s\omega_c^{-(s+1)} \quad (4.6)$$

leading to the spectral function

$$\begin{aligned} J(\omega) &= \frac{\alpha}{2\omega_c^2} \int_{-\pi}^{\pi} \delta(\omega - \omega(k)) dk \\ &= \frac{\alpha}{2\omega_c^2} (s+1)\pi\omega^s\omega_c^{-(s+1)} \int_{-\pi}^{\pi} \delta(k - k_+) + \delta(k - k_-) dk \\ &= \alpha\pi(s+1)\omega^s\omega_c^{1-s}. \end{aligned} \quad (4.7)$$

Strictly speaking, the two solutions k_{\pm} collapse for $\omega = 0$ which results in $\omega(0) = 0$. The bath however, features a soft gap behaviour with vanishing spectral density at $\omega = 0$. Thus, a factor of two in the spectrum does not pose a problem at zero frequency. Having chosen a dispersion $\omega(k)$, the corresponding hopping parameters t_x of the original chain in real space can be calculated. They are connected to the dispersion via (cf. section 2.1):

$$\begin{aligned} t_x &= \frac{1}{2\pi} \int_{-\pi}^{\pi} \omega(k) e^{-ikx} dk \\ &= \frac{\omega_c}{2\pi} \int_{-\pi}^{\pi} \left| \frac{k}{\pi} \right|^{\frac{1}{s+1}} e^{-ikx} dk = \frac{\omega_c}{2} \pi^{-\frac{s+2}{s+1}} \int_0^{\pi} k^{\frac{1}{s+1}} \cos(kx) dk \end{aligned} \quad (4.8)$$


Figure 5:

a) Dispersion $\omega(k) = \omega_c \sqrt{|k|/\pi}$ in momentum space for an ohmic bath with a linear spectrum.

b) The crosses show the negative hopping parameters t_x in units of ω_c in real space corresponding to the dispersion $\omega(k)$. They were calculated using equation (4.11). The red line shows the t_x where the FresnelS function in (4.11) has been replaced by its limiting value of $1/2$ for $x \rightarrow \infty$. The power-law behaviour of the hopping amplitudes reads $t_x \sim x^{-3/2}$.

By substituting $u = \left[\frac{2kx}{\pi}\right]^{\frac{1}{s+1}}$ and integrating by parts the hopping amplitudes t_x for integer values of $x > 0$ read

$$t_x = -\frac{\omega_c}{\pi} (2x)^{-\frac{s+2}{s+1}} \int_0^{(2x)^{\frac{1}{s+1}}} \sin(\pi u^{s+1}/2) du \quad (4.9)$$

and

$$t_0 = \frac{\omega_c}{2} \frac{s+1}{s+2} \quad (4.10)$$

by directly solving the integral appearing in (4.8). The integral over the sine is of order 1 for all values of x and does not contribute to the scaling of the t_x as a function of x . The hopping t_0 is an on-site energy that is homogeneous throughout the system and can be understood as a shift in the chemical potential. Figure 5 a) shows the dispersion $\omega(k)$ for an ohmic bath with $s = 1$ in units of the high-frequency cutoff ω_c . Figure 5 b) shows the corresponding hopping parameters t_x in real space together with their asymptotic behaviour. To obtain the prefactor of the asymptotic behaviour of the t_x for large x , equation (4.9) is evaluated for an ohmic spectrum with $s = 1$ to

$$t_x = -\frac{\omega_c}{2\sqrt{2}\pi x^{3/2}} \text{FresnelS}(\sqrt{2x}) \quad (4.11)$$

where

$$\text{FresnelS}(\sqrt{2x}) = \int_0^{\sqrt{2x}} \sin(\pi u^2/2) du \xrightarrow{x \rightarrow \infty} \frac{1}{2} \quad (4.12)$$

is an oscillating function with a maximal value of ~ 0.71 that is reached for $x = 1$ [53].

By adjusting the dispersion $\omega(k)$ of the one-dimensional chain it is thus possible to model a desired power-law spectral density $J(\omega) \sim \omega^s$. The corresponding hopping parameters in real space drop in a power-law manner as $t_x \sim x^{-(s+2)/(s+1)}$. The same choice for the dispersion and thus the real-space hopping amplitudes t_x is made for the two-spin-boson model. In the following, the form of the spectra from the even and the odd bath modes for this choice of $\omega(k)$ is discussed.

4.2. Two-spin-boson model

In case of the two-spin-boson model it was discussed in section 2.2 that the bath modes can be split into even and odd ones. These enter an effective theory of the impurities via the two separate spectral functions

$$J_e(\omega, R) = \alpha \left[\frac{1}{2} \int_{-\epsilon}^{\epsilon} \delta(\omega - \omega(0)) dk + \int_{0^+}^{\pi} \cos^2(kR/2) \delta(\omega - \omega(k)) dk \right] \quad (4.13)$$

$$J_o(\omega, R) = \alpha \int_{0^+}^{\pi} \sin^2(kR/2) \delta(\omega - \omega(k)) dk \quad (4.14)$$

where $R = 2r$ is the total distance between the two impurity spins residing at positions $\pm r$ in the chain. The two functions can be obtained from the single spectral function $J(\omega)$ in equation (4.3). The fact that the dispersion $\omega(k)$ was chosen to be even (cf. equation (4.4)), leads to

$$J(\omega) = \frac{\alpha}{2} \int_{-\pi}^{\pi} \delta(\omega - \omega(k)) [\cos^2(kR/2) + \sin^2(kR/2)] dk \quad (4.15)$$

$$= \frac{\alpha}{2} \int_{-\epsilon}^{\epsilon} \delta(\omega - \omega(0)) dk + \alpha \int_{0^+}^{\pi} \delta(\omega - \omega(k)) [\cos^2(kR/2) + \sin^2(kR/2)] dk \quad (4.16)$$

$$= J_e(\omega, R) + J_o(\omega, R). \quad (4.17)$$

Thus the total spectrum splits into the spectra of the even bath modes and the odd bath modes, that can be seen by the even/odd linear combinations of the spins residing at positions $\pm r$ respectively. In position space each spin, of course, sees locally both the even and the odd modes of the bath, encapsulated in the total spectral function $J(\omega)$. However, the even and the odd linear combinations of the spins are coupled to the even and the odd modes in k -space, respectively. Again the dispersion $\omega(k) = |k/\pi|^{1/(s+1)} \omega_c$ is employed to perform the integrals over the delta-distributions

in k -space. For an arbitrary number of sites $R = 2r$ in the chain that separate the two impurity spins, the even and odd spectral function read

$$J_e(\omega, R) = \alpha\pi(s+1)\omega^s\omega_c^{1-s}\cos^2(\omega^{s+1}\pi R/2\omega_c^{s+1}), \quad (4.18)$$

$$J_o(\omega, R) = \alpha\pi(s+1)\omega^s\omega_c^{1-s}\sin^2(\omega^{s+1}\pi R/2\omega_c^{s+1}). \quad (4.19)$$

It is mainly the even bath which provides a spectral weight close to zero frequency. Expanding the trigonometric functions in the spectral functions around $\omega = 0$ their behaviour is found to read

$$J_e(\omega, R) \approx \alpha(s+1)\omega^s\omega_c^{1-s}, \quad (4.20)$$

$$J_o(\omega, R) \approx \alpha(s+1)\omega^{3s+2}\omega_c^{-(3s+1)}(\pi R/2)^2. \quad (4.21)$$

The expansion is reasonable once the system is at energies $\omega \lesssim (2/\pi R)^{1/(s+1)}$. From its low-frequency behaviour it is inferred, that the odd bath is negligible once that energy-scale is reached from above. With an effective power-law exponent $\tilde{s} = 3s + 2$ it is always super-ohmic for $s > -1/3$ in that region. Figure 6 presents the even and odd spectral function of an ohmic bath for a total distance $R = 20$ between the two spins. The low frequency behaviour can be seen to differ strongly between the spectra of the even and the odd excitations.

4.3. Free bath propagator in position space

In the previous section a specific choice for the dispersion of the one-dimensional chain (4.4) was made. The knowledge of the dispersion enables the calculation of the free bath propagators

$$G_{x,y}^{(0)}(\omega + i\epsilon) = \frac{1}{2\pi} \int_{-\pi}^{\pi} \frac{e^{ik(y-x)}}{\omega + i\epsilon - \omega(k)} dk \quad (4.22)$$

for arbitrary positions x and y in real space. The spectral functions $G_{x,y}^{(0)}(\omega)$ are required in the calculation of the change in the average site occupation $\Delta\langle\hat{n}_x\rangle$ for a large number of distances $x - y$ (cf. equations (3.44) and (3.50) for the dissipative oscillator model and the two-spin-boson model respectively). They show strong oscillatory behaviour in frequency space which makes their numerical calculation very demanding. In this section the analytic results for the imaginary parts of the free propagators $G_{x,y}^{(0)}(\omega + i\epsilon)$ in frequency space are presented. Afterwards it is discussed, how the real part of those propagators can be calculated by making use of the Kramers-Kronig relation and fast Fourier transform algorithms.

In order to obtain a local power-law spectral density $J(\omega) \sim \omega^s$ the bath dispersion is chosen to be $\omega(k) = |k/\pi|^{1/(s+1)}\omega_c$ (cf. equation (4.4)). The imaginary part of $G_{x,y}^{(0)}(\omega)$ on the real axis can be obtained in the same manner as was done for $x = y = 0$

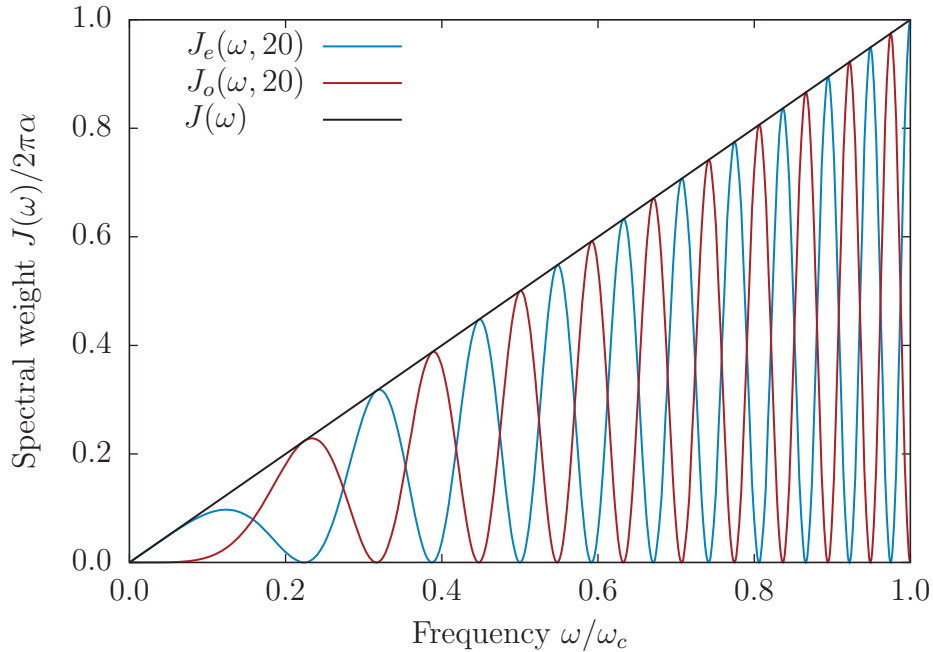


Figure 6:

Spectral functions for the even (blue) and the odd (red) excitations of a one-dimensional chain of bosons as seen by two spins with a distance of $R = 20$ lattice sites in between them. The even and the odd spectral functions add up to the original spectral function $J(\omega)$, shown in black. At small frequencies $\omega < 0.1 \times \omega_c$ almost all the spectral weight is due to the even excitations, which adapt the original power-law behaviour. For an ohmic bath the odd spectrum then vanishes as $J_o(\omega, 20) \sim \omega^5$ for small frequencies.

when the bath spectral function $J(\omega)$ from the imaginary part of $G_{0,0}^{(0)}(\omega)$ in the beginning of section 4.1 (see equation (4.1)) was derived. It is obtained to read

$$\text{Im}[G_{x,y}^{(0)}(\omega)] = \begin{cases} -\pi(s+1)\omega^s\omega_c^{-(s+1)} \cos(\omega^{s+1}\pi(y-x)/\omega_c^{s+1}) & \text{for } 0 \leq \omega \leq \omega_c \\ 0 & \text{else.} \end{cases} \quad (4.23)$$

Since the dispersion $\omega(k)$ is even, the free bath propagators depend only on the modulus of the distance $y-x$ and not on the direction of the propagation. Thus, $G_{x,y}^{(0)}(\omega) = G_{y,x}^{(0)}(\omega)$ holds for all sites x, y . The real part of the propagators can be obtained in two different ways.

i) It can be determined by numerically evaluating the integral

$$\text{Re}[G_{x,y}^{(0)}(\omega + i\epsilon)] = \frac{1}{2\pi} \int_{-\pi}^{\pi} \frac{\cos(k(y-x))(\omega - \omega(k))}{(\omega - \omega(k))^2 + \epsilon^2} dk \quad (4.24)$$

for a small imaginary part, e. g. $\epsilon = 10^{-3}$.

ii) The Kramers-Kronig relations [3]

$$\operatorname{Re}[G_{x,y}^{(0)}(\omega)] = \frac{1}{\pi} \mathcal{P} \left[\int_{-\infty}^{\infty} \frac{\operatorname{Im}[G_{x,y}^{(0)}(\omega')]}{\omega' - \omega} d\omega' \right] \quad (4.25)$$

$$\operatorname{Im}[G_{x,y}^{(0)}(\omega)] = -\frac{1}{\pi} \mathcal{P} \left[\int_{-\infty}^{\infty} \frac{\operatorname{Re}[G_{x,y}^{(0)}(\omega')]}{\omega' - \omega} d\omega' \right] \quad (4.26)$$

that connect the real- and imaginary part of an analytic function can be employed. Here, $\mathcal{P}[\dots]$ denotes the Cauchy principal value of the integral.

Once a free propagator $G_{x,y}^{(0)}(\omega)$ is known in a desired interval of frequencies, the free displacement-displacement correlation function $D_{x,y}^{(0)}(\omega)$ can be obtained immediately in the same region. For a general complex frequency z it is given by (cf. equation (3.60))

$$\begin{aligned} D_{x,y}^{(0)}(z) &= \langle\langle a_x + a_x^\dagger, a_y + a_y^\dagger \rangle\rangle_z^{(0)} \\ &= \langle\langle a_x, a_y^\dagger \rangle\rangle_z^{(0)} + \langle\langle a_x^\dagger, a_y \rangle\rangle_z^{(0)} \\ &= G_{x,y}^{(0)}(z) + G_{x,y}^{(0)}(-z). \end{aligned} \quad (4.27)$$

The last step uses the fact that $\langle\langle a_x^\dagger, a_y \rangle\rangle_z^{(0)} = \langle\langle a_y, a_x^\dagger \rangle\rangle_{-z}^{(0)} = \langle\langle a_x, a_y^\dagger \rangle\rangle_{-z}^{(0)}$ holds for the free bath propagator. Evaluated on the real axis the free displacement-displacement correlator reads

$$D_{x,y}^{(0)}(\omega) = \operatorname{Re}[G_{x,y}^{(0)}(\omega)] + \operatorname{Re}[G_{x,y}^{(0)}(-\omega)] + i \left(\operatorname{Im}[G_{x,y}^{(0)}(\omega)] - \operatorname{Im}[G_{x,y}^{(0)}(-\omega)] \right). \quad (4.28)$$

and therefore the results obtained for the real and imaginary part of the free propagator $G_{x,y}^{(0)}$ at positive and negative frequencies need to be combined accordingly. Figure 7 presents both the free propagator $G_{10,0}^{(0)}(z)$ (part a)) and the free displacement-displacement correlation function $D_{10,0}^{(0)}(z)$ (part b)). Details on the calculation of $\operatorname{Re}[G_{10,0}^{(0)}(z)]$ are discussed in the following section on the Kramers-Kronig relation via fast Fourier transformation. After that the free displacement-displacement correlator $D_{10,0}^{(0)}(\omega)$ was calculated from equation (4.28). For any other distance x one could obtain $G_{x,0}^{(0)}(\omega)$ and from that $D_{x,0}^{(0)}(\omega)$ in the same manner. As the distance x grows, the number of sample points needs to be increased to retain smooth functions for the highly oscillating free correlation functions.

In section 3.4, integral expressions were derived that need to be evaluated in order to calculate the change of the average site occupation $\Delta \langle \hat{n}_x \rangle$ and the change of the squared amplitude of the oscillator displacement $\langle (a_x + a_x^\dagger)^2 \rangle$ at position x in the

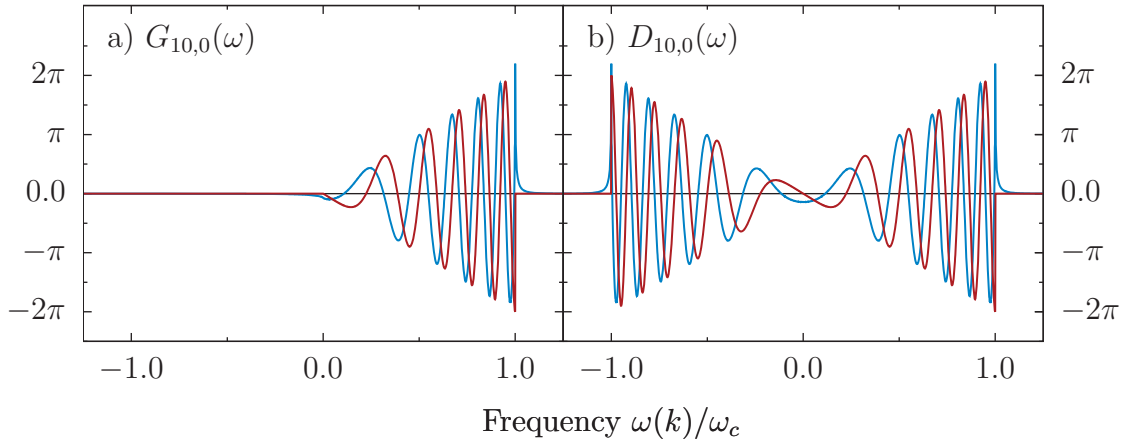


Figure 7:

Free correlation functions a) $G_{10,0}^{(0)}(\omega)$ and b) $D_{10,0}^{(0)}(\omega)$ for an ohmic bath with power-law exponent $s = 1$. Note that the real part (blue) drops fast to zero outside the interval, where the imaginary part (red) is finite, for both functions. This allows to restrict the support needed in the FFT algorithms to the rather small frequency interval $[-2, 2]$. Details on the numerical calculation to obtain the real parts of both functions are provided in the end of this section.

chain both in the dissipative oscillator model and in the two-spin-boson model. The following section describes how to calculate the free propagators $G_{x,0}^{(0)}(\omega)$. Apart from the free bath correlation functions, scattering matrices on the impurities enter the calculation of the thermal averages in both models. As it will be illustrated in section 4.4, they elude an analytic evaluation except for special sets of model parameters. To obtain them for a larger range of model parameters, their Lehmann-representation will be calculated using the Numerical Renormalization Group method that provides approximate eigenenergies and -states of the system.

Kramers-Kronig relation via fast Fourier transformation

Two methods were presented to obtain the real part of a function $G_{x,y}^{(0)}(\omega)$ of interest whose imaginary part is known. Both methods rely upon the solution of a specific integral. In the first method the integral

$$\text{Re}[G_{x,y}^{(0)}(\omega + i\epsilon)] = \frac{1}{2\pi} \int_{-\pi}^{\pi} \frac{\cos(k(y-x))(\omega - \omega(k))}{(\omega - \omega(k))^2 + \epsilon^2} dk$$

needs to be solved for a small imaginary part ϵ and for each frequency of interest individually. The method is stable even for $\epsilon = 0$, as long as $\omega < 0$ or $\omega > \omega_c$ where the imaginary part of G is strictly zero. However, the method is not very fast since

the numerical integration has to be performed for each desired point ω in frequency space in order to obtain a smooth function. Hence this method is computationally very demanding if a high resolution of the function in frequency space is desired.

The second method is very stable inside the interval $[0, \omega_c]$ and there is a fast way to perform the integral via Fourier-transformation for a large number of frequencies in one go. This method makes use of the fact that the integral in (4.25) is a convolution for which the convolution theorem in Fourier calculus [7] can be used. The convolution theorem states that the Fourier transformation $\mathcal{F}[\dots]$ of the convolution

$$(f * g)(\omega) = \int_{-\infty}^{\infty} f(\omega')g(\omega - \omega') d\omega' \quad (4.29)$$

of two functions f and g is given by the product of the Fourier transformations of the individual functions:

$$\mathcal{F}[(f * g)(\omega)](t) = \sqrt{2\pi}\mathcal{F}[f(\omega)](t)\mathcal{F}[g(\omega)](t). \quad (4.30)$$

Here, the Fourier transformation and its inverse are defined as

$$\mathcal{F}[f(\omega)](t) = \tilde{f}(t) = \frac{1}{\sqrt{2\pi}} \int_{-\infty}^{\infty} f(\omega)e^{-i\omega t} d\omega \quad (4.31)$$

$$\mathcal{F}^{-1}[\tilde{f}(t)](\omega) = f(\omega) = \frac{1}{\sqrt{2\pi}} \int_{-\infty}^{\infty} \tilde{f}(t)e^{i\omega t} dt \quad (4.32)$$

$$(4.33)$$

for a given function $f(\omega)$. The method uses the Fourier transformation of $g(\omega) = \omega^{-1}$ which reads

$$\tilde{g}(t) = -i\sqrt{\frac{\pi}{2}} \text{sign}(t). \quad (4.34)$$

With this knowledge, first the transformation \mathcal{F} on the integral in (4.25) is performed and afterwards its inverse transformation \mathcal{F}^{-1} . Thereby the real part of $G_{x,y}^{(0)}(\omega)$ is obtained from

$$\text{Re}[G_{x,y}^{(0)}(\omega)] = \mathcal{F}^{-1}\left[\mathcal{F}[\text{Re}[G_{x,y}^{(0)}(\omega')]](t)\right](\omega) = \mathcal{F}^{-1}\left[\text{Im}[\tilde{G}_{x,y}^{(0)}(t)]i \text{sign}(t)\right](\omega). \quad (4.35)$$

Both the inverse transformation on the right hand side and the forward transformation of the imaginary part of G can be performed efficiently on a computer using fast Fourier transformation (FFT) algorithms for a finite number of data points $(\omega, \text{Im}[G_{x,y}^{(0)}(\omega)])$ [54].

Figure 7 in the previous section presents both the real and the imaginary part of $G_{x,0}^{(0)}(\omega)$ for $x = 10$ in the frequency interval $[-1.25, 1.25]$ in units of ω_c (part a)). While the imaginary part is given by the analytic expression (4.23) the real part was obtained by combining the two different methods discussed above. The first Kramers-Kronig

relation (4.25) was performed via Fourier-transformation employing equation (4.35) for a frequency range $[-2, 2]$ in units of ω_c with a resolution of 0.001. As the results around the borders of the support are fluctuating and rather imprecise, the results of $\text{Re}[G_{x,y}^{(0)}(\omega)]$ in the frequency range $[0, 1]$ from those results were picked. Outside the interval $[0, 1]$ a numerical integration of equation (4.24) within Mathematica via the function `NIntegrate[]` [55] was executed. The resolution in frequency space was again set to 0.001.

4.4. Impurity scattering matrix

The impurity scattering matrix of the dissipative oscillator model was derived in section 3.4.2 to read

$$\mathcal{T}_{\text{do}}(z, T) = \frac{\alpha}{4} \langle\langle b + b^\dagger, b + b^\dagger \rangle\rangle_z(T) = \frac{\alpha}{4} D_{\text{imp}}(z, T)$$

and is the single quantity needed to describe the effect of the impurity and its environment onto each other within the framework of *equations of motion*. It is given by the displacement-displacement correlation function $D_{\text{imp}}(z, T) = \langle\langle b + b^\dagger, b + b^\dagger \rangle\rangle_z(T)$ of the impurity and the factor $\alpha/4$ encoding the interaction-strength with the zero orbital of the one-dimensional chain in real space. A closed set of equations for $D_{\text{imp}}(\omega)$ can be obtained since the dissipative oscillator model incorporates only bosonic degrees of freedom. Consequently the possibility exists to relate the scattering matrix to a set of other correlators, most of which are free ones that can be evaluated numerically with high precision. In appendix A the relation

$$D_{\text{imp}}(z, T) = \left[D_{\text{imp}}^{(0)}(z)^{-1} - \frac{\alpha}{4} D^{(0)}(x=0, z) - U [\Sigma_1(z, T) + \Sigma_2(z, T)] \right]^{-1} \quad (4.36)$$

is derived for the displacement-displacement correlation function of the impurity. There the functions

$$D_{\text{imp}}^{(0)}(z) = \frac{1}{z - \Delta} - \frac{1}{z + \Delta} \quad (4.37)$$

$$D^{(0)}(x=0, z) = \frac{1}{2\pi} \int_{-\pi}^{\pi} \frac{1}{z - \omega(k)} - \frac{1}{z + \omega(k)} dk \quad (4.38)$$

are introduced as well. They are the bare displacement-displacement correlation functions of the impurity with frequency Δ for zero self-interaction U , and the one of the bath at the origin $x=0$ in real space respectively. Furthermore the two self-energy functions

$$\Sigma_1(z, T) = \frac{\Delta + z}{2\Delta} \frac{\langle\langle b^\dagger b b, b + b^\dagger \rangle\rangle_z(T)}{D_{\text{imp}}(z, T)} \quad (4.39)$$

$$\Sigma_2(z, T) = \frac{\Delta - z}{2\Delta} \frac{\langle\langle b^\dagger b^\dagger b, b + b^\dagger \rangle\rangle_z(T)}{D_{\text{imp}}(z, T)} \quad (4.40)$$

are introduced which have the function $D_{\text{imp}}(z, T)$ of interest in their denominator. There are two routes to calculate $D_{\text{imp}}^{(0)}(\omega, T = 0)$ for real frequencies.

- i) Calculating the matrix elements of the operator $b + b^\dagger$ that are needed in the evaluation of the Lehmann-sum for $D_{\text{imp}}(\omega, T = 0)$ in the eigenbasis that was obtained via the NRG. Then the obtained poles need to be broadened appropriately to get a smooth function for $\mathcal{T}_{\text{do}}(\omega, T = 0)$ (see the discussion in section 5.4 for details on obtaining a spectral function from NRG data).
- ii) Calculating the matrix elements of the two correlators $\langle\langle b^\dagger b b, b + b^\dagger \rangle\rangle_\omega$ and $\langle\langle b^\dagger b^\dagger b, b + b^\dagger \rangle\rangle_\omega$, appearing in the expressions for the self-energies Σ_1 and Σ_2 in their zero-temperature limit. Those self-energies are then used in equation (4.36) in order to get a second estimate for the \mathcal{T} -matrix of the impurity.

In this work, the first method is used. The zero temperature Lehmann-sums, needed for the calculation of $\mathcal{T}_{\text{do}}(z, T = 0)$, show already to be smooth. They do not feature any oscillations, like e. g. the Coulomb part of the self energy of the single impurity Anderson model (SIAM). There, oscillations appear on energy-scales lower than the finite temperature for which the self-energy is calculated, if only the simple calculation i) is performed [11]. Once obtained, the smooth functions for the scattering matrix in different parameter-regimes of the model are used to calculate the change in both the average site occupation $\langle \hat{n}_x \rangle$ and the average of the squared displacement amplitude $\langle (a_x + a_x^\dagger)^2 \rangle$.

Two-spin-boson model

In case of the two-spin-boson model a 2×2 scattering matrix was deduced in section 3.4.2 with the different matrix entries

$$T_{2\text{sbm}}(z, T)_{i,j} = \frac{\alpha}{4} \langle\langle \sigma_{z,i}, \sigma_{z,j} \rangle\rangle_z(T), \quad i, j = 1, 2. \quad (4.41)$$

For those correlators the spin commutation relations

$$[\sigma_{\alpha,j}, \sigma_{\beta,k}] = 2i\delta_{j,k}\epsilon_{\alpha\beta\gamma}\sigma_\gamma, \quad j, k \in \{1, 2\}, \quad \alpha, \beta, \gamma \in \{x, y, z\} \quad (4.42)$$

spoil the possibility to derive a closed set of equations of motion like in case of the damped harmonic oscillator model. They lead to higher order correlation functions between the bath and the impurities that cannot be simply absorbed in other correlators. Therefore the correlators $\langle\langle \sigma_{z,i}, \sigma_{z,j} \rangle\rangle_z(T)$ themselves need to be calculated numerically via the NRG from the outset to obtain information on the change in the average site occupation. Results for the scattering matrix $\mathcal{T}_{2\text{sbm}}(\omega, T = 0)$ in its zero temperature limit can be found in section 6.2.4.





5. Numerical Renormalization Group

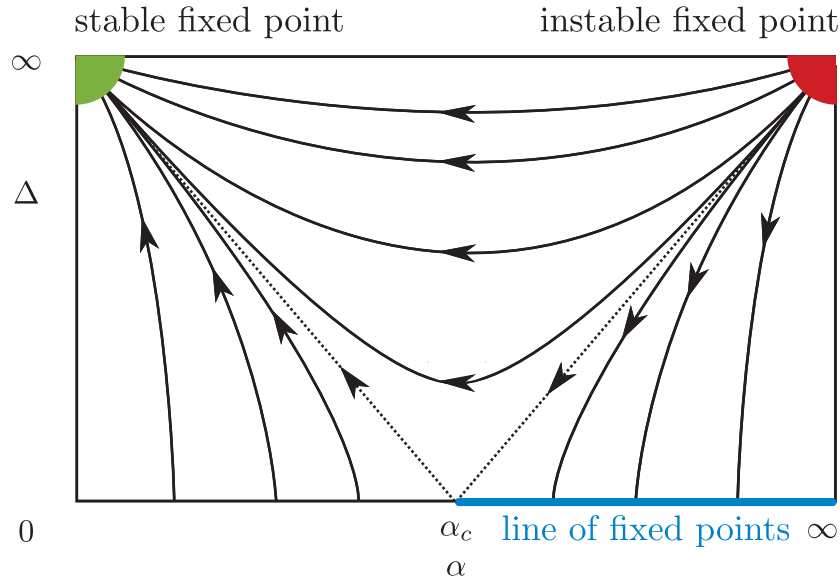
Both the dissipative oscillator model (2.5) and the two-spin-boson model (2.24) introduced in section 2 are quantum impurity models that feature a small subsystem consisting of either one or two impurities which is coupled to a dissipative environment. Their Hamiltonians have the general form

$$H = H_{\text{imp}} + H_{\text{bath}} + H_{\text{int}}$$

where H_{imp} describes the local subsystem (the impurities) while H_{bath} describes the non-interacting environment in which the impurities reside. The interaction between the impurities and their environment is then comprised in H_{int} . Due to their structure the Hamiltonians are in general not analytically solvable and have to be solved by an approximative method.

The method of choice in this thesis is the Numerical Renormalization Group method put forward by Kenneth G. Wilson in 1975 [52]. In general, renormalization techniques were already used in the 1950's by e.g. Gell-Mann and Low who employed them to study the effects of the vacuum polarisation around an electric charge both on the charge itself and its mass within quantum electrodynamics [20]. Wilson made huge contributions to this field in the mid-seventies of the twentieth century using renormalization group (RG) methods in real-space (block-spin method) as well as in field theories. He also connected statistical renormalisations and field theoretical renormalization group ideas.

The typical starting point within field theory is to write down the action S corresponding to the Hamiltonian H of the problem at hand. In the following, the model parameters entering the action S are denoted by P , such that $S(P)$ can be considered to reside in a multi-dimensional space spanned by those model parameters. The next step is to integrate out the high-energy part of the theory in S leading to a renormalization of the model's parameters $P \rightarrow P'$ in the remaining low-energy sector. This step is typically denoted by applying a renormalization group mapping R to the action such that $S(P') = R[S(P)]$. A key concept within renormalization group techniques is that of fixed points P^* of the mapping $R[\dots]$ where $S(P^*) = R[S(P^*)]$ is invariant under R . Around these fixed points there are relevant, irrelevant or marginal operators that either drive the system away from or towards the fixed point or that do neither respectively as the mapping $R[\dots]$ is repeatedly applied to the action $S(P)$. Stable fixed points P^* in the parameter space where all operators are irrelevant or marginal can be identified with stable phases of the model. The fixed points where all operators need to be considered relevant are identified with ideal phases that cannot be reached in reality (e.g. zero-temperature fixed points). Between stable fixed points and ideal fixed points there have to be points where both relevant and irrelevant operators are present. Such fixed points are identified with phase transitions and thus are of large interest of their own. Figure 8 sketches the set of fixed points and the Renormalization Group flow between them in the α - Δ -plane for the ohmic spin-boson-model.

**Figure 8:**

RG-flow of the coupling α and tunnelling rate Δ of the spin boson model. The model features a stable fixed point where the coupling between impurity and bath has been renormalized to zero and the tunnelling rate is infinite (green corner). This fixed point is termed the localised fixed point. An unstable fixed point is positioned at infinite coupling strength and infinite tunnelling rate (red corner) which is of no physical relevance as it cannot be reached. At zero tunnelling rate, a line of fixed points appears for couplings larger than a critical value α_c . These fixed points are all localised fixed points where the bath oscillators are displaced by an amount set by the fixed point value of α . The dashed line connecting the points $(\alpha_c, 0)$ and (∞, ∞) is a separatrix which separates the flow of the system towards either the delocalised or any of the localised fixed points.

While there are typically trivial fixed points where one or more parameters renormalise to a finite value or zero, there can as well appear fixed points in which one or more parameters renormalise to infinity. A famous example would be the Coulomb-interaction U in the Anderson impurity model (AIM) which, as it flows to infinity basically projects the theory down to the sector with a single electron occupying the impurity [52]. In that limit, the AIM becomes the renowned Kondo model which eluded a solution until the 1970s. Within standard RG the spin-spin interaction J of the model diverges as the system is integrated out close to the band edge D of the conduction electrons. In a perturbative expansion the second order term $\sim J^2 \log(D/k_B T)$ features a logarithmic divergence once $k_B T < D$, where k_B is the Boltzmann-constant and T is the temperature. Thus, the model becomes strongly interacting in J and a perturbative expansion around small J is not feasible any longer.

In his extensive work, Kenneth G. Wilson introduced a numerical, non-perturbative method—termed the Numerical Renormalization Group (NRG)—by which he was able to resolve the breakdown in the perturbative expansion, also known as the “Kondo problem” [52]. Using the NRG, he was able to determine the ground state of the Kondo model in the strong coupling limit by investigating the parameter flow and the fixed point structure of the model. In doing so, he went beyond the limit of perturbation theory in the spin-spin interaction J of the model. Later on, in 1982 he was awarded the Nobel Prize in Physics “for his theory for critical phenomena in connection with phase transitions” [37].

The NRG itself has since been used and extended to a whole zoo of other models. Its role as an impurity solver for dynamical mean field calculations [31, 8, 48] and the extension from fermionic systems to bosonic ones [13, 12, 41] as well as the extension to multi-channel models in the recent past [32, 33] and the development of a time-dependent version [4] make the NRG still an up-to-date numerical method. While it is known to fail in obtaining the correct dynamical exponents for the spin-boson model [46, 47] for $s \leq 1/2$ in its crudest version, there is still lots of information to be gained apart from those exponents for $s > 1/2$. The fixed points of the models as well as information on the entropy, the ground states of the systems and correlation functions in their zero temperature limit can be obtained from the NRG for the bosonic models studied in this work.

It is the purpose of this section to introduce the NRG-method to the reader. Here it is shown how to discretise the continuous dissipative environments appearing in the models under discussion and how to map them onto a chain of modes that allows the application of an iterative numerical algorithm. Additionally, the concept of a flow of the Hamiltonian under the renormalization group mapping is introduced. An identification of different types of fixed points in this flow is presented. A comprehensive introduction to the method of the NRG together with a series of applications to different models can e. g. be found in [9]. The notation and argumentation in the following derivation of the mappings that need to be performed to the Hamiltonian is mainly along the lines of that work.

This section also demonstrates how to gain the correlation functions derived in section 3.1, which were described in terms of their Lehmann representation, from the NRG. [10], Section 5.5 identifies the main features in the numerical implementation of the models and discusses the demands in computational cost of a bosonic NRG implementation. It is presented how to get around certain bottlenecks arising especially in the two-spin-boson model where two dissipative environments need to be incorporated into the calculations.

Introduction

A set of mappings is applied in the following, in order to gain a numerically solvable model both for the dissipative oscillator model and the two-spin-boson model. These

mappings affect the environments of the impurities only. Since the parts H_{bath} and H_{int} are linear in the different channels for the two-spin-boson model (cf. equation (2.24)), the mappings can be applied to each channel individually. Therefore, the discussion concentrates on the mapping that needs to be performed for a single channel model, i. e. the dissipative oscillator model (2.5). Its Hamiltonian is given by

$$H_{\text{do}} = H_{\text{imp}} + \int_0^{\omega_c} g(\omega) a_\omega^\dagger a_\omega d\omega + \left(\frac{b + b^\dagger}{2} \right) \int_0^{\omega_c} h(\omega) (a_\omega + a_\omega^\dagger) d\omega. \quad (5.1)$$

Here, ω_c is a high-frequency cutoff, $g(\omega)$ encapsulates what excitations at frequency ω there are in the bath and $h(\omega)$ is the coupling between the impurity oscillator and that frequency. The operator b^\dagger is the creator of an excitation on the impurity while an operator a_ω^\dagger creates an excitation at frequency ω in the environment. Applying the equations of motion to H_{do} with the bath in its frequency representation (5.1) reveals that the bath enters an effective theory for the impurity only via the quantity

$$\begin{aligned} J(\omega) &= - \lim_{\delta \rightarrow 0} \text{Im} \left[\int_0^{\omega_c} \frac{h^2(\tilde{\omega})}{\omega + i\delta - g(\tilde{\omega})} d\tilde{\omega} \right] \\ &= \pi \int_0^{\omega_c} h^2(\tilde{\omega}) \delta(\omega - g(\tilde{\omega})) d\tilde{\omega} \\ &= \pi h^2(\epsilon(\omega)) \left| \frac{d\epsilon(\omega')}{d\omega'} \right|_{\omega'=\omega} \end{aligned} \quad (5.2)$$

which is in general termed the bath spectral function. In the last equation the fact that $g(\tilde{\omega})$ is invertible on the interval $[0, \omega_c]$ and therefore only has a single solution to $g(\tilde{\omega}) - \omega = 0$ for a given ω was used. Its inverse function is defined to be $\epsilon(\tilde{\omega}) := g^{-1}(\tilde{\omega})$. The crucial point about the bath entering only via a specific combination of g and h is the freedom it poses in their choice so long as they combine to the desired spectral function $J(\omega)$. This freedom of choice is employed in the following discretisation process. In general there are three steps that need to be taken in order to arrive at the kind of model that can be solved on a computer.

- 1) The continuous bath, described by $J(\omega)$ needs to be discretised in order to allow for a numerical treatment of the system. To this end, the whole frequency range is divided into a set of intervals whose width decreases exponentially. This is achieved by introducing a logarithmic discretisation parameter $\Lambda > 1$ and defining a set of points

$$x_n = \Lambda^{-n} \omega_c, \quad n = 0, 1, 2, \dots \quad (5.3)$$

From the x_n a series of intervals I_n is defined to be

$$I_n := (x_{n+1}, x_n] = (\Lambda^{-(n+1)} \omega_c, \Lambda^{-n} \omega_c], \quad n = 0, 1, 2, \dots \quad (5.4)$$

In each of the intervals I_n the bath is then represented by a single mode, characteristic of the bath in that interval. That way, an infinite but countable number of bath-modes is obtained, describing the environment of the impurity down to lowest energy scales. Details of the discretisation process are discussed in section 5.1.

- 2) The discretised bath needs to be mapped onto a semi-infinite chain (the so-called Wilson-chain), which is iteratively treatable. This mapping is described in section 5.2.
- 3) The Wilson-chain needs to be diagonalised iteratively. That is achieved by truncating the number of states kept after a diagonalisation to a finite number N_{kept} . That way, the dimension of the total Hamiltonian in each iteration stays finite and it is possible to successively add orbitals from the Wilson-chain and thus to describe the system at lower and lower energies. The diagonalisation and truncation scheme are discussed in full detail in section 5.3 for both models.

As mentioned before, the NRG is a non-perturbative method. However, it is not an exact method in the sense that the steps 1) and 3) inherit approximations. To what extent those approximations are justified and controllable is discussed in the corresponding sections 5.1 and 5.3 as well as in the results section.

5.1. Logarithmic discretisation

A modern computer, be it a personal computer or a big computing-cluster is always limited to perform only a discrete and finite number of tasks in a finite amount of time. While the computational resources *number of floating point operations per second* (FLOPS) that can be performed by one or more processing units (CPUs or GPUs) and the *amount of random access memory* (RAM) available can differ by several orders of magnitude, they always remain finite. It is therefore not possible to solve a quantum impurity system like the dissipative oscillator model which incorporates a continuous environment of excitations exactly on a computer in a finite amount of time. It is thus necessary to somehow discretise the continuous environment and make the model computationally calculable.

Like mentioned under point 1) in the previous section, the discretisation can be achieved by introducing a logarithmic discretisation parameter $\Lambda > 1$ which is used to introduce a set of points $x_n = \Lambda^{-n}\omega_c$ and split the interval $[0, \omega_c]$ into a series of intervals $I_n = (\Lambda^{-(n+1)}\omega_c, \Lambda^{-n}\omega_c]$. After that a corresponding set of excitations that are a good description of the environment in those intervals needs to be chosen. From the way the intervals I_n are distributed in frequency space one can already expect that the excitations that represent the bath in each interval will drop of exponentially as $\sim \Lambda^{-n}$. It is in fact this exponential behaviour that will lead to a decent separation in

energy scales between different iterations of the NRG algorithm and allow to discard the high energy states in each iteration.

Within each interval I_n , a complete set of orthogonal functions $\psi_{n,p}(\omega)$ is introduced via Fourier-transformation. They are given by

$$\psi_{n,p}(\omega) = \begin{cases} \frac{1}{\sqrt{d_n}} e^{ik_n p \omega}, & \omega \in I_n \\ 0, & \omega \notin I_n \end{cases}, \quad p \in \mathbb{Z} \quad (5.5)$$

where $d_n = \Lambda^{-n} \omega_c (1 - \Lambda^{-1})$ is the width of the interval I_n , the p label all different momenta and $k_n = 2\pi/d_n$ is the fundamental mode of interval I_n . The set of basis states is then used to express the original bosonic operators a_ω in this new basis:

$$a_\omega = \sum_{n,p} a_{n,p} \psi_{n,p}(\omega). \quad (5.6)$$

The corresponding inverse transformation reads

$$a_{n,p} = \int_0^{\omega_c} a_\omega \bar{\psi}_{n,p}(\omega) d\omega \quad (5.7)$$

and one may check that due to the unitary transformation between the a_ω and the $a_{n,p}$ the usual bosonic commutation relations also hold for the latter. The Hamiltonian of the dissipative oscillator model is then expressed in terms of the new operators $a_{n,p}$. The environmental part of the interaction H_{int} is transformed as

$$\begin{aligned} \int_0^{\omega_c} h(\omega) (a_\omega + a_\omega^\dagger) d\omega &= \int_0^{\omega_c} h(\omega) \sum_{n,p} (a_{n,p} \psi_{n,p}(\omega) + a_{n,p}^\dagger \bar{\psi}_{n,p}(\omega)) d\omega \\ &= \sum_{n,p} \int_{x_{n+1}}^{x_n} h(\omega) (a_{n,p} \psi_{n,p}(\omega) + a_{n,p}^\dagger \bar{\psi}_{n,p}(\omega)) d\omega. \end{aligned} \quad (5.8)$$

By choosing the function $h(\omega) = h_n$ to be a constant in each interval I_n all integrals in (5.8) are zero except for the ones where $p = 0$. Thus the equation simplifies to

$$\int_0^{\omega_c} h(\omega) (a_\omega + a_\omega^\dagger) d\omega = \sum_{n=0}^{\infty} h_n \sqrt{d_n} (a_{n,0} + a_{n,0}^\dagger) \quad (5.9)$$

which is the desired result of a discrete number of states to which the impurity oscillator couples. The constants h_n are set to the square root of the average spectral weight contained in $J(\omega)$ in interval I_n :

$$h_n = \left[\frac{1}{\pi d_n} \int_{I_n} J(\omega) d\omega \right]^{1/2} := \frac{1}{\sqrt{\pi d_n}} \gamma_n. \quad (5.10)$$

The transformation (5.6) is also applied to the free part of the Hamiltonian H_{bath} which becomes

$$\int_0^{\omega_c} g(\omega) a_\omega^\dagger a_\omega d\omega = \sum_{n,p} \xi_n a_{n,p}^\dagger a_{n,p} + \sum_{n,p \neq p'} c_n(p, p') a_{n,p}^\dagger a_{n,p'} \quad (5.11)$$

where the first sum is over equal indices $p = p'$ and the functions

$$c_n(p, p') = \frac{1}{d_n} \int_{I_n} g(\omega) \exp \left[\frac{2\pi i(p' - p)\omega}{d_n} \right] d\omega, \quad \xi_n = c_n(p, p) = \frac{1}{d_n} \int_{I_n} g(\omega) d\omega \quad (5.12)$$

are introduced. With the choice (5.10) for the constants h_n in each interval I_n , the integrals leading to the ξ_n can be rewritten as

$$\xi_n = \frac{1}{d_n} \int_{I_n} g(\omega) d\omega \equiv \int_{I_n} \omega J(\omega) d\omega / \int_{I_n} J(\omega) d\omega. \quad (5.13)$$

They are then given by the normalised expectation to find an excitation at frequency ω under the probability distribution $J(\omega)$. As the identity (5.13) is not entirely trivial to see it's proof is presented in appendix B to the interested reader.

By Fourier-transformation of the operators a_ω in a set of countable intervals I_n it is thus achieved that the impurity couples to a single mode $a_{n,0}$ in each interval only. The previously diagonal bath part of the Hamiltonian however has gained a more complex structure. In each interval I_n the different p modes in (5.11) are coupled via the $c_n(p, p')$. Were it not for those interactions it would be feasible to take the $p = 0$ part $\sum_n \xi_n a_{n,0}^\dagger a_{n,0}$ of the transformed H_{bath} and neglect all other modes from the theory since they do not couple to the impurity. Here actually the first approximation in the whole treatment of the model is made. It is assumed, that all couplings $c_n(p, p')$ are indeed zero (an approximation that becomes exact in the limit $\Lambda \rightarrow 1$, which would restore the continuous model). Bulla et al. estimate the $c_n(p, p')$ by choosing a linear dispersion $g(\omega) = \omega$ for which the integrals appearing in the definition of the $c_n(p, p')$ can be solved analytically (cf. [9]). They obtain

$$c_n(p, p') = \Lambda^{-n} \omega_c \frac{1 - \Lambda^{-1}}{2\pi i(p' - p)} \exp \left[\frac{2\pi i(p' - p)}{1 - \Lambda^{-1}} \right]. \quad (5.14)$$

The approximation of neglecting all terms $c_n(p, p')$ for $p \neq p'$ is still quite good even for values of Λ in the range of $\sim 1.5 - 10$ (the latter can be achieved using the so-called “z-trick”, cf. [56, 40]). This however can not easily be seen from the simple definition of the $c_n(p, p')$ as there are infinitely many of them that are ignored.

Here a real-space argument, similarly already given by Wilson in his original work on the Kondo-model [52] provides insight in why it is safe to neglect the $c_n(p, p')$, even when adapted for the bosonic environment within this work. By inverting the dispersion relation $\omega(k) = |k/\pi|^{1/(s+1)} \omega_c$ the frequencies in a given interval I_n can

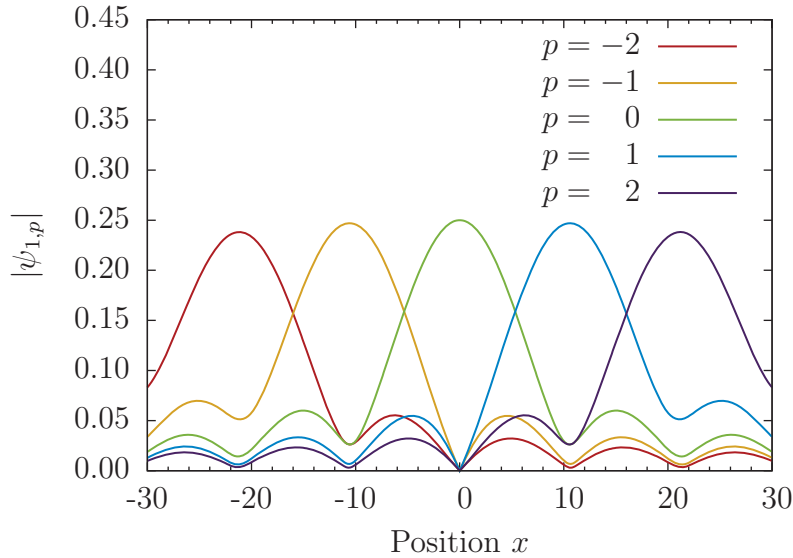


Figure 9:

Modulus of the overlap between plane waves $e^{-ik(\omega)x}$ and the functions $\psi_{n,p}$ for $n = 1$ and a logarithmic discretisation parameter $\Lambda = 2.0$. The overlap is large around an $x \sim p$ and thus only the $p = 0$ functions are peaked right at the origin $x = 0$ where the impurity resides in the dissipative oscillator model.

be connected to a range of corresponding lattice momenta $k(\omega) = \pi|\omega/\omega_c|^{s+1}$. It is those momenta which are then important in the Fourier-transformation that connects functions in momentum space and real space. A calculation of the overlap in frequency space of any state $\psi_{n,p}(\omega)$ with plane waves $e^{-ik(\omega)x}$ for different values of x reveals a peaked structure around $x \sim p$ in case of an ohmic environment with $s = 1$ for all values of p (cf. figure 9). It is thus safe to neglect those terms with $p \neq 0$ for which the $\psi_{n,p}(\omega)$ are peaked far away from the impurity in real space. Neglecting all terms with $p \neq p'$ and dropping the index $p = 0$ one finally arrives at the desired Hamiltonian which reads

$$H_{\text{do}}^{\text{star}} = H_{\text{imp}} + \sum_{n=0}^{\infty} \left\{ \xi_n a_n^\dagger a_n + \left(\frac{b + b^\dagger}{2} \right) \frac{\gamma_n}{\sqrt{\pi}} (a_n + a_n^\dagger) \right\} \quad (5.15)$$

and is sometimes also referred as *star*-Hamiltonian (cf. [12]). As mentioned above the ξ_n and γ_n appearing are nothing but the expectation value to find an excitation at frequency ω in each interval I_n under the distribution $J(\omega)$ and the square root of the expectation value of the distribution $J(\omega)$ itself respectively. Thus the discretisation process leads to a model where the impurity couples to a set of bath modes with characteristic frequencies ξ_n with a corresponding coupling strength of $\gamma_n/\sqrt{\pi}$. Again,

in the limit of $\Lambda \rightarrow 1$, the continuous model would be retained where the bath modes lie dense in the interval $[0, \omega_c]$. The γ_n and the ξ_n drop exponentially as $\Lambda^{-n(s+1)/2}$ and Λ^{-n} respectively for baths with a spectral density $J(\omega) = \alpha\pi(s+1)\omega^s\omega_c^{1-s}$, $\omega \in [0, \omega_c]$ (cf. equation (2.6)) for which they read

$$\gamma_n^2 = \int_{I_n} J(\omega) d\omega = \alpha\pi\omega_c^2(1 - \Lambda^{-(s+1)})\Lambda^{-n(s+1)} \quad (5.16)$$

$$\xi_n = \gamma_n^{-2} \int_{I_n} \omega J(\omega) d\omega = \frac{s+1}{s+2} \frac{1 - \Lambda^{-(s+2)}}{1 - \Lambda^{-(s+1)}} \Lambda^{-n} \omega_c. \quad (5.17)$$

Figure 10 presents a sketch illustrating the logarithmically discretised *star*-Hamiltonian (5.15). For the dissipative oscillator model under discussion, only power-law

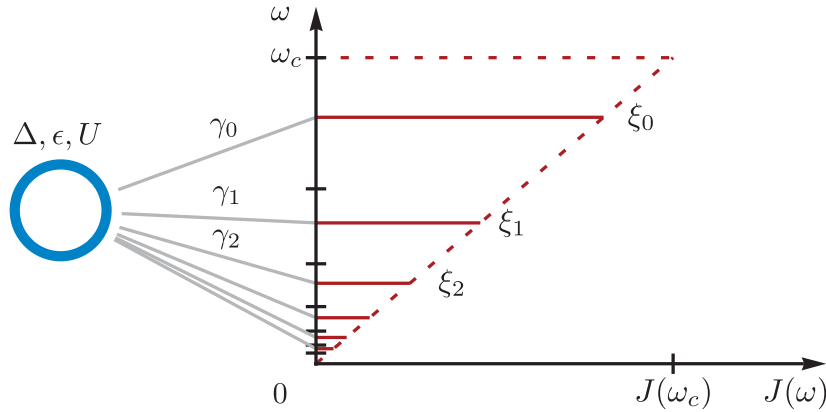


Figure 10:

The impurity (blue circle) with energy scales Δ, ϵ, U couples to a discrete set of bosonic modes at energies ξ_n (red lines) with a corresponding coupling strength of γ_n (light grey). The original linear spectrum $J(\omega) \sim \omega$ is depicted by the dashed red lines. The energies ξ_n and the couplings γ_n both drop exponentially as Λ^{-n} in case of the ohmic spectral density.

spectral functions $J(\omega)$ are considered which are in essence featureless within each interval I_n , i.e. they are smooth and do not show single broad peaks which could be identified with characteristic excitations of the environment. This behaviour is very different from that of the spectral functions $J_e(\omega)$ and $J_o(\omega)$ of the even and the odd environmental excitations that do appear in the two-spin-boson model. While both originate as well from a power-law spectrum of the environment as $J(\omega)$, they are modulated by a \cos^2 and a \sin^2 respectively and thus show a more complicated behaviour as they alternate frequently between zero and the original power-law. The following discussion focusses on the behaviour of the even spectral function for a fixed number of lattice spaces R between the spins. For a high-frequency cutoff $\omega_c = 1$ the even spectral function was derived in section 4.2 to read

$$J_e(\omega, R) = \alpha\pi(s+1)\omega^s \cos^2(\pi R\omega^{s+1}/2).$$

Therefore the oscillatory behaviour becomes more pronounced as ω is increased. There are three different scenarios for the behaviour of $J_e(\omega, R)$ within a given interval I_n where $\omega \sim \Lambda^{-n}$:

- i) $\Lambda^{n(s+1)} \ll \pi R/2$: In such an interval there are no oscillations of the spectral function and its behaviour can be assumed to be smooth meaning that the averages calculated in order to obtain the ξ_n and γ_n are well justified. This kind of behaviour is reached for large n .

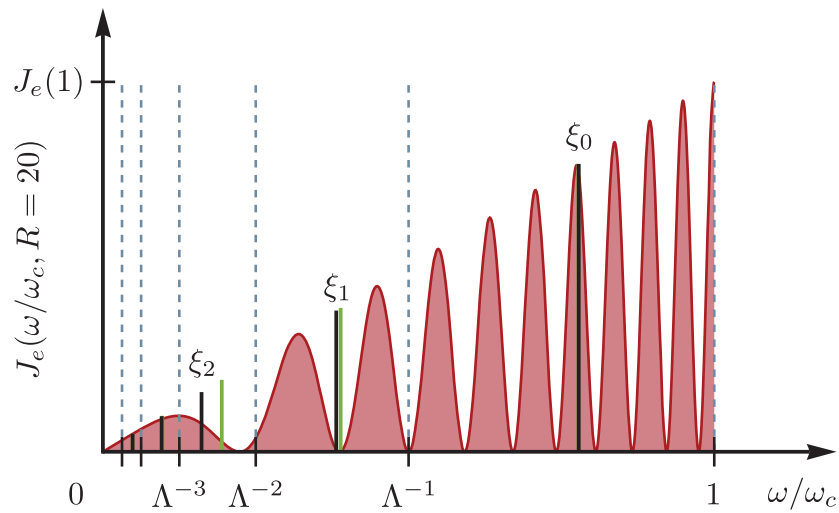


Figure 11:

Plot of the spectral function $J_e(\omega, R = 10)$ together with the first few ξ_n that are calculated numerically from equation (5.13) for a discretisation parameter $\Lambda = 2.0$ and a power-law exponent $s = 1$. The thin, dashed lines mark the borders of the first few intervals I_n . There, the different quality of the averages that are taken in order to position the ξ_n can be seen: in interval I_0 there are 8 peaks which are represented by a single excitation. Since the density of the peaks is rather high, the possible error in positioning ξ_0 becomes small. Interval I_1 features two peaks but the averaging process leads to a single ξ_1 that is positioned where there is nearly no spectral weight in J_e . From the interval I_2 on, the averaging process leads to excitations ξ_n that are characteristic of the bath in those intervals. In green there are depicted the corresponding excitations that are obtained for the simple ohmic bath that enters the theory for the distance $R = 0$. They differ to a visible extent only in the intervals I_1 and I_2 where the condition $\Lambda^{n(s+1)} \sim \pi R/2$ is met.

- ii) $\Lambda^{n(s+1)} \gg \pi R/2$: In this region the spectral function is highly oscillating leading to a set of sharp peaks that are densely distributed over the interval. There the approximation to simply pick one excitation ξ_n as a representative of the environment is again well justified. It is the typical situation of the first few iterations where n is small.
- iii) $\Lambda^{n(s+1)} \approx \pi R/2$: On this scale the bath spectral function does feature a small number of oscillations. It is not obvious why the simple average leading to the ξ_n leads to a good description of the excitations of the bath in that regime. Consider e. g. a situation like in figure 11 where two broad peaks of the spectrum are located at the borders of the interval I_1 while there is minimal weight in its central region. From a statistical point of view it would be a very bad decision to describe such a distribution by one single average and not by two averages that take only into account either of the two halves of the interval I_1 . However, the logarithmic discretisation scheme presented here will always use one single excitation for each interval only no matter what the explicit features of the spectrum are.

In general there is a solution to the dilemma of not approximating the features of the bath spectral function correctly. It is referred to as the “ z -trick” or interleaved method (cf. [56, 40]) and it was originally introduced in order to reach larger values of the discretisation parameter Λ which had long been used only up to values of $\Lambda = 3.0$. A larger value of $\Lambda \approx 10.0$ effectively leads to a smaller number of iterations that need to be performed in order to reach a given energy scale, reducing in total the numerical cost. But at the same time it also leads to a rougher approximation of the environment. The main idea of the interleaved method is to reposition the interval borders x_n for $n \geq 1$ slightly by introducing a global factor Λ^{-z} leading to interval-borders $\tilde{x}_n = \Lambda^{-(n+z)}$. After solving the model numerically with the NRG for different values of $z \in [0, 1]$ one could then average over those different discretisations of the bath and thus hope to average out errors made in the discretisation process.

It is the purpose of this work to obtain physical quantities as a function of the impurity-impurity distance R for the two-spin-boson model. However, for a fixed Λ and different R the interval in which the approximation becomes bad will also change. Hence an optimised value of Λ and a set of decently chosen z would be needed for each value of R individually. Also two environments with an even and an odd spectrum enter the calculations. The even spectrum has its peaks where the odd spectrum has no weight at all and vice versa. So in principle one would also need to discretise them with different values of Λ that still allow for a meaningful definition of an energy scale in each iteration of the NRG. This procedure is not feasible for the range of R -values that is considered in this work ($R \in \{0, 1, 2, \dots, 1000\}$) and therefore I refrain from using the z -average method in the following. The approximation made in the corresponding interval I_n is

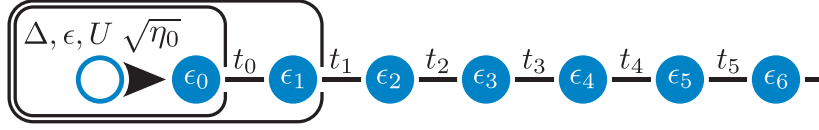
considered as not important for the physics that govern the low-temperature regime. There the question is mainly whether a bath has enough spectral weight in its low energy tail leading to either a complete freezing of the impurity in one state or residual oscillatory behaviour. These physics should be governed by the distribution of and the coupling strength to excitations at the lowest energy scales. The details of the bath around the characteristic energy-scale set by the condition $\Lambda^{n(s+1)} \approx \pi R/2$ will influence the flow of the system between different fixed points within the NRG and the calculation of e.g. the critical coupling $\alpha_c(R)$. However, the fixed points themselves and their structure should not be influenced by those particular details in the flow between them.

The *star*-Hamiltonian in equation (5.15) can already be used in an iteration-scheme where one bosonic mode after another is coupled to the impurity starting at high energies and going down to lower ones. This approach has been taken e.g. in [12] where the main emphasis was to find a decent basis describing the bosonic excitations. When using the *star*-Hamiltonian the problem has to be faced that the Hilbert-space in which the impurity needs to be described grows exponentially with the number of iterations until a proper truncation scheme sets in. It is not obvious that the truncated basis then still captures the low-energy sector of the theory and especially of the impurity properly.

The need to keep track of the impurities Hilbert-space can be overcome as the environment is mapped onto a semi-infinite chain, the so-called Wilson-chain. There the impurity couples to the first site of the chain only and in going from one iteration to the next one simply needs to keep track of the operators from the current chain site and from the previous one. Details on the mapping of the environment onto a semi-infinite chain are discussed in the following. baths

5.2. Mapping onto a chain-Hamiltonian

The starting point for the following mapping is the *star*-Hamiltonian given in equation (5.15). As already mentioned this Hamiltonian will be mapped onto a configuration where the impurity couples to the first site of a semi-infinite chain. This chain is also referred to as the Wilson-chain, as it is the configuration that Kenneth G. Wilson used in his original work [52] in order to tackle the Kondo-model. A schematic of the impurity coupling to the Wilson-chain can be seen in figure 12 where further details on the iterative solution of the system are mentioned, to be explained in more detail in the following. The main features of the chain will be on-site energies ϵ_n and nearest-neighbour hopping amplitudes t_n which both drop of exponentially as Λ^{-n} . In order to arrive at the desired chain configuration a basis transformation is performed from the operators a_n to new bosonic operators d_n , not to be confused with the width of Interval I_n . First of all the interaction part that couples the impurity to all bath-modes ξ_n is considered. The aim is here to collect all the excitations to which the


Figure 12:

The impurity (depicted by the blue circle) with energy-scales Δ, ϵ, U couples with a coupling strength $\sqrt{\eta_0}$ to the first site of a semi-infinite linear chain of bosons (the Wilson-chain). The chain features on-site energies ϵ_n and nearest neighbour hopping amplitudes t_n which both drop off exponentially as Λ^{-n} where Λ is the logarithmic discretisation parameter. The rounded boxes enclose the subsystems corresponding to the Hamiltonians H_0 and H_1 of the NRG iteration process. In a first step, H_0 is diagonalised. After truncation to the lowest N_{kept} states, the next site is coupled and one arrives at H_1 . The process of diagonalisation, truncation and adding of the next site is then iterated until a desired temperature-range $T \sim \Lambda^{-l}$ is reached in the last iteration l .

impurity couples in the *star*-Hamiltonian into a single bosonic mode d_0 that is defined by (cf. [12, pp. 18-19])

$$d_0 = \frac{1}{\sqrt{\eta_0}} \sum_{n=0}^{\infty} \gamma_n a_n \quad (5.18)$$

where

$$\eta_0 = \sum_{n=0}^{\infty} \gamma_n^2 = \int_0^{\omega_c} J(\omega) d\omega \quad (5.19)$$

is the normalisation factor. More generally speaking one wants to perform an orthogonal basis transformation $\mathbf{d} = U\mathbf{a}$ where U is the orthogonal matrix and the vectors $\mathbf{d} = (d_0, d_1, \dots)^T$ and $\mathbf{a} = (a_0, a_1, \dots)^T$ comprise all operators in the new and the old basis respectively. From equation (5.18) it can already be read off that

$$U_{0n} = \frac{\gamma_n}{\sqrt{\eta_0}}, \quad n = 0, 1, \dots, \infty \quad (5.20)$$

and indeed the first row of U normalises to one: $\sum_{n=0}^{\infty} U_{0n}^2 = 1$. That way the interaction part of the *star*-Hamiltonian is transformed to

$$\left(\frac{b+b^\dagger}{2}\right) \sum_{n=0}^{\infty} \frac{\gamma_n}{\sqrt{\pi}} (a_n + a_n^\dagger) = \left(\frac{b+b^\dagger}{2}\right) \sqrt{\frac{\eta_0}{\pi}} (d_0 + d_0^\dagger). \quad (5.21)$$

The next goal is to transform the rest of the bath modes via a tridiagonalisation to a set of new bath modes $\{d_n\}$ which also obey the standard commutation relations (U is an orthogonal transformation) such that the total Hamiltonian reads

$$H_{\text{do}}^{\text{chain}} = H_{\text{imp}} + \sum_{n=0}^{\infty} \left[\epsilon_n d_n^\dagger d_n + t_n (d_{n+1}^\dagger d_n + d_n^\dagger d_{n+1}) \right] + \left(\frac{b + b^\dagger}{2} \right) \sqrt{\frac{\eta_0}{\pi}} (d_0 + d_0^\dagger) \quad (5.22)$$

which is also referred to here and in the following as the *chain*-Hamiltonian. The mapping is called a tridiagonalisation because the bath part of the Hamiltonian could be written as a bilinear form employing a tridiagonal matrix:

$$H_{\text{bath}}^{\text{chain}} = (d_0^\dagger, d_1^\dagger, d_2^\dagger, \dots) \begin{pmatrix} \epsilon_0 & t_0 & & \\ t_0 & \epsilon_1 & t_1 & \\ & t_1 & \epsilon_2 & \ddots \\ & & \ddots & \ddots \end{pmatrix} \begin{pmatrix} d_0 \\ d_1 \\ d_2 \\ \vdots \end{pmatrix}. \quad (5.23)$$

Plugging the inverse transformation $\mathbf{a} = U^T \mathbf{d}$ into the bath part of the *star*-Hamiltonian one finds

$$H_{\text{bath}}^{\text{star}} = \sum_{n=0}^{\infty} \xi_n a_n^\dagger a_n = \sum_{n=0}^{\infty} \xi_n \sum_{i,j=0}^{\infty} U_{in} U_{jn} d_i^\dagger d_j \stackrel{!}{=} H_{\text{bath}}^{\text{chain}}. \quad (5.24)$$

Now the two bath parts $H_{\text{bath}}^{\text{star}}$ and $H_{\text{bath}}^{\text{chain}}$ in (5.24) can be compared in order to obtain the prefactors ϵ_n and t_n of the new bosonic operators d_n . Since the U_{0n} are already given one obtains

$$\epsilon_0 = \sum_{n=0}^{\infty} \xi_n U_{0n}^2 = \int_0^{\omega_c} \omega J(\omega) d\omega / \int_0^{\omega_c} J(\omega) d\omega \quad (5.25)$$

and from that one can calculate the parameter t_0 . One then iteratively solves for the different U_{mn} , ϵ_m and t_m starting from $m = 1$. Bulla et al. present analytic expressions connecting the parameters U_{mn} , ϵ_m , t_m amongst each other and with the ξ_n obtained in the logarithmic discretisation which read [9]:

$$\epsilon_m = \sum_{n=0}^{\infty} \xi_n U_{mn}^2 \quad (5.26)$$

$$t_m = \left[\sum_{n=0}^{\infty} [(\xi_n - \epsilon_m) U_{mn} - t_{m-1} U_{m-1n}]^2 \right]^{1/2} \quad (5.27)$$

$$U_{m+1n} = \frac{1}{t_m} [(\xi_n - \epsilon_m) U_{mn} - t_{m-1} U_{m-1n}] \quad (5.28)$$

There are then two ways to obtain the parameters ϵ_m and t_m of the Wilson-Chain.

- i) The recurrence relations for the desired parameters could be implemented numerically in a calculation that necessarily has to truncate the evaluation of the U_{mn} at a large n (typically one uses $n \approx 400$). This numerical scheme is the standard way to go for an arbitrary given spectral function $J(\omega)$ and in fact I use this method for the spectral functions J_e and J_o that appear in the two-spin-boson model.
- ii) For certain special functions $J(\omega)$ one may obtain analytic results for the different ϵ_m and t_m . In case of the standard power-law spectrum which is not modulated by a \cos^2 or a \sin^2 , Chin et al. actually solved the recurrence relation (5.28) analytically using orthogonal polynomials [14]. From the U_{mn} they then also find analytic expressions for the on-site energies ϵ_m and the hopping amplitudes t_m that read

$$\epsilon_m = \xi_s (A_m + C_m) \quad (5.29)$$

$$t_m = \xi_s \frac{N_{m+1}}{N_m} A_m \quad (5.30)$$

with the definitions

$$\xi_s = \frac{s+1}{s+2} \frac{1 - \Lambda^{-(s+2)}}{1 - \Lambda^{-(s+1)}} \omega_c \quad (5.31)$$

$$A_m = \Lambda^{-m} \frac{(1 - \Lambda^{-(m+s+1)})^2}{(1 - \Lambda^{-(2m+s+1)})(1 - \Lambda^{-(2m+s+2)})} \quad (5.32)$$

$$C_m = \Lambda^{-(m+s)} \frac{(1 - \Lambda^{-m})^2}{(1 - \Lambda^{-(2m+s)})(1 - \Lambda^{-(2m+s+1)})} \quad (5.33)$$

$$N_m^2 = \frac{\Lambda^{-m(s+1)} (\Lambda^{-1}; \Lambda^{-1})_m^2}{(\Lambda^{-(s+1)}; \Lambda^{-1})_m^2 (1 - \Lambda^{-(2m+s+1)})} \quad (5.34)$$

and in the last line the q -shifted factorials [14] were used which read

$$(a; q)_m = (1 - a)(1 - aq)(1 - aq^2) \cdot \dots \cdot (1 - aq^{m-1}). \quad (5.35)$$

In case of the two-spin-boson model I implemented the iterative solution of the equations (5.26)-(5.28). It is the evaluation of the analytic expressions in (5.29) and (5.30) that I implemented and used for the cases where simple power-law spectral functions are considered. They are numerically stable and circumvent the necessity to actually calculate any matrix elements U_{mn} of the underlying orthogonal transformation from the *star*- to the *chain*-Hamiltonian. Note that in the actual implementation one can calculate the factor N_{m+1}/N_m appearing in (5.30) quite efficiently since all but the last factors in the q -shifted factorials cancel in the numerator and the denominator. Also note that the chain parameters ϵ_m and t_m do not depend on the coupling strength α

of the impurity to the original bath. The coupling α enters the *chain*-Hamiltonian in the coupling of the impurity to the ϵ_0 -mode only.

In case of the two-spin-boson model already the integrals in equations (5.16) and (5.17) need to be evaluated numerically in order to obtain the coefficients $\gamma_{n,s}$ and $\xi_{n,s}$ for the even ($s = e$) and the odd ($s = o$) bath independently. The resulting *star*-Hamiltonian for this model reads

$$H_{2\text{sbm}}^{\text{star}} = H_{\text{imp}} + \sum_{s=e,o} \left[\sum_{n=0}^{\infty} \left\{ \xi_{n,s} a_{n,s}^\dagger a_{n,s} + \frac{\sigma_{z,s}}{2} \frac{\gamma_{n,s}}{\sqrt{\pi}} (a_{n,s} + a_{n,s}^\dagger) \right\} \right]. \quad (5.36)$$

From that, the same mapping from *star*- to *chain*-Hamiltonian as before is performed in the even and the odd bath independently and equations (5.26) – (5.28) need to be evaluated numerically to determine the on-site energies $\epsilon_{n,s}$ and nearest-neighbour hopping amplitudes $t_{n,s}$ of both chains. The *chain*-Hamiltonian of the two-spin-boson model then reads

$$H_{2\text{sbm}}^{\text{chain}} = H_{\text{imp}} + \sum_{s=e,o} \left[\sum_{n=0}^{\infty} \left\{ \epsilon_{n,s} d_{n,s}^\dagger d_{n,s} + t_{n,s} (d_{n+1,s}^\dagger d_{n,s} + d_{n,s}^\dagger d_{n+1,s}) \right\} + \frac{\sigma_{z,s}}{2} \sqrt{\frac{\eta_{0,s}}{\pi}} (d_{0,s} + d_{0,s}^\dagger) \right]. \quad (5.37)$$

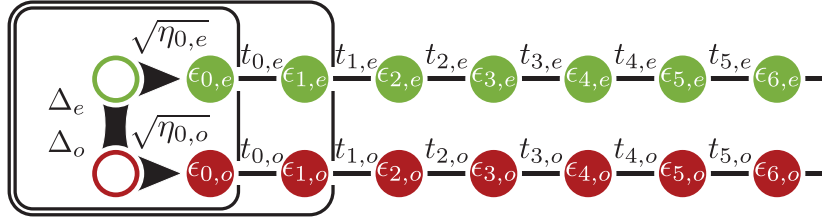
In figure 13 the system with the even and the odd chain is presented along with details on the first few iterations that are performed in order to solve the two-spin-boson model within the NRG. In the following section the iterative numerical scheme to actually solve the *chain*-Hamiltonians (5.22) and (5.37) on a computer both for the dissipative oscillator model and the two-spin-boson model is explained.

5.3. Diagonalisation and truncation

The numerical solution of a system that features one or two Wilson-chains builds upon defining a series of Hamiltonians H_N that converges to the desired one (here either $H_{\text{do}}^{\text{chain}}$ or $H_{2\text{sbm}}^{\text{chain}}$). Instead of solving the full system one solves the series of Hamiltonians iteratively thereby hopefully converging to the solution of the full system. In what sense the convergence of the series is reached will be discussed as the solution scheme is presented. Solving a single H_N actually means in this context diagonalizing its matrix-representation numerically on a computer. For the moment the discussion focusses on the dissipative oscillator model where only a single semi-infinite chain is coupled to the impurity.

The series H_N is designed to fulfil

$$H_{\text{do}}^{\text{chain}} = \lim_{N \rightarrow \infty} \Lambda^{-N} H_N \quad (5.38)$$


Figure 13:

The even (green circle) and odd (red circle) impurity combinations couple with strength $\sqrt{\eta_{0,e/o}}$ to the first site of semi-infinite linear chains of bosons (the Wilson-chains of the even and odd bath). Both chains feature on-site energies $\epsilon_{n,s}$ and nearest neighbour hopping amplitudes $t_{n,s}$ which both drop off exponentially as Λ^{-n} where Λ is the logarithmic discretisation parameter. The even and odd impurities still interact with each other via the tunnelling terms $\Delta_{e/o}$. The rounded boxes enclose the subsystems corresponding to the Hamiltonians H_0 and H_1 of the NRG iteration process. In a first step, H_0 is diagonalised. After truncation to the lowest N_{kept} states, the next site of both the even and the odd chain is coupled and one arrives at H_1 . The process of diagonalisation, truncation and adding of the next sites is then iterated until the desired temperature-range $T \sim \Lambda^{-l}$ is reached where l is the last NRG iteration to be performed.

where the different H_N are defined as

$$H_N = \Lambda^N \left[H_{\text{imp}} + \sum_{n=0}^N \epsilon_n d_n^\dagger d_n + \sum_{n=0}^{N-1} t_n (d_{n+1}^\dagger d_n + d_n^\dagger d_{n+1}) + \left(\frac{b + b^\dagger}{2} \right) \sqrt{\frac{\eta_0}{\pi}} (d_0 + d_0^\dagger) \right]. \quad (5.39)$$

They describe (up to a pre-factor) the physics of the impurity that is coupled to a Wilson-chain truncated to the first $N + 1$ sites. As the ϵ_n and t_n drop down exponentially roughly as Λ^{-n} , the last site coupled features an on-site energy $\sim \Lambda^{-N}$. This feature of the on-site energies and the hopping parameters holds true for all chains that are derived in the logarithmic discretisation scheme as described in the previous section. In case of a bath with a power-law spectrum $J(\omega) \sim \omega^s$ the expressions (5.29) and (5.30) for the chain parameters show a large n behaviour as

$$\epsilon_n \sim \Lambda^{-n}, \quad (5.40)$$

$$t_n \sim \Lambda^{-(n+(s+1)/2)}. \quad (5.41)$$

Rescaling the Hamiltonians H_N by a factor of Λ^N leads to a low energy-sector of each Hamiltonian which is roughly of the order of one. This allows for a direct comparison of the energy-spectra of the H_N between different iterations. In the identification of fixed points within the NRG the comparability between different iterations is important as

the spectra of several consecutive Hamiltonians should look identical once the system is close to a fixed point.

Two consecutive Hamiltonians of the series H_N are connected as

$$H_{N+1} = \Lambda H_N + \Lambda^{N+1} \left[\epsilon_{N+1} d_{N+1}^\dagger d_{N+1} + t_N (d_{N+1}^\dagger d_N + d_N^\dagger d_{N+1}) \right]. \quad (5.42)$$

It is this relation between the different Hamiltonians that makes up for the renormalization group character of the algorithm and allows for an interpretation of the equation as a renormalization group transformation R [9]:

$$H_{N+1} = R(H_N). \quad (5.43)$$

Instead of fixed points P^* in parameter space (cf. discussion in section 5) one then tries to identify fixed point Hamiltonians H^* of the mapping (5.43). A renormalization group transformation R is then in general characterised by a set of fixed point Hamiltonians H^* which are invariant under R and, around these fixed points, sets of relevant or (dangerously) irrelevant perturbations¹. In this work, each Hamiltonian H_N is characterized by its set of eigenenergies $\{E_r(N), r = 1, \dots, N_{\text{kept}}\}$ which obey

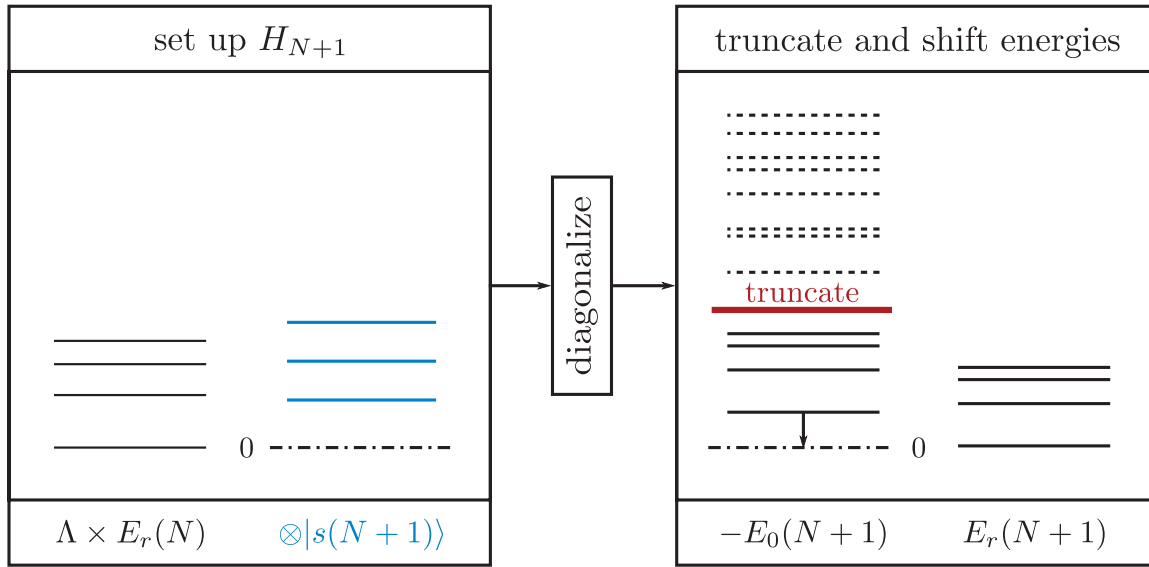
$$H_N |r\rangle_N = E_r(N) |r\rangle_N, \quad (5.44)$$

where N_{kept} is the total number of eigenpairs kept in iteration N and the energies are shifted such that $E_0(N) = 0$. Finding a set of fixed points H^* then corresponds to finding fixed points in the flow of the eigenenergies $E_r(N)$ as a function of N . Around each fixed point one could then study what influence different operators have on its structure, cf. [26]. The mapping of a set of eigenstates $E_r(N)$ to the next one $E_r(N+1)$ works as follows:

- i) The shifted energies are rescaled by a factor of Λ when setting up H_{N+1} (cf. (5.47)).
- ii) In diagonalizing H_{N+1} the new set of energies $E_r(N+1)$ are obtained. This set of energies will be truncated to contain at most the N_{kept} lowest eigenstates.
- iii) All energies $E_r(N+1)$ are shifted such that the ground-state energy $E_0(N+1)$ is zero.

A schematic plot of this process is shown in figure 14 while an actual flow of the first nine excited states of the dissipative oscillator model is shown in figure 15 for an already strong self-interaction $U = 1000$. Setting up the Hamiltonian H_{N+1} in

¹The fixed points themselves are either stable, metastable or unstable depending on whether no, at least one or all perturbations around a fixed point are considered relevant and can carry the system away from the fixed point. There are also marginal (irrelevant) perturbations which stay constant in the vicinity of a fixed point.


Figure 14:

Connection between two consecutive energy spectra $E_r(N)$ and $E_r(N+1)$ within the NRG. The N_{kept} eigenenergies that were obtained in iteration N enter the Hamiltonian H_{N+1} , rescaled by a factor of Λ , together with the N_b degrees of freedom that are coupled in the current iteration (blue). Those degrees of freedom reside in the truncated Hilbert-space $|s(N+1)\rangle$. After the Hamiltonian is diagonalised the spectrum $E_r(N+1)$ is truncated again to contain only N_{kept} states. The ground state energy of the new spectrum is then shifted to zero (dash-dotted line) and all states $E_r(N+1)$, $r = 0, \dots, N_{\text{kept}} - 1$ can be compared to those from the previous iteration. Here the parameters $N_{\text{kept}} = 4$ and $N_b = 3$ were chosen for simplicity.

equation (5.42) works as follows (cf. figure 2 in [9]). The Hamiltonian H_N can be expressed in terms of its eigenenergies and corresponding eigenstates $\{(E_r(N), |r\rangle_N)\}$ that are obtained from a numerical diagonalisation of its matrix-representation. The states of the Hilbert-space from the newly added site with creation operator d_{N+1}^\dagger are labelled as $|s(N+1)\rangle$, where $s = 0, \dots, N_b - 1$ has to be truncated to a finite number N_b . The truncation is necessary to allow for a numerical treatment of the otherwise infinite dimensional Hilbert-space that the bosonic mode created by d_{N+1}^\dagger naturally lives in. In the NRG one also needs to truncate the Hilbert-space of the impurity oscillator to a finite number $N_{b,\text{imp}}$ that can differ from the N_b used for the different chain sites added in the iterative process. As there are no kept states from a previous iteration when setting up the initial Hamiltonian H_0 one may also choose a comparably large value $N_{b,0}$ of states for the first site of the chain while still keeping the dimension of H_0 small enough to allow for a numerical diagonalisation. There are several suggestions on how to choose this finite basis properly like standard and

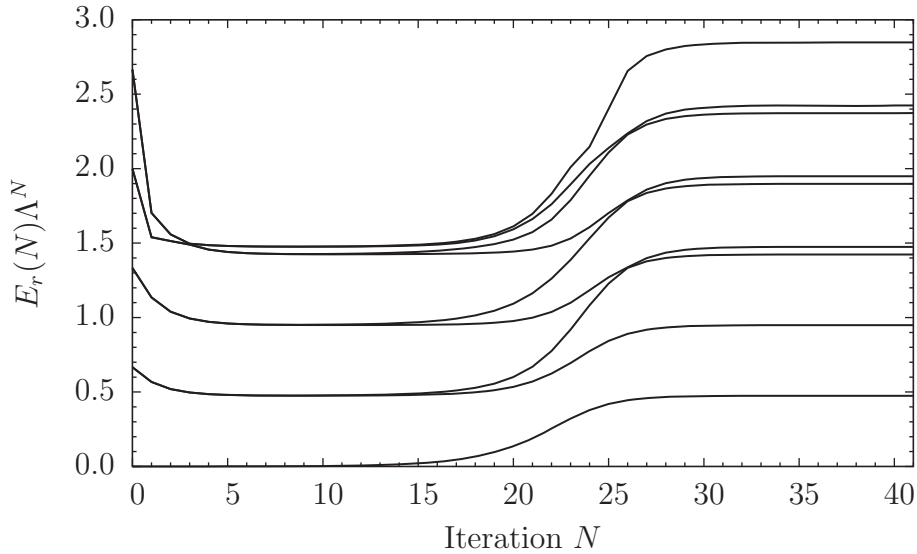


Figure 15:

Flow of the first nine energy levels $E_r(N)$ above the ground state as obtained from the NRG for the dissipative oscillator model. There are two fixed points that can be identified in the flow: a high-temperature fixed point between iterations $\sim 5 - 15$ where all states are doubly degenerate and a low-temperature fixed point where the spectrum is given by that of the free chain. The early-iteration fixed point is the localised fixed point of the spin-boson model where the impurities subspace has been projected down to only two states and the oscillator frequency $\Delta = 10^{-4}$ has not yet been resolved. The low-temperature fixed point is the delocalised fixed point of the spin-boson model where the oscillator frequency has been renormalized to infinity. For an extended discussion of the different fixed points in the model see section 6.1.2. Further model parameters were $U = 1000$, $\alpha = 0.25$, $s = 1$, $\Lambda = 2$, $N_{b,\text{imp}} = 24$, $N_{b,0} = 400$, $N_b = 24$, $N_{\text{kept}} = 500$.

displaced harmonic oscillator eigenstates [12] as well as iteratively optimised states like in a Density Matrix Renormalization Group (DMRG) setup [22, 23]. In this work the simplest states, i. e. the standard harmonic oscillator eigenstates that fulfil

$$d_{N+1}^\dagger d_{N+1} |s(N+1)\rangle = s |s(N+1)\rangle \quad (5.45)$$

are chosen. These are known to work well for the spin-boson model in its delocalised phase where the impurity spin can still oscillate between its two possible configurations $|\uparrow\rangle$ and $|\downarrow\rangle$ [12]. The total basis in which H_{N+1} needs to be described is then given by the direct product of the bases $\{|r\rangle_N\}$ from iteration N and $\{|s(N+1)\rangle\}$ from the newly added site:

$$|r, s\rangle_{N+1} = |r\rangle_N \otimes |s(N+1)\rangle. \quad (5.46)$$

In this basis the matrix elements of H_{N+1} read

$$\begin{aligned} {}_{N+1}\langle r', s' | H_{N+1} | r, s \rangle_{N+1} &= \left[\Lambda E_r(N) + \Lambda^{N+1} s \epsilon_{N+1} \right] \delta_{r',r} \delta_{s',s} \\ &\quad + \Lambda^{N+1} t_N \sqrt{s} \left[{}_N\langle r' | d_N^\dagger | r \rangle_N \delta_{s'+1,s} + {}_N\langle r' | d_N | r \rangle_N \delta_{s'-1,s} \right]. \end{aligned} \quad (5.47)$$

The new Hamiltonian H_{N+1} has again to be diagonalised numerically in order to obtain a new set of eigenenergies $\{E_r(N+1)\}$ and corresponding eigenstates $\{|r\rangle_{N+1}\}$. Since a site with a Hilbert-space of size N_b is added in each iteration it is easy to see that the total dimension of H_{N+1} is $N_{b,\text{imp}} \times N_{b,0} \times N_b^N$, which grows exponentially with the length of the chain. One thus needs to truncate the number of states kept at some point to a finite number N_{kept} in order to keep further iterations calculable on a computer.

It is the truncation of the Hilbert-space of the bosons added to at most N_b states and the truncation to a small number of states N_{kept} which might spoil the convergence of the series of H_N towards $H_{\text{do}}^{\text{chain}}$ (given that all other operations could in principle be performed numerically exact in the algorithm). The truncation of the total number of states kept is known to be justified if the discarded high lying states do not influence the low lying ones in further iterations. Then a true splitting of energy scales is given and one could probe those different scales by iterating through the different chains given by the H_N . However, the truncation needs to be justified for each model in hindsight, e. g. by probing the influence of the truncation cut-off N_{kept} on the flow of the $E_r(N)$.

For the two-spin-boson model, whose *chain*-Hamiltonian was given by

$$\begin{aligned} H_{2\text{sbm}}^{\text{chain}} &= H_{\text{imp}} + \sum_{s=e,o} \left[\sum_{n=0}^{\infty} \left\{ \epsilon_{n,s} d_{n,s}^\dagger d_{n,s} + t_{n,s} (d_{n+1,s}^\dagger d_{n,s} + d_{n,s}^\dagger d_{n+1,s}) \right\} \right. \\ &\quad \left. + \frac{\sigma_{z,s}}{2} \sqrt{\frac{\eta_{0,s}}{\pi}} (d_{0,s} + d_{0,s}^\dagger) \right], \end{aligned}$$

the series of H_N is then defined as

$$\begin{aligned} H_N &= \Lambda^N \left(H_{\text{imp}} + \sum_{s=e,o} \left[\sum_{n=0}^N \epsilon_{n,s} d_{n,s}^\dagger d_{n,s} + \sum_{n=0}^{N-1} t_{n,s} (d_{n+1,s}^\dagger d_{n,s} + d_{n,s}^\dagger d_{n+1,s}) \right. \right. \\ &\quad \left. \left. + \frac{\sigma_{z,s}}{2} \sqrt{\frac{\eta_{0,s}}{\pi}} (d_{0,s} + d_{0,s}^\dagger) \right] \right) \end{aligned}$$

where now two consecutive Hamiltonians are connected by the relation

$$H_{N+1} = \Lambda H_N + \Lambda^{N+1} \sum_{s=e,o} \left\{ \epsilon_{N+1,s} d_{N+1,s}^\dagger d_{N+1,s} + t_{N,s} (d_{N+1,s}^\dagger d_{N,s} + d_{N,s}^\dagger d_{N+1,s}) \right\} \quad (5.48)$$

which adds site $N + 1$ both in the even and in the odd chain. The matrix elements of a Hamiltonian H_{N+1} in the total basis

$$|r, s_e, s_o\rangle_{N+1} = |r\rangle_N \otimes |s_e(N + 1)\rangle \otimes |s_o(N + 1)\rangle \quad (5.49)$$

then read

$$\begin{aligned} & {}_{N+1}\langle r', s'_e, s'_o | H_{N+1} | r, s_e, s_o \rangle_{N+1} \\ &= \left[\Lambda E_r(N) + \Lambda^{N+1} (s_e \epsilon_{N+1,e} + s_o \epsilon_{N+1,o}) \right] \delta_{r',r} \delta_{s'_e, s_e} \delta_{s'_o, s_o} \\ &+ \Lambda^{N+1} t_{N,e} \sqrt{s_e} \delta_{s'_e, s_o} \left[{}_N\langle r' | d_{N,e}^\dagger | r \rangle_N \delta_{s'_e+1, s_e} + {}_N\langle r' | d_{N,e} | r \rangle_N \delta_{s'_e-1, s_e} \right] \\ &+ \Lambda^{N+1} t_{N,o} \sqrt{s_o} \delta_{s'_e, s_e} \left[{}_N\langle r' | d_{N,o}^\dagger | r \rangle_N \delta_{s'_o+1, s_o} + {}_N\langle r' | d_{N,o} | r \rangle_N \delta_{s'_o-1, s_o} \right]. \end{aligned} \quad (5.50)$$

At least two Kronecker-deltas appear in each expression contributing to Hamiltonian H_{N+1} , making its matrix-representation even more sparse as compared to the one of the dissipative oscillator model.

When actually storing a Hamiltonian like H_{N+1} in any of the models, sparse matrices are used, where only non-zero matrix elements are stored together with index-fields enlisting their position in the original matrix. Since the different operator-contributions to H_{N+1} all contain at least one Kronecker-delta one would store a lot of entries that are zero if one were to keep the full matrix in its dense representation. Before presenting details on the numerical implementation of the NRG that was used to obtain the results presented in this work in section 5.5, it is discussed how spectral functions can be obtained from the results provided by the NRG.

5.4. Obtaining spectral functions from NRG data

One goal of this thesis is to calculate changes in the zero temperature averages $\langle \hat{n}_x \rangle$ and $\langle (a_x + a_x^\dagger)^2 \rangle$ in the one-dimensional bosonic environment in real-space due to the coupling of either bosonic or magnetic impurities to the chain. Here x labels the site of the chain and thus also the distance to the impurity in case of the dissipative oscillator model. To this end the connection of those averages to specific spectral functions was derived in section 3.3. The spectral functions themselves were derived to be basically the imaginary parts of corresponding correlation functions. In section 3.2 it was stated that a general correlation function $G^R(\hat{A}, \hat{B}, z) = \langle\langle \hat{A}, \hat{B} \rangle\rangle_z$ for two operators \hat{A} and \hat{B} can be evaluated in the eigenbasis $\{|n\rangle\}$ of the underlying Hamiltonian by means of the Lehmann-representation as

$$G^R(\hat{A}, \hat{B}, z) = \frac{1}{\mathcal{Z}} \sum_{n,m} \frac{e^{-\beta E_n} - e^{-\beta E_m}}{z + E_n - E_m} \langle n | \hat{A} | m \rangle \langle m | \hat{B} | n \rangle.$$

Here, $z = \omega + i\epsilon$ is in general complex frequency with a small positive imaginary part ϵ and the retarded Green's function $G^R(\hat{A}, \hat{B}, z)$ will be evaluated on the real axis in the limit of ϵ going to zero. As it is not possible to solve, i. e. diagonalise the Hamiltonians of the two models under investigation analytically for the whole range of model parameters, the Numerical Renormalization Group was introduced as the method of choice to solve them approximately in those cases. The results obtained from applying the NRG to a certain model are sets of eigenpairs $\{(E_{N,r}, |r\rangle_N)\}$ for every iteration $N = 0, 1, \dots, l$ where l is the last iteration for which the diagonalisation is performed. Here the eigenenergies of an iteration N are of order $\Lambda^{-N}\omega_c$ with Λ being the logarithmic discretisation parameter and ω_c is the high-frequency cutoff in the bath. It is then necessary to patch the informations gained in the different iterations of the NRG together in order to be able to evaluate $G^R(\hat{A}, \hat{B}, z)$ in a large range of frequencies. Bulla et al. present in [10] a way to collect the informations from a whole NRG run together in order to calculate an approximate Lehmann-representation of the spectral functions $A(\hat{A}, \hat{B}, z)$ corresponding to the retarded Green's function $G^R(\hat{A}, \hat{B}, z)$. First they calculate for each iteration N —corresponding to a system of length $N + 1$ —a spectral function $A_N(\hat{A}, \hat{B}, \omega)$ on the real frequency axis as

$$A_N(\hat{A}, \hat{B}, \omega) = \frac{1}{\mathcal{Z}_N} \sum_{n,m} \left[(e^{-\beta E_n(N)} - e^{-\beta E_m(N)})_N \langle n | \hat{A} | m \rangle_{NN} \langle m | \hat{B} | n \rangle_N \delta(\omega - (E_n(N) - E_m(N))) \right]. \quad (5.51)$$

Here, \mathcal{Z}_N is the partition function of the cluster of length $N + 1$ in the grand canonical ensemble. The spectral function $A_N(\hat{A}, \hat{B}, \omega)$ is then a collection of different delta-peaks (poles) at frequencies $\omega_{nm} = E_n(N) - E_m(N)$ with weights $W_N(\omega_{nm}) = {}_N \langle n | \hat{A} | m \rangle_{NN} \langle m | \hat{B} | n \rangle_N$. The information that is contained in the set of all spectral

functions $\{A_N\}$ is then combined in a next step. Here extra care has to be taken of those poles from consecutive iterations that are positioned in a frequency window $[\omega_{\min}^N, \omega_{\max}^{N+1}]$ where ω_{\min}^N is the energy of the first excited state of iteration N and ω_{\max}^{N+1} is the energy corresponding to the highest state kept in iteration $N + 1$ ². There, any pole at position $\omega' \in [\omega_{\min}^N, \omega_{\max}^{N+1}]$ with weight $W_N(\omega')$ from the last iteration N is weighted with a linear increasing function as

$$W_N(\omega') \rightarrow W_N(\omega') \frac{\omega' - \omega_{\min}^N}{\omega_{\max}^{N+1} - \omega_{\min}^N} \quad (5.52)$$

and a pole $W_{N+1}(\omega')$ at frequency ω' from the next iteration $N + 1$ is weighted with a linear decreasing function as

$$W_{N+1}(\omega') \rightarrow W_{N+1}(\omega') \frac{\omega_{\max}^{N+1} - \omega'}{\omega_{\max}^{N+1} - \omega_{\min}^N}. \quad (5.53)$$

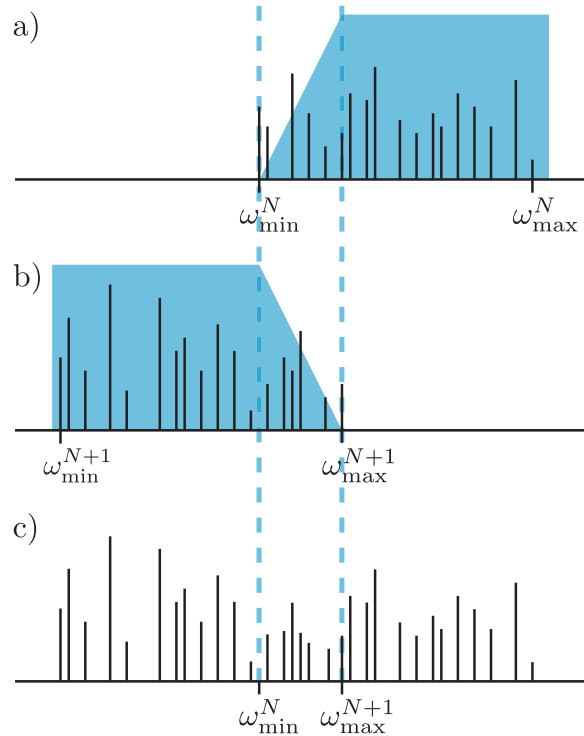
A cartoon of the combination of two spectral functions A_N and A_{N+1} is sketched in figure 16. The weighting procedure is devised to counteract a problem resulting from the connection of consecutive Hamiltonians with truncated bases which is termed over-counting. As one moves from one iteration N to the next $N + 1$, the eigenstates $|r\rangle_N$ are extended to reside in the Hilbert-space of iteration $N + 1$ as

$$|r, s\rangle_{N+1} = |r\rangle_N \otimes |s(N + 1)\rangle$$

where the states $|s(N + 1)\rangle$ span the Hilbert-space of the degrees of freedom that are coupled to the chain(s) in iteration $N + 1$. If by chance a state $|r\rangle_N$ is also an eigenstate of the current iteration then all states $|r, s\rangle_{N+1}$ are eigenstates and without a proper weighting procedure one would count all poles to which the eigenstate $|r\rangle_N$ contributes once in iteration N and a second time in iteration $N + 1$. For this special case the linear weighting procedure adds two poles $W_N(\omega')$ and $W_{N+1}(\omega') \equiv W_N(\omega')$ that belong to the same physical process correctly to one. As the states from one iteration are not in general eigenstates of the next iteration as well, the simple linear patching however is not exact and one needs to be a bit more cautious.

In the end of 2006, Anders and Schiller suggested a way to calculate spectral functions in a complete basis where discarding high-energy states in an iteration N is understood as simply splitting the full Hilbert-space of iteration N into a set of kept states and a set of discarded ones that still could formally be combined to make up the whole basis [4]. Then all states coming from every iteration in the NRG can be exactly traced and any spectral function can be calculated accurately as proper

²The frequency ϵ_{N+1} of the newly added site is strictly below the energy-scales of iteration N . However, as a large number N_{kept} of order $\mathcal{O}(100)$ is kept in each iteration, the highest states kept in iteration $N + 1$ are likely to have an energy that is larger than the first excited state $E_1(N)$ of the previous iteration.


Figure 16:

a) The poles of iteration N before weighting (black lines) together with the weighting function (blue) that is applied. For frequencies larger than ω_{\max}^{N+1} they are unchanged and thus the scaling factor is 1. In the range $[\omega_{\min}^N, \omega_{\max}^{N+1}]$, marked by the blue dashed lines, the weighting factor increases linearly. b) Poles and weighting function for the poles of iteration $N + 1$. c) The combined set of poles from iterations N and $N + 1$.

weighting between different iterations is possible. More comprehensive introductions to the calculation of Green's functions in what is known as the Anders-Schiller-basis can be found in [42] and [50] which both give insight into the complete basis description highlighting different aspects of the method. In order to perform calculations in the Anders-Schiller-basis one needs to store all matrices U_N that diagonalise the Hamiltonians H_N in the NRG procedure as they contain the information on how different states need to be weighted in the following. This method is already very demanding concerning the storage of all U_N on a hard drive in the fermionic case and is not used to calculate the spectral functions investigated in this thesis. There is a drawback when it comes to bosonic models apart from the size of the matrices U_N that are not block-diagonal as there are in general no conserved quantum numbers in bosonic models. While the basis of each site added in a fermionic chain is inherently finite, the finiteness of the bosonic basis is only artificial stemming from an approximation

that is necessary even before a single site can be coupled to the impurity. Thus the complete basis picture from [4, 42] breaks down and one would need to restrain the method to a complete description of a chain of bosons where the Hilbert-space of each bosonic degree of freedom is truncated from the outset.

Spectral functions $A_N(\hat{A}, \hat{B}, \omega)$ investigated in this work are all obtained via equation (5.51) in their zero temperature limit $\beta = (k_B T)^{-1} \rightarrow \infty$, where they read

$$\lim_{\beta \rightarrow \infty} A_N(\hat{A}, \hat{B}, \omega) = \frac{1}{g_N} \sum_{n \neq i, i} \left[{}_N \langle g_i | \hat{A} | n \rangle_{NN} \langle n | \hat{B} | g_i \rangle_N \delta(\omega - (E_0(N) - E_n(N))) \right. \\ \left. - {}_N \langle n | \hat{A} | g_i \rangle_{NN} \langle g_i | \hat{B} | n \rangle_N \delta(\omega - (E_n(N) - E_0(N))) \right]. \quad (5.54)$$

Here g_N is the number of ground-states $|g_i\rangle$ in iteration N . The poles in overlapping frequency regions are then weighted via the linear weighting method using equations (5.52) and (5.53).

In principle the models under consideration feature an environment with a continuous spectrum in the interval $[0, \omega_c]$. Due to the logarithmic discretisation process however, the environment is discrete and thus all correlation functions under consideration are discretised as well. It is desirable to obtain smooth, continuous spectral functions $A(\hat{A}, \hat{B}, \omega)$ that resemble the continuous limit of the method ($\Lambda \rightarrow 1$) and in order to do so one needs to somehow broaden the delta-peaks in (5.51). For zero temperature all poles are approximated by Gaussians on a logarithmic grid as

$$\delta(\omega - \omega_n) \rightarrow \frac{e^{-b^2/4}}{\sqrt{\pi} b \omega_n} \exp\left(-\frac{[\ln(\omega) - \ln(\omega_n)]^2}{b^2}\right) \quad (5.55)$$

where b is a broadening parameter that needs to be adjusted and it can be checked that the Gaussians are properly normalised, i. e. the total spectral weight of the delta-peaks is retained in the broadening process (cf. [10]). Once all spectral functions A_N are patched together one can proceed to obtain a continuous spectrum $A(\hat{A}, \hat{B}, \omega)$ by broadening all poles according to equation (5.55). The real part of the retarded Green's function $G^R(\hat{A}, \hat{B}, \omega)$ may be obtained on the real frequency axis by use of the Kramers-Kronig-relations (4.25) and (4.26) as described in section 4.3.

5.5. Numerical implementation

For a given model the numerical implementation of an iteration step j of a standard NRG consists of

- i) setting up the matrix containing the Hamiltonian H_j ,
- ii) diagonalizing the matrix H_j and truncating it to the lowest N_{kept} states,
- iii) transforming any operator of interest A_i into the eigenbasis of H_j by performing the matrix-matrix multiplications

$$A'_i = U^T A_i U \quad (5.56)$$

where U is the orthogonal matrix whose columns are given by the lowest N_{kept} eigenvectors of H_j .

For each iteration, step i)-iii) need to be performed both for fermionic and for bosonic models. However, the computational cost between a fermionic and a bosonic NRG differ drastically. In the bosonic case one can in general not make use of conserved quantum numbers and the Hilbert-space of each boson is in principle infinite dimensional. Thus the sizes of the matrices to be diagonalised are in general significantly larger for a bosonic NRG than for a fermionic one.

In the following, the computational costs of all three steps are discussed in case where the Hamiltonian H_j is kept in its dense representation and an exact diagonalisation is performed in step ii). The exact diagonalisation routine performs a set of matrix-transformations numerically on a computer which are known to diagonalise a given matrix exactly if they were performed analytically. Parallel to that the computational costs for the NRG are discussed if the H_j is stored in a sparse matrix representation. There the exact diagonalisation has to be traded for an iterative Lanczos diagonalisation algorithm that returns only the set of the lowest N_{kept} eigenenergies and -vectors. Details of the different diagonalisation algorithms as well as their implementation are discussed after considering the differences in storing the Hamiltonian. The NRG itself was implemented in FORTRAN and thus all discussions concerning memory consumption are with respect to the data types available in FORTRAN [30].

The results obtained for the numerical demands of all three steps are summarised in table 1 at the end of the section.

5.5.1. Storage of the Hamiltonian

As each hermitian Hamiltonian H_j considered in this work is purely real, it can be represented by a real symmetric matrix of dimension $l \times l$. Since H_j is symmetric one actually only needs to store its main diagonal and its upper or lower triangle. However, a typical exact diagonalisation routine for the full matrix containing H_j is

fed with an array of size $l \times l$ and the part where no information on the matrix is stored can be used by the diagonalisation routine to store intermediate results.

The linear size l for a single bath bosonic NRG is given by $l = N_{b,\text{imp}} \times N_{b,0}$ in the first iteration and by $l = N_{\text{kept}} \times N_b$ in all further iterations. Here, the different N_b are the sizes of the truncated bases of the different bosonic sites on either the impurity or the chain. For a NRG with two bosonic baths like needed for the two-spin-boson model it is $l = N_{\text{kept}} \times N_{b,e} \times N_{b,o}$ in all iterations $j > 0$, where now each bath increases the basis by a factor of $N_{b,e/o}$ respectively. To see how severe the addition of a second bosonic channel becomes consider the actual memory consumption in a typical setup. All matrix entries will be stored in double precision where one double precision number is stored in 8 bytes in FORTRAN. A desktop computer like the one used by the author provides 4096 MB of RAM (1 MegaByte (MB) = 1.000.000 byte). The scientific computer cluster CHEOPS from the RRZK in Cologne, Germany provides several hundred compute-nodes of which the majority feature 24 GB of RAM [2].

Say that 400 states are kept in each iteration and each additional bosonic site will be described by a Hilbert-space truncated to contain only the lowest ten states of the occupation number operator. Both numbers are modest and realistic in a typical NRG. Then an amount of $4.000 \times 4.000 \times 8 \text{ byte} = 128.000.000 \text{ byte} = 128 \text{ MB}$ of memory is needed to store the Hamiltonian of a single channel model and $40.000 \times 40.000 \times 8 \text{ byte} = 12.800 \text{ MB}$ for a model comprising two channels employing a dense matrix storage scheme. The latter is clearly beyond the limit of available memory on the desktop machine and—since more than just the Hamiltonian needs to be stored—a two bath NRG implementation featuring dense matrix representation and exact diagonalisation already reaches the memory limits of a typical single compute-node of the CHEOPS cluster.

At this point the sparsity of each Hamiltonian H_j is employed (cf. (5.47)) by storing only those elements of the matrices which are non-zero. To this end, a derived type `sparse_matrix` is defined in which the compressed sparse row (CSR) format like in the Intel MKL [25] is used. The `sparse_matrix` type is loosely defined as

```
type sparse_matrix
  integer, public :: dim1 = 0, dim2 = 0
  double precision, allocatable, public :: val(:)
  integer          , allocatable, public :: col(:), row(:)
  contains
  ...
end type sparse_matrix
```

and contains two integers holding the dimensions of the matrix together with three one-dimensional arrays and a set of routines that are defined after the `contains`



statement but are of no concern at this moment. The arrays have the following purpose:

`val(:)` A double precision array storing all values of a matrix that are non-zero row by row in consecutive order.

`col(:)` An integer array of the same length as `val(:)` storing the column indices of the matrix-elements contained in `val(:)`. It is also filled row by row such that `col(i)` contains the column index of the matrix element `val(i)`.

`row(:)` An integer array of length `dim1 + 1`. The element `row(i)` contains the index of the element in the array `val(:)` that is the first non-zero element in row `i` of the matrix. The last element `row(dim1+1)` contains the length of the arrays `val(:)` and `col(:)` plus one. The first element `row(1)` is always set to 1 such that `row(i+1) - row(i)`, `i=1, ..., dim1` is the number of matrix-elements that are non-zero in every row `i`. If by chance a complete row `i` (other than the first) of the matrix is zero, then `row(i)` is set such that `val(row(i) - 1)` contains the last element of the row `i-1` of the matrix. Then the next row index will be set to `row(i+1) = row(i)`.

Consider for example a matrix

$$M = \begin{pmatrix} 1 & 0 & 3 \\ 0 & 0 & 0 \\ 0 & 4 & 7 \end{pmatrix}. \quad (5.57)$$

While there is hardly any need to store such a small matrix in the presented sparse format memory-wise, the `sparse_matrix` type is employed in this minimal example for educative purposes.

Going through the matrix M row by row one simply collects all non-zero elements and stores them in the array `val(:)` as double precision floating point numbers to obtain `val = [1.0d0, 3.0d0, 4.0d0, 7.0d0]`. Now the array `col(:)` is filled, again going row by row through M and this time storing the column-number in which the non-zero elements of M reside. That way one obtains `col = [1, 3, 2, 3]`. Finally the information where in the arrays `val(:)` and `col(:)` a new row of M begins needs to be stored in the array `row(:)`. Keeping in mind that `row(1) = 1` one needs to check where row number 2 will start. Since there are no matrix elements in row 2 of M one needs to set `row(2) = 3` to make sure that `val(row(2) - 1)` contains the last non-zero element of row 1 of M . In the end one obtains `row = [1, 3, 3, 5]`. A FORTRAN code that stores M in the `sparse_matrix` type then reads:

```
program main
implicit none
type(sparse_matrix) :: M
M%dim1 = 3
M%dim2 = 3
allocate( M%val(1:4), source = [1,0d0, 3.0d0, 4.0d0, 7.0d0] )
allocate( M%col(1:4), source = [1, 3, 2, 3] )
allocate( M%row(1:4), source = [1, 3, 3, 5] )
end program main
```

In order to see the benefit of the sparse matrix storage format as compared to a dense storage scheme the amount of memory that is consumed in either case is compared in the following. Assume that a matrix of interest $M \in \mathbb{R}^{l \times l}$ has only a fraction $p \ll 1$ of non-zero elements but its dimensionality is large ($l \gg 1$). While the dense matrix would consume $m_d = 8l^2$ bytes of memory, the `sparse_matrix` type needs $m_s = 8pl^2 + 4pl^2 + 4(l+1) + 2 \times 4 \approx 12pl^2 + 4l$ bytes. Thus the ratio of sparse matrix memory consumption to dense matrix memory consumption is

$$\frac{m_s}{m_d} \approx \frac{12pl^2 + 4l}{8l^2} = \frac{3}{2}p + \frac{1}{2l} \quad (5.58)$$

The factor of $3/2$ in front of the filling fraction p is due to the necessity to store both the value and a column index for any non-zero matrix element. Thus the format becomes even more demanding than the dense format, once a filling factor of $p \sim 2/3$ is reached. Anyway, in this limit one would no longer talk of a sparse matrix and the `sparse_matrix` type should not be used in that regime.

Consider a matrix of linear size $l = 4 \times 10^4$ like in the example for the two-spin-boson model. Its Hamiltonian could then at most have 1.441×40.000 entries (cf. (5.50)) which corresponds to a fraction of $p = 1.441/40.000 \approx 0.036$ of non-zero elements. Then the sparse-matrix storage format needs only roughly 5.4% of the full storage format and takes up roughly 692 MB instead of 12.800 MB allowing for a numerical treatment on such compute-nodes as provided on the CHEOPS cluster. For a symmetric matrix one actually only needs to store its main diagonal plus its upper triangular part. This corresponds to roughly halving the demand on actual memory consumption. The established `sparse_matrix` storage scheme is then used in a Lanczos diagonalisation algorithm that is performed for a Hamiltonian stored in this format. In order to understand the differences of a Lanczos algorithm to an exact diagonalisation for a dense matrix, first of all the exact diagonalisation is discussed briefly together with its computational demands.

5.5.2. Exact Diagonalisation

Consider a real symmetric matrix $M \in \mathbb{R}^{l \times l}$ that has to be diagonalised. A standard way to do so is to first bring the matrix to a tridiagonal form T by performing an orthogonal similarity transformation U such that

$$U^T M U = T$$

and then performing a QR or QL algorithm in order to diagonalise the tridiagonal matrix T .

The reduction to tridiagonal form can always be achieved for a real symmetric matrix M and can e.g. be performed numerically with the routine `dsytrd` from the LAPACK software package [5]. This routine uses the HOUSEHOLDER method in order to perform a set of $l - 2$ orthogonal transformations that in total result in applying U to M (cf. [44, p. 462-469]). In the limit of large l the routine `dsytrd` will perform $4l^3/3 + \mathcal{O}(l^2)$ operations if both eigenvalues and eigenvectors are desired as is the case for the NRG [5].

One may then use the routine `dsteqr` from the LAPACK software package [5] to perform a set of QR decompositions and QL decompositions with implicit shifts on T in order to diagonalise it [6]. Alternatively, more advanced routines like `dstedc` may be used that implement a divide-and-conquer diagonalisation algorithm [45]. To get an estimate of the operation count of `dsteqr` it is compared to the routine `tqli` that performs QL decompositions with implicit shifts only. The routine `tqli` will use roughly $3l^3 + 30l^2$ operations in order to obtain both the eigenvalues and vectors of the tridiagonal matrix T in the limit of large l . Thus the total operation count of an exact diagonalisation via HOUSEHOLDER reduction and QL decomposition with implicit shifts scales as $13/3l^3 + 30l^2$ making it an order $\mathcal{O}(l^3)$ algorithm in terms of runtime. The memory that is needed to store the matrix together with additional arrays by the routines `dsytrd` and `dsteqr` is $l^2 + \mathcal{O}(l)$ in both cases, making the exact diagonalisation in total an algorithm of order $\mathcal{O}(l^2)$ in terms of memory consumption.

While being applicable to a one bath bosonic NRG like the one used for the damped harmonic oscillator model, this exact diagonalisation strategy does not work for bosonic two bath models. Remember that the dimension $N_{b,o}$ of the Hilbert-space of the odd bath enters the matrix size l linearly. Thus a value of $N_{b,o} = 10$ would increase the operation count and thus the runtime of the algorithm by a factor of 1000 as compared to the single bath model. For any minute spent in the single bath NRG within the exact diagonalisation routine one thus would need to spend 16h 40min in the two bath NRG. Since a single bath NRG calculation typically takes several minutes to complete this means that a two bath NRG for a single set of model parameters takes several days of runtime. Run times of this magnitude are not feasible if one is interested in obtaining e.g. phase diagrams from the NRG where one typically needs to vary one or two parameters and thus perform lots of independent NRG runs.

5.5.3. Lanczos Algorithm

Assume now that the matrix $M \in \mathbb{R}^{l \times l}$ has again only a small fraction $p \ll 1$ of non-zero matrix elements like it is the case for the Hamiltonians H_j in the bosonic NRGs. Within the NRG one needs to keep the lowest $N_{\text{kept}} \ll l$ eigenvalues and eigenvectors of M in each iteration only. Thus it would be a huge numerical overhead to calculate the full spectrum and set of eigenvectors of M and discard its majority as one goes to very large matrices. Here the Lanczos algorithm comes into play that builds around the notion of Krylov-subspaces. Its main idea is to first project the matrix M into a subspace that is built by the eigenvectors of M corresponding to the largest eigenvalues in magnitude. In the rather small subspace one could then again diagonalise the matrix by an exact diagonalisation.

The r th Krylov-subspace $\mathcal{K}_r(M, \mathbf{v})$ of a vector \mathbf{v} to a linear operator M is defined as the span of vectors that is generated by repeatedly applying M to \mathbf{v} :

$$\mathcal{K}_r(M, \mathbf{v}) = \text{span}\{\mathbf{v}, M\mathbf{v}, M^2\mathbf{v}, \dots, M^{r-1}\mathbf{v}\}. \quad (5.59)$$

It is truly one-dimensional if and only if \mathbf{v} is an eigenvector of M . One may obtain $\mathcal{K}_r(M, \mathbf{v})$ by calculating the series of vectors $\mathbf{v}_i = M\mathbf{v}_{i-1}$ where $i = 2, \dots, r$, starting with $\mathbf{v}_1 = \mathbf{v}$. Letting the matrix M act n times onto a vector \mathbf{v} in terms of the eigenbasis $\{\mathbf{e}_1, \dots, \mathbf{e}_l\}$ of M reads

$$M^n \mathbf{v} = \sum_{i=1}^l \lambda_i^n \mathbf{e}_i \langle \mathbf{v}, \mathbf{e}_i \rangle. \quad (5.60)$$

Here the λ_i are the eigenvalues of M and it is assumed that they are ordered such that $\lambda_i \geq \lambda_{i+1} \geq 0$ for all $0 < i < r-1$. This can always be achieved by relabelling the eigenvalues and shifting the spectrum by an offset $\lambda_i \rightarrow \lambda_i + \tau$. Applying the matrix M in its n th power to a given vector \mathbf{v} thus mainly enhances the contribution of \mathbf{v} along the direction of the eigenvector which corresponds to the largest eigenvalue. Thus, the series $\mathbf{v}_i / \|\mathbf{v}_i\|$ should converge to the eigenvector \mathbf{e}_1 and the series $\|\mathbf{v}_{i+1}\| / \|\mathbf{v}_i\|$ should converge to the largest eigenvalue λ_1 . Likewise, if one now projects out the first eigenvector \mathbf{e}_1 from \mathbf{v} via

$$\mathbf{v} \rightarrow \mathbf{v} - \langle \mathbf{v}, \mathbf{e}_1 \rangle \mathbf{e}_1 \quad (5.61)$$

after each application of M one could hope to find the second eigenvector \mathbf{e}_2 and its corresponding eigenvalue λ_2 and so on.

The idea behind the Lanczos algorithm in finding a set of N_{kept} desired eigenvalues and eigenvectors of M is now to calculate a Krylov-subspace $\mathcal{K}_r(M, \mathbf{v})$ for a random initial \mathbf{v} where $r > N_{\text{kept}}$ ($r = 4N_{\text{kept}}$ in the implementation used for the results presented in this work). Taking an r that is larger than the actual number N_{kept} of eigenpairs one is interested in allows for a better convergence of the algorithm. In

shifting the spectrum of M previous to the calculation of \mathcal{K}_r such that the lowest eigenvalues now correspond to the largest eigenvalues in magnitude one will actually build the Krylov-subspace around the low-energy sector of the Hamiltonian H_j to which M corresponds (in the end, the spectrum has of course to be re-shifted). In this subspace one then again wants to tridiagonalise the matrix with a similarity transformation $U_{\mathcal{K}_r}$ such that it has the form

$$U_{\mathcal{K}_r}^T M U_{\mathcal{K}_r} = T = \begin{pmatrix} a_1 & b_1 & & \\ b_1 & a_2 & b_2 & \\ & b_2 & a_3 & \ddots \\ & & \ddots & \ddots \end{pmatrix} \quad (5.62)$$

where the $a_i = t_{i,i}$ now denote the diagonal elements and the $b_i = t_{i,i+1} = t_{i+1,i}$ denote the off-diagonal elements. Both, building up \mathcal{K}_r and reducing M to the tridiagonal form T , can be achieved by one algorithm. Let \mathbf{v} be an array of size $l \times (r+1)$ to which the r vectors \mathbf{v}_r are stored together with a vector \mathbf{v}_0 which is zero and only considered in the first iteration. Furthermore let \mathbf{a} and \mathbf{b} be arrays of size r to store the matrix-elements of T . Then the pseudo-code

```

1 v(1:l,0) = 0
2 v(1:l,1) = random normalized vector
3 a(1:r) = 0
4 b(0:r-1) = 0
5
6 do i = 1, r-1
7   w = M.v(1:l,i)
8   a(i) = w.v(1:l,i)
9   w = w - a(i)*v(1:l,i) - b(i-1)*v(1:l,i-1)
10  b(i) = norm(w)
11  v(1:l,i+1) = w/b(i)
12 end do
13
14 w = M.v(1:l,r)
15 a(r) = w.v(1:l,r)
    
```

both calculates the matrix elements a_i and b_i of T and the vectors \mathbf{v}_i that are the columns of the transformation $U_{\mathcal{K}_r}$ which maps M onto T . Here, the dot product $\mathbf{x} \cdot \mathbf{y}$ is either a matrix-vector product or a scalar product depending on the nature of \mathbf{x} .

While the exact number of numerical operations performed by the Lanczos-algorithm depends on its converge for a specific input matrix M , in general it scales with the parameters of the matrix as follows: To set up the Krylov-subspace \mathcal{K}_r one needs

to perform roughly r matrix-vector products Mv . The matrix M has $p \times l^2$ non-zero matrix elements that need to be multiplied with the elements of a given vector v and all added up to form the new vector w . Thus roughly $2rpl^2$ operations need to be performed. All other operations in the pseudo-code scale as rl and therefore can be neglected in comparison to the ones performed for the matrix-vector product. An exact diagonalisation of the matrix $T \in \mathbb{R}^{r \times r}$ is then again an $\mathcal{O}(r^3)$ algorithm with respect to runtime and $\mathcal{O}(r^2)$ with respect to memory consumption. In the end the matrix $V \in \mathbb{R}^{r \times r}$ that diagonalises T needs to be multiplied with the matrix $U_{\mathcal{K}_r} \in \mathbb{R}^{l \times r}$ in order to obtain the desired eigenvectors of M which follows from

$$T_{\text{diag}} = V^T T V = [U_{\mathcal{K}_r} V]^T M [U_{\mathcal{K}_r} V] \quad (5.63)$$

The matrix-matrix product $U_{\mathcal{K}_r} V$ takes $2lr^2 - l$ operations and thus the algorithm runtime of the Lanczos-diagonalisation is of order $\mathcal{O}(lr[r + pl])$ where typically r and pl are of similar magnitude. The memory consumption of the algorithm is mainly due to the storage of the matrices M and $U_{\mathcal{K}_r}$, since V is rather small. Therefore it is of order $\mathcal{O}(l[r + pl])$.

I adapted the program `dssimp` from the ARPACK software package [28] by incorporating a routine performing the matrix-vector product in line 7 of the pseudo-code for a sparse symmetric matrix and a dense vector.

In order to obtain numerically an orthogonal basis truly spanning the full \mathcal{K}_r one in principle needs to re-orthogonalise \mathbf{w} in an iteration i with respect to all previously obtained \mathbf{v}_j for $j = 1, \dots, i - 1$. This will prevent numerical rounding errors to build up in the calculation of further vectors \mathbf{v}_i which otherwise could lead to a linear dependence of the \mathbf{v}_i amongst each other. If convergence is reached for a vector \mathbf{v}_s with $s < r$ one needs to use a different starting vector \mathbf{u} to be able to build a basis of \mathcal{K}_r . A proper re-orthogonalisation scheme together with an implicit restarting of the algorithm is implemented into `dssimp` by the authors of the ARPACK package [28], making it an Implicitly Restarted Arnoldi Method (IRAM). The routine `dssimp` mainly calls the two subroutines `dsaupd` and `dseupd` also provided in the ARPACK package which—together with the matrix-vector product provided by the author of this work—return a properly orthogonalised Lanczos-basis of \mathcal{K}_r and “converged approximations to eigenvalues” and “the corresponding approximate eigenvectors” [28] of the input matrix M respectively.

5.5.4. Operator transformation

After having diagonalised the Hamiltonian H_j in a given iteration j one typically needs to transform a set of operators $\{A_i\}$ into the new diagonal basis of H_j . Those operators are either bosonic creation- and annihilation operators d_j^\dagger, d_j of the last added chain-site j or operators which are needed in order to calculate spectral functions like e. g. $S_{z,e}$ for $\langle\langle S_{z,e}, S_{z,e} \rangle\rangle_z$. The operators $\{A_i\}$ are typically only transformed in the subspace spanned by the lowest N_{kept} eigenstates of H_j since those are the ones that

are used in the next NRG iteration $j + 1$. If the orthogonal matrix $U \in \mathbb{R}^{l \times N_{\text{kept}}}$ diagonalises H_j like

$$H_{j,\text{diag}} = U^T H_j U \in \mathbb{R}^{N_{\text{kept}} \times N_{\text{kept}}} \quad (5.64)$$

then one also needs to transform the set of operators $\{A_i\}$ like

$$A'_i = U^T A_i U. \quad (5.65)$$

The operators A_i are all sparse with an individual sparsity of p_i leading to a rather small numerical cost for the matrix product $B_i = A_i U$. This first product needs $\mathcal{O}(N_{\text{kept}} p_i l^2)$ operations and $\mathcal{O}(N_{\text{kept}} l)$ memory. The resulting matrix B_i is now dense and of size $l \times N_{\text{kept}}$. Thus the second product $A'_i = U^T B_i$ needs $\mathcal{O}(N_{\text{kept}}^2 l)$ operations and $\mathcal{O}(N_{\text{kept}} l)$ memory.

In total the transformation (5.65) performs $\mathcal{O}(N_{\text{kept}} l [N_{\text{kept}} + p_i l])$ operations and needs $\mathcal{O}(N_{\text{kept}} l)$ memory. This is independent of whether the transformation matrix U was obtained via an exact diagonalisation or via the Lanczos-algorithm. Since for each matrix A_i it is known where non-zero elements are stored one never needs to perform a dense matrix-matrix multiplication $B_i = A_i U$ but can always rely on performing only operations with non-zero elements of A_i , be it with a general sparse-matrix storage format for the A_i or by programming the calculation of the B_i for each i individually by hand. If one were to perform the first matrix-matrix multiplication with two dense matrices, the total numerical cost would be of the order of $\mathcal{O}(N_{\text{kept}} l^2)$ with respect to the operation-count and $\mathcal{O}(l^2)$ with respect to the memory consumption.

Table 1 summarises the numerical cost of the three different steps that need to be performed in each NRG iteration both for a dense and a sparse matrix format of a Hamiltonian H_j of size $l \times l$ with a filling factor of p for step i). For the diagonalisation in step ii) the results for the discussed exact diagonalisation and the diagonalisation using the Lanczos-algorithm are shown. There the r dependence in the latter has been replaced by the dependence on the number of calculated eigenstates N_{kept} (remember that $r = 4N_{\text{kept}}$). The operator transformation (5.65) in step iii) where the product $B_i = A_i U$ is calculated should always make use of the sparsity of the A_i .



$\mathcal{O}(\dots)$	Dense w. Exact Diag.		Sparse w. Lanczos Diag.	
	Memory	Runtime	Memory	Runtime
Store H_j	l^2	pl^2	pl^2	pl^2
Diagonalise H_j	l^2	l^3	$l[N_{\text{kept}} + pl]$	$N_{\text{kept}}l[N_{\text{kept}} + pl]$
Transform operators A_i	l^2	$N_{\text{kept}}l^2$	$N_{\text{kept}}l$	$N_{\text{kept}}l[N_{\text{kept}} + p_i l]$

Table 1:

Comparison of the numerical demands for the different steps in an NRG iteration between a dense matrix representation with an exact diagonalisation and a sparse matrix representation with a Lanczos diagonalisation. First, one needs to set up the Hamiltonian H_j of size $l \times l$ that has only a fraction of p non-zero matrix elements. The filling takes up the same time both for sparse and dense matrices since one could initialise a whole 2d-array very efficiently to zero and then simply has to add the non-zero elements like for the sparse matrix. In a second step, N_{kept} eigenvalues and -vectors are calculated either via an exact or a Lanczos diagonalisation. In a third step, a set of sparse operators $\{A_i\}$ with fractions p_i of non-zero matrix elements needs to be transformed into the basis spanned by the first N_{kept} eigenvectors of H_j .



6. Results

6.1. Dissipative oscillator model

Here the results obtained for the dissipative oscillator model in this work are presented. First, the model is investigated in case of zero self-interaction on the impurity oscillator analytically, where the equations of motion involve only free correlation functions. The impurity's scattering matrix is there calculated numerically from exact analytic results. In its imaginary part, the delta peak of the free oscillator at frequency Δ is smoothly shifted and broadened to a flat curve as the interaction between impurity and environment is increased. The total weight contained in the scattering matrix's spectrum shows universal scaling, suggesting a quantum phase transition (QPT) with a critical coupling $\alpha_c = 0 + \mathcal{O}(\frac{\Delta}{\omega_c})$.

For finite self-interaction on the impurity, the system is investigated with the aid of the Numerical Renormalization Group method (NRG). From the NRG results, the flow and fixed points of the model are derived. A whole line of quantum phase transitions in the α - U -plane is identified that connects the zero self-interaction quantum phase transition and the well known one of the spin-boson model in the limit of infinite self-interaction [27]. For a large range of the impurity's self-interaction we study the impurity scattering matrix. Ultimately, the differences between the clean system and the one with an impurity are investigated by means of zero temperature thermal averages. Both, the site occupation and oscillator displacement within the environment drop in a power-law manner as a function of growing distance to the impurity. The power-laws in most cases show a x^{-1} behaviour with small corrections in the exponent. Only for individual parameters, a deviation from that power-law drop can be seen which is assigned to problems in the numerical evaluation of the appearing integrals.

6.1.1. Analytic results for $U = 0$

An analytic expression for the impurity scattering matrix $\mathcal{T}_{\text{do}}(z) = \frac{\alpha}{4} \langle\langle b + b^\dagger, b + b^\dagger \rangle\rangle_z = \frac{\alpha}{4} D_{\text{imp}}(z)$ can be gained if the density-density interaction on the impurity is absent. It can be evaluated without obtaining the eigenbasis or spectrum of the model with help of e. g. the NRG or other methods. The imaginary part of the scattering matrix $\mathcal{T}_{\text{do}}(z)$ is used to study the changes in the average site occupation $\Delta \langle \hat{n}_x \rangle$ and in the average square of the displacement amplitude $\Delta \langle (a_x + a_x^\dagger)^2 \rangle$ via equations (3.44) and (3.61) as given in sections 3.4 and 3.5 respectively. In appendix A we derive the displacement-displacement correlation function $D_{\text{imp}}(z)$ to read

$$D_{\text{imp}}(z, T) = \left[D_{\text{imp}}^{(0)}(z)^{-1} - \frac{\alpha}{4} D^{(0)}(x=0, z) \right]^{-1} \quad (6.1)$$

in case of zero self-interaction. Here $D_{\text{imp}}^{(0)}(z)^{-1} = (z - \Delta)^{-1} - (z + \Delta)^{-1}$ is the bare displacement-displacement correlator of the impurity and $D^{(0)}(x=0, z)$ is the free displacement-displacement correlation function of the bath at the origin, reading

$$D^{(0)}(x = 0, z) = \frac{1}{2\pi} \int_{-\pi}^{\pi} \frac{1}{z - \omega(k)} - \frac{1}{z + \omega(k)} dk. \quad (6.2)$$

In section 4.1 the dispersion was set to $\omega(k) = |k/\pi|^{1/(s+1)}\omega_c$ in order to arrive at a spectral density $J(\omega) = \alpha\pi(s+1)\omega^s\omega_c^{1-s}$ that features a power-law behaviour. The imaginary part of $D^{(0)}(x = 0, \omega)$ on the real axis, i.e. $z = \omega$, resulting from that choice reads

$$\text{Im}[D^{(0)}(x = 0, \omega)] = \begin{cases} -\pi(s+1)\omega_c^{1-s}|\omega|^s \text{sign}(\omega) & , \omega \in [-\omega_c, \omega_c] \\ 0 & , \text{else.} \end{cases} \quad (6.3)$$

For the ohmic bath with a linear spectrum ($s = 1$) this expression simplifies to

$$\text{Im}[D^{(0)}(x = 0, \omega)] = -2\pi\omega\Theta(\omega_c^2 - \omega^2). \quad (6.4)$$

The real part is obtained analytically by evaluation of the integral in the Kramers-Kronig relation (4.25) to

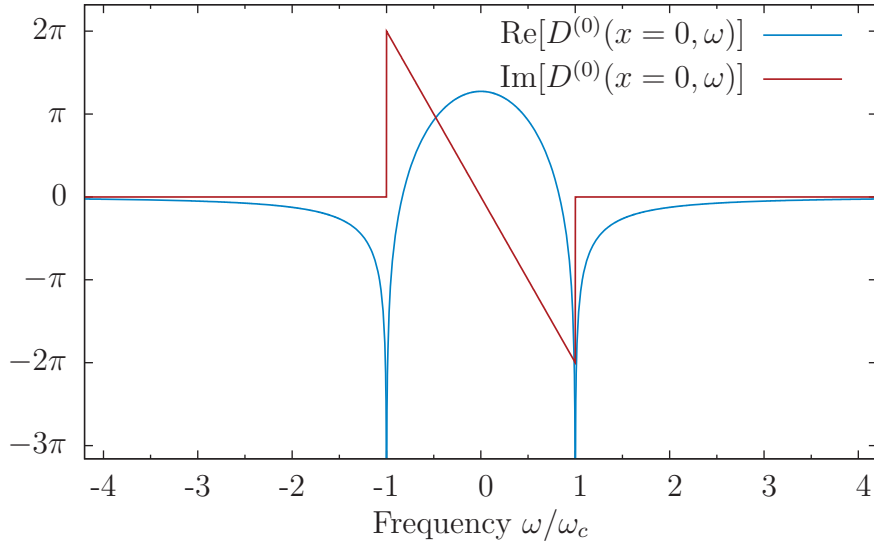
$$\text{Re}[D^{(0)}(x = 0, \omega)] = 4\omega_c + \omega \ln \left[\left(\frac{\omega_c - \omega}{\omega_c + \omega} \right)^2 \right], \quad (6.5)$$

which is true on the entire real axis. It features logarithmic divergences right at the cutoff frequencies $\pm\omega_c$ and a finite $\omega = 0$ value of $4\omega_c$. A plot, both of the real and the imaginary part of the bare displacement-displacement correlation function $D^{(0)}(x = 0, \omega)$, is presented in figure 17. The limiting behaviour of the impurity \mathcal{T} -matrix in case of very small and very large couplings can be obtained right away from (6.1) to be

$$\mathcal{T}_{\text{do}}(z) = \begin{cases} \frac{\alpha}{4} D_{\text{imp}}^{(0)}(z), & \alpha \ll 1, \\ -D^{(0)}(x = 0, z)^{-1}, & \alpha \gg 1. \end{cases} \quad (6.6)$$

Thus, for large couplings between impurity and environment all features of the bare impurity have vanished as only the bath displacement-displacement correlations enter the \mathcal{T} -matrix in that limit. There the impurity oscillator may no longer be understood as an individual particle. In figure 18 results on the negative imaginary part of $\mathcal{T}_{\text{do}}(z = \omega + i\epsilon)$ are presented for a large range of couplings α between 2^{-15} and 2^5 , where the transition between the two limiting behaviours can be seen. The imaginary part of the argument z was set to a very small value of 10^{-10} for those calculations and only the positive frequency part was plotted as the imaginary part of \mathcal{T}_{do} is antisymmetric on the real axis.

There exists a coupling strength α where both, the contribution from the bare impurity oscillator and from the bare bath oscillator at the origin are of the same order of


Figure 17:

Real- and imaginary part of the bare displacement-displacement correlation function $D^{(0)}(x=0, \omega)$ which enters the impurity \mathcal{T} -matrix. The real part has been rescaled by ω_c such that $D^{(0)}(x=0, \omega) = 4$. Right at the cutoff frequencies $\pm\omega_c$ the real part show logarithmic divergences (cf. equation (6.5)).

magnitude. The value of α can be extrapolated by investigating the total weight that is contained in the spectrum corresponding to $D_{\text{imp}}(\omega)$. As the integral of an antisymmetric function over the whole frequency space vanishes we investigate here only the single sided weight $-\int_0^\infty \text{Im}[D_{\text{imp}}^{(0)}(\omega)] d\omega/\pi$. For small couplings α the weight is unity, stemming from the delta-peak at the bare oscillator frequency Δ (cf. figure 19 a)). In this regime, the eigenenergies of the oscillator are sharply peaked around Δ and the impurity oscillator is basically free as there is almost no dissipation due to the thermal environment. Thus, if the oscillator is initialised at time zero in a coherent state, it will perform many oscillations before decoherence due to a mismatch of the eigenenergies kicks in. Likewise, the amplitude of those oscillations drops slowly in time as the dissipation due to the bath is very small. For very large couplings between impurity and environment, the total weight contained in the imaginary part of $D_{\text{imp}}(\omega)$ vanishes $\sim \alpha^{-1}$ (cf. figure 20 where the total weight contained in $\mathcal{T}_{\text{do}}(\omega) = \frac{\alpha}{4} D_{\text{imp}}(\omega)$ becomes constant in that regime). In that limit the original impurity oscillator is strongly bound to the oscillator at the origin of the bath and its free character is lost. Its spectrum is then fully characterised by that of the bath oscillator at the origin.

The energy-spectrum of the dissipative oscillator model for zero self-interaction U —obtained by means of the NRG—shows a unique ground state for small initial couplings between impurity and environment. For large initial couplings the ground

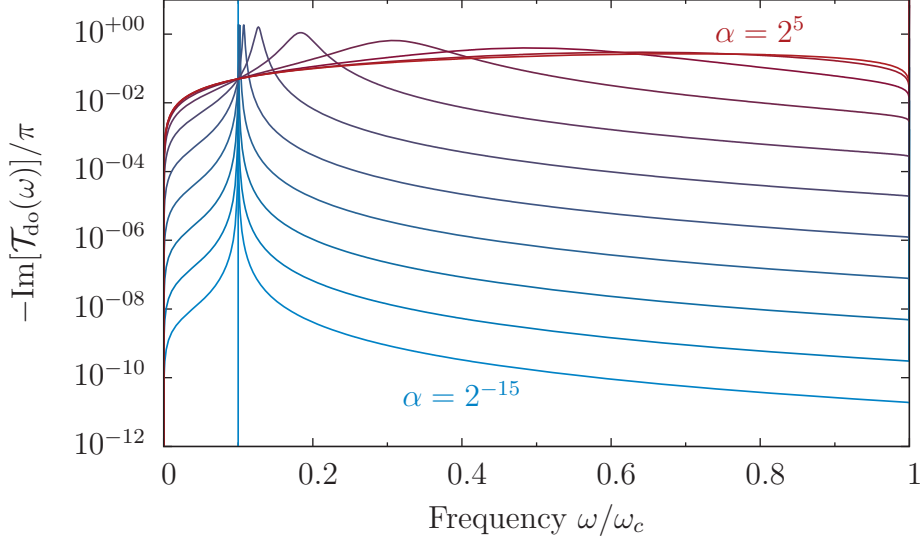


Figure 18:

Negative imaginary part of the impurity \mathcal{T} -matrix for several couplings α between impurity and environment, plotted for positive frequencies only. The bare eigenfrequency of the impurity oscillator was set to $\Delta = 0.1$ and its position is depicted in the plot by the vertical line. The coupling parameters were $\alpha = 2^{-15}, 2^{-13}, \dots, 2^5$ and an imaginary part of $\epsilon = 10^{-10}$ was used for the frequency $z = \omega + i\epsilon$ in the evaluation of equation (6.1). Two effects can be seen as the coupling strength increases from small (blue) to large (red) values: for small couplings the delta peak structure of the curve is retained and simply scaled by a factor of $\alpha/4$. At larger couplings the peak of the curve that can be identified with the oscillator frequency is shifted to ever larger values. At the same time it is broadened and eventually turns into a flat curve which is mainly given by the bath spectrum $\sim \omega$ in the ohmic case.

state is doubly degenerate in the even- and the odd-parity sector of the theory (cf. discussion on the flow and fixed points of the model within the NRG in section 6.1.2). In between, there is a critical coupling strength α_c where the nature of the ground state(s) changes abruptly and a quantum phase transition in the system takes place. The scale on which the behaviour between the weak and the strong coupling limit changes is numerically extrapolated from the analytic results on $D_{\text{imp}}(\omega)$. It is chosen as that coupling strength where the total weight contained in $D_{\text{imp}}(\omega)$ has dropped to $1/2$ from the original delta-peak weight of unity.

In figure 19 a), the total weight contained in the imaginary part of $D_{\text{imp}}(\omega)$ is presented as a function of the coupling strength α for several initial bare oscillator frequencies Δ . The extrapolated critical coupling $\alpha_c(\Delta)$ is presented in part b) of fig-

ure 19 and is found to behave as $\alpha_c(\Delta) = (1.50 \pm 0.04)\Delta^{0.999 \pm 0.004}$ for small frequencies $\Delta \ll 1$.

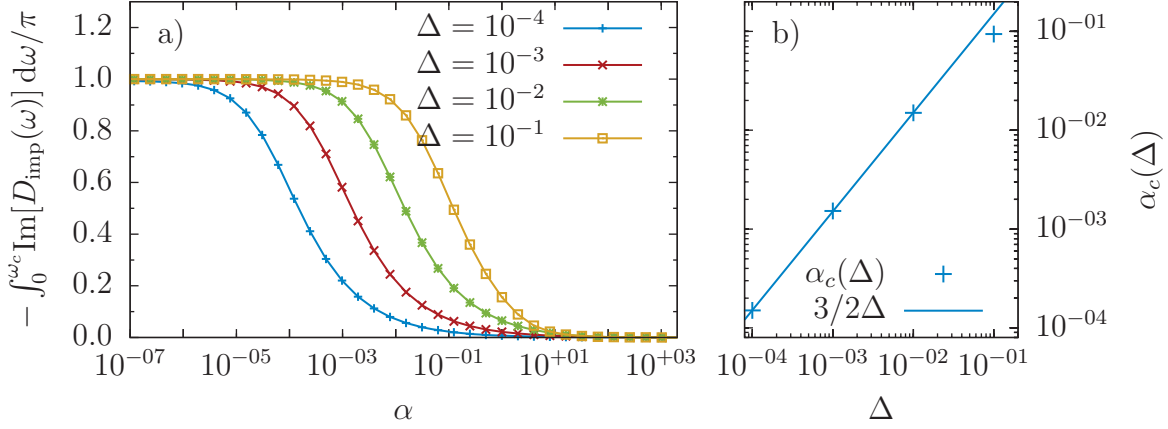


Figure 19:

a) Total weight contained in the spectrum $-\int_0^{\omega_c} \text{Im}[D_{\text{imp}}(\omega)] d\omega/\pi$ within the positive frequency range. For small couplings α the peak of $D_{\text{imp}}(\omega)$ at Δ is almost unchanged and its spectral weight remains close to one. In the strong coupling regime the delta peak has vanished (cf. figure 18) and the term $\frac{\alpha}{4}D^{(0)}(x=0, \omega)$ in the denominator of $D_{\text{imp}}(\omega)$ dominates. There the total remaining weight drops down exponentially as $\sim \alpha^{-1}$. b) The coupling strength $\alpha_c(\Delta)$ where the total weight has dropped to $1/2$ is chosen to mark the crossing region between the two limiting behaviours where both contributions from the bare propagators $D_{\text{imp}}^{(0)}(\omega)^{-1}$ and $\frac{\alpha}{4}D^{(0)}(x=0, \omega)$ are of the same order of magnitude (crosses). For small values of $\Delta < 0.1$ a fit of the data results in $\alpha_c(\Delta) = (1.50 \pm 0.04)\Delta^{0.999 \pm 0.004}$ (line).

Plotting the total weight contained in the \mathcal{T} -matrix spectrum as a function of $\alpha \times 2\alpha_c(\Delta)$ reveal that all curves collapse to a single one (cf. figure 20), implying universal scaling and indeed the existence of a quantum phase transition as a function of α . The total weight contained in the spectrum of the scattering matrix shows a maximum for intermediate couplings α before it drops to the constant in the strong coupling limit. As its position is close to one, it is assigned to the quantum phase transition taking place. With the results for the scattering matrix $\mathcal{T}_{\text{do}}(\omega)$, derived in this section, we are now able to investigate the change in the average site occupation of the bosonic sites in the chain due to the presence of the impurity oscillator.

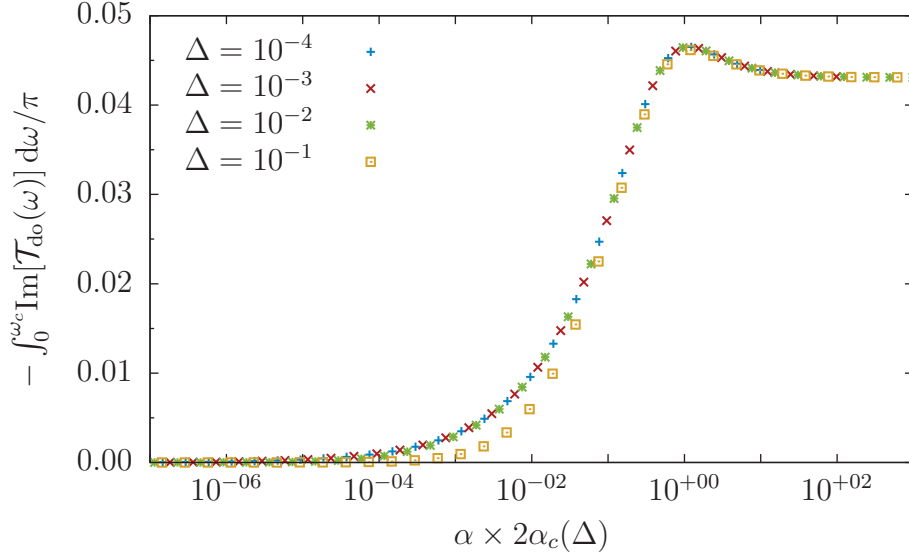


Figure 20:

Total weight contained in the spectrum $-\int_0^{\omega_c} \text{Im}[\mathcal{T}_{\text{do}}(\omega)]/\pi d\omega$ within the positive frequency range for several bare oscillator frequencies Δ . For large couplings, the total weight becomes a constant as only the spectrum of $D^{(0)}(x=0, \omega)^{-1}$ enters the \mathcal{T} -matrix. For values of $\Delta < 0.1$ all curves collapse onto a single universal curve. There appears then a maximum in the total weight at an intermediate coupling strength of $\alpha \times 2\alpha_c(\Delta) \approx 1$.

Change in the average site occupation

In section 3.4, the change in the environmental average site occupation was derived to read

$$\Delta \langle \hat{n}_x \rangle = \frac{1}{\pi} \int_{-\infty}^0 \text{Im}[G_{x,0}^{(0)}(\omega) \mathcal{T}_{\text{do}}(\omega, T=0) G_{0,x}^{(0)}(\omega)] d\omega$$

in its zero temperature limit. As the free Green's functions $G_{x,0}^{(0)}(\omega) \equiv G_{0,x}^{(0)}(\omega)$ have a non-vanishing imaginary part only in the positive frequency domain and they are equal, the integral simplifies to

$$\Delta \langle \hat{n}_x \rangle = \frac{1}{\pi} \int_{-1}^0 \text{Im}[\mathcal{T}_{\text{do}}(\omega, T=0)] \text{Re}[G_{x,0}^{(0)}(\omega)]^2 d\omega.$$

For the calculations, the high-frequency cutoff was set to $\omega_c = 1$. Hence, the lower bound in the integral is set to $-\omega_c = -1$ because the imaginary part of the scattering matrix is numerically finite above ω_c only due to the small imaginary part ϵ of the frequency argument $\omega + i\epsilon$. Results for the change in the average site occupation $\langle \hat{n}_x \rangle$ for a large range of couplings α are presented in figure 21 for several decades

in x . There an imaginary part $\epsilon = 10^{-3}$ was used for the evaluation of the impurity scattering matrix. The change in the average site occupation is found to drop in a

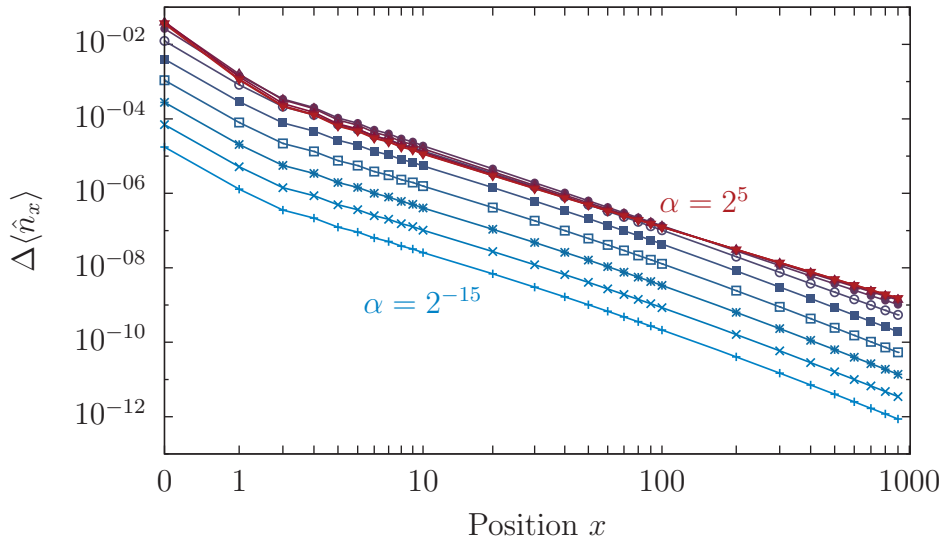


Figure 21:

Change of the average site occupation $\Delta\langle\hat{n}_x\rangle$ for couplings $\alpha = 2^{-15}, 2^{-13}, \dots, 2^5$. The initial value of the impurity oscillator frequency was set to $\Delta = 0.1$. For small couplings α , the amplitude of the curves scale with α , while for large couplings the curves collapse as $\mathcal{T}(\omega) \sim D^{(0)}(x=0, \omega)^{-1}$ becomes independent of α .

power-law manner $\sim x^p$ for large distances x . The power-law exponent p however, is different in the weak coupling regime and the strong coupling regime. For small couplings between impurity and bath, we find a power-law exponent of $p = -5/2$ while in the strong coupling limit it turns out to be $p = -2$. Figure 22 shows the two limiting curves of $\langle\hat{n}_x\rangle$ for $\alpha = 2^{-15}$ and $\alpha = 2^5$ along with the corresponding power-laws of their large-distance behaviour. At small couplings, the curves of $\langle\hat{n}_x\rangle$ scale with the coupling α as the delta peak at the bare impurity oscillator frequency Δ in the imaginary part of the \mathcal{T} -matrix is almost unchanged. In the strong coupling regime the results then again do not depend any longer on the specific value of α and all curves collapse onto a single one. As all curves for $\langle\hat{n}_x\rangle$ drop in a power-law manner for the positions x investigated, no characteristic length-scale of the problem shows in this quantity.

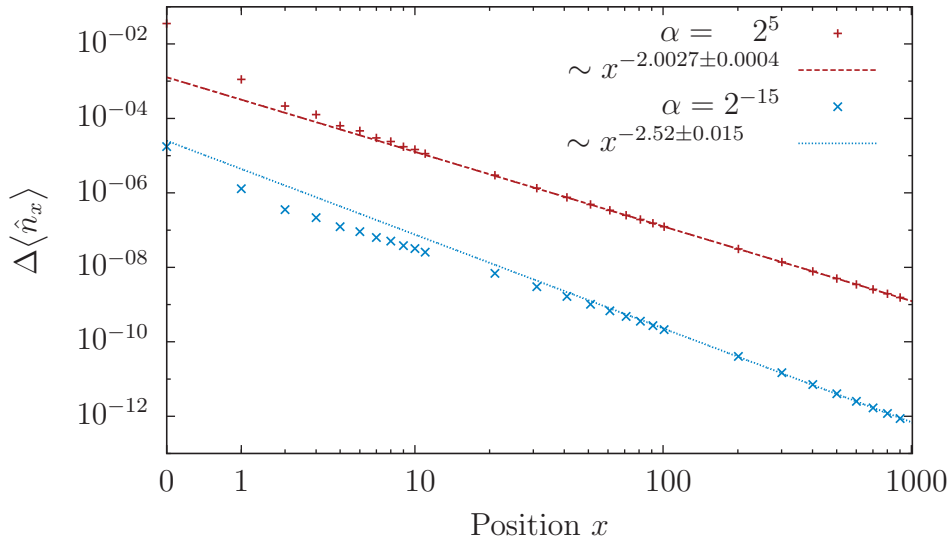


Figure 22:

Extrapolation of the large distance power-law behaviours of the change in the average site occupation $\Delta\langle\hat{n}_x\rangle$ for large (red) and small (blue) values of the coupling $\alpha = 2^5$ and $\alpha = 2^{-15}$, respectively. The power-laws were fitted in the region $100 \leq x \leq 1000$.

Change in the average displacement amplitude

The change of the oscillator displacements in the chain due to the presence of the impurity oscillator is investigated next. To this end, the integral

$$\Delta\langle(a_x + a_x^\dagger)^2\rangle = \frac{1}{\pi} \int_{-\infty}^0 \text{Im}[D_{x,0}^{(0)}(\omega)\mathcal{T}_{\text{do}}(\omega, T=0)D_{0,x}^{(0)}(\omega)] d\omega \quad (6.7)$$

has to be evaluated numerically. It was derived in section 3.5.1 for the change of the squared displacement amplitude at position x in the chain. The results for an impurity oscillator frequency of $\Delta = 0.1$ and several couplings α are presented in figure 23. In the strong coupling limit, all oscillators in the environment are displaced by an amount that is proportional to the coupling strength α . In the regime of couplings $\alpha < 1$, the change of the oscillator displacement in the environment shows oscillatory behaviour close to the impurity. Far away from the impurity the average displacement is again increased by a constant amount $\sim \alpha$.

In this intermediate regime, a length-scale can be assigned to the impurity, over which it can be seen in the environment. Beyond that length scale, it causes a constant change in the oscillators' amplitudes.

For very weak couplings $\alpha < 10^{-3}$, the numerical data show oscillations in the sign of $\Delta\langle(a_x + a_x^\dagger)^2\rangle$ and a negative total change, i. e. a reduction of the bath oscillator

displacement far away from the impurity. From the slope of the curves for very weak coupling we can infer, that the change will eventually turn positive again. This point of the last sign change marks supposedly also the region, over which the impurity can be seen in the environment. To conclude, the change of the bath oscillator displace-

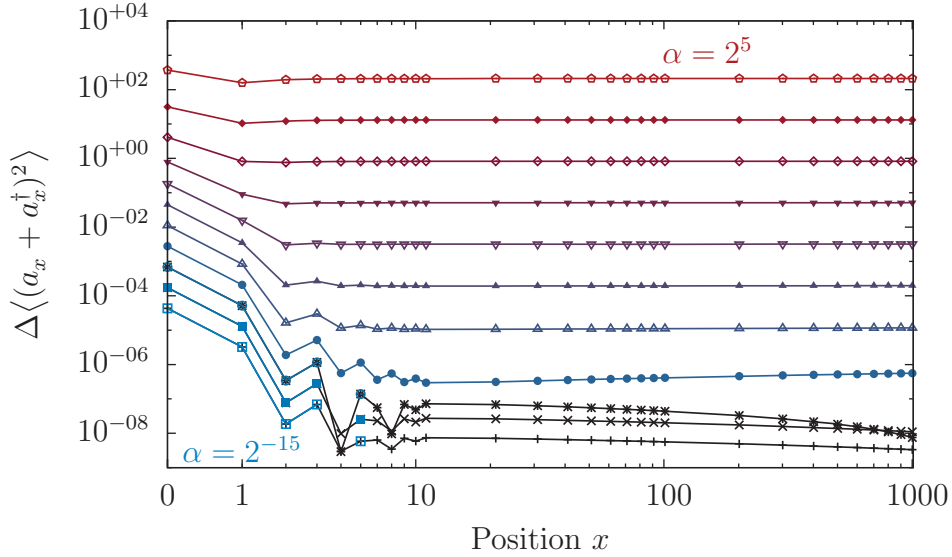


Figure 23:

Change of the average square of the displacement amplitude for an oscillator frequency of $\Delta = 0.1$ and different couplings $\alpha = 2^{-15}, 2^{-13}, \dots, 2^5$. For very small couplings, the sign of the difference oscillates. Therefore, the modulus of the data is shown as well in black. Close to the impurity, the change in the oscillators amplitude shows fluctuations in case of small initial coupling. At sites $x > 10$, the change turns into a constant value that is $\sim \alpha$. In the limit of large couplings, the oscillators throughout the entire bath become displaced by an amount $\sim \sqrt{\alpha}$.

ment indicates indeed a length-scale over which the impurity oscillator influences its environment. A constant change far away from the impurity, that is proportional to the coupling strength α , can be seen in all cases. However, a non-uniform change of the oscillator displacements may only be seen close to the impurity for intermediate couplings. For very weak couplings between impurity and environment, the length-scale over which the impurity can be seen, seems several orders of magnitude larger than in the intermediate coupling regime.

In the following, the numerical results that were obtained with the NRG method are presented in order to investigate the dissipative oscillator model in case of a finite self-interaction U .

6.1.2. Identification of fixed points

In section 5 the NRG method was introduced as the numerical method of choice to investigate the dissipative oscillator model for arbitrary model parameters. The Hamiltonian of the dissipative oscillator model was mapped within this framework onto a model featuring a semi-infinite chain of harmonic oscillators instead of a continuous set of bath modes. The Hamiltonian after the mapping (5.22) was derived to read

$$H_{\text{do}}^{\text{chain}} = H_{\text{imp}} + \sum_{n=0}^{\infty} \left[\epsilon_n d_n^\dagger d_n + t_n (d_{n+1}^\dagger d_n + d_n^\dagger d_{n+1}) \right] + \left(\frac{b + b^\dagger}{2} \right) \sqrt{\frac{\eta_0}{\pi}} (d_0 + d_0^\dagger) \quad (6.8)$$

where

$$H_{\text{imp}} = \epsilon \left(\frac{b + b^\dagger}{2} \right) + \Delta \left(\hat{n}_b + \frac{1}{2} \right) + \frac{U}{2} \hat{n}_b (\hat{n}_b - 1) \quad (6.9)$$

is the unchanged impurity part of the Hamiltonian.

The semi-infinite chain is called a Wilson-chain and features on-site energies ϵ_n and nearest neighbour hopping amplitudes t_n that both drop exponentially as Λ^{-n} where $\Lambda > 1$ is the logarithmic discretisation parameter introduced in section 5.1. Instead of solving (6.8) directly we set up a series of Hamiltonians H_N that contain the impurity plus a chain truncated to the first N sites. Two consecutive Hamiltonians of the series are connected by the transformation

$$H_{N+1} = \Lambda H_N + \Lambda^N \left[\epsilon_{N+1} d_{N+1}^\dagger d_{N+1} + t_N (d_{N+1}^\dagger d_N + d_N^\dagger d_{N+1}) \right] - E_0(N+1) \quad (6.10)$$

where the ground state energy of H_{N+1} is already shifted to zero. The initial Hamiltonian H_0 is defined as

$$H_0 = H_{\text{imp}} + \epsilon_0 d_0^\dagger d_0 + \left(\frac{b + b^\dagger}{2} \right) \sqrt{\frac{\eta_0}{\pi}} (d_0 + d_0^\dagger), \quad (6.11)$$

constituting of the impurity and the zero orbital of the chain. In the limit of $N \rightarrow \infty$ the series converges to $H_{\text{do}}^{\text{chain}}$ as

$$H_{\text{do}}^{\text{chain}} = \lim_{N \rightarrow \infty} \Lambda^{-N} H_N. \quad (6.12)$$

As outlined in section 5.3 the mapping (6.10) can be understood as a renormalization group mapping R such that

$$H_{N+1} = R(H_N). \quad (6.13)$$

It was stated that an important feature of R to investigate is its set of fixed points H^* for which $R(H^*) = H^*$. Depending on the character of the perturbations around those fixed points they are either attractive, corresponding to stable phases of matter, or feature at least one or only relevant operators that carry the system away from the

fixed points marking phase transitions and ideal, unreachable fixed points of matter respectively.

The following analysis of the dissipative oscillator model (6.8) begins by considering its different fixed points. Those are identified and discussed in a combination of analytical arguments together with numerical data obtained from the NRG (cf. [26] for a similar analysis of the Anderson Impurity Model). There a delocalised fixed point and a whole set of localised fixed points is found. While the impurity oscillator has a finite frequency Δ in the delocalised phase it will become completely frozen in the localised phase. The different localised fixed points then all differ by the amount to which the environmental oscillators are displaced, which turns out to be $\sim \sqrt{\alpha_c - \alpha}$.

For each value of the self-interaction parameter investigated, a critical coupling $\alpha_c(U)$ is found that marks a quantum phase transition between the localised and the delocalised phase. Numerical results on $\alpha_c(U)$ are presented in section 6.1.3. In the limit of zero self-interaction, the critical coupling vanishes as $\alpha_c(U = 0, \Delta) \sim \Delta$. In the limit of $U \rightarrow \infty$, the critical coupling of the spin-boson model $\alpha_c = 1 + \mathcal{O}(\frac{\Delta}{\omega_c})$ can be retained.

In the delocalised phase the effects of the impurity on the bath will be obtained by calculating the scattering matrix of the impurity in section 6.1.4. With the scattering matrix at hand, it is possible to calculate the change in the average site occupation $\Delta \langle \hat{n}_x \rangle$ and that of the average displacement amplitude squared $\Delta \langle (a_x + a_x^\dagger)^2 \rangle$ in the one-dimensional chain of the original model (cf. equation (2.2)).

In the following, the displacement ϵ of the impurity oscillator is always set to zero and the original bath features an ohmic spectral density $J(\omega) \sim \omega$. With these constraints it is possible to identify two different kinds of fixed points in the flow of the energy spectrum $E_r(N)$ for the dissipative oscillator model, apart from the one of the non-interacting system.

Free impurity and free chain Hamiltonian

If the impurity and the chain of bosons are non-interacting the system is trivial to understand. In this case, the impurity Hamiltonian is already diagonal and its eigenstates and corresponding -energies are given by

$$H_{\text{imp}}(\Delta, U)|n\rangle = \left[\Delta n + \frac{U}{2}n(n-1) \right] |n\rangle \quad (6.14)$$

if the energy of the ground state is set equal to zero. Here the states $|n\rangle$ are the eigenstates of the occupation number operator $b^\dagger b$ at the impurity. The free chain spectrum can be obtained by re-diagonalizing the Hamiltonian

$$H_{chain}^{(0)}(N) = \Lambda^{N-1}(d_0, d_1, \dots, d_N) \begin{pmatrix} \epsilon_0 & t_0 & & & \\ t_0 & \epsilon_1 & \ddots & & \\ & \ddots & \ddots & t_{N-2} & \\ & & & t_{N-2} & \epsilon_{N-1} \end{pmatrix} \begin{pmatrix} d_0 \\ d_1 \\ \vdots \\ d_{N-1} \end{pmatrix} \quad (6.15)$$

onto which the bath was originally mapped. This provides the single particle energies of the chain of length N in a first step. From those, the many-particle spectrum of the chain is calculated in a second step by combining the energies of the single particle excitations and taking only the lowest ones of interest. Figure 24 presents the spectra $E_r(N)$ of the series of Hamiltonians $H_{chain}^{(0)}(N)$ for a logarithmic discretisation parameter of $\Lambda = 2$. In that case, the chain reaches its low temperature fixed point $H_{chain}^*(N) = H_{chain}^{(0)}(N)$ already for iteration $N \approx 10$, as for $N \gtrsim 10$ the spectrum appears constant. The ground state of the impurity oscillator is unique. Hence, the total fixed point of the system is then given by a harmonic oscillator of frequency Δ in its ground state and a free chain with fixed point $H_{chain}^*(N)$.

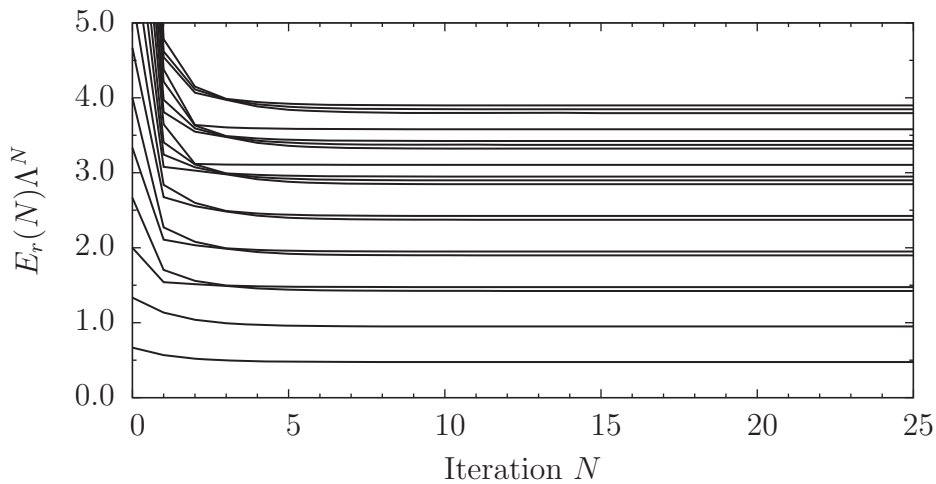


Figure 24:

Flow of the first twenty states of the many-particle spectrum $E_r(N)$, calculated for the Hamiltonians $H_{chain}^{(0)}(N)$ for iterations N between 0 and 25 for a logarithmic discretisation parameter of $\Lambda = 2$. Already for iterations $N > 10$ no further change in the spectrum is visible as the chain has reached its low temperature fixed point $H_{chain}^*(N)$.

Delocalised fixed point

To describe the delocalised fixed point, the bare impurity oscillator frequency Δ is sent to infinity while keeping the self-interaction U arbitrary but fixed. Again, the impurity oscillator will be in its ground state, as no other states are accessible at finite temperatures. In this case, the coupling α to the zero orbital of the chain in H_0 (6.11) can be ignored since it couples the zero orbital to higher impurity states of energy $\sim \Delta$. Thus, the fixed point is described by the free chain fixed point with the impurity confined to its single ground state:

$$H_{del}^* = |0\rangle\langle 0| \otimes H_{chain}^*(N). \quad (6.16)$$

The subscript *del* (for delocalised) indicates that the impurity oscillator in its ground state is not localised. This means, that the average displacement $\langle 0|b + b^\dagger|0\rangle$ of the impurity oscillator in its ground state vanishes, much like the average magnetisation ${}_{\text{sbm}}\langle 0|\sigma_z|0\rangle_{\text{sbm}}$ in the spin-boson model vanishes in its delocalised phase. Thus the oscillator is not localised at a finite position in space.

Within the NRG, the delocalised fixed point can be reached as long as the coupling α between impurity and chain is smaller than a critical value α_c . Then, the bath renormalizes the initial parameters Δ and U of the impurity to smaller, finite values $\tilde{\Delta}$ and \tilde{U} . As the frequency $\tilde{\Delta}$ reaches a fixed but finite value $\tilde{\Delta}^*$, the first excited state on the effective impurity will eventually be projected out as soon as the energy-scale Λ^{-N} reaches $\tilde{\Delta}^*$. In further iterations, the energy-scale $\tilde{\Delta}^*$ can be considered large and is ultimately projected out of the low energy sector, which is kept in each iteration of the NRG.

Figure 25 presents the energy-spectra $E_r(N)$ obtained from the NRG, rescaled by Λ^N . The initial set of model parameters for the calculations was $\alpha = 2 \times 10^{-5}$, $\Delta 10^{-4}$ and $U = 10^{-3}$. For the numerical implementation a logarithmic discretisation of $\Lambda = 2$ is chosen and the lowest $N_{\text{kept}} = 500$ states are kept in each iteration. Furthermore the sizes of the different Hilbert-spaces were truncated to the first $N_{b,imp} = 60 = N_{b,0}$ states for the impurity and the zero orbital of the chain and to $N_b = 16$ states for all further orbitals of the chain. With the choice of $\Delta = 10^{-4}$ and $U = 10^{-3}$ it is ensured, that the lowest states of H_0 are well below the energy ϵ_0 of the first excited state of the site zero in the chain. Thereby it was possible to fit the first twenty states of H_0 to the spectrum of an effective impurity Hamiltonian with rescaled parameters $\tilde{\Delta}$ and \tilde{U} that is no longer coupled to the zero orbital of the chain. In figure 25, the different states are projected out successively as their energy becomes large compared to the low-energy sector of the chain.

The renormalizing effect of the bath on the impurity is observable in figure 26, where the unscaled spectra of the first eight iterations are presented for the same set of parameters as in figure 25. The lowest eigenstates of the full system are almost unchanged, as the impurity is weakly coupled to the environment.

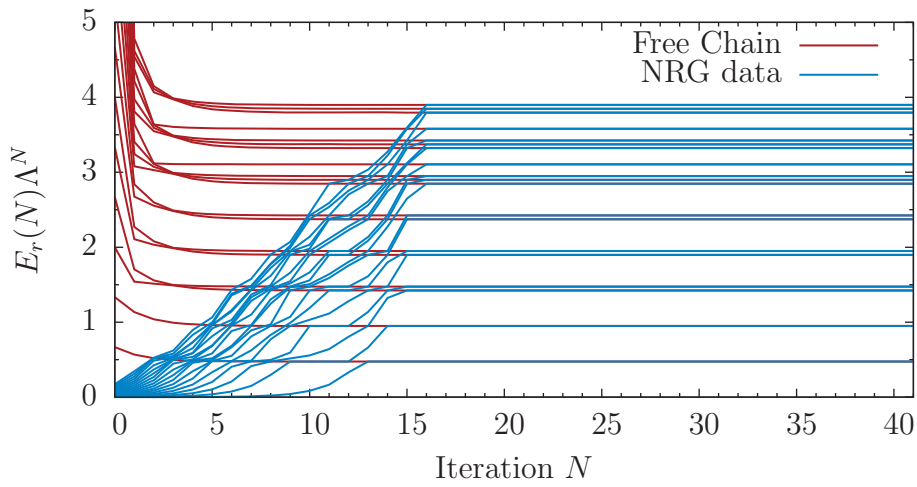
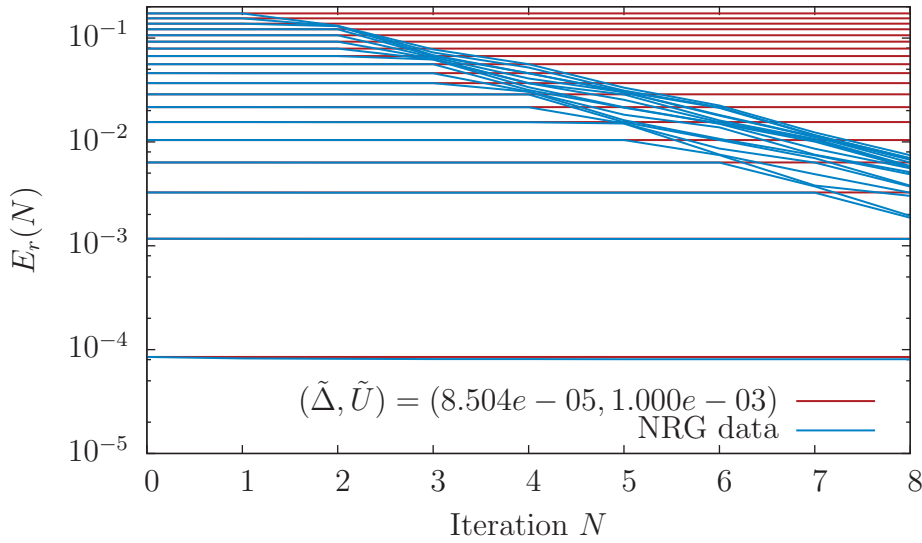


Figure 25:

Energy levels obtained from the NRG (blue) in comparison to the spectrum of a free ohmic chain (red) for a coupling of $\alpha = 2 \times 10^{-5}$ and bare impurity parameters $\Delta = 10^{-4}$, $U = 10^{-3}$. For early iterations the spectrum resembles that of a free impurity (cf. figure 26). In later iterations the low energy spectrum of the total system is given by that of the free Wilson-chain. Further parameters were $\Lambda = 2.0$, $N_{\text{kept}} = 500$, $N_{b,\text{imp}} = N_{b,0} = 60$ and $N_b = 16$ for a chain sites after the first.


Figure 26:

Energy levels obtained from the NRG (blue) in comparison to the spectrum of a free impurity (red) for the same parameters as given in figure 25. The energy levels of the free impurity are given by $E_n = \tilde{\Delta}n + \tilde{U}n(n-1)/2$. The first twenty levels of the diagonalised initial Hamiltonian H_0 were used to fit renormalized values of $\tilde{\Delta}$ and \tilde{U} to the spectrum. The parameter $U = 10^{-3}$ remains almost unchanged and the bare oscillator frequency $\Delta = 10^{-4}$ has been renormalized to a value of $\tilde{\Delta} = 0.8504 \times 10^{-4}$. In further iterations the structure of the impurity spectrum remains unchanged and the higher lying states of the impurity are projected out successively as the low-energy sector of the almost uncoupled chain drops down exponentially as Λ^{-N} .

Localised fixed point

A second kind of fixed point of the renormalization group mapping (6.10) can be identified in the flow of the spectra of the Hamiltonians H_N (cf. figure 27). At these fixed points the spectrum is given by that of the free chain $H_{chain}^*(N)$ where now each state is doubly degenerate. As the coupling α becomes large, all oscillators in the chain get displaced by an amount $\sim \sqrt{\alpha}$. That the ground state of the initial Hamiltonian H_0 is indeed twofold degenerate in the limit of large α can be understood from symmetry considerations. As the displacement ϵ of the impurity is zero, each Hamiltonian H_N conserves the parity $P_\pi(N) = e^{i\pi(n_b + \sum_{i=0}^N n_i)} = \pm 1$. For the following line of arguments the self-interaction U is considered large, such that only the states $|0\rangle$ and $|1\rangle$ of the impurity are important for the low energy sector of the theory. In

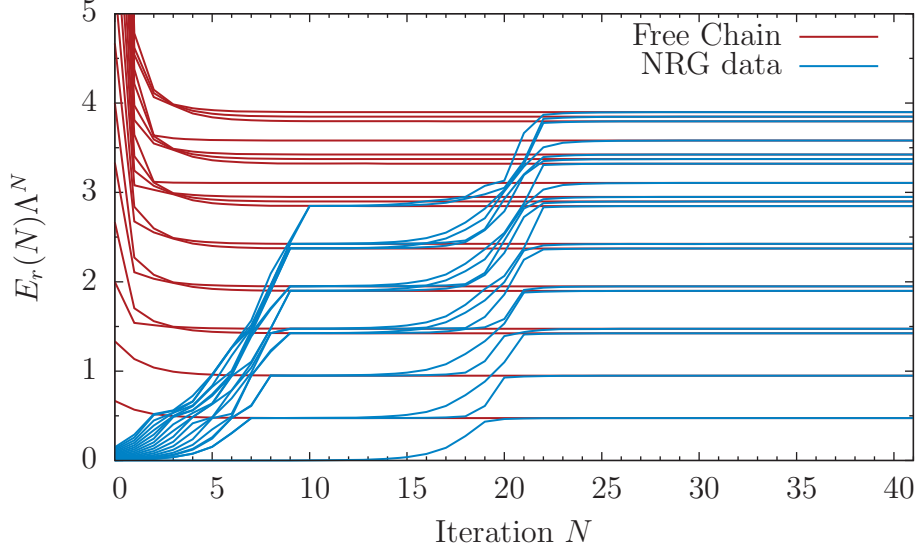


Figure 27:

Energy levels obtained from the NRG (blue) in comparison to the spectrum of a free chain (red) for a coupling of $\alpha = 2 \times 10^{-3}$. For early iterations the spectrum resembles that of a free impurity (cf. figure 26). An intermediate fixed point is reached for iterations $\sim 8 - 15$. There the spectrum is that of the free chain where each state is twofold degenerate. In later iterations the spectrum of the total system is given by that of the free Wilson-chain where possible degeneracies are only accidental. There the system has reached the delocalised fixed point. The further NRG parameters were: $\Lambda = 2$, $N_{b,imp} = 60$, $N_{b,0} = 60$, $N_b = 16$, $s = 1$, $N_{kept} = 500$.

that case, the initial Hamiltonian $H_0 - \Delta/2$ reduces to that of the spin-boson model (cf. equation (2.11))

$$H_0 = -\frac{\Delta}{2}\sigma_z + \epsilon_0 d_0^\dagger d_0 + \sqrt{\frac{\eta_0}{\pi}} \frac{\sigma_x}{2} (d_0 + d_0^\dagger) \quad (6.17)$$

where the states $|\uparrow\rangle \hat{=} |0\rangle$ and $|\downarrow\rangle \hat{=} |1\rangle$ are identified on the impurity. Rotating the coordinate system of the impurity by $-\pi/2$ about the y -axis leads to

$$H_0 = \frac{\Delta}{2}\sigma_x + \epsilon_0 d_0^\dagger d_0 + \sqrt{\frac{\eta_0}{\pi}} \frac{\sigma_z}{2} (d_0 + d_0^\dagger).$$

From that, the Hamiltonian H_0 is projected into an even and an odd parity sector by the transformation $U = \frac{1}{\sqrt{2}}(\mathbb{1} - i\sigma_y P_\pi(0))$ [19] as

$$\begin{aligned} \tilde{H}_0 &= U^T H_0 U = \begin{pmatrix} H_+ & 0 \\ 0 & H_- \end{pmatrix} \\ &= \begin{pmatrix} \epsilon_0 d_0^\dagger d_0 + \frac{1}{2} \sqrt{\frac{\eta_0}{\pi}} (d_0 + d_0^\dagger) + \frac{\Delta}{2} P_\pi(0) & 0 \\ 0 & \epsilon_0 d_0^\dagger d_0 - \frac{1}{2} \sqrt{\frac{\eta_0}{\pi}} (d_0 + d_0^\dagger) - \frac{\Delta}{2} P_\pi(0) \end{pmatrix}. \end{aligned} \quad (6.18)$$

The limit of $\alpha \sim \eta_0$ going to infinity renders the terms $\pm \frac{\Delta}{2} P_\pi(0)$ unimportant. In that case, the Hamiltonian \tilde{H}_0 describes a harmonic oscillator with frequency ϵ_0 , displaced by an amount $\sim \pm \sqrt{\alpha}$ in the even/odd parity sector. However, displacing the oscillator does not change its energy and hence the eigenenergies of the even and the odd sector agree in the limit of $\alpha \rightarrow \infty$ leading to a twofold degeneracy. In the same sense the eigenenergies of the original Hamiltonian H_0 for arbitrary values of Δ and U agree in the sectors of even and odd parity as the coupling strength α is sent to infinity. It can be proved numerically, that the ground states are almost degenerate for finite initial values of the parameters Δ and U , where they are small as compared to α .

The localised fixed point spectrum can appear for intermediate iterations in the flow of the system if α is large but still below its critical value. As long as the energy-scales Δ and U are not resolved, the system shows an almost double degeneracy of all states. For couplings $\alpha > \alpha_c$ the system has renormalized the oscillator frequency to zero, and it is no longer able to flow to the delocalised fixed point. Hence, the system stays at one of infinitely many localised fixed points.

Figure 28 shows the flow of the first few eigenenergies within the NRG for the model parameters $\alpha = 1 > \alpha_c$ for $U = 10$ and $\Delta = 10^{-4}$. It demonstrates that the energy of the first excited state drops faster than the expected exponential behaviour $\sim \Lambda^{-N}$ of the rest of the states. Thus, there is no low energy scale that might be resolved at some point in the iterative NRG process. On the contrary, as more and more sites are couple to the chain, the ground state of the system becomes more and more degenerate.

That the ground state and the first excited state indeed belong to different sectors of parity may be checked by calculating the matrix elements ${}_N\langle 0|\hat{n}_b|1\rangle_N$ and ${}_N\langle 0|b|1\rangle_N$ between the ground state and the first excited state of iteration N . While the operator \hat{n}_b does commute with the parity operators $P_\pi(N)$ and thus does not mix the different parity sectors, the operator b does mix these sectors. The destruction of a single particle leads to a difference in the total number of particles of one. This leads to a factor $e^{i\pi} = -1$ when applying $P_\pi(N)$ to that state, making it belong to the opposite parity sector. In figure 29 both ${}_N\langle 0|\hat{n}_b|1\rangle_N$ and ${}_N\langle 0|b|1\rangle_N$ are shown for the model

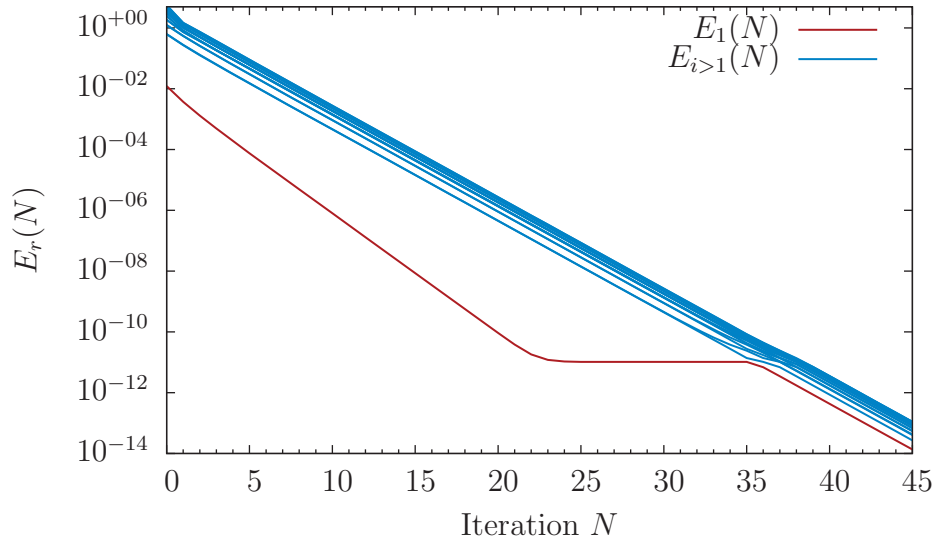
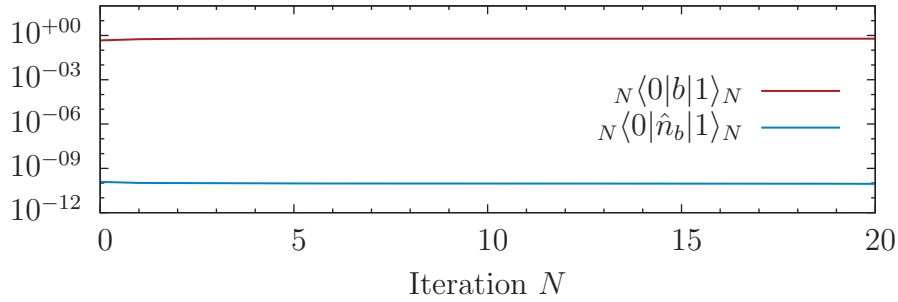


Figure 28:

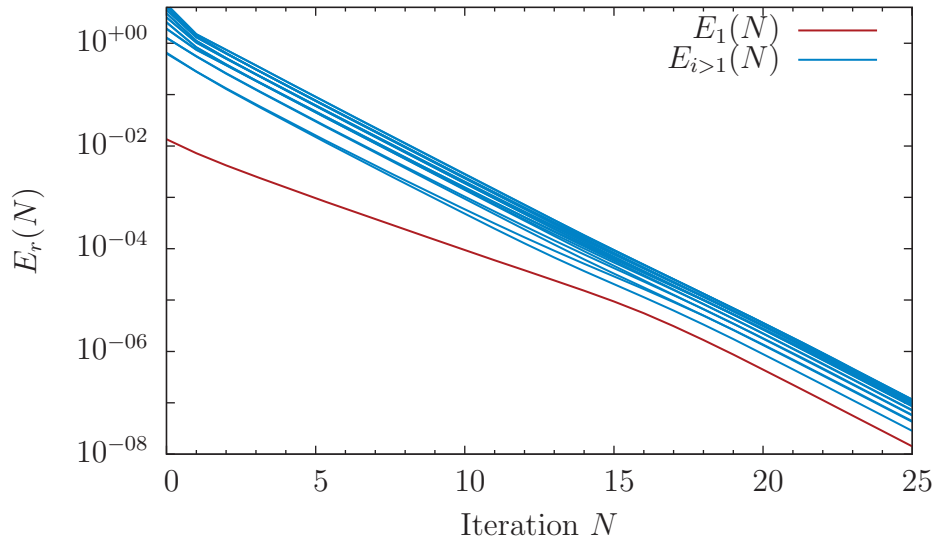
Energy levels obtained from the NRG (blue) for a coupling of $\alpha = 1 > \alpha_c$ for $U = 10$ and $\Delta = 10^{-4}$. The first excited state (red) drops faster than the scale with which the energies in the system can be resolved, i.e. $\propto \Lambda^{-N}$. Thus, the system stays at the fixed point where all states are twofold degenerate. As the energy of the first excited state reaches the order of the numerical resolution (around iteration 22), the flow leads away from the localised fixed point. However, this flow is due to numerical errors that lift the degeneracy. It is not caused by any underlying physics that would pick either of the ground states. The further NRG parameters were: $\Lambda = 2$, $N_{b,imp} = 60$, $N_{b,0} = 60$, $N_b = 16$, $s = 1$, $N_{kept} = 500$.

parameters $\alpha = 1 > \alpha_c$, $U = 10$ and $\Delta = 10^{-4}$. The matrix element ${}_N\langle 0|\hat{n}_b|1\rangle_N$ vanishes numerically, while ${}_N\langle 0|b|1\rangle_N$ obtains a finite value.

Keeping the values for $U = 10$ and $\Delta = 10^{-4}$ fixed and reducing the coupling to $\alpha = 0.6 < \alpha_c(U)$ leads to a significant change in the flow of the first excited level as compared to that in figure 28. There, the energy of the first excited state grows faster than the exponential drop of the general set of states. At iterations where $E_1 \approx E_2$, the system will ultimately flow to the delocalised fixed point (cf. figure 30).


Figure 29:

Matrix elements ${}_N\langle 0|b|1\rangle_N$ and ${}_N\langle 0|\hat{n}_b|1\rangle_N$ for a coupling $\alpha = 1 > \alpha_c$ and the impurity parameters $U = 10$ and $\Delta = 10^{-4}$. The system starts out in the localised phase, where the ground state and the first excited state are close to being degenerate (cf. figure 28). The parity-conserving operator \hat{n}_b vanishes numerically between the states of different parity while the operator b connecting the even and the odd parity sector remains finite suggesting that indeed $|0\rangle$ and $|1\rangle$ live in different parity sectors. The finiteness of ${}_N\langle 0|\hat{n}_b|1\rangle_N$ results from the large sizes of the basis of the H_N that were $N_{\text{kept}} \times N_b = 500 \times 16 = 8000$ together with numerical errors of the order 10^{-14} of each individual basis coefficient.


Figure 30:

Energy levels obtained from the NRG (blue) for a coupling of $\alpha = 0.6 < \alpha_c$ for $U = 10$ and $\Delta = 10^{-4}$. The first excited state (red) drops slower in energy than the resolution in energies that is $\propto \Lambda^{-N}$. As soon as its energy reaches the order of the second excited state, the system flows to the delocalised fixed point. The further NRG parameters were: $\Lambda = 2$, $N_{b,\text{imp}} = 60$, $N_{b,0} = 60$, $N_b = 16$, $s = 1$, $N_{\text{kept}} = 500$.

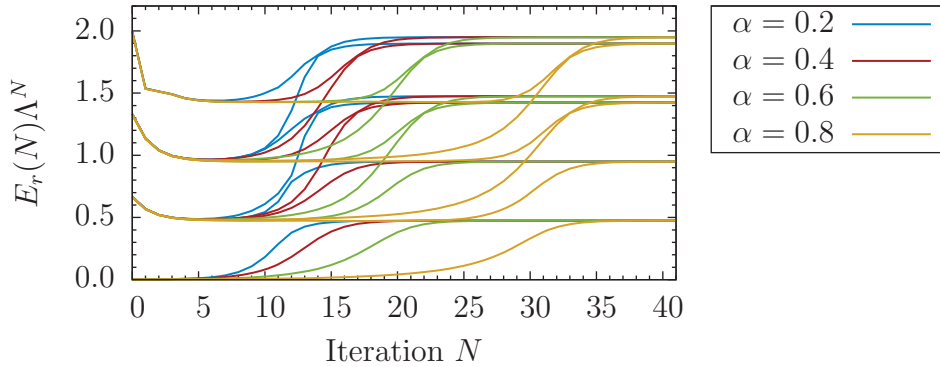
6.1.3. Determination of the phase diagram

It is precisely the aforementioned behaviour of the first excited state that is investigated in this thesis in order to determine the value of the critical coupling α_c for several values of U , as will be done in the following. If the first excited state drops down in energy faster than the resolution Λ^{-N} , the system is understood to be above the critical coupling and the low energy fixed point is a localised fixed point (cf. figure 28). If, however, the first excited state does drop slower or almost as Λ^{-N} , the system will ultimately flow to the delocalised fixed point (cf. figure 30). The point where the system approaches the delocalised fixed point can be pushed to lower energies by increasing the coupling strength α from below α_c .

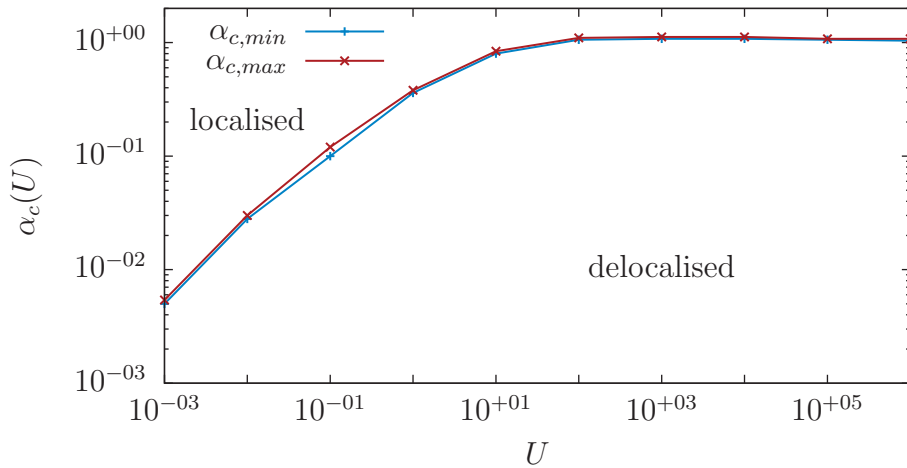
Figure 31 presents the flow of the first six excited energy levels above the ground state for a fixed self-interaction parameter $U = 100$ and an initial impurity oscillator frequency of $\Delta = 10^{-4}$ for several values of the coupling strength $\alpha < \alpha_c$. For a fixed value of the coupling strength α , the bare oscillator frequency Δ is renormalised to smaller values as more and more sites of the chain are coupled within the NRG. As long as the coupling α stays below its critical value, the renormalised oscillator frequency will reach a fixed but finite value $\Delta^*(\alpha)$. $\Lambda^{-N} \sim \Delta^*$ and can be considered large for further iterations leading to the delocalised fixed point with $\Delta^* = \infty$. By increasing the initial coupling strength, the value of $\Delta^*(\alpha)$ will drop to lower values and ultimately to zero once the critical coupling is reached. Once the renormalized $\tilde{\Delta}$ is zero, there is no iteration for which $\Lambda^{-N} \sim \tilde{\Delta}$ holds and the system stays at the localised fixed point with a fixed point value $\Delta^* = 0$.

Bounds on the critical values of α for an ohmic bath are presented in figure 32. For $\alpha_{c,max}$ the first excited state dropped down faster in energy than Λ^{-N} and for $\alpha_{c,min}$ the flow of the system was ultimately still to the delocalised fixed point. The limiting value $\alpha_c(U = \infty) = \alpha_c^{SBM} = 1 + \mathcal{O}\left(\frac{\Delta}{\omega_c}\right)$ for large self-interactions U is clearly identified, which is the literature-value of the critical coupling in the spin-boson model [12]. For small self-interactions it can be inferred that the critical coupling drops to $\alpha_c(U = 0) = 0 + \mathcal{O}\left(\frac{\Delta}{\omega_c}\right)$ as derived in section 6.1.1.

The interpolation between these two limits in terms of the systems energy levels can be tracked in figure 33. The first six energy levels above the ground state are presented for a fixed bare oscillator frequency of $\Delta = 10^{-4}$ and a coupling strength $\alpha = 0.6 < \alpha_c(U)$ below its critical value for several values of the self-interaction U . As the self-interaction U is increased, the scale on which the system flows to the delocalised fixed point is decreased and is thus seen at later iterations. The flow of the energies in the spin-boson model (dashed black lines) can already be matched for a value of $U = 1000$. For larger values of U (yellow and purple lines) numerical errors start to kick in and the flow is again different from that of the spin-boson model. This is most likely due to the large difference in the energy scales $\Delta = 10^{-4}$ and $U \geq 10^4$ in combination with the large number of states $N_{b,imp} = 60$ by which the impurity was


Figure 31:

The first six energy levels above the ground state are plotted for several values of the coupling strength α for a fixed self-interaction parameter $U = 100$ and an impurity oscillator frequency of $\Delta = 10^{-4}$. As the coupling strength approaches the critical coupling $\alpha_c(U = 100) \approx 1.08$ from below, the transition from the intermediate fixed point to the delocalised fixed point is shifted to later iterations and thus to smaller energies. The energy scale at which the transition happens can be identified with the impurity's rescaled oscillator frequency $\Delta^*(\alpha)$ that is suppressed to zero as $\alpha \rightarrow \alpha_c$ from below. The further NRG parameters were: $\Lambda = 2$, $N_{b,imp} = 60$, $N_{b,0} = 60$, $N_b = 16$, $s = 1$, $N_{kept} = 500$.


Figure 32:

Critical coupling α_c as a function of U . In the limit of $U \rightarrow \infty$ the critical coupling becomes that of the spin-boson model where $\alpha_c = 1 + \mathcal{O}(\frac{\Delta}{\omega_c})$. As U decreases to zero, the critical coupling also turns to zero with corrections of the order of $\mathcal{O}(\frac{\Delta}{\omega_c})$. The further NRG parameters were: $\Lambda = 2$, $N_{b,imp} = 60$, $N_{b,0} = 60$, $N_b = 16$, $s = 1$, $N_{kept} = 500$.

described. As $N_{b,imp}$ is lowered with increasing U , the NRG flow of the dissipative harmonic oscillator model and the spin-boson model agree again.

In the next section the impurity's \mathcal{T} -matrix is calculated within the delocalised phase of the system. For the localised phase, such a calculation is beyond reach as the system will eventually pick artificially a unique ground state due to numerical errors and the spectrum of the \mathcal{T} -matrix can not be obtained in the desired frequency range.

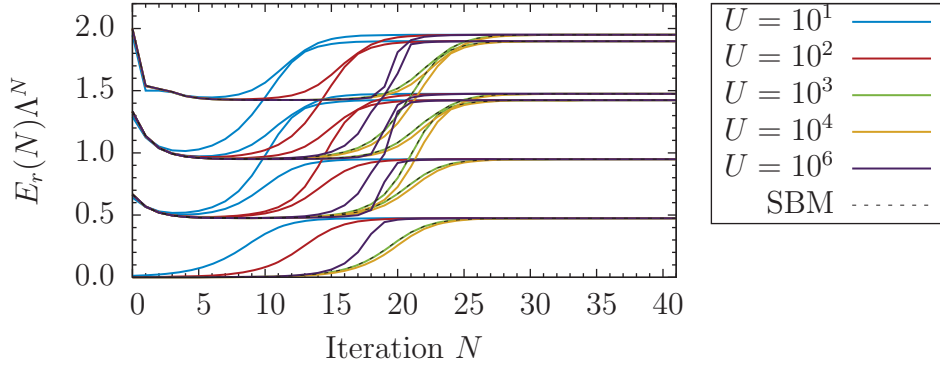


Figure 33:

The first six energy levels above the ground state are plotted for several values of the self-interaction parameter U for a fixed $\alpha = 0.6 < \alpha_c(U)$. Already for $U = 1000$ (green lines) the flow is no longer discernible from that of the spin-boson model (dashed black lines). Larger values of U then lead to numerical errors as the relative difference in energy-scales $U/\Delta \gtrsim 10^7$ becomes large. The further NRG parameters were: $\Lambda = 2$, $N_{b,0} = 60$, $N_b = 16$, $s = 1$, $N_{\text{kept}} = 500$.

6.1.4. Impurity scattering matrix and local averages

In sections 3.4 and 3.5, expressions have been derived to calculate the change of the average site occupation $\langle \hat{n}_x \rangle$ and of the square of the displacement amplitude $\langle (a_x + a_x^\dagger)^2 \rangle$ respectively as a function of the position x in the chain. The scattering or \mathcal{T} -matrix of the impurity

$$\mathcal{T}_{\text{do}}(z) = \frac{\alpha}{4} \langle\langle b + b^\dagger, b + b^\dagger \rangle\rangle_z \quad (6.19)$$

was derived to be the single quantity entering these averages apart from free correlators in the bath. In this section, the spectrum, i. e. the imaginary part of $\mathcal{T}_{\text{do}}(\omega)$ is presented on the real axis for data obtained by means of the NRG. The spectral function corresponding to the scattering matrix in the limit of zero temperature reads (cf. equation (3.16))

$$\lim_{\beta \rightarrow \infty} A_{\mathcal{T}}(\omega, \beta) = \frac{\alpha}{4} \sum_{N=0}^{\infty} \sum_{m=1}^{N_{\text{kept}}} |{}_N \langle 0 | b + b^\dagger | m \rangle_N|^2 [\delta(\omega + (E_0(N) - E_m(N))) - \delta(\omega - (E_0(N) - E_m(N)))] \quad (6.20)$$

for a non-degenerate ground state as can be found in the delocalised phase. The spectrum (6.20) was calculated combining the poles of the different NRG iterations N as described in section 5.4 and broadening them afterwards³.

In the following, the spectra $A_{\mathcal{T}}(\omega)$ are presented for three different values of the self-interaction $U = 10^{-3}, 1, 10^3$, which cover a wide range of the phase-diagram derived in the previous section. The bare oscillator frequency is set to $\Delta = 10^{-4}$ and for the coupling α between impurity oscillator and environment different, appropriate values were chosen. From the full scattering matrices the change of the average site occupation

$$\Delta \langle \hat{n}_x \rangle = \frac{1}{\pi} \int_{-\infty}^0 \text{ImRe}[G_{x,0}^{(0)}(\omega)]^2 \mathcal{T}_{\text{do}}(\omega, T=0) d\omega \quad (6.21)$$

and the change of the squared displacement amplitude

$$\Delta \langle (a_x + a_x^\dagger)^2 \rangle = \frac{1}{\pi} \int_{-\infty}^0 \text{Im}[D_{x,0}^{(0)}(\omega) \mathcal{T}_{\text{do}}(\omega, T=0) D_{0,x}^{(0)}(\omega)] d\omega \quad (6.22)$$

are calculated in their zero-temperature limit that were derived in sections 3.4 and 3.5, respectively. Here, the expression for the change of the average site occupation has been simplified, since the imaginary part of the free propagators $G_{x,0}^{(0)}(\omega) = G_{0,x}^{(0)}(\omega)$ vanishes in the negative frequency domain and they are identical.

³The broadening was performed with the program `broadenVonG` in version V2.0 that was made available to us by Andrew K. Mitchell. It is programmed by Martin Galpin [18] and uses the broadening of Gaussian peaks on a logarithmic scale from Bulla et al. [10] that has also been described in section 5.4. In order to obtain the real part, the program `broadenVonG` performs the integral appearing in the Kramers-Kronig relation 4.25 using the FFT trick pointed out in section 4.3.

Spin-boson limit

For the large self-interaction $U = 10^3$ and small couplings α a single peak is identified in the spectrum $A_{\mathcal{T}}(\omega)$ that corresponds to the oscillator frequency $\Delta = 10^{-4}$. Parameters for the NRG were $\Lambda = 2.0$, $N_{\text{kept}} = 500$, $N_{b,\text{imp}} = N_{b,0} = 60$ and $N_b = 16$ for all chain sites after the first. As the coupling strength α increases, this peak shifts to lower frequencies, corresponding to the reduction of the oscillator frequency Δ to lower values. At the same time, the peak is broadened and its maximal height increases with stronger couplings. This behaviour can be seen in figure 34, where the spectra $A_{\mathcal{T}}(\omega)$ for several couplings α are shown. For small frequencies, the spectrum

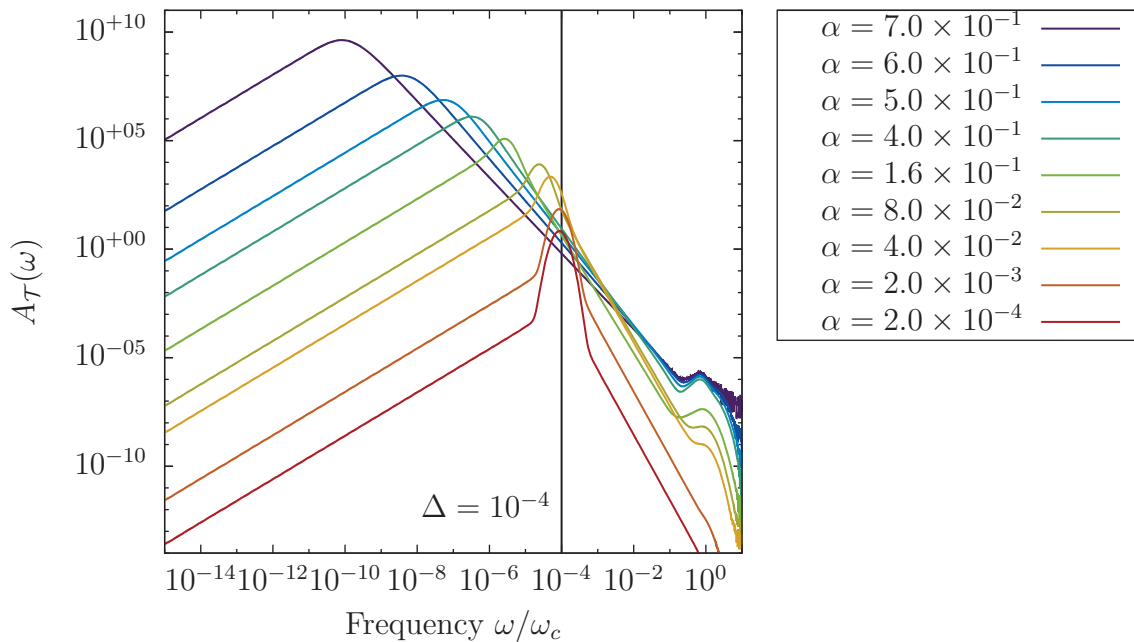


Figure 34:

Spectrum $A_{\mathcal{T}}(\omega)$ for zero temperature in the positive frequency domain for a large self-interaction $U = 1000$. For small couplings to the bath, the peak-like structure of the bare propagator at $\Delta = 10^{-4}$ is almost retained. The broad shape around Δ is due to the broadening parameter $b = 0.5$ that was used in order to get smooth curves for $A_{\mathcal{T}}(\omega)$. As the coupling strength is increased, the peak is shifted to lower frequencies and is broadened. For frequencies well below the peak the spectrum behaves $\sim \omega$. The peaks at the band edge ω_c are negligible, as they are about fifteen orders of magnitude smaller than the mayor peak.

vanishes as $A_{\mathcal{T}}(\omega) \sim \omega$, corresponding to the behaviour of the spin-spin correlation function $C(\omega)$ in the spin-boson model (cf. discussion in [12]). The change of the average site occupation due to the presence of the effective impurity spin is presented

in figure 35 for the same couplings α that were used to calculate the scattering matrix spectra in figure 34 and a large range of distances x from the impurity. In the

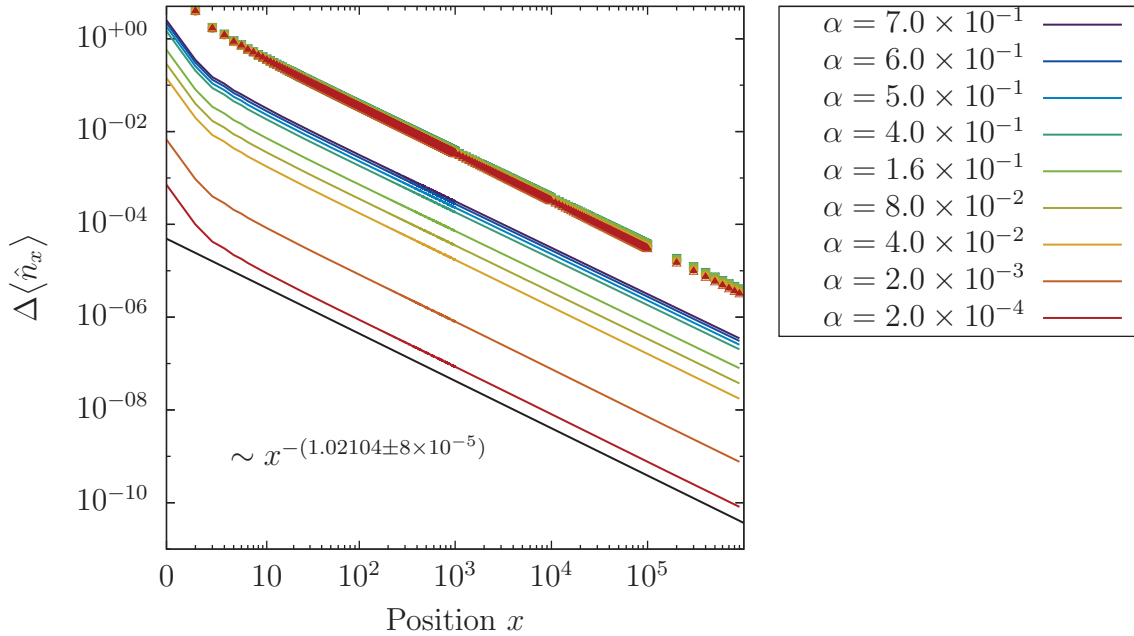


Figure 35:

Change of the average site occupation $\Delta\langle\hat{n}_x\rangle$ in the spin-boson limit of the dissipative oscillator model. Right at the impurity, the change is most significant. In the long distance limit, all curves drop in a power-law manner as $x^{-(1.02104\pm 8\times 10^{-5})}$ (fitted to the curve for $\alpha = 2.0 \times 10^{-4}$, black line). All curves collapse as the coupling $\alpha/4$ is scaled out (coloured dots). Parameters are given in the beginning of the section.

long range limit, all curves drop as $x^{-(1.02104\pm 8\times 10^{-5})}$, and only for the first few sites a deviation from that behaviour can be seen. Furthermore, all curves collapse as the coupling $\alpha/4$ stemming from the scattering matrix is scaled out. This results from the character of the real part of the free propagators $G_{x,0}^{(0)}(\omega)$ entering the integral for the average site occupation. These propagators are mainly evaluated close to zero frequency, where the peak in the scattering matrix spectrum appears. In this range the free propagators vary only slowly and the shift of the broadened peak in the scattering matrix becomes negligible.

The numerical evaluation of the integrals in 6.22 turns out to be stable only for rather small distances x to the impurity. The displacement-displacement correlation functions $D_{x,0}^{(0)}(\omega)$ in the environment are oscillating stronger close to zero frequency. Hence, for larger values of x , they are highly sensitive to the peak stemming from the scattering matrix. Figure 36 shows the results obtained for the change in the

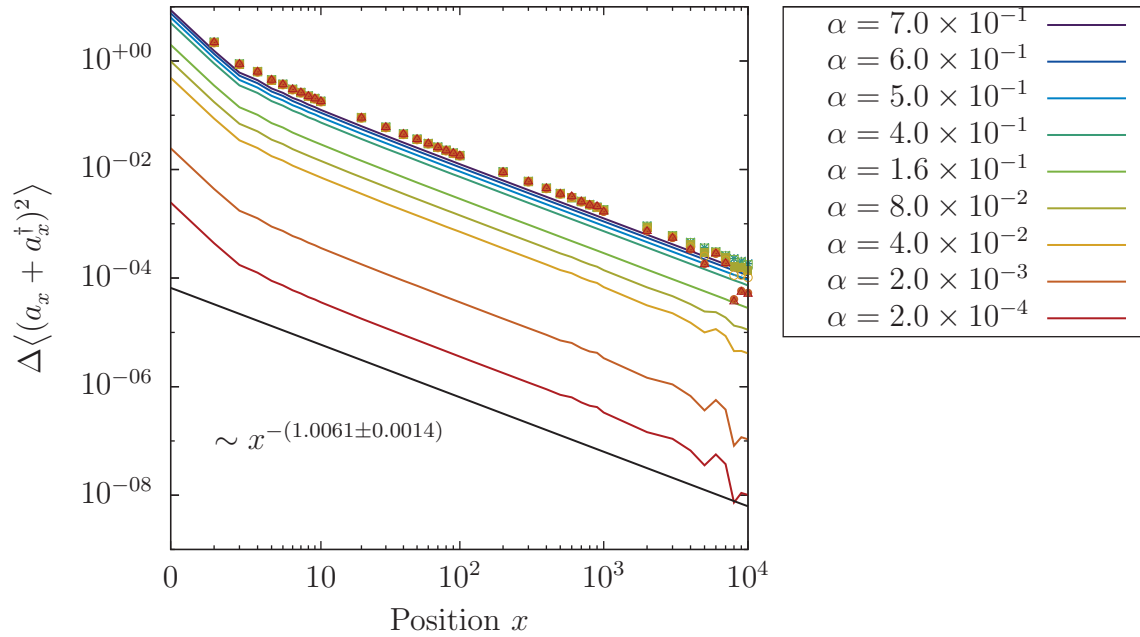


Figure 36:

Change of the average displacement amplitude of the oscillators in the environment due to the coupling of an effective spin-1/2 impurity. For small couplings $\alpha < 0.1$ large fluctuations can be seen on distances $x \approx 10000$. Apart from the fluctuations, all curves collapse to a single one (coloured symbols). A fit of the curve for $\alpha = 0.7$ reveals a power-law behaviour $\sim x^{-(1.0061 \pm 0.0014)}$ (black curve). Parameters are given in the beginning of the section.

square of the displacement amplitude due to the presence of the effective spin-1/2 impurity. For large couplings which are still below the critical value $\alpha_c \approx 1$, rather broad peaks appear in the scattering matrix. There the change $\Delta \langle (a_x + a_x^\dagger)^2 \rangle$ shows again a power-law drop like $x^{-(1.0061 \pm 0.0014)}$ far away from the impurity. In case of very small couplings, the original peak at $\Delta = 10^{-4}$ is still sharp. There the numerical evaluation of integral 6.22 leads to large fluctuations. Apart from the fluctuations at large distances $\approx 10^4$ and small couplings α , the curves again collapse upon rescaling.

Intermediate self-interaction regime

The same calculations as before are repeated in case of an intermediate self-interaction $U = 1$ of the impurity oscillator. Now, the self-interaction is of the same order as the high-frequency cutoff ω_c in the environment and the spectrum of the scattering matrix reveals two peaks (cf. figure 37). One peak can be assigned to the energy-scale U that appears around its initial value for all couplings α investigated. The second

peak is initially again at the bare oscillator frequency $\Delta = 10^{-4}$. Therefore, it can be identified with the impurity oscillator. This peak is shifted first to larger values as the coupling to its environment is increased. At the same time, there appears some weight in the flanks of both peaks. Only for large couplings $\alpha \gtrsim 0.3$ the peak is broadened and shifted to lower frequencies, like in case of the spin-boson limit. The richer structure

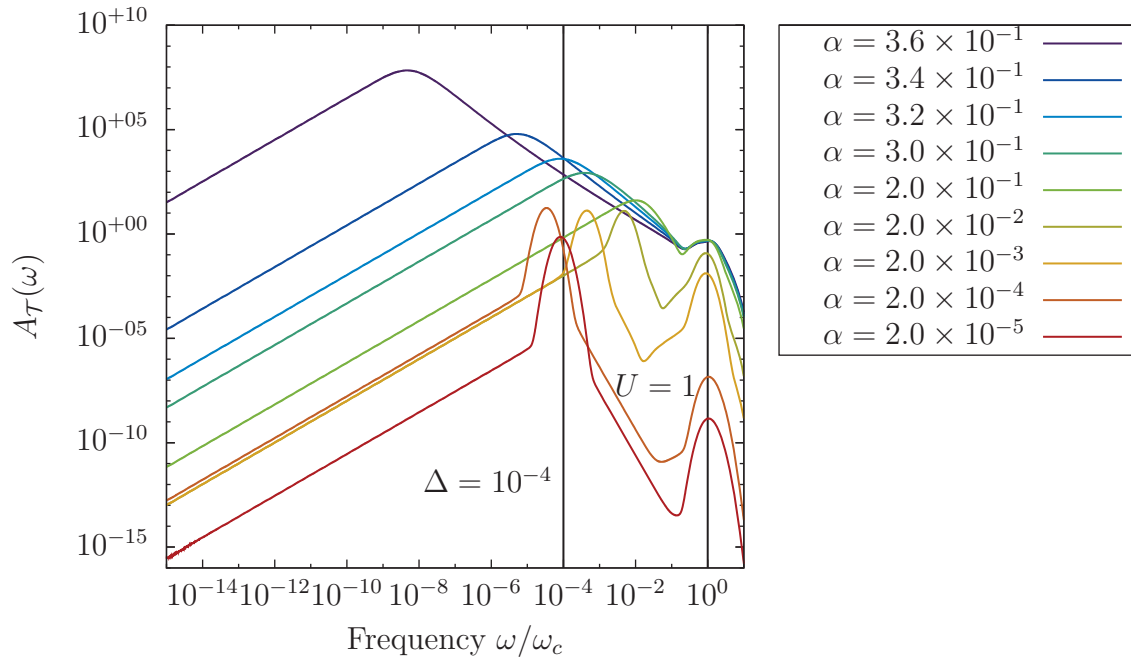


Figure 37:

Spectrum of the scattering matrix for a self-interaction $U = 1$ and several couplings $\alpha < \alpha_c(U)$. Two peaks can be identified that can be assigned to the bare parameters $\Delta = 10^{-4}$ and $U = 1$ (vertical lines). The behaviour of the peak associated to the oscillator frequency is more intricate than in to the spin-boson limit. Also, features in the flanks of the two dominant peaks arise. Parameters are given in the beginning of the section.

in the scattering matrix directly enters the zero temperature averages $\Delta \langle \hat{n}_x \rangle$ and $\Delta \langle (a_x + a_x^\dagger)^2 \rangle$ as can be seen in figures 38 and 39, respectively. In the average site occupation, there appear again power-laws x^{-1} in the limit of large and small couplings with small corrections in the exponent. A fit for a large coupling $\alpha = 0.36$, e. g. results in a power-law $\sim x^{-(1.00909 \pm 0.00013)}$. However, in the intermediate regime, where the peak at $\omega = 1$ dominates, there appears a faster drop of $\Delta \langle \hat{n}_x \rangle$ for intermediate distances $10^2 < x < 10^6$. This drop basically follows the amount of weight that the real part of the free propagators $G_{x,0}^{(0)}(\omega)$ contributes around that frequency. In the change of the average displacement amplitude appears a transition from a power-law drop for

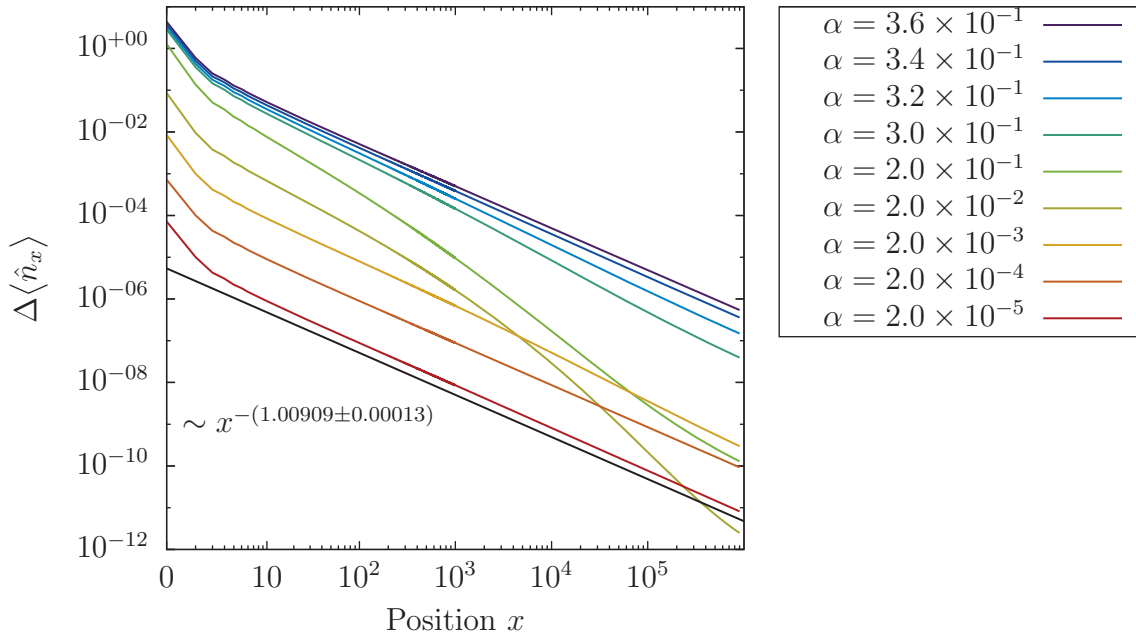


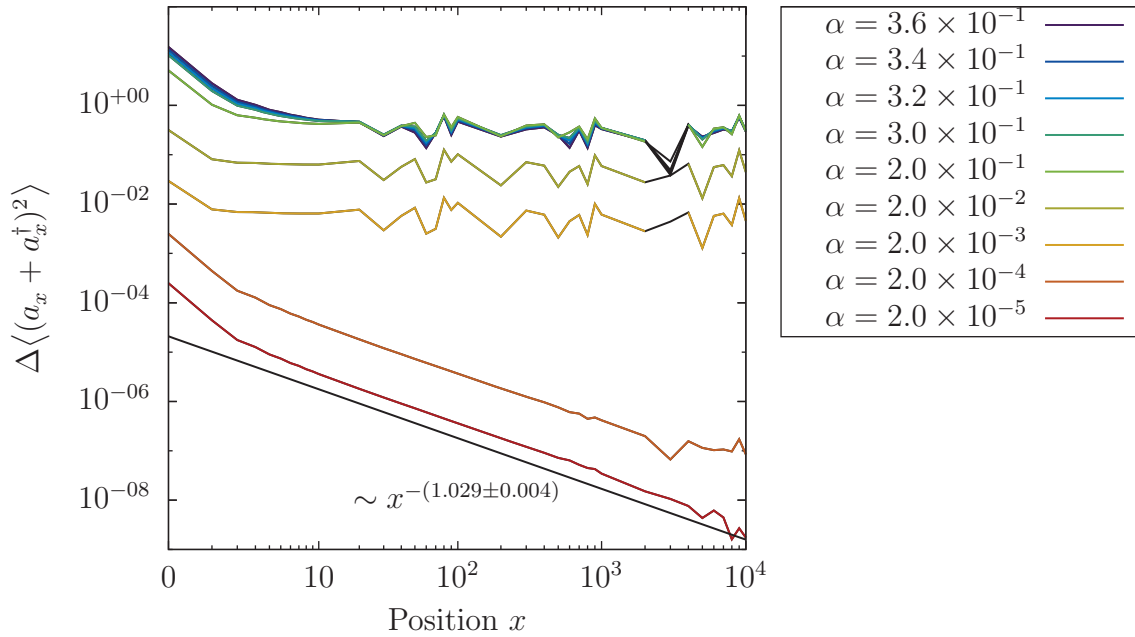
Figure 38:

Change of the average site occupation in the chain due to the presence of the oscillator impurity. Small and intermediate couplings lead to power-law drops of $\Delta\langle\hat{n}_x\rangle$. In the intermediate regime of $\alpha \sim 0.1$ the peak in the scattering matrix right at the band edge $\omega = \omega_c$ dominates. The drop occurs faster than x^{-1} as the free bath propagators $G_{x,0}^{(0)}(\omega)$ are small in that regime. Parameters are given in the beginning of the section.

small couplings, which follows $\Delta\langle(a_x + a_x^\dagger)^2\rangle \sim x^{-(1.029 \pm 0.004)}$, to a constant behaviour (apart from fluctuations around a constant mean-value). The latter behaviour was also observed in the analytic discussion of the $U = 0$ case. There, all oscillators far away from the impurity show an average extra amount of displacement, which is proportional to $\sqrt{\alpha}$.

Weak self-interaction regime

In the regime, where the energy-scales $\Delta = 10^{-4}$ of the bare oscillator frequency and its self-interaction strength $U = 10^{-3}$ become comparable, the impurity scattering matrix again features mainly two peaks. The lower energy peak can still be identified with a renormalized oscillator frequency, since it is suppressed towards lower frequencies and its shape becomes broadened as the coupling to the environment α is increased (cf. figure 40). The second, higher energy peak, in the imaginary part of the scattering matrix is shifted to an energy $\omega \approx 0.01\omega_c$ when approaching the


Figure 39:

Change of the average displacement amplitude for a self-interaction $U = 1$. Only for weak couplings the power-law drop $\sim x^{-(1.029 \pm 0.004)}$ can be seen. For intermediate and large couplings between impurity and environment, all bath oscillators far away from the impurity are displaced by a significant amount that is $\sim \sqrt{\alpha}$. Here, the fluctuations are large and eventually lead to negative values. The regions of negative changes in the displacement amplitude are coloured black. Parameters are given in the beginning of the section.

critical coupling strength $\alpha_c(U = 10^{-3}) \approx 5.2 \times 10^{-3}$ from below. Many different low-energy states on the impurity are mixed due to their coupling to the environment. As a result, for intermediate couplings between impurity and environment, the effective impurity states entering the scattering matrix show no clear trend in the location of the main excitations on the impurity. The change of the average site occupation $\Delta \langle \hat{n}_x \rangle$ in the environment features again mainly a power-law behaviour x^{-1} for all values of the coupling strength (cf. figure 41). As the low-energy peak, corresponding to the renormalized oscillator frequency, is dominant in the spectrum of the scattering matrix, the bare bath propagators $G_{x,0}^{(0)}(\omega)$ are mainly evaluated close to zero frequency. For the change of the average oscillator displacement amplitude $\Delta \langle (a_x + a_x^\dagger)^2 \rangle$ in the environment, we obtain again a power-law behaviour x^{-1} for intermediate distances $5 < x < 300$ in case of all investigated values of the coupling parameter α (cf. figure 42). Only at larger distances, the average displacement seems

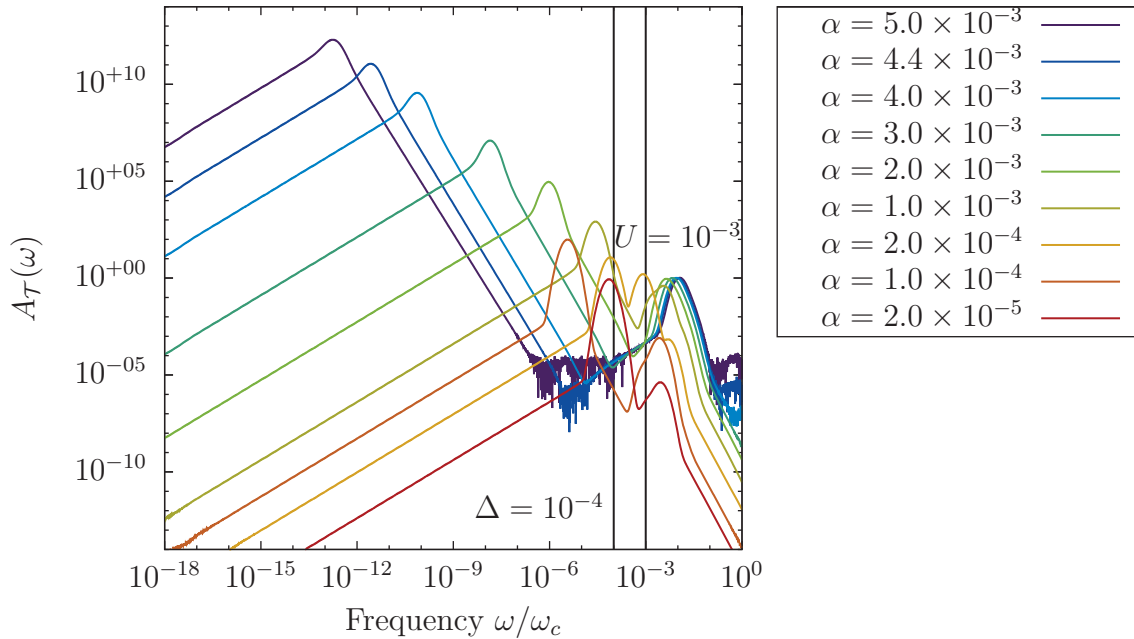
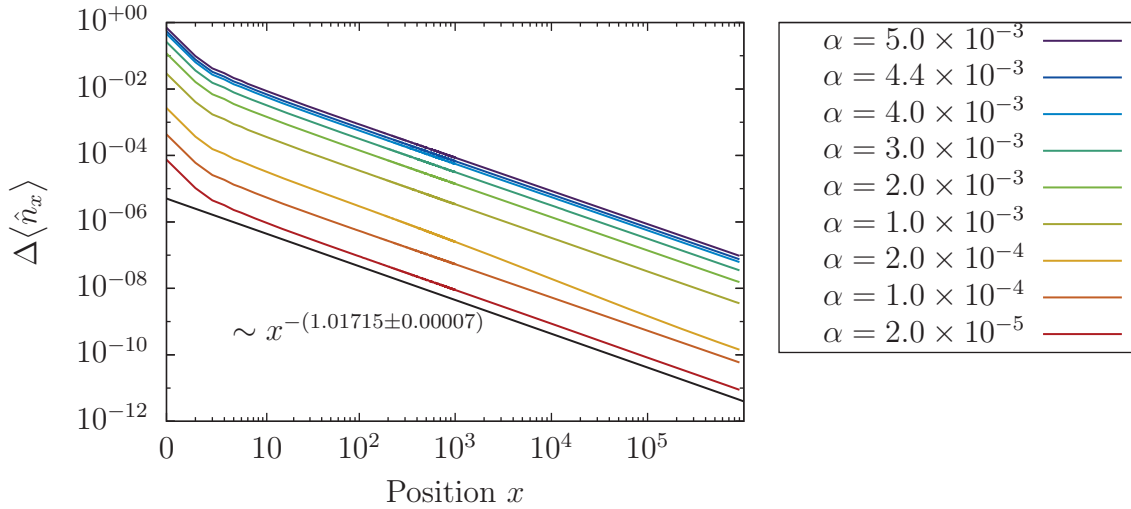


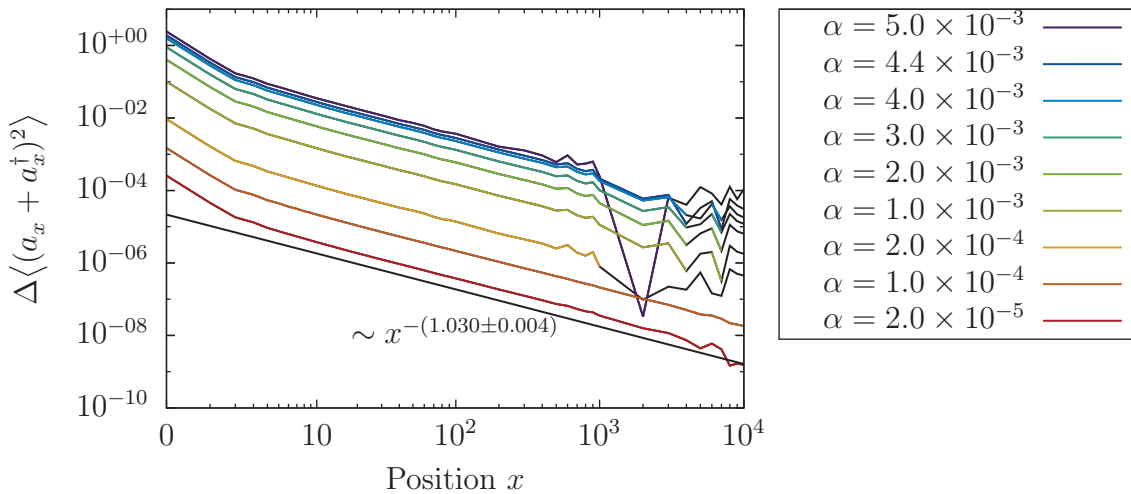
Figure 40:

For very weak self-interaction $U = 10^{-3}$, the spectrum of the scattering matrix shows again mainly two peaks. While one of them is suppressed and broadened in the limit of large couplings, the other one is pushed to a frequency $\omega \approx 0.01 \omega_c$. For weak couplings no clear trend for the behaviour of the different peaks is visible. Parameters are given in the beginning of the section.

to be increased by a constant amount with fluctuations around that constant. To what extent these fluctuations can be suppressed by increasing the numerical precision in the evaluation of the integral (6.22) needs to be investigated in the future.


Figure 41:

Change of the average site occupation for several couplings α . Since the low-energy peak in the spectrum of $\mathcal{T}_{\text{do}}(\omega)$ always dominates, the drop in $\Delta\langle\hat{n}_x\rangle$ is $\sim x^{-1}$ for all couplings. A fit of the curve for $\alpha = 2 \times 10^{-5}$ reveals a power-law of $x^{-(1.01715 \pm 0.00007)}$ (black line). Parameters are given in the beginning of the section.


Figure 42:

Change of the average displacement amplitude of the environmental oscillators. For weak couplings, the drop is again in a power-law manner as $\sim x^{-(1.030 \pm 0.004)}$ (black line). At intermediate and strong coupling between bath and impurity, the displacements turn eventually into a constant behaviour with fluctuations around a constant mean value for large distances to the impurity. Parameters are given in the beginning of the section.

6.1.5. Conclusion

Within this work, a new bosonic two-channel Numerical Renormalization Group method has been implemented. It makes use of a Lanczos diagonalisation routine from the ARPACK [28] and uses a sparse matrix storage format to handle the large-dimensional matrices appearing in models with more than one channel.

The NRG implementation itself has been devised to study the two-spin-boson model considered in this thesis, as well. Before applying the method to the full two-spin-boson model, it was tested on a simpler single-channel model, namely the dissipative oscillator model. This model provides an easily accessible limit for an infinite value of the self-interaction on the impurity oscillator, i.e. the spin-boson model. In its application to the dissipative oscillator model, the NRG implementation has proven trustworthy, as the spin-boson limit could be retained.

Apart from the known limits of zero and infinite self-interaction of the impurity oscillator, the investigations within this work revealed a whole line of quantum phase transitions for finite values of the self-interaction. The transition line separates a delocalised phase, where the impurity is free to oscillate with an average displacement of zero, and a phase where it is localised far away from its potential minimum.

Furthermore, it was investigated whether the presence of the impurity oscillator influences its environment on a typical length scale. Such a length scale can e.g. be identified in case of an exponential behaviour of the distance dependent averages calculated in the environment. The change of the average site occupation drops in a power-law fashion in all investigated situations. Hence, in this case no typical length scale exists in the investigated region. As a second signal, the change of the average oscillator displacement in the environment was calculated. This average proved to be very sensitive both to the model parameters investigated and the numerical evaluation of relevant integrals. In the spin-boson limit power-law behaviour was observed. For intermediate and small values of the impurity's self-interaction, fluctuations around a constant displacement occur at intermediate to long distances.

Whether the fluctuations in the change of the average displacement amplitude are due to numerical issues or stemming from the physical nature of the model needs to be investigated in the future⁴. If they can be assigned to numerical issues and a constant change of the oscillator displacement far away from the impurity occurs, indeed a length scale can be identified, where the initial drop in the signal close to the impurity vanishes.

Since the implementation of the NRG method itself proved successful, it is applied to the two-spin-boson model in the following.

⁴For the numerics, there are mainly two sources of possible errors that need to be addressed. The first one is the resolution with which the free environmental correlation functions can be calculated, as they show strong oscillatory behaviour for large distances to the impurity. A second source of error may result for intermediate values of the self-interaction parameter from the simple combination of the NRG data from different iterations to single spectral functions, where no clear trend for the impurity's spectral function was visible.

6.2. Two-spin-boson model

The two-spin-boson model is investigated in this thesis with the NRG method. To this end, a two-channel bosonic NRG was devised and implemented. The results are presented in the following. Within the NRG, different fixed points show up in the flow of the Hamiltonians. These fixed points are classified and discussed in the following. First, results for zero inter-impurity distance from the literature are summarized, which allow an understanding of the fixed points observed at finite inter-impurity distances. For different model parameters, the impurities' scattering matrix is calculated and from that the changes of local averages in the environment. Both, the change of the average site occupation and that of the average displacement amplitude show strong peaks at the sites to which the impurities are coupled. The changes are found to decrease in a power-law manner like x^{-1} as the distance to the impurities is increased. Between the impurities, these changes drop to a finite amount, that is comparably large.

6.2.1. Identification of fixed points

The different fixed points H^* of the Numerical Renormalization Group mapping $R(H)$, now in case of the two-spin-boson model, are identified and discussed. The Hamiltonian of the two-spin-boson model was derived in section 5.3 to read

$$H_{2\text{sbm}}^{\text{chain}} = H_{\text{imp}} + \sum_{s=e,o} \sqrt{\frac{\eta_{0,s}}{\pi}} \sigma_{z,s} (d_{0,s} + d_{0,s}^\dagger) + H_e^{\text{chain}} + H_o^{\text{chain}} \quad (6.23)$$

where the impurities were described by

$$H_{\text{imp}} = \sum_{s=e,o} \sigma_{x,s} \Delta_s + \sigma_{z,s} \varepsilon_s + \frac{K}{4} (\mathbf{1}_e - \mathbf{1}_o). \quad (6.24)$$

to the even and the odd chain which read

$$H_s^{\text{chain}} = \sum_{n=0}^{\infty} \left[\epsilon_{n,s} d_{n,s}^\dagger d_{n,s} + t_{n,s} (d_{n+1,s}^\dagger d_{n,s} + d_{n,s}^\dagger d_{n+1,s}) \right], \quad s = e, o. \quad (6.25)$$

Here the on-site energies $\epsilon_{n,s}$ and nearest-neighbour hopping amplitudes $t_{n,s}$ both drop off exponentially as $\sim \Lambda^{-n}$ for the two baths. The renormalisation group mapping

$$H_{N+1} = R(H_N) \quad (6.26)$$

is given by

$$H_{N+1} = \Lambda H_N + \Lambda^N \sum_{s=e,o} \left[\epsilon_{N+1,s} d_{N+1,s}^\dagger d_{N+1,s} + t_{N,s} (d_{N+1,s}^\dagger d_{N,s} + d_{N,s}^\dagger d_{N+1,s}) \right]. \quad (6.27)$$

The initial Hamiltonian H_0 features the two impurities that are coupled to the zero orbitals of both chains:

$$H_0 = H_{\text{imp}} + \sum_{s=e,o} \left[\sqrt{\frac{\eta_{0,s}}{\pi}} \sigma_{z,s} (d_{0,s} + d_{0,s}^\dagger) + \epsilon_{0,s} d_{0,s}^\dagger d_{0,s} \right]. \quad (6.28)$$

In the limit of $N \rightarrow \infty$, the series of the H_N converges to the full Hamiltonian (6.23) as

$$H_{2\text{sbm}}^{\text{chain}} = \lim_{N \rightarrow \infty} \Lambda^{-N} H_N. \quad (6.29)$$

In the following the discussion is restricted to two impurities, which are considered identical, and only see a magnetic field Δ in x -direction. Here, the interaction between them is mediated only by the common environment. The original bosonic chain is chosen to feature an ohmic dissipation. First the different fixed points and corresponding phases in case of zero inter-impurity distance R of the two-spin-boson model are briefly discussed. Those results have been obtained before by Orth et al. [41] and the author of this work [24], and are summarised here to allow a comparison with the results obtained in this work for finite inter-impurity distances $R > 0$.

6.2.2. Zero inter-impurity distance

For a distance $R = 0$ between the two spin-1/2 impurities, a rather simple single bath NRG can be applied as there are no odd excitations to which the impurities might couple (cf. equations (4.18) and (4.19) for the even- and odd-bath spectral functions). Hence, the two spins see the exact same environment as they couple to the same site of the linear chain and thus only a single bath has to be incorporated into the NRG.

Free impurity fixed point at zero distance

In the simplest case, the magnetic field Δ as well as the coupling to the chain α are set to zero. This leads to a simple fixed point H_{fi}^* , given by the free chain fixed point Hamiltonian $H_{\text{chain}}^*(N) = H_{\text{chain}}^{(0)}(N)$ (cf. equation (6.15)) and either of the four states $|\uparrow\uparrow\rangle$, $|\uparrow\downarrow\rangle$, $|\downarrow\uparrow\rangle$ or $|\downarrow\downarrow\rangle$ of the impurities. The subscript fi denotes the free impurity fixed point. As all impurity states are degenerate, the fixed point features the free chain spectrum where each state is fourfold degenerate. For finite values of the magnetic field Δ , this fixed point can still be identified in the flow of the energy-spectra $E_r(N)$, as long as the coupling α is small and the energy scale Δ has not yet been resolved. The four eigenstates and corresponding energies on the impurity in case of a finite magnetic field Δ are given by

$$|v_1\rangle = \frac{1}{2} [|\uparrow\uparrow\rangle + |\downarrow\downarrow\rangle - |\uparrow\downarrow\rangle - |\downarrow\uparrow\rangle], \quad E_1 = -\Delta, \quad (6.30)$$

$$|v_2\rangle = \frac{1}{\sqrt{2}} [|\uparrow\uparrow\rangle - |\downarrow\downarrow\rangle], \quad E_2 = 0, \quad (6.31)$$

$$|v_3\rangle = \frac{1}{\sqrt{2}} [|\uparrow\downarrow\rangle - |\downarrow\uparrow\rangle], \quad E_3 = 0, \quad (6.32)$$

$$|v_4\rangle = \frac{1}{2} [|\uparrow\uparrow\rangle + |\downarrow\downarrow\rangle + |\uparrow\downarrow\rangle + |\downarrow\uparrow\rangle], \quad E_4 = \Delta. \quad (6.33)$$

The free impurity fixed point is typically reached for early iterations if the initial Δ is much smaller than one. In figure 43 a) the rescaled energy-spectra $E_r(N)$ are shown for a value of $\Delta = 10^{-4}$ and a coupling strength of $\alpha = 10^{-5}$. The fourfold degeneracy of the energy-levels is lifted, once the energy scale Δ is resolved in iteration N where $\Delta \sim \Lambda^N$ is satisfied. There the zero temperature fixed point is that of a free chain with the impurity in its single ground state. For early iterations, the system is at the free impurity fixed point where all impurity states are thermally accessible.

Delocalised fixed point at zero distance

The coupling of the impurities to their environment can cause a reduction of the energy scale Δ , felt by the impurities. This behaviour also occurred in the dissipative oscillator model. As long as the coupling α of the impurities to the chain is small, Δ is rescaled to a smaller but finite value $\tilde{\Delta} > 0$. Here the system flows to a fixed point with a free chain and the impurities in their common ground state. Once the rescaled energy scale $\tilde{\Delta}$ is resolved in the NRG, it is considered large in all further iterations. The fixed point value Δ^* is infinite and the coupling strength α^* at the fixed point is zero. The delocalised fixed point Hamiltonian can thus be gained by setting $\Delta = \infty$ and $\alpha = 0$, leading to

$$H_{del}^*(N) = |v_1\rangle\langle v_1| \otimes H_{chain}^*(N) \quad (6.34)$$

with the free chain $H_{chain}^*(N)$ (cf. (6.15)) and the impurities in a common ground state $|v_1\rangle$. In figure 43 the flow of the energy-levels is shown for zero distance between the impurities, an initial magnetic field $\Delta = 10^{-4}$ and several values of the coupling strength α . In sub-figures a) and b) there remains a finite magnetic field $\tilde{\Delta}$ as long as $\alpha < \alpha_c$. As the coupling strength is increased from a) to b), the value of $\tilde{\Delta}$ is lowered and thus resolved later in the flow of the energy-levels. Also, an intermediate fixed point is reached where all states are doubly degenerate. For large couplings $\alpha > \alpha_c$, the delocalised fixed point cannot be reached any longer and all states remain doubly degenerate (figure 43 c)). There the system remains at one of infinitely many localised fixed points.

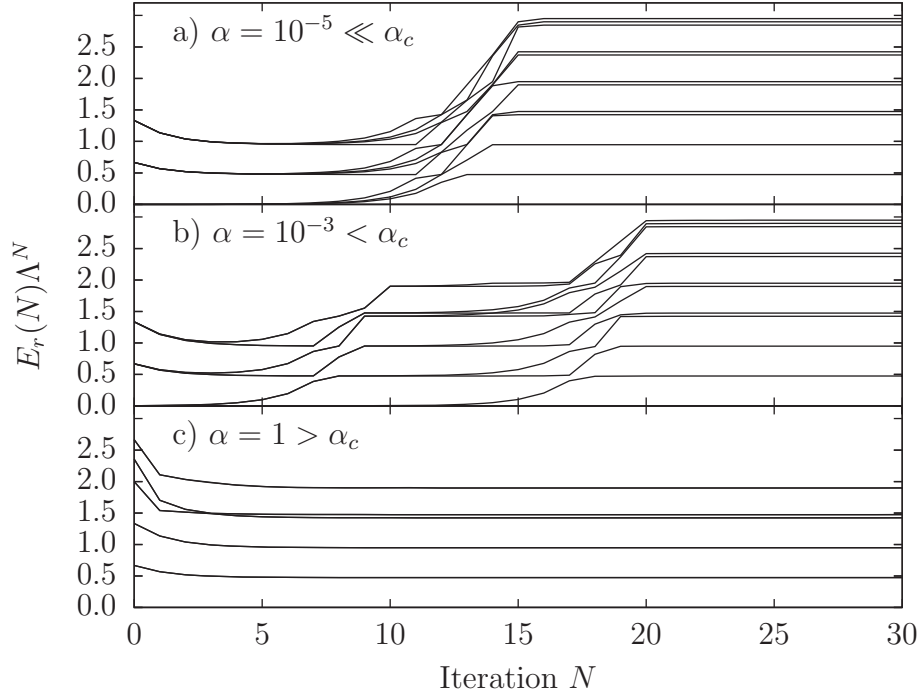


Figure 43:

Energy flow of the first eleven states above the ground state as obtained from the NRG for zero distance of the impurities, an initial tunnelling rate $\Delta = 10^{-4}$ and different values of the coupling strength α . In subfigure a) the flow is directly from the free impurity fixed point to the delocalised fixed point around iteration 12, where the energy scale Δ is resolved. As the coupling strength is increased from a) to b), there are two effects. First of all the initial tunnelling rate Δ is renormalised to a lower value. Second, an additional fixed point is found at intermediate iterations. It is one of infinitely many localised fixed points, where all eigenstates of the free chain are twofold degenerate. Subfigure c) depicts the situation where the initial coupling strength α is large enough to renormalise the tunnelling rate Δ to zero and the system remains at the localised fixed point. The chain couples only to the states $|\uparrow\uparrow\rangle$ and $|\downarrow\downarrow\rangle$, where it induces a ferromagnetic interaction favouring these configurations above the anti-ferromagnetic ones. Thus, the two states span the impurities Hilbert-space at the localised fixed point. Further NRG parameters were $\Lambda = 2.0$, $N_{\text{kept}} = 500$, $N_{b,e}(0) = 800$ and $N_{b,e} = 16$.

Localised fixed points at zero distance

In case of zero distance between the two impurities, only the even spin combinations $|\uparrow\uparrow\rangle$ and $|\downarrow\downarrow\rangle$ couple to the chain. As Orth et. al. discussed in [41], a finite coupling α of the impurities via their z -components to a common environment leads to a renormalisation of the bare Ising coupling strength $\tilde{K} = K - 2\alpha\omega_c(s+1)/s$ due to an indirect ferromagnetic interaction stemming from coherent phonon exchange between the impurities. Here, s is again the power-law exponent of the bath spectral function. Thus, for an initial value of $K = 0$ the anti-parallel spin configurations $|\uparrow\downarrow\rangle$ and $|\downarrow\uparrow\rangle$ are penalised by an energy $\sim \alpha$. If the initial coupling strength α is larger than a critical value α_c , the tunnelling rate Δ of the impurities gets renormalised to zero while their coupling to the environment remains finite. Exactly at the localised fixed point the tunnelling rate Δ is zero and the Hamiltonian in the basis $\{|\uparrow\uparrow\rangle, |\downarrow\downarrow\rangle, |\uparrow\downarrow\rangle, |\downarrow\uparrow\rangle\}$ reads

$$\begin{aligned}
H_{2\text{sbm}}^{\text{chain}} = & |\uparrow\uparrow\rangle\langle\uparrow\uparrow| \left[-\frac{\alpha\omega_c(s+1)}{2s} + 2\sqrt{\frac{\eta_0}{\pi}}(d_0 + d_0^\dagger) \right] \\
& + |\downarrow\downarrow\rangle\langle\downarrow\downarrow| \left[-\frac{\alpha\omega_c(s+1)}{2s} - 2\sqrt{\frac{\eta_0}{\pi}}(d_0 + d_0^\dagger) \right] \\
& + \frac{\alpha\omega_c(s+1)}{2s} \left[|\uparrow\downarrow\rangle\langle\uparrow\downarrow| + |\downarrow\uparrow\rangle\langle\downarrow\uparrow| \right] \otimes \mathbb{1}_{\text{bos}} + \mathbb{1}_{\text{imp}} \otimes H_{\text{chain}}^{(0)} \quad (6.35)
\end{aligned}$$

where the renormalisation of the Ising coupling K has already been taken into account. The low energy sector of the theory is found in the ferromagnetic impurity sector, spanned by the spin configurations $|\uparrow\uparrow\rangle$ and $|\downarrow\downarrow\rangle$. As the coupling strength α remains finite, there is a whole line of fixed points with fixed point values of $\alpha^* \in (0, \infty)$ and $\Delta^* = 0$ as in the spin-boson model. Within the two-dimensional ferromagnetic impurity sector, the coupling of the impurities to the chain leads to a positive/negative displacement of the harmonic oscillators in the Wilson-chain and the displacement is proportional to the coupling strength $\sqrt{\alpha}$. Since positive and negative displaced oscillators have the same energy, the fixed point spectrum of the Hamiltonian is twofold degenerate (cf. figure 43 c).

6.2.3. Finite inter-impurity distances

For finite distances R between the impurities an investigation of the flow of the energy-spectra $E_r(N)$, obtained from the bosonic two-channel NRG, reveals the same kind of fixed points as for zero distance. However, the fixed point spectra look different from the single channel model that was investigated for $R = 0$, since there are two chains, each with their own spectrum.

Free impurity fixed point at finite distances

For very small couplings between impurities and environment, the impurities remain almost unaffected and they form the eigenstates $|v_1\rangle, \dots, |v_4\rangle$ with corresponding eigenenergies as given in equations (6.30) - (6.33). The single energy scale on the impurities is the bare tunnelling rate Δ , which can be resolved for all investigated distances $R = 1, \dots, 1000$ between the impurities within the flow of the eigenspectrum $E_r(N)$. The free impurity fixed point is that of the two chains, where now each state is fourfold degenerate and the chains form the fixed point

$$H_{chain}^*(N) = H_e^{chain}(N) + H_o^{chain}(N). \quad (6.36)$$

It appears in early iterations of the NRG as long as the scale Δ has not been resolved (cf. figure 44). The spectra of the even and the odd chain turn out to be similar in early iterations for large distances R between the impurities. There the highly oscillating characters of the even and the odd spectral functions are averaged out to almost identical chain parameters $\epsilon_{n,e/o}$ and $t_{n,e/o}$, as both the sine and the cosine lead to similar averages. The point at which the two chain spectra start to differ is decreased to lower frequencies, and thus later NRG iterations, as the distance R between the impurities is increased.

Delocalised fixed point at finite distances

At the delocalised fixed point, the spectrum is that of the free chains (6.36), where the impurities form a common, single ground state. Due to the coupling to the chain, the tunnelling rate Δ is renormalised to a smaller, but finite value $\tilde{\Delta}$. Once this energy scale is resolved in the NRG, the system flows to the delocalised fixed point, as all higher energetic impurity states are projected out of the model. The effective coupling strength between the common impurity states and the even and the odd chain decreases with increasing distance R between the impurities. This behaviour can be traced in figure 45 for a coupling between impurities and environment of $\alpha = 10^{-2}$. The energy scale, at which the renormalised tunnelling rate $\tilde{\Delta}$ can be identified, is resolved in earlier iterations for larger distances. For $R \approx 1000$, the tunnelling frequency is almost unaffected and eventually turns larger than the energy scale at which the two environments start to differ in their behaviour. Thus, for distances much larger than 1000 lattice sites we expect the flow to be again directly from the free impurities fixed point to the delocalised fixed point. There further calculations need to verify this expected behaviour.

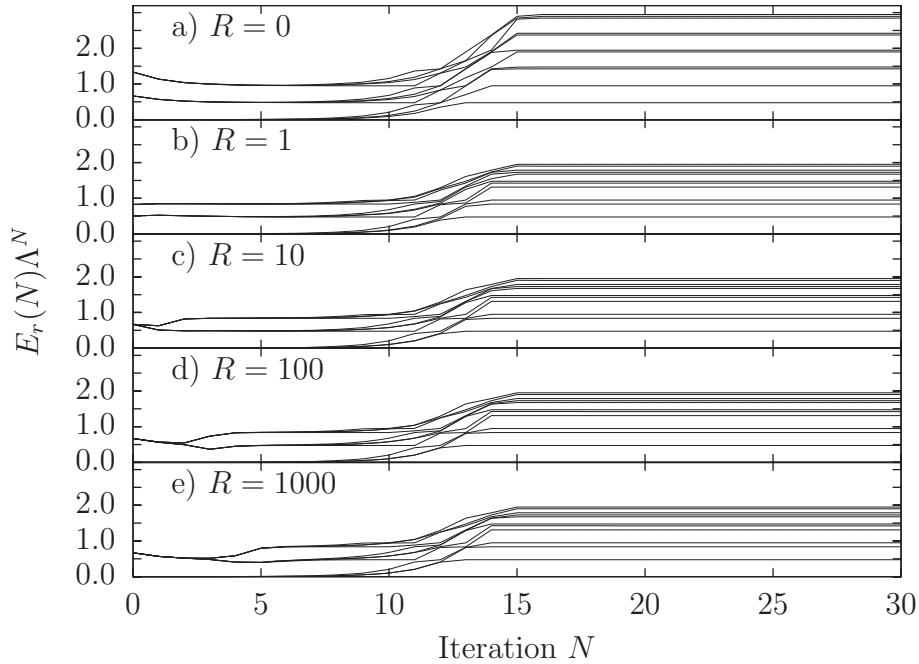


Figure 44:

Energy flow of the first eleven states above the ground state for a coupling of $\alpha = 10^{-5}$ for several distances R of the impurity-spins. The tunnelling rate $\Delta = 10^{-4}$ is almost not affected by the bath and is resolved around the same iteration for all distances. In early iterations, the even and the odd chain seem more and more alike as the distance $R > 0$ grows. Thus in the beginning, the two independent chains have the same spectrum leading to a huge degeneracy of the states on top of the already fourfold degeneracy stemming from the impurities. The flow is from the free impurity fixed point, where each state is fourfold degenerate, to the delocalised fixed point with infinite Δ in the single ground state of the impurities and otherwise free chains. For the logarithmic discretisation a value of $\Lambda = 2$ was chosen. Further NRG parameters were $N_{\text{kept}} = 200$, $N_{b,e/o}(0) = 50$ and $N_{b,e/o} = 12$ in case of finite distances $R > 0$. For $R = 0$ the odd bath does not enter and we chose $N_{b,e}(0) = 50$, $N_{b,e} = 16$ and $N_{\text{kept}} = 500$.

Localised fixed points at finite distances

In case of strong coupling between the impurities and the dissipative environment, the tunnelling rate Δ on the impurities gets eventually renormalised to zero and the spectrum is again that of the two free chains, where each state is twofold degenerate. This corresponds to a situation, where the environmental oscillators are either positively or negatively displaced. As the displacement of the oscillators does not cost

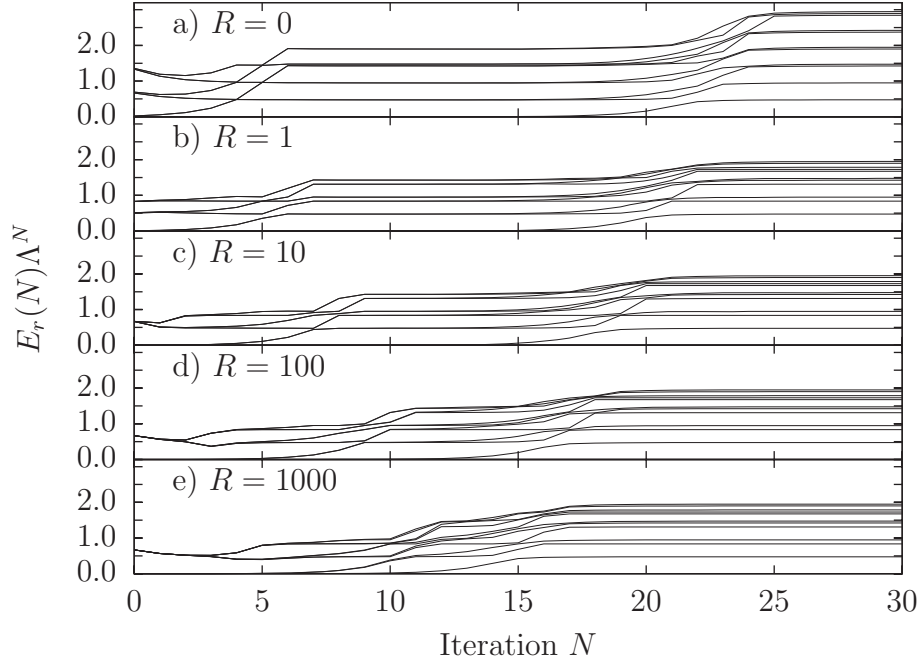


Figure 45:

Energy flow of the first eleven states above the ground state for an intermediate coupling of $\alpha = 10^{-2}$ and an initial tunnelling rate $\Delta = 10^{-4}$ for several distances R of the impurity-spins. The systems flow from the free impurity fixed point to the localised fixed point with a twofold degeneracy of all states. The energy scale at which the localised fixed point is reached drops as the distance R between the impurities is increased. From the localised fixed point, the flow is towards the delocalised fixed point at late iterations where the renormalised tunnelling rate $\tilde{\Delta}$ is large and the impurities are in their unique ground state. The energy scale at which the second transition happens grows with distance R and eventually the intermediate localised fixed point cannot be identified any longer when the scales of the two transitions become identical for distances R larger than 1000. Model parameters were the same as given in figure 44.

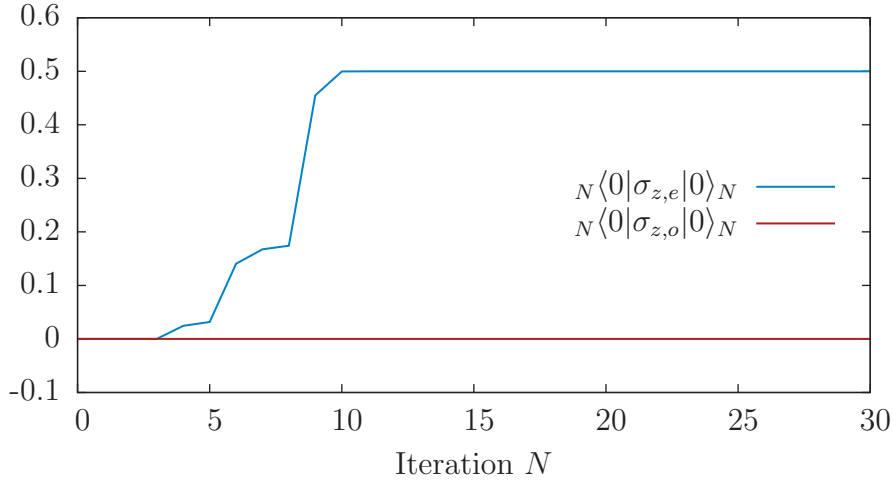


Figure 46:

Ground state expectation values of $N\langle 0|\sigma_{z,e}|0\rangle_N$ and $N\langle 0|\sigma_{z,o}|0\rangle_N$ for a coupling strength of $\alpha = 1$ and an inter-impurity distance $R = 1000$. While the spins in the even spin sector become polarised, those of the odd sector do not show any finite expectation value.

any energy, both configurations are energetically degenerate. For different couplings α , the oscillators are displaced by an amount that is proportional to $\sqrt{\alpha}$.

In the limit of infinite distance between the spins, each spin can be considered independently. For couplings larger than a critical value, each spin is localised in configuration $|\uparrow\rangle$ or $|\downarrow\rangle$. The oscillators in the environment are all displaced by an amount $\sim \pm\sqrt{\alpha}$. For the two anti-parallel spin configurations $|\uparrow\rangle_1 \otimes |\downarrow\rangle_2$ and $|\downarrow\rangle_1 \otimes |\uparrow\rangle_2$, there can be no net displacement of the oscillators, as their opposite amplitudes cancel. These two configurations are effectively projected out in the NRG flow for finite distances. This can be seen in figure 46, where the expectation values $N\langle 0|\sigma_{z,e}|0\rangle_N$ and $N\langle 0|\sigma_{z,o}|0\rangle_N$ are presented for a large distance of $R = 1000$ between the spins. The even spin configuration shows a finite expectation value, which grows until it reaches 0.5 once the state is fully localised. There the expectation value $N\langle 0|\sigma_{z,o}|0\rangle_N$ vanishes numerically exact to zero, suggesting that the odd spin sector has indeed been projected out of the Hamiltonian. In figure 47 the localised fixed point spectrum can be seen for a coupling strength of $\alpha = 1$ and different distances R . There, two states rise in their energy in early iterations, starting at zero energy, until they are eventually projected out of the system.

In the following, results for the impurity scattering matrix $\mathcal{T}_{2\text{sbm}}(\omega)$ in the delocalised phase of the system are presented. Additionally the expectation values for the change of the average site occupation and the oscillator displacement in the environment are discussed.

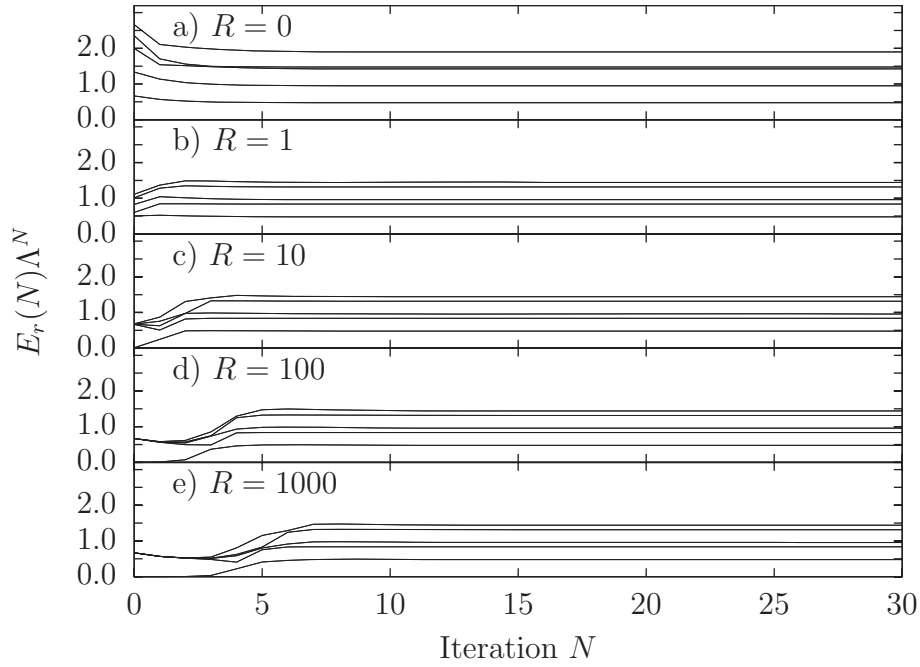


Figure 47:

Energy flow of the first eleven states above the ground state for a large coupling of $\alpha = 1 > \alpha_c(R)$ and an initial tunnelling rate $\Delta = 10^{-4}$ for several distances R of the impurity-spins. Here the system stays always in the localised phase where the spins are completely frozen out. The spectrum is that of the two free chains where now each state is twofold degenerate. As the distance R increases, the region where the two chains look identical increases as the energy scale at which they start to differ decreases. Model parameters were the same as given in figure 44.

6.2.4. Impurity scattering matrix and local averages

The impurity scattering matrix $\mathcal{T}_{2\text{sbm}}(\omega)$ for the two-spin-boson model is a 2×2 matrix of frequency dependent, complex functions. It is defined as

$$\mathcal{T}_{2\text{sbm}}(z)_{ij} = \frac{\sqrt{\alpha_i \alpha_j}}{4} \langle\langle \sigma_{z,i}, \sigma_{z,j} \rangle\rangle_z, \quad i, j = 1, 2 \quad (6.37)$$

in the complex plane and has been derived in section 3.4, equation (3.49). Here the temperature dependence is dropped as only the zero temperature limit is considered. As the two impurity spins are equal, the scattering matrix shows the symmetries $\mathcal{T}_{2\text{sbm}}(z)_{11} = \mathcal{T}_{2\text{sbm}}(z)_{22}$ and $\mathcal{T}_{2\text{sbm}}(z)_{12} = \mathcal{T}_{2\text{sbm}}(-z)_{21}$. Hence, only the imaginary part of the two independent functions $\mathcal{T}_{2\text{sbm}}(z)_{11}$ and $\mathcal{T}_{2\text{sbm}}(z)_{12}$, evaluated on the real axis, are presented in case of different distances between the spins. For the inter-impurity distances $R = 1, \dots, 1000$ studied in this thesis, the two functions show always similar

trends as the coupling strength approaches its critical value from below. Therefore, only the matrix elements in case of two typical distances $R = 10$ and $R = 100$ are presented in the following, to exemplify this similarity.

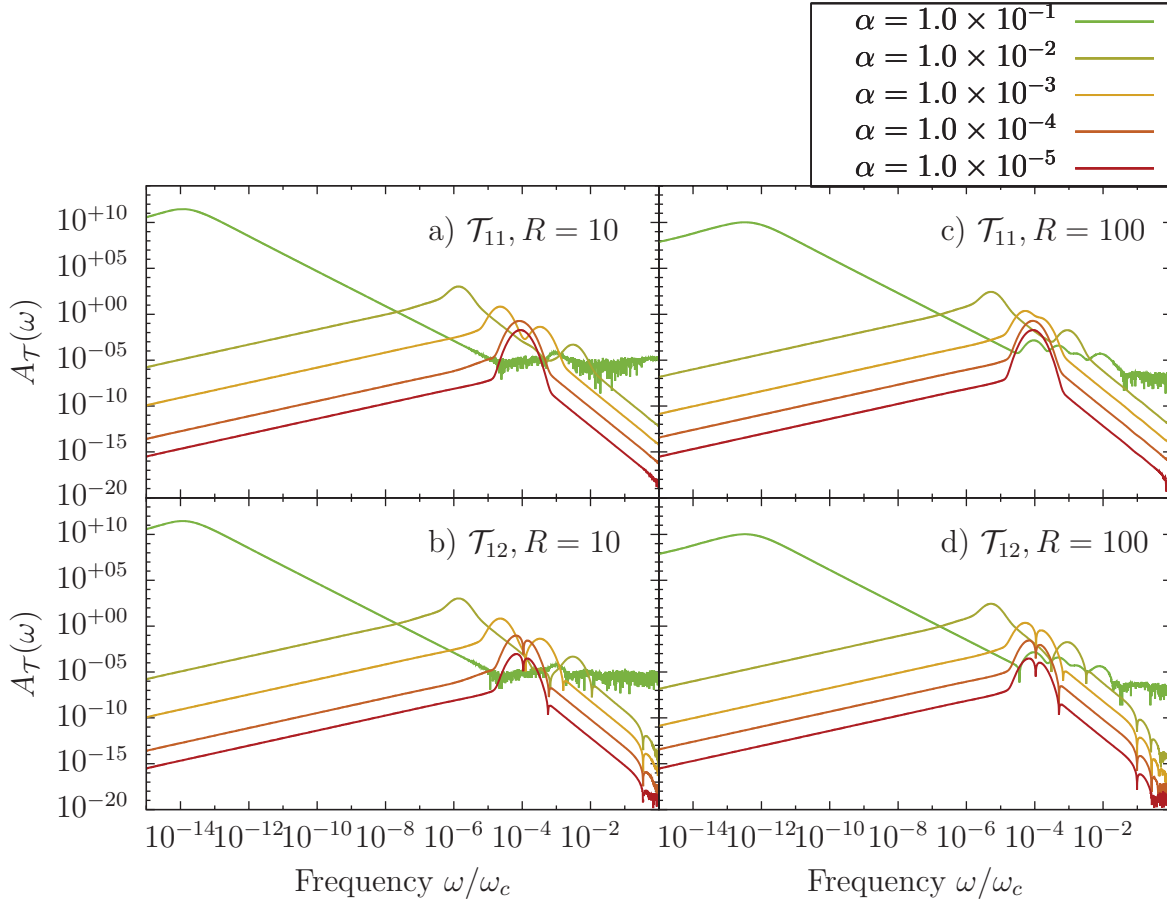


Figure 48:

Comparison of the scattering matrix elements $\mathcal{T}_{2\text{sbm}}(\omega)_{11}$ (top) and $|\mathcal{T}_{2\text{sbm}}(\omega)_{12}|$ (bottom) for two distances $R = 10$ and $R = 100$ between the impurities and several values of α . The general behaviour of the two scattering matrix components is similar, where $\mathcal{T}_{2\text{sbm}}(\omega)_{12}$ additionally features sharp kinks where its sign changes. At small couplings, the impurities remain free and the single energy scale Δ is resolved in the scattering matrix. As the coupling of the environment to the impurities is increased, the single peak splits into two. The lower energy peak is broadened and shifted to lower frequencies as the coupling becomes larger. This peak is assigned to a renormalized tunnelling frequency Δ .

Figure 48 presents the imaginary parts of the scattering matrix elements $\mathcal{T}_{2\text{sbm}}(\omega)_{11}$ and $\mathcal{T}_{2\text{sbm}}(\omega)_{12}$ in the positive frequency range for distances $R = 10$ and $R = 100$. As the off-diagonal element $\mathcal{T}_{2\text{sbm}}(\omega)_{12}$ is a non-local correlation function, whose imaginary part is not strictly positive or negative, only its modulus is presented. The chosen couplings α between impurities and environment cover several orders of magnitude and the limit of the free impurities can be seen for $\alpha = 10^{-5}$ in both cases. In the diagonal element $\mathcal{T}_{2\text{sbm}}(\omega)_{11}$, a single peak at the bare frequency $\Delta = 10^{-4}$ arises, which is split for larger values of the coupling. One of the arising peaks is shifted to larger frequencies. At the same time its total weight is lowered. The second peak arising for intermediate couplings is shifted to lower frequencies and broadened. At the same time its maximal height increases as the critical coupling α_c , corresponding to the transition to the localised phase, is approached from below. This second, low-energy peak is assigned to the renormalized tunnelling rate Δ . The same general behaviour is seen in the off-diagonal element $\mathcal{T}_{2\text{sbm}}(\omega)_{12}$, which furthermore shows several changes of sign, situated at the sharp kinks in the curves.

The changes in the local averages of the environmental oscillator are calculated via

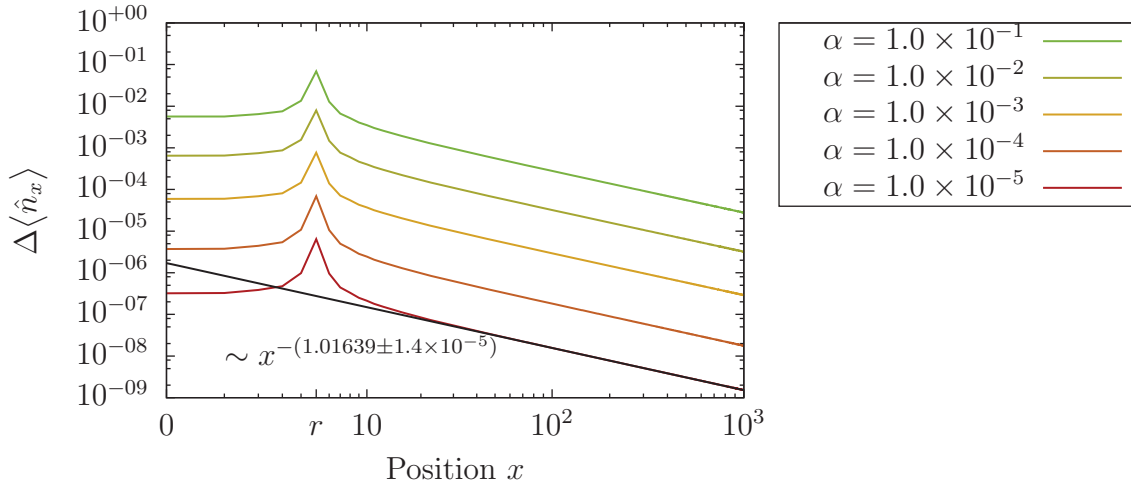
$$\Delta \langle \hat{n}_x \rangle = \frac{1}{\pi} \int_{-\infty}^0 \text{Im}[(G_{x,r}^{(0)}(\omega), G_{x,-r}^{(0)}(\omega)) \mathcal{T}_{2\text{sbm}}(\omega, T=0) (G_{r,x}^{(0)}(\omega), G_{-r,x}^{(0)}(\omega))^T] d\omega \quad (6.38)$$

and

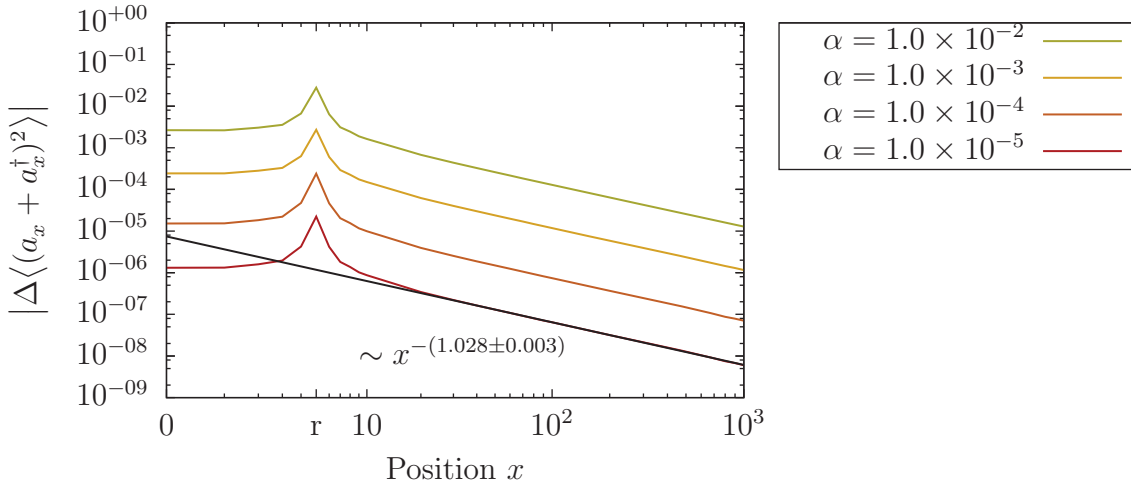
$$\Delta \langle (a_x + a_x^\dagger)^2 \rangle = \frac{1}{\pi} \int_{-\infty}^0 \text{Im}[(D_{x,r}^{(0)}(\omega), D_{x,-r}^{(0)}(\omega)) \mathcal{T}_{2\text{sbm}}(\omega, T=0) (D_{r,x}^{(0)}(\omega), D_{-r,x}^{(0)}(\omega))^T] d\omega \quad (6.39)$$

as derived in sections 3.4 and 3.5, respectively. The results for the change in the average site occupation are presented in figures 49 and 51 for the distances $R = 10$ and $R = 100$, respectively. As the change of the displacement amplitude $\Delta \langle (a_x + a_x^\dagger)^2 \rangle$ shows strong fluctuations of the sign between the impurities, figures 50 and 52 present its modulus.

Both changes in the averages show clear peaks right at the location of the impurities ($r = \pm 5$ and $r = \pm 50$). The magnitude of the change scales with the coupling strength between impurities and environment in all cases. Therefore, close below the transition from the delocalised to the localised phase, the oscillator occupation and its displacement represent strong signals within the environment, in the vicinity of the impurities.


Figure 49:

Change of the average site occupation in the environment for a finite inter-impurity distance $R = 10$ and several couplings α . A clear peak is seen at the position $r = 5$ where impurity σ_1 resides. The amplitude of the curves scales with the coupling α and for large distances a power-law drop $\sim x^{-1}$ is seen for the different curves. At the origin of the chain, right in between the two impurities, a comparably large finite signal remains.


Figure 50:

Modulus of the average change in the oscillator displacement amplitude for a finite inter-impurity distance $R = 10$ and several couplings α . A clear peak is seen at the position $r = 5$ where impurity σ_1 resides. The data show the same qualitative behaviour as the results for the change of the average site occupation in figure 49.

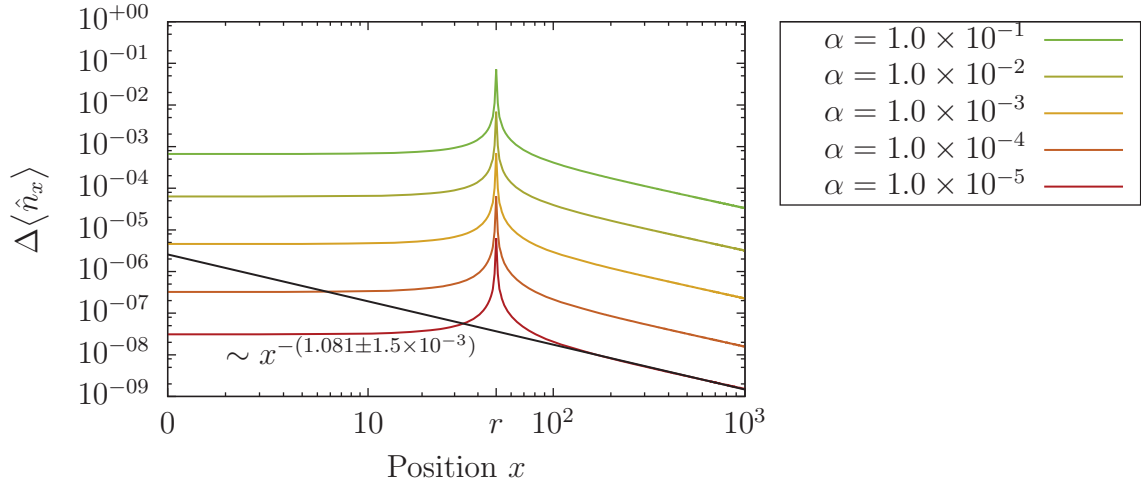


Figure 51:

Change of the average site occupation in the environment for a finite inter-impurity distance $R = 100$ and several couplings α . The same general behaviour is seen as for a distance of $R = 10$ that has been presented in figure 50.

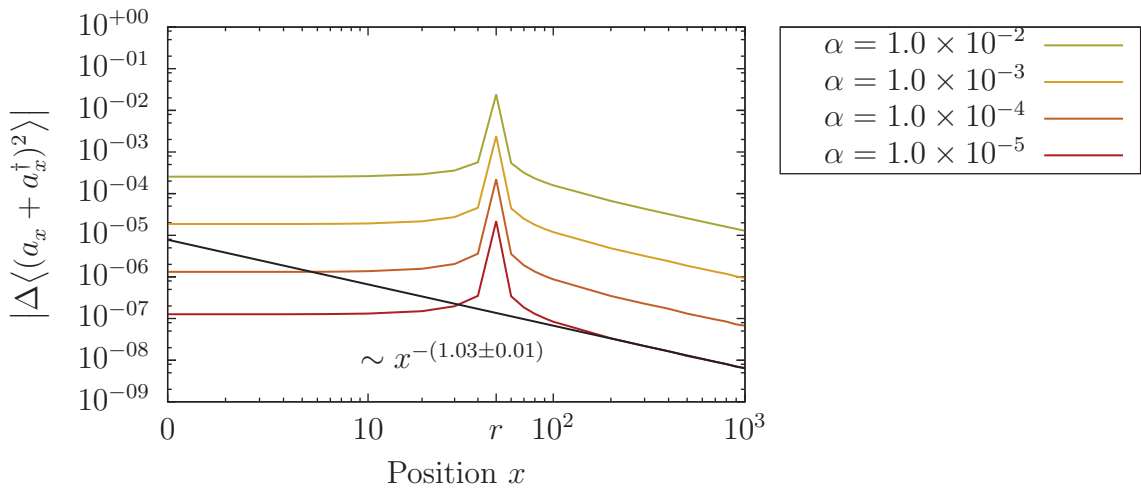


Figure 52:

Modulus of the average change in the oscillator displacement amplitude for a finite inter-impurity distance $R = 10$ and several couplings α . A clear peak is seen at the position $r = 5$ where impurity σ_1 resides. The same general behaviour is seen as for a distance of $R = 10$ that has been presented in figure 50.

6.2.5. Conclusion

The impurities affect the environmental oscillators in the region between each other to a considerable amount. There the total strengths of the signals drop about one to two orders of magnitude in comparison to the peak signal, but they remain large compared to the outer region. Thus, the two impurities appear to be connected via their common environment in real-space, although no initial direct coupling was present in the calculations. As the distance between the impurities is large in units of the lattice spacing, this connection between the impurities by means of their common environment may prove important when constructing a multi qubit quantum register.

The original motivation to investigate the effect of the two impurities on their environment was to answer the question, whether a characteristic length scale can be assigned to the impurities as they interact with their environment. Such a length scale can arise in two possible scenarios. If the drop far away from the impurity is exponential, a typical length scale can be assigned. At this length, the signal has dropped to $1/e$ of its initial strength. Alternatively, an abrupt change in the averages can occur as an intrinsic length scale of the problem is surpassed.

In this work, the signals investigated within the dissipative environment rule out the first scenario. Far away from the impurities, their effects on the environmental oscillators diminishes in a power-law manner as x^{-1} with small corrections in the exponent only. The power-law corresponds to the drop of the zero frequency value in the real part of the bare propagators $G_{x,0}^{(0)}(\omega = 0)$ and $D_{x,0}^{(0)}(\omega = 0)$ as a function of distance x . To clarify whether a length scale might arise farther away from the impurities, the local averages need to be calculated for larger distances x than investigated in this thesis.





Summary

In this work two dissipative quantum impurity models have been investigated. For the dissipative environment a linear one-dimensional chain of bosons was used that features an ohmic spectrum. This environment was chosen as it allows to calculate thermal averages as a function of the distance to the impurities. The main goal was to determine, to what extent two impurities that are coupled to a common environment can interact with each other through that environment. For a quantum register it is crucial to ensure precise control of the different qubits; interaction effects mediated by the common environment may spoil the functionality of the register.

To model two qubits in a common environment, the well studied two-spin-boson model was extended to finite inter-impurity distances. A meaningful description of this model requires the treatment of two local bosonic channels, which is computationally very demanding. To treat the two-spin-boson model in case of finite distances between the impurities, a bosonic two channel Numerical Renormalization Group method (NRG) has been devised in this work, which is capable of dealing with the model in the whole range from zero to large finite distances.

It was successfully tested on a different quantum impurity model, namely the dissipative oscillator model, which is known to have two well behaved limits. The limits of zero and infinite self-interaction of the impurity oscillator have been recovered in this thesis with the newly devised NRG method. At the same time, a whole line of quantum phase transitions was found to exist for all finite values of the self-interaction. This line separates a delocalised phase, where the impurity is free to oscillate with an average displacement of zero, and a phase where it is localised far away from its potential minimum.

From NRG calculations the different fixed points of the two-spin-boson model have been explored. There a localized phase with a twofold degenerate ground state and a delocalised phase with a unique ground state have been found for all investigated inter-impurity distances.

In both models, the changes of space dependent local averages in the environment have been calculated in order to investigate, whether characteristic length scales can be assigned to either a bosonic or magnetic impurity. The signals investigated were the change of the local site occupation in the chain and the change of the average displacement of the environmental oscillators. For almost all investigated parameters a power-law drop of the change in those signals has been found, leading to the conclusion that no such length scale exists in the regions investigated in this work. The only exception is the dissipative oscillator model in the region of small to intermediate values of the self-interaction. In that region, further efforts are required to clarify the long distance behaviour of the two thermal averages.



Outlook

Two interesting effects were observed in this work, that call for more detailed investigations:

- i) The two-spin-boson model contains a line of quantum phase transitions, that separates the localised from the delocalised phase. Its dependence on the inter-impurity distance can eventually reveal the distance at which the two spins can be treated as being independent. Furthermore, thermodynamic quantities like the entropy or the systems specific heat have been neglected completely from the investigations in this work. Such quantities require a larger set of basis states than the two hundred that were kept in the calculations for the two-spin-boson model. The analysis of the scaling of the NRG algorithm with the number of states kept revealed a linear increase in memory and a quadratic increase in runtime. Therefore it is possible to investigate such quantities in the future with an increased amount of computational resources.
- ii) The change of the average displacement amplitude shows fluctuations in the dissipative oscillator model in case of intermediate self-interactions on the impurity oscillator. These fluctuations might be due to numerical issues in the evaluation of the relevant integrals and smoothed spectral functions. If they can be identified as such, a true length scale of the impurity oscillator could be identified. Thus, it is desirable to further investigate the origin of the fluctuations. Numerical issues may be excluded by performing the calculations with higher precision.

The two-channel NRG devised in this work is well suited to study the situation of a single spin coupled to two rivalling dissipative environments. This model is known to show so-called *frustration of decoherence* if the coupling to the two environments is identical. None of the two environments is capable of localizing the spin in either of its configurations in such a scenario[39].



A. Impurity displacement-displacement correlation function

Here it is derived, how the displacement-displacement correlation function in the harmonic oscillator can be obtained using the *equations of motion*. Thereby its connection to other correlation functions is obtained. The correlator of interest reads

$$D_{\text{imp}}(z, T) = \langle\langle b + b^\dagger, b + b^\dagger \rangle\rangle_z(T) \quad (\text{A.1})$$

and is proportional to the impurity's scattering matrix $\mathcal{T}_{\text{do}}(z, T)$. The Hamiltonian of the damped harmonic oscillator model was given by

$$\begin{aligned} H = & \frac{\epsilon}{2}(b + b^\dagger) + \Delta\left(\hat{n}_b + \frac{1}{2}\right) + \frac{U}{2}\hat{n}_b(\hat{n}_b - 1) \\ & + \int_{-\pi}^{\pi} \omega(k)a_k^\dagger a_k + \frac{1}{2}\sqrt{\frac{\alpha}{2\pi}}(b + b^\dagger) \int_{-\pi}^{\pi} (a_k + a_k^\dagger)dk. \end{aligned} \quad (\text{A.2})$$

The Hamiltonian is split into a free part H_0 and an interaction part V as

$$H_0 = \frac{\epsilon}{2}(b + b^\dagger) + \Delta\left(\hat{n}_b + \frac{1}{2}\right) + \int_{-\pi}^{\pi} \omega(k)a_k^\dagger a_k \quad (\text{A.3})$$

$$V = \frac{U}{2}\hat{n}_b(\hat{n}_b - 1) + \frac{1}{2}\sqrt{\frac{\alpha}{2\pi}}(b + b^\dagger) \int_{-\pi}^{\pi} (a_k + a_k^\dagger)dk \quad (\text{A.4})$$

such that both, the bath and the impurity are non-interacting. The direct interaction of the impurity with itself is then due to the density-density interaction $\sim U$ and the interaction with the bath modes is due to the second term in V . First of all the free displacement-displacement correlators $D_{\text{imp}}^{(0)}(z)$ of the impurity and $D^{(0)}(x=0, z)$ of the bath at the origin are calculated. Here all correlators with respect to the free Hamiltonian H_0 wear an index (0) . Applying the equation of motion (3.11) twice on either $D_{\text{imp}}^{(0)}(z)$ or $D^{(0)}(x=0, z)$ immediately leads to

$$\begin{aligned} D_{\text{imp}}^{(0)}(z) &= \langle\langle b + b^\dagger, b + b^\dagger \rangle\rangle_z = \langle\langle b, b^\dagger \rangle\rangle_z + \langle\langle b^\dagger, b \rangle\rangle_z \\ &= \frac{1}{z - \Delta} - \frac{1}{z + \Delta} \end{aligned} \quad (\text{A.5})$$

and

$$\begin{aligned} D^{(0)}(x=0, z) &= \langle\langle a_0 + a_0^\dagger, a_0 + a_0^\dagger \rangle\rangle_z = \langle\langle a_0, a_0^\dagger \rangle\rangle_z + \langle\langle a_0^\dagger, a_0 \rangle\rangle_z \\ &= \frac{1}{2\pi} \int_{-\pi}^{\pi} \langle\langle a_k + a_k^\dagger, a_k + a_k^\dagger \rangle\rangle_z dk \\ &= \frac{1}{2\pi} \int_{-\pi}^{\pi} \frac{1}{z - \omega(k)} - \frac{1}{z + \omega(k)} dk. \end{aligned} \quad (\text{A.6})$$

Omitting in the notation the temperature dependence (T), the following set of equations is obtained for the full correlation functions:

$$zD_{\text{imp}}(z) = \Delta \langle\langle b - b^\dagger, b + b^\dagger \rangle\rangle_z + U \langle\langle b^\dagger bb, b + b^\dagger \rangle\rangle_z - U \langle\langle b^\dagger b^\dagger b, b + b^\dagger \rangle\rangle_z \quad (\text{A.7})$$

$$z \langle\langle b - b^\dagger, b + b^\dagger \rangle\rangle_z = 2 + \Delta D_{\text{imp}}(z) + \int_{-\pi}^{\pi} \langle\langle a_k + a_k^\dagger, b + b^\dagger \rangle\rangle_z dk + U \langle\langle b^\dagger bb, b + b^\dagger \rangle\rangle_z + U \langle\langle b^\dagger b^\dagger b, b + b^\dagger \rangle\rangle_z \quad (\text{A.8})$$

$$\int_{-\pi}^{\pi} \langle\langle a_k + a_k^\dagger, b + b^\dagger \rangle\rangle_z dk = \frac{\alpha}{2} D^{(0)}(x=0, z) D_{\text{imp}}(z) \quad (\text{A.9})$$

Using the results (A.9) and (A.8) in equation (A.7) and solving for $D_{\text{imp}}(z, T)$ (with restored notation of the temperature dependence) leads to

$$D_{\text{imp}}(z, T) = \left[D_{\text{imp}}^{(0)}(z)^{-1} - \frac{\alpha}{4} D^{(0)}(x=0, z) - U[\Sigma_1(z, T) + \Sigma_2(z, T)] \right]^{-1}. \quad (\text{A.10})$$

Here the two self-energy functions

$$\Sigma_1(z, T) = \frac{\Delta + z}{2\Delta} \frac{\langle\langle b^\dagger bb, b + b^\dagger \rangle\rangle_z(T)}{D_{\text{imp}}(z, T)} \quad (\text{A.11})$$

$$\Sigma_2(z, T) = \frac{\Delta - z}{2\Delta} \frac{\langle\langle b^\dagger b^\dagger b, b + b^\dagger \rangle\rangle_z(T)}{D_{\text{imp}}(z, T)} \quad (\text{A.12})$$

are defined that enter the full displacement-displacement correlator due to the finite self-interaction with a strength of U .

B. Calculation of the ξ_n

Here it is argued, that the parameters ξ_n of the logarithmically discretised Hamiltonian, introduced in equation (5.12), can be calculated from

$$\xi_n = \int_{I_n} \omega J(\omega) d\omega \Big/ \int_{I_n} J(\omega) d\omega \quad (\text{B.1})$$

for each interval $I_n = (x_{n+1}, x_n]$ independently. The proof itself is mainly based on a geometric interpretation of the integrals appearing in (5.12)⁵. Starting from the definition (5.12)

$$\xi_n = \frac{1}{d_n} \int_{I_n} g(\omega) d\omega \quad (\text{B.2})$$

the integral over $g(\omega) = \nu$ can be expressed as an integral over its inverse function $\epsilon(\nu) = \omega$. The function ϵ has the boundary values $\epsilon(x_m) = x_m$ both for $m = n, n + 1$ in interval I_n if the function h is chosen appropriately. Likewise, it is $g(x_m) = x_m$ for $m = n, n + 1$ in interval I_n since g is the inverse function to ϵ . The derivative of $\epsilon(\nu)$ was related to the spectral density $J(\nu)$ by

$$J(\nu) = \pi h^2(\epsilon(\nu)) \left| \frac{d\epsilon(\nu')}{d\nu'} \right|_{\nu'=\nu} \quad (\text{B.3})$$

The function h was chosen to be a constant $h_n = \left(\int_{I_n} J(\omega) d\omega / (\pi d_n) \right)^{1/2}$ in each interval I_n . Solving for the derivative $\epsilon'(\nu)$ leads to

$$\epsilon'(\nu) = J(\nu) d_n \Big/ \int_{I_n} J(\omega) d\omega, \quad \nu \in I_n \quad (\text{B.4})$$

Integrating this equation over the whole interval I_n leads to

$$\epsilon(x_n) - \epsilon(x_{n+1}) = \int_{I_n} J(\nu) d_n d\nu \Big/ \int_{I_n} J(\omega) d\omega = d_n = x_n - x_{n+1}. \quad (\text{B.5})$$

A comparison of the coefficients leads to $\epsilon(x_m) = x_m$ up to a constant both for $m = n, n + 1$. This constant can be set to zero since it does not enter the spectral function $J(\nu)$ anyway. A sketch both of g and ϵ is presented in figure 53. The two areas A and B depicted in that figure are connected as

$$A + B = x_n^2 - x_{n+1}^2. \quad (\text{B.6})$$

⁵Private communications with Priv. Doz. Dr. Ralf Bulla, University of Cologne, Germany.

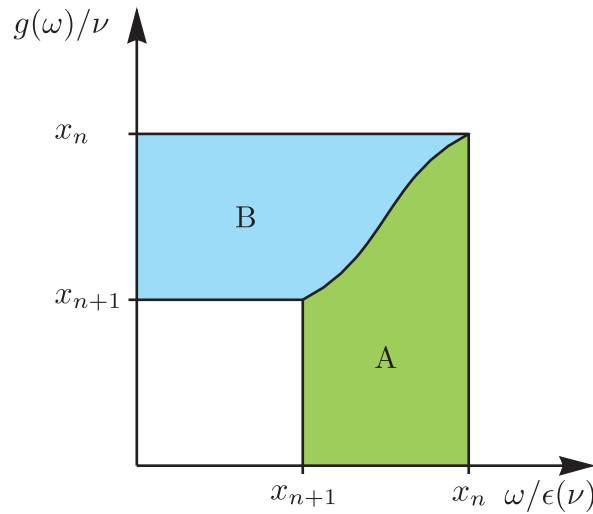


Figure 53:

Schematics of the functional behaviour of $g(\omega) = \nu$ in the ω interval $I_n = (x_{n+1}, x_n]$. The area A corresponds to the integral $\int_{I_n} g(\omega)d\omega$. At the same time, the function drawn is the inverse function $\epsilon(\nu) = \omega$ of g in the ν interval I_n . That way the area B corresponds to the integral $\int_{I_n} \epsilon(\nu)d\nu$.

On the other hand, A is given by the integral $\int_{I_n} g(\omega)d\omega$ while B is given by the integral $\int_{I_n} \epsilon(\nu)d\nu$. Using these integrals, equation (B.6) can be rewritten as

$$\begin{aligned} \int_{I_n} g(\omega)d\omega &= x_n^2 - x_{n+1}^2 - \int_{I_n} \epsilon(\nu)d\nu \\ &= x_n^2 - x_{n+1}^2 - \epsilon(\nu)\nu \Big|_{x_{n+1}}^{x_n} + \int_{I_n} \nu\epsilon'(\nu)d\nu. \end{aligned} \quad (\text{B.7})$$

In the last equation a partial integration of $\epsilon(\nu) \times 1$ was performed. The surface term $\epsilon(\nu)\nu \Big|_{x_{n+1}}^{x_n}$ exactly cancels the term $x_n^2 - x_{n+1}^2$ resulting in

$$\int_{I_n} g(\omega)d\omega = \int_{I_n} \nu\epsilon'(\nu)d\nu. \quad (\text{B.8})$$

By using equation (B.4) to replace $\epsilon'(\nu)$, equation (B.2) transforms to

$$\xi_n = \frac{1}{d_n} \int_{I_n} g(\omega)d\omega = \int_{I_n} \nu J(\nu)d\nu \Big/ \int_{I_n} J(\omega)d\omega \quad (\text{B.9})$$

which, up to relabelling of $\nu \rightarrow \omega$ is the initial identity to be shown.



References

- [1] M. Abramowitz and I. A. Stegun.
Handbook of Mathematical Functions with Formulas, Graphs, and Mathematical Tables.
Dover, 1964.
- [2] V. Achter, S. Borowski, L. Nieroda, L. Packschies, and V. Winkelmann.
CHEOPS Brief Instructions, Version 07.10.2013.
RRZK, University of Cologne, Oct 2013.
<http://rrzk.uni-koeln.de/cheops.html>.
- [3] A. Altland and B. D. Simons.
Condensed Matter Field Theory.
Cambridge University Press, second edition, 2010.
- [4] F. B. Anders and A. Schiller.
Spin precession and real-time dynamics in the Kondo model: Time-dependent numerical renormalization-group study.
Phys. Rev. B, 74:245113, Dec 2006.
- [5] E. Anderson, Z. Bai, C. Bischof, S. Blackford, J. Demmel, J. Dongarra, J. Du Croz, A. Greenbaum, S. Hammarling, A. McKenney, and D. Sorensen.
LAPACK Users' Guide Third Edition.
Society for Industrial and Applied Mathematics, Aug 1999.
http://www.netlib.org/lapack/lug/lapack_lug.html.
- [6] E. Anderson, Z. Bai, and J. Dongarra.
Generalized QR factorization and its applications.
Linear Algebra and its Applications, 162-164(0):243–271, 1992.
- [7] W. Appel.
Mathematics for Physics & Physicists.
Princeton University Press, Princeton and Oxford, 2007.
- [8] R. Bulla.
Zero Temperature Metal-Insulator Transition in the Infinite-Dimensional Hubbard Model.
Phys. Rev. Lett., 83:136–139, Jul 1999.
- [9] R. Bulla, T. A. Costi, and T. Pruschke.
Numerical renormalization group method for quantum impurity systems.
Rev. Mod. Phys., 80:395–450, Apr 2008.
- [10] R. Bulla, T. A. Costi, and D. Vollhardt.
Finite-temperature numerical renormalization group study of the Mott transition.
Phys. Rev. B, 64:045103, Jun 2001.



- [11] R. Bulla, A. C. Hewson, and T. Pruschke.
Numerical renormalization group calculations for the self-energy of the impurity Anderson model.
Journal of Physics: Condensed Matter, 10(37):8365, 1998.
- [12] R. Bulla, H.-J. Lee, N.-H. Tong, and M. Vojta.
Numerical renormalization group for quantum impurities in a bosonic bath.
Phys. Rev. B, 71:045122, Jan 2005.
- [13] R. Bulla, N.-H. Tong, and M. Vojta.
Numerical Renormalization Group for Bosonic Systems and Application to the Sub-Ohmic Spin-Boson Model.
Phys. Rev. Lett., 91:170601, Oct 2003.
- [14] A. W. Chin, Á. Rivas, S. F. Huelga, and M. B. Plenio.
Exact mapping between system-reservoir quantum models and semi-infinite discrete chains using orthogonal polynomials.
Journal of Mathematical Physics, 51(9):092109, Sep 2010.
- [15] F. Deppe, M. Mariani, E. P. Menzel, A. Marx, S. Saito, K. Kakuyanagi, H. Tanaka, T. Meno, K. Semba, H. Takayanagi, E. Solano, and R. Gross.
Two-photon probe of the jaynes-cummings model and controlled symmetry breaking in circuit QED.
Nat Phys, 4(9):686–691, Sep 2008.
- [16] R. P. Feynman.
Simulating physics with computers.
International Journal of Theoretical Physics, 21(6-7):467–488, 1982.
- [17] M. Friesen, P. Rugheimer, D. E. Savage, M. G. Lagally, D. W. van der Weide, R. Joynt, and M. A. Eriksson.
Practical design and simulation of silicon-based quantum-dot qubits.
Phys. Rev. B, 67:121301, Mar 2003.
- [18] M. Galpin, Apr 2014.
<http://galpin.chem.ox.ac.uk/index.shtml>.
- [19] B. Gardas.
Exact solution of the Schrödinger equation with the spin-boson Hamiltonian.
Journal of Physics A: Mathematical and Theoretical, 44(19):195301, 2011.
- [20] M. Gell-Mann and F. E. Low.
Quantum electrodynamics at small distances.
Phys. Rev., 95:1300–1312, Sep 1954.
- [21] M. Greiner, O. Mandel, T. Esslinger, T. W. Hansch, and I. Bloch.
Quantum phase transition from a superfluid to a mott insulator in a gas of ultracold atoms.
Nature, 415(6867):39–44, Jan 2002.



- [22] C. Guo, A. Weichselbaum, J. von Delft, and M. Vojta.
Critical and strong-coupling phases in one- and two-bath spin-boson models.
Phys. Rev. Lett., 108:160401, Apr 2012.
- [23] C. Guo, A. Weichselbaum, J. von Delft, and M. Vojta.
Supplementary information for "critical and strong-coupling phases in one- and two-bath spin-boson models".
Phys. Rev. Lett., 108:160401, Apr 2012.
- [24] E. Gärtner.
Coupled Qubits in a Dissipative Environment: A Numerical Renormalization Group Approach to the Two-Spin-Boson Model.
Diploma thesis, University of Cologne, May 2010.
- [25] Intel Corporation.
Reference Manual for Intel® Math Kernel Library 11.1 Update 2, 2014.
http://software.intel.com/en-us/mkl_11.1_ref.
- [26] H. R. Krishna-murthy, J. W. Wilkins, and K. G. Wilson.
Renormalization-group approach to the Anderson model of dilute magnetic alloys. I. Static properties for the symmetric case.
Phys. Rev. B, 21:1003–1043, Feb 1980.
- [27] A. J. Leggett, S. Chakravarty, A. T. Dorsey, M. P. A. Fisher, A. Garg, and W. Zwerger.
Dynamics of the dissipative two-state system.
Rev. Mod. Phys., 59:1–85, Jan 1987.
- [28] R. B. Lehoucq, D. C. Sorensen, and C. Yang.
ARPACK Users' Guide: Solution of Large Scale Eigenvalue Problems with Implicitly Restarted Arnoldi Methods, Oct 1997.
<http://www.caam.rice.edu/software/ARPACK/UG/ug.html>.
- [29] M. Lewenstein, A. Sanpera, V. Ahufinger, B. Damski, A. Sen(De), and U. Sen.
Ultracold atomic gases in optical lattices: mimicking condensed matter physics and beyond.
Advances in Physics, 56(2):243–379, 2007.
- [30] M. Metcalf, J. Reid, and M. Cohen.
Modern Fortran explained.
Numerical Mathematics and Scientific Computation. Oxford University Press, seventh edition, 2011.
- [31] W. Metzner and D. Vollhardt.
Correlated Lattice Fermions in $d = \infty$ Dimensions.
Phys. Rev. Lett., 62:324–327, Jan 1989.
- [32] A. K. Mitchell.



- Two-channel Kondo phases in coupled quantum dots.*
PhD thesis, University of Oxford, Trinity, 2009.
- [33] A. K. Mitchell, M. R. Galpin, S. Wilson-Fletcher, D. E. Logan, and R. Bulla.
Generalized Wilson Chain for solution of multichannel quantum impurity problems.
arXiv:1308.1903 [cond-mat], Aug 2013.
- [34] J. E. Moore.
The birth of topological insulators.
Nature, 464(7286):194–198, Mar 2010.
- [35] V. Mourik, K. Zuo, S. M. Frolov, S. R. Plissard, E. P. a. M. Bakkers, and L. P. Kouwenhoven.
Signatures of majorana fermions in hybrid superconductor-semiconductor nanowire devices.
Science, 336(6084):1003–1007, May 2012.
PMID: 22499805.
- [36] M. A. Nielsen and I. L. Chuang.
Quantum Computation and Quantum Information.
Cambridge University Press, New York, NY, USA, 2000.
- [37] Nobelprize.org.
The nobel prize in physics 1982.
http://www.nobelprize.org/nobel_prizes/physics/laureates/1982/, Dec 2013.
- [38] Nobelprize.org.
The nobel prize in physics 2012.
http://www.nobelprize.org/nobel_prizes/physics/laureates/2012/, Apr 2014.
- [39] E. Novais, A. H. Castro Neto, L. Borda, I. Affleck, and G. Zarand.
Frustration of decoherence in open quantum systems.
Phys. Rev. B, 72:014417, Jul 2005.
- [40] W. C. Oliveira and L. N. Oliveira.
Generalized numerical renormalization-group method to calculate the thermodynamical properties of impurities in metals.
Phys. Rev. B, 49:11986–11994, May 1994.
- [41] P. P. Orth, D. Roosen, W. Hofstetter, and K. Le Hur.
Dynamics, synchronization, and quantum phase transitions of two dissipative spins.
Phys. Rev. B, 82:144423, Oct 2010.
- [42] R. Peters, T. Pruschke, and F. B. Anders.



- Numerical renormalization group approach to Green's functions for quantum impurity models.
Phys. Rev. B, 74:245114, Dec 2006.
- [43] J. R. Petta, A. C. Johnson, J. M. Taylor, E. A. Laird, A. Yacoby, M. D. Lukin, C. M. Marcus, M. P. Hanson, and A. C. Gossard.
Coherent manipulation of coupled electron spins in semiconductor quantum dots.
Science, 309(5744):2180–2184, Sep 2005.
PMID: 16141370.
- [44] W. H. Press, S. A. Teukolsky, W. T. Vetterling, and B. P. Flannery.
Numerical Recipes in FORTRAN.
Cambridge University Press, second edition, 1992.
- [45] J. Rutter.
A serial implementation of cuppen's divide and conquer algorithm for the symmetric tridiagonal eigenproblem.
Computer Science Division Report UCB/CSD 94/799, University of California, Berkeley, 1994.
- [46] M. Vojta, N.-H. Tong, and R. Bulla.
Quantum Phase Transitions in the Sub-Ohmic Spin-Boson Model: Failure of the Quantum-Classical Mapping.
Phys. Rev. Lett., 94:070604, Feb 2005.
- [47] M. Vojta, N.-H. Tong, and R. Bulla.
Erratum: Quantum Phase Transitions in the Sub-Ohmic Spin-Boson Model: Failure of the Quantum-Classical Mapping [*Phys. Rev. Lett.* 94, 070604 (2005)].
Phys. Rev. Lett., 102:249904, Jun 2009.
- [48] D. Vollhardt.
Dynamical mean-field theory for correlated electrons.
Ann. Phys., 524:1–19, Jan 2012.
- [49] A. Wallraff, D. I. Schuster, A. Blais, L. Frunzio, R.-S. Huang, J. Majer, S. Kumar, S. M. Girvin, and R. J. Schoelkopf.
Strong coupling of a single photon to a superconducting qubit using circuit quantum electrodynamics.
Nature, 431(7005):162–167, Sep 2004.
- [50] A. Weichselbaum and J. von Delft.
Sum-Rule Conserving Spectral Functions from the Numerical Renormalization Group.
Phys. Rev. Lett., 99:076402, Aug 2007.
- [51] U. Weiss.



- Quantum Dissipative Systems*, volume 13 of *Series in Modern Condensed Matter Physics*.
World Scientific Publishing Co. Pte. Ltd., third edition, 2008.
- [52] K. G. Wilson.
The renormalization group: Critical phenomena and the Kondo problem.
Rev. Mod. Phys., 47:773–840, Oct 1975.
- [53] Wolfram.
Wolfram Mathematica 9 Documentation Center, 2014.
<http://reference.wolfram.com/mathematica/ref/FresnelS.html>.
- [54] Wolfram.
Wolfram Mathematica 9 Documentation Center, 2014.
<http://reference.wolfram.com/mathematica/tutorial/FourierTransforms.html>.
- [55] Wolfram.
Wolfram Mathematica 9 Documentation Center, 2014.
<http://reference.wolfram.com/mathematica/ref/NIntegrate.html>.
- [56] M. Yoshida, M. A. Whitaker, and L. N. Oliveira.
Renormalization-group calculation of excitation properties for impurity models.
Phys. Rev. B, 41:9403–9414, May 1990.
- [57] J. Zabludil, R. Hammerling, L. Szunyogh, and P. Weinberger.
Electron Scattering in Solid Matter A Theoretical and Computational Treatise.
Springer, 2005.



Danksagungen

An dieser Stelle ist es an der Zeit, mich bei allen Weggefährten der letzten Jahre zu bedanken, die mich in verschiedenster Form immer wieder unterstützt und aufgemuntert haben.

Mein Dank gilt insbesondere Priv. Doz. Dr. Ralf Bulla für die Betreuung der vorliegenden Arbeit und dafür, dass seine Türe stets offen und er mir mit Rat und Tat zur Seite stand.

Des Weiteren bedanke ich mich ganz herzlich bei Prof. Dr. Simon Trebst, der sich als Zweitgutachter für diese Arbeit zur Verfügung gestellt hat und der mich in die schöne neue Welt von Python eingeführt hat.

Danke auch an Prof. Dr. Thomas Michely und Priv. Doz. Dr. Markus Garst, die sich bereit erklärt haben, die Prüfungskommission zu vervollständigen.

Andreas Sindermann danke ich für die kompetente Führung unseres Institutsrechenzentrums und die schnelle Hilfe bei Userproblemen. Stefan Borowski aus dem Kölner Rechenzentrum danke ich für die fachkundige Beratung in Fragen der Ressourcennutzung und Routinenauswahl auf CHEOPS. Frau Gotzmann aus dem Dekanat danke ich für die unbürokratische und schnelle Hilfe rund um diese Promotion.

Vielen lieben Dank meinen Freunden und (ehemaligen) Arbeitskollegen: Karin Everschor-Sitte für unzählige gemeinsam gelöste Übungs- und sonstige Probleme, Zoobesuche und ihre unbändige Energie. Matthias Sitte für seine Hilfsbereitschaft in allen Fragen und bei den Fehlersuchen in Mathematica sowie für die konsequente Unterscheidung zwischen $.$, $.$ und $.$. Danke Lucas Hollender für die gemeinsamen Jahre im und außerhalb des Büros, auch wenn man sich zuletzt dank der großen Bildschirme aus den Augen verloren hatte. Vielen Dank Mario Zacharias für Organisation und Durchführung diverser lehrreicher Fahrten und Ausflüge in schöne deutsche Städte und deren Nachtleben und für das Tragen diverser Kisten und Möbel. Danke Carolin Küppersbusch und allen weiteren regelmäßigen Mitgliedern der Kaffeerrunde für angeregte Gespräche über Alles und Nichts und ein soziales Miteinander. Robert Bamler danke ich für seine offene, hilfsbereite Art, der ich unter anderem Korrekturvorschläge und aufgebaute Kleiderschränke zu verdanken habe. Danke Stefan Buhardt für das Engagement rund um die Bundesstadt! Bonn und die Korrekturlesungen. Danke Maximilian Genske für interessante Wettideen und ebenfalls für die Korrekturvorschläge. Christoph Schütte danke ich für die langen Fachsimpeleien über alle möglichen und unmöglichen Programmiersprachen. Danke Johannes Waizner für die schönen Kostproben auf dem Dudelsack. Fanny Groll danke ich für all die angenehmen Gespräche, die leider viel zu oft nur auf Tagungen stattgefunden haben. Danke Jan Müller für den unschätzbaren Pendelbetrieb bei unserem Umzug. Vielen Dank Johannes Helmes für die Einführung in dörfliche Bräuchtümer etwa rund um die Wartung von Hydranten. Danke Max Gerlach für diverse Hilfen rund um den Computer und angeregte Gespräche zu den Themen Kaffee und Fahrradfahren. Thank you, Andrew Mitchell



for all the endless discussion on the NRG, the English language and all the patience with my lack of applying its rules to written text.

Bevor ich mich bei weiteren Freunden und meiner Familie bedanke, ist es Zeit einem Menschen zu danken, der beides für mich ist. Meiner wunderbaren Exfreundin und Ehefrau Birthe Hülsen-Gärtner danke ich für all die gemeinsamen Momente. Für ihre Überzeugungskraft auch mal in Urlaub zu fahren und den Antrag bei den Riesenenten. Danke für deine Unterstützung, die ich über die Jahre erfahren durfte, nicht zuletzt in nächtelangen Korrektursitzungen.

Meinem Freundeskreis danke ich für das aufgebrachte Verständnis der letzten Jahre und die notwendige Zerstreung neben der Arbeit. Danke Martin und Anke Klemmstein für die langjährige Freundschaft und die uneingeschränkte Unterstützung in allen Lebenslagen (die unter anderem so ein Umzug mit sich bringt) und für all die Filmabende, bei denen irgendwie die Handlung zur Nebensache wurde. Danke Irina Eickel für die Verdienste um unsere mehr als gelungene Hochzeit und all die leckere (Probe)torten. Vielen Dank Kevin Weimar für den Beistand als Trauzeugen und all die endlosen Telefonate während deines Auslandssemesters. Danke Julia und Roman Litzinger für ausgiebige und anregende Unterhaltungen rund um die Themen Hochzeit und Familie. Danke auch allen anderen Monheimer, Leichlinger und Kölner Freunden, die ich hier nicht alle namentlich erwähne.

In meiner Familie gilt mein Dank zunächst meiner Schwester Sabrina. Danke für Rat und Tat, Süßigkeiten und Nächte voller Korrekturlesungen und für Verständnis in Dingen, die kein anderer Mensch nachvollziehen kann. Vielen Dank Vanessa, dass du trotz deiner Physiker-Geschwister so normal geblieben bist. Danke für die Bereitstellung der Wohnung an Karneval und deine unkomplizierte Art. Meiner Omma Emmi danke ich für die gemütliche Stube, ihre ehrliche Art, tolle Urlaube unter Spaniens Sonne und viele warme Socken im Winter. Danke Oma Else für die stete Versorgung mit Haselnusskranz, all die reich gefüllten und voll besetzten Tafeln in eurem Haus und für den fahrbaren Untersatz. Vielen Dank Tante Anita und Onkel Manfred für all das Fachwissen rund um die Themen Garten und Kochen.

Ich bin froh, dass die Zahl meiner Eltern bislang stets gewachsen ist, die so sehr um mein Wohlergehen besorgt sind. Danke Mama und Gerd für Taxidienste, einen stets vollen Kühlschrank und das mehr oder weniger gut sortierte Werkzeugangebot. Danke Papa und Waltraud für das ganzjährig geöffnete Naherholungsgebiet in Unterfranken. Für die uneingeschränkte Unterstützung, auch aus der Ferne, und die Versorgung mit Käse, Marmelade und Adventskalendern. Danke Doro und Bernhard für den schönen Hobbykeller, Anekdoten rund um das Sauerland und eure Top-Tochter und Trauzeugin par excellence Irina. Danke auch an meine Schwiegereltern Brigitte und Werner für Kaffee, laute Großfamilienfeste und den blauen Großtransporter - er wird in Zukunft schmerzlich vermisst werden. Meinen Schwägerinnen und Schwägern Jürgen, Thorsten, Ilka, Björn, Wiebke, Marco und Silke: Danke für eure tatkräftige Unterstützung, die offenen Türen (sofern man pünktlich ist), die Notfallversorgung mit Pommes aus der Fritteuse und das Vertrauen, mich zum Patenonkel zu machen. Danke auch mei-



nem Neffen Marvin und meiner Nichte und Patentochter Melissa für ihre unbändige Lebensfreude.

Und, last but not least: Danke Yvonne Alexandra Bothur für die Einführung in einige Feinheiten der englischen Sprache und für den Enthusiasmus, mich im Lachen stets zu übertönen.





Erklärung

Gemäß §4 Abs. (1) Nr. 9 der Promotionsordnung der Mathematisch-Naturwissenschaftlichen Fakultät der Universität zu Köln in der Fassung vom 2. Februar 2006.

Ich versichere, dass ich die von mir vorgelegte Dissertation selbständig angefertigt, die benutzten Quellen und Hilfsmittel vollständig angegeben und die Stellen der Arbeit – einschließlich Tabellen, Karten und Abbildungen –, die anderen Werken im Wortlaut oder dem Sinn nach entnommen sind, in jedem Einzelfall als Entlehnung kenntlich gemacht habe; dass diese Dissertation noch keiner anderen Fakultät oder Universität zur Prüfung vorgelegen hat; dass sie – abgesehen von unten angegebenen Teilpublikationen – noch nicht veröffentlicht worden ist sowie, dass ich eine solche Veröffentlichung vor Abschluss des Promotionsverfahrens nicht vornehmen werde. Die Bestimmungen der Promotionsordnung sind mir bekannt. Die von mir vorgelegte Dissertation ist von Priv. Doz. Dr. Ralf Bulla betreut worden.

Etienne Gärtner





Lebenslauf

Dipl.-Phys. Etienne Gärtner



Name	Etienne Gärtner
Geburtsdatum	09.06.1983
Geburtsort	Leverkusen
Nationalität	deutsch
Familienstand	verheiratet

Schul- und Hochschulbildung

Seit 09/2010	Promotionsstudium am Institut für Theoretische Physik der Universität zu Köln
10/2003 - 05/2010	Physikstudium an der Universität zu Köln
05/2010	Diplom in Physik
06/2006	Vordiplom in Physik
04/2004 - 05/2010	Mathematikstudium an der Universität zu Köln
10/2006	Vordiplom in Mathematik
1993 – 2002	Otto-Hahn-Gymnasium in Monheim am Rhein
06/2002	Abitur

Bisherige Tätigkeiten

Universität zu Köln

09/2010 - 04/2014	Wissenschaftlicher Mitarbeiter
07/2010 - 08/2010	Wissenschaftliche Hilfskraft
05/2006 - 05/2010	Studentische Hilfskraft

Zivildienst

08/2002 - 05/2003	Evangelisches Pflgeteam der Bergischen Diakonie Apprath in Monheim am Rhein
--------------------------	---





